

7-11-2013

# MOBILE, HYBRID COMPTON/CODED APERTURE IMAGING FOR DETECTION, IDENTIFICATION AND LOCALIZATION OF GAMMA-RAY SOURCES AT STAND-OFF DISTANCES

Shawn Tornga

Follow this and additional works at: [https://digitalrepository.unm.edu/ne\\_etds](https://digitalrepository.unm.edu/ne_etds)

---

## Recommended Citation

Tornga, Shawn. "MOBILE, HYBRID COMPTON/CODED APERTURE IMAGING FOR DETECTION, IDENTIFICATION AND LOCALIZATION OF GAMMA-RAY SOURCES AT STAND-OFF DISTANCES." (2013).  
[https://digitalrepository.unm.edu/ne\\_etds/3](https://digitalrepository.unm.edu/ne_etds/3)

This Dissertation is brought to you for free and open access by the Engineering ETDs at UNM Digital Repository. It has been accepted for inclusion in Nuclear Engineering ETDs by an authorized administrator of UNM Digital Repository. For more information, please contact [disc@unm.edu](mailto:disc@unm.edu).

**Shawn Robert Tornga**

*Candidate*

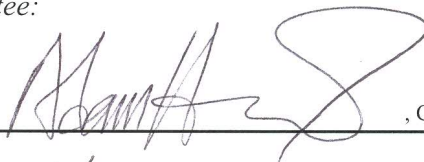
**Chemical and Nuclear Engineering**

*Department*

This dissertation is approved, and it is acceptable in quality and form for publication:

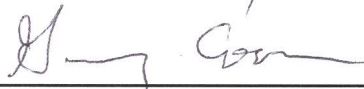
*Approved by the Dissertation Committee:*

**Adam Hecht**



, Chairperson

**Gary Cooper**



**Doug Fields**



**John Sullivan**



MOBILE, HYBRID COMPTON/CODED APERTURE IMAGING  
FOR DETECTION, IDENTIFICATION AND LOCALIZATION OF  
GAMMA-RAY SOURCES AT STAND-OFF DISTANCES

BY

SHAWN R. TORNGA

B.S. PHYSICS, MICHIGAN STATE UNIVERSITY, 2005

M.S. NUCLEAR ENGINEERING, UNIVERSITY OF NEW MEXICO, 2009

DISSERTATION

Submitted in Partial Fulfillment of the  
Requirements for the Degree of

Doctor of Philosophy

Engineering

The University of New Mexico

Albuquerque, New Mexico

May, 2013

ii

© 2013, Shawn Robert Tornga

# MOBILE, HYBRID COMPTON/CODED APERTURE IMAGING FOR DETECTION, IDENTIFICATION AND LOCALIZATION OF GAMMA-RAY SOURCES AT STANDOFF DISTANCES

By

Shawn R. Tornga

B.S., Physics, Michigan State University, 2005

M.S., Nuclear Engineering, University of New Mexico, 2009

Ph.D., Engineering, University of New Mexico, 2013

## ABSTRACT

The Stand-off Radiation Detection System (SORDS) program is an Advanced Technology Demonstration (ATD) project through the Department of Homeland Security's Domestic Nuclear Detection Office (DNDO) with the goal of detection, identification and localization of weak radiological sources in the presence of large dynamic backgrounds. The Raytheon-SORDS Tri-Modal Imager (TMI) is a mobile truck-based, hybrid gamma-ray spectroscopic and imaging system able to quickly detect, identify and localize, radiation sources at standoff distances through improved sensitivity provided by multiple detection modes while minimizing the false alarm rate. Reconstruction of gamma-ray sources is performed using a combination of gamma-ray spectroscopy and two imaging modalities; coded aperture and Compton scatter imaging. The TMI consists of 35 sodium iodide (NaI) crystals ( $5 \times 5 \times 2$  in<sup>3</sup> each), arranged in a random coded aperture mask array (CA), followed by 30 position sensitive NaI

bars ( $24 \times 2.5 \times 3 \text{ in}^3$  each) called the detection array (DA). The CA array acts as both a coded aperture mask and scattering detector for Compton events. The large-area DA array acts as a collection detector for both Compton scattered events and coded aperture events. In this thesis, the implemented spectroscopic, coded aperture, Compton and hybrid imaging algorithms will be described along with their performance. It will be shown that multiple imaging modalities can be fused to improve detection sensitivity over a broader energy range than any mode alone.

Since the TMI is a moving system, peripheral data, such as a Global Positioning System (GPS) and Inertial Navigation System (INS) must also be incorporated. A method of adapting static imaging algorithms to a moving platform has been developed. Also, algorithms were developed in parallel with detector hardware, through the use of extensive simulations performed with the Geometry and Tracking Toolkit v4 (GEANT4). Simulations have been well validated against measured data. Results of image reconstruction algorithms at various speeds and distances will be presented as well as localization capability. Utilizing imaging information will show signal-to-noise gains over spectroscopic algorithms alone.

# Contents

<b>1</b>	<b>INTRODUCTION</b>	<b>1</b>
1.1	Coded Aperture Imaging . . . . .	5
1.2	Compton Imaging . . . . .	5
1.3	Overview of Thesis . . . . .	6
<b>2</b>	<b>BACKGROUND</b>	<b>9</b>
2.1	Survey of Technology . . . . .	9
2.1.1	Coded Aperture Imaging . . . . .	9
2.1.2	Compton Scatter Imaging . . . . .	14
2.1.3	Considerations . . . . .	17
2.2	Radioactive Decay . . . . .	18
2.2.1	Alpha Decay . . . . .	18
2.2.2	Beta Decay . . . . .	19
2.2.3	Electron Capture . . . . .	20
2.3	Interaction Processes . . . . .	20
2.3.1	Photoelectric Absorption . . . . .	22
2.3.2	Compton Scattering . . . . .	22
2.3.3	Pair Production . . . . .	24
2.3.4	Doppler Broadening . . . . .	25
2.4	Summary . . . . .	25
<b>3</b>	<b>THE RAYTHEON-SORDS TRI-MODAL IMAGER</b>	<b>27</b>
3.1	Navigation Hardware . . . . .	29
3.1.1	Specifications . . . . .	30
3.1.2	GPS/INS Performance . . . . .	32
3.1.3	Validation . . . . .	32
3.2	Detector Hardware . . . . .	33
3.2.1	Active Coded Mask - The CA Array . . . . .	34
3.2.2	Absorption Elements - The DA Array . . . . .	39
3.3	Gain Matching . . . . .	43

3.4	Energy Calibration . . . . .	47
3.5	Position Calibration . . . . .	49
3.6	Front-end Electronics . . . . .	54
	3.6.1 Sensor Electronics . . . . .	56
	3.6.2 High-Voltage Electronics . . . . .	56
	3.6.3 Event Characterization Unit . . . . .	59
3.7	Data Processing . . . . .	62
3.8	Field-of-View . . . . .	62
3.9	Summary . . . . .	63
<b>4</b>	<b>SIMULATION AND MODELING</b>	<b>65</b>
4.1	Detector Modeling . . . . .	67
4.2	Background Modeling . . . . .	69
4.3	Summary . . . . .	77
<b>5</b>	<b>SPECTROSCOPIC ALGORITHMS</b>	<b>79</b>
5.1	Data Segmentation . . . . .	79
5.2	Energy Windowing . . . . .	80
5.3	Region-of-Interest . . . . .	84
5.4	Supplemental Algorithms . . . . .	87
5.5	Summary . . . . .	87
<b>6</b>	<b>CODED APERTURE IMAGING ALGORITHMS</b>	<b>89</b>
6.1	Energy Windowing . . . . .	91
6.2	Data Segmentation . . . . .	92
6.3	Array Flat Fielding . . . . .	96
	6.3.1 Realtime Corrections . . . . .	98
	6.3.2 Historical Corrections . . . . .	101
6.4	Geometric Pre-calculation . . . . .	102
	6.4.1 Offsets . . . . .	104
	6.4.2 Pixel Mapping . . . . .	106
	6.4.3 Image Smoothing . . . . .	107
6.5	Backprojection . . . . .	113
6.6	Summary . . . . .	114
<b>7</b>	<b>COMPTON IMAGING ALGORITHMS</b>	<b>116</b>
7.1	Energy Windowing . . . . .	118
7.2	Data Segmentation . . . . .	119
7.3	Back-projection . . . . .	120
	7.3.1 Angular Uncertainty . . . . .	124



7.3.2	Cone Weighting . . . . .	126
7.4	Background Suppression . . . . .	127
7.4.1	Realtime Corrections . . . . .	130
7.4.2	Historical Corrections . . . . .	131
7.5	Summary . . . . .	133
<b>8</b>	<b>MOBILE/HYBRID ALGORITHMS</b>	<b>135</b>
8.1	Image Registration . . . . .	135
8.2	Distance Determination . . . . .	138
8.3	Image Fusion . . . . .	138
8.4	Non-imaging Fusion . . . . .	142
8.5	Alarm Triggering . . . . .	142
8.6	Summary . . . . .	146
<b>9</b>	<b>BACKGROUND CHARACTERIZATION</b>	<b>147</b>
9.1	Primary Components . . . . .	148
9.2	NORM Variations . . . . .	149
9.3	Background Measurements . . . . .	150
9.4	Component Analysis . . . . .	152
9.5	Clustering Analysis . . . . .	158
9.5.1	K-Means Clustering . . . . .	160
9.6	Results . . . . .	161
9.6.1	Geographic Distribution . . . . .	162
9.7	Summary . . . . .	165
<b>10</b>	<b>DATA INJECTION</b>	<b>168</b>
10.1	Source Simulation . . . . .	170
10.1.1	Simulation Geometry . . . . .	171
10.1.2	Simulation Down Sampling . . . . .	171
10.1.3	Time Correction . . . . .	174
10.1.4	Down Sampling Validation . . . . .	176
10.2	Background Extraction . . . . .	176
10.2.1	Nuisance Sources . . . . .	179
10.3	Injection . . . . .	180
10.4	Validation . . . . .	182
10.4.1	Event Composition . . . . .	182
10.4.2	Spectroscopy . . . . .	183
10.4.3	Imaging . . . . .	184
10.5	Injection Analysis . . . . .	187
10.6	Summary . . . . .	190

<b>11 PERFORMANCE RESULTS</b>	<b>192</b>
11.1 Receiver Operator Characteristic Analysis . . . . .	192
11.1.1 Binary Classifier . . . . .	193
11.1.2 Cumulative Distribution Functions . . . . .	194
11.1.3 Generating the Curve . . . . .	196
11.1.4 Area Under the ROC Curve . . . . .	196
11.2 Imaging Modality Fusion . . . . .	198
11.3 Imaging/Non-Imaging Modality Fusion . . . . .	200
11.4 Minimum Detectable Activity . . . . .	201
11.5 Injection Results . . . . .	205
11.6 Summary . . . . .	207
<b>12 FIELD TESTING</b>	<b>212</b>
12.1 Consistency Checking . . . . .	213
12.2 Distant Sources . . . . .	213
12.3 Multiple Sources . . . . .	214
12.4 Shielded Sources . . . . .	216
12.5 Backside Sources . . . . .	217
12.6 Elevated Sources . . . . .	219
12.7 Medical Sources . . . . .	220
12.8 High Speed Detection . . . . .	222
12.9 Summary . . . . .	224
<b>13 FUTURE WORK</b>	<b>225</b>
13.1 SORDS Spiral Development . . . . .	225
13.2 Background Modeling . . . . .	226
13.3 Sensor Fusion . . . . .	226
<b>14 CLOSING REMARKS</b>	<b>228</b>
<b>15 ACKNOWLEDGEMENTS</b>	<b>230</b>
<b>16 ACRONYMS</b>	<b>238</b>

# List of Figures

1.1	Total count rate as a function of sequential data segment for a 3.2 km stretch of road in Lexington, MA. Count rates vary from 24 to 44 kHz depending on location. . . . .	2
1.2	Total count rate as a function of latitude along a north bound section of road. Shown here are data from 1 August 2009 (blue) and 2 August 2009 (red). Background rates vary by up to 10% along an identical stretch of road when measured only 24 hours apart. . . . .	2
1.3	The TMI prototype system with the side panel removed to allow visibility into the detector system. . . . .	4
1.4	Example of incident photons casting a coded shadow onto a detector array. The coded pattern can be unscrambled to reconstruct the source image [7]. . . . .	6
1.5	Example of three Compton scattering events that overlap at the correct source location. . . . .	7
2.1	Photon attenuation values ( $cm^{-1}$ ) for NaI (top) and the contribution to total attenuation (bottom). . . . .	21
2.2	The Compton scattering interaction. . . . .	23
2.3	The nuclear pair production interaction. . . . .	24
3.1	The Raytheon-SORDS Tri-Modal Imager. The TMI is a hybrid coded aperture / Compton imager deployed in the back of a truck in order to perform mobile gamma-ray imaging. . . . .	28
3.2	Front, side, and top views of the TMI geometry. . . . .	29
3.3	Photo of the KVH Industries Inc. CNS-5000 INS. The system combines an inertial navigation system with a high-accuracy GPS receiver in a single small enclosure. . . . .	30
3.4	Calculation of the CEP resolution for the GPS location shows to be less than 3.4 cm over 82 seconds. . . . .	33
3.5	CA detector element assembly with photomultiplier tube attached. . . . .	37

3.6	Measured energy spectrum from a single CA detector element from a $^{137}\text{Cs}$ point source taken during field measurements. The FWHM energy resolution at 662 $keV$ is shown to be 7.36%. . . . .	38
3.7	Measured centroid (top) and width (bottom) of the $^{137}\text{Cs}$ photo peak for each of the 35 CA detector elements. The average resolution is $7.69 \pm 0.2\%$ FWHM. . . . .	39
3.8	Two NaI bars used in the DA array with attached 2" PMTs at both ends and LED pulser port at the center. . . . .	41
3.9	Measured energy spectrum from a single DA detector element from a $^{137}\text{Cs}$ point source taken during field measurements. The FWHM energy resolution at 662 $keV$ is shown to be 7.46% integrating over all energy depositions along the length of the bar. . . . .	44
3.10	Measured centroid (top) and width (bottom) of the $^{137}\text{Cs}$ photo peak for each of the 30 DA detector elements. The average resolution is $7.29 \pm 0.15\%$ FWHM. . . . .	45
3.11	Event by event plot of pulse height amplitude as measured by the PMTs at both ends of a single DA array bar [44]. . . . .	48
3.12	Measured ADC channel distribution for 15 points along the face of a single DA detector element (top) and the resulting calibration curve using centroids of the fits to the 15 distributions (bottom). . . . .	51
3.13	Derived position calibration curves for each of the DA detector bars from measured data at 15 points along the each bar. . . . .	52
3.14	The flow of signals and electronics on the TMI. Data is eventually sent to the data analysis system (DAS). . . . .	55
3.15	Sensor CCAs for the CA array mounted in a rack prior to integration on the TMI. . . . .	57
3.16	Images of a high-voltage circuit card assembly (left) with PMT resistive divider in the center and the HVCCA output connector (right) showing the 20-pin ribbon cable connector. . . . .	58
3.17	Image of the ECU with all serial lines from the CA detector array (red) and the DA detector array (teal) shown coming in from the top and bottom. . . . .	60
3.18	Angular measurements taken for TMI horizontal FOV calculations. Each measurement was taken with a 879 $\mu Ci$ , $^{137}\text{Cs}$ source at a radius of 25 meters, with 20 seconds of integration time. At each location an image from the TMI is shown where the background color (purple) indicates a flat background image. . . . .	63

3.19	Two off-axis (vertical) measurements taken for field-of-view calculations. Each measurement was taken with a 879 $\mu Ci$ , $^{137}Cs$ source at a radius of 25 meters, with 20 seconds of integration time. The vertical FOV is shown to be (at least) -0.33 radians (B) to +0.4 radians (A) or 0.73 radians total. . . . .	64
4.1	GEANT4 model of the SORDS truck platform. . . . .	66
4.2	Reconstructed image using simulated data of the TMI for a 0.5 $mCi$ $^{137}Cs$ source at 15 $mph$ and minimum approach of 25 meters. . . . .	67
4.3	Cross-sectional view of the simulated model for one of the 5x5x2 $inch$ sodium iodide (NaI) front-plane detectors. . . . .	68
4.4	Comparison of measured and simulated data for a SORDS 5x5x2 $in^3$ NaI detector exposed to a $^{60}Co$ source. . . . .	69
4.5	Comparison of measured and simulated data for a SORDS 2.5x3x24 $in^3$ NaI detector exposed to a $^{60}Co$ source. . . . .	70
4.6	100 most intense gamma-ray emission energies from a sample of soil constructed in the simulation. . . . .	72
4.7	Gamma-ray energy spectrum emitted from the simulated soil model. The model includes both self-attenuation effects and scattering within the soil. . . . .	73
4.8	Comparison between measured data with the TMI arrays (black) and simulated data (red) for the DA detector elements (top) and the CA detector elements (bottom). . . . .	74
4.9	Decline of simulated count rate as a function of ground plane radius (top) and the gamma-ray photon origin point for all simulated energy depositions in the TMI above a 20x20 $m^2$ ground plane. . . . .	76
4.10	Comparison of the simple ASP detector response to the constructed soil model. . . . .	77
5.1	Sample measurement past a 0.5 $mCi$ , $^{137}Cs$ point source. The total count rate in the TMI is indicated by the height and color of the bars. Each bar represents the integration of total energy deposited in a 2.0 second interval. The location of the source is not easily located due to fluctuations in the total count rate. . . . .	81
5.2	Example of the NORM background as well as the energy windows applied for several gamma-ray sources. . . . .	82
5.3	Expected energy resolution of the DA detector array ( $\sigma$ ) as a function of total energy deposited in the NaI. . . . .	83
5.4	Count rate as a function of location for all measured events within the $^{137}Cs$ energy window. The location of the source is now clearly visible. . . . .	83

5.5	Example measured energy spectrum (blue) with a 2.0 second integration time in the $^{137}\text{Cs}$ energy window with energy regions and estimations shown. . . . .	86
5.6	Signal-to-noise ratio as a function of location as a result of the ROI algorithm applied to the $^{137}$ isotope spectra. The location of the source is now clearly visible and background is stable at all other locations. .	87
5.7	ROI alarm for a measured run past a 0.5 <i>mCi</i> , $^{137}\text{Cs}$ source at 25 <i>m</i> . The alarm was generated by the TMI at the location of the red arrow and the estimated area of possible source locations is shown with a green ring. The ground truth location of the source shown to be within the ring. . . . .	88
6.1	Diagram of the coded aperture imager integrated into the TMI. . . .	90
6.2	Reconstructed coded aperture images using all measured photons (top) and only those that have a total energy deposited within the $^{137}\text{Cs}$ energy window (top). The non-windowed image has a calculated significance of 5.80 with location accuracy of $\pm 2.40$ <i>m</i> and was detected in 9.52 seconds. The windowed image has a calculated significance of 11.27 with location accuracy of $\pm 2.37$ <i>m</i> and was detected in 7.46 seconds. . . . .	92
6.3	Optimization of the energy window width. A width of $1.5\sigma$ corresponds to the highest significance in the coded aperture image. . . . .	93
6.4	Sample DA snapshot (1.46 seconds, 2.00 meters, 324 events) in the $^{137}\text{Cs}$ energy window. . . . .	95
6.5	Example coded aperture event segment with the average calculated (red square) and the imaging FOV shown (red lines). The location of the TMI for each measurement is shown in blue and the interaction locations are shown in green. . . . .	96
6.6	Example measured coded aperture backplane data before and after flat-fielding. . . . .	98
6.7	Example coded aperture reconstructed images without (top) and with (bottom) array flat fielding enabled. . . . .	99
6.8	Realtime background estimator for $^{137}\text{Cs}$ . As time progresses the background estimator improves and adjusts to the current sensitivity of the system. The three estimators shown are for 4.33 seconds into the run (A), 14.30 seconds (B) and 94.7 seconds (C). . . . .	100
6.9	Historical flat field estimator for $^{137}\text{Cs}$ . The flat field history was aggregated over 7086 seconds of background data including 1.5 million measured photons. . . . .	101

6.10	Graphical view of the variables used the in calculation of the number of image pixels that correspond to the movement of a single detector element in $x$ and $y$ for the DA array (top) and the CA array (bottom).	105
6.11	Example coded aperture mask projection for 3 individual points on the DA detector array; the lower left element (top), the middle element (middle) and the upper right element (bottom). Black pixels are projections through open mask element (+1), white are projections through closed elements (-1) and grey pixels are zero because no information was available to add to them. . . . .	108
6.12	Example back-projected coded aperture image formed from the overlap of projections from each of the 720 DA array elements assuming a single count in each of the DA detector elements. . . . .	109
6.13	The expected $1\sigma$ position resolution of the NaI bars as a function of energy deposited. . . . .	110
6.14	Example Gaussian smoothing kernel for $^{137}\text{Cs}$ (left) and $^{131}\text{I}$ (right). Since the average energy of $^{131}\text{I}$ (364 keV) is lower than $^{137}\text{Cs}$ (662 keV) there is more uncertainty in the $Y$ dimension of the iodine kernel due to the uncertainty in the measured DA element position. . . . .	112
6.15	A single mask projection before (top) and after (bottom) smoothing using the Gaussian kernel. . . . .	113
6.16	Example measured DA snapshot (top) and the associated back-projected coded aperture image (bottom) for a 10 mCi $^{137}\text{Cs}$ source at 25 m. The image is formed from the overlap of mask projections from each of the 720 DA array elements. Both historical flat fielding and Gaussian smoothing have been applied to the image. . . . .	114
7.1	Diagram of the Compton imager integrated into the TMI. . . . .	117
7.2	Example of energy windowing applied to Compton scatter image reconstruction. The top image does not have energy windowing applied and the bottom image does. . . . .	119
7.3	Example Compton event segment with the average calculated (red square) and the imaging FOV shown (red lines). The location of the TMI for each event is shown in blue and the interaction locations are shown in green. . . . .	121
7.4	Back-projection of a single event sequence. . . . .	122
7.5	A single event cone projected onto the imaging plane at $z=50m$ . . . .	127
7.6	Example reconstructed Compton scatter image of 3 events before (top) and after background suppression (bottom). There is no source present in the image. . . . .	129

7.7	Example runs past a source without (top) and with (bottom) background suppression applied. . . . .	130
7.8	On-the-fly Compton flat field estimator for $^{137}\text{Cs}$ . As time progresses the flat field estimator improves and adjusts to the current sensitivity of the system. The three estimators shown include 9 events (top), 100 events (middle) and 131 events (bottom). . . . .	132
7.9	Historical background estimator for $^{137}\text{Cs}$ at 50 meters. The flat field history was aggregated over 4774 seconds of background data including 30,000 measured photons. . . . .	133
8.1	Example image registration for the coded aperture imaging planes. Each image has an associated geographic location and can be aligned in the algorithms such that an aggregate image is formed from the overlap of all reconstructed images. . . . .	137
8.2	. . . . .	139
8.3	Example hybrid CA/CI image of a 0.5 <i>mCi</i> , $^{137}\text{Cs}$ source at 25 <i>m</i> Distance of Closest Approach (DCA) and 15 <i>mph</i> . The coded aperture and Compton images are registered in the same geographic coordinates and can therefore be fused to cancel background and improve source reconstruction. . . . .	141
8.4	Minimum persistence time required as a function of imaging distance for a candidate imaging peak to trigger an alarm. . . . .	144
8.5	Candidate peak (top) and signal (red) and background (green) regions used in the calculation of image significance (bottom). . . . .	145
9.1	Complete decay chains for the principle NORM background components $^{238}\text{U}$ (top), $^{232}\text{Th}$ (bottom-right) and $^{40}\text{K}$ (bottom-left). Alpha decays are shown with blue arrows, beta and electron capture are shown with red and green arrows respectively. The daughter nuclei with the most easily characterizable lines are shown in blue ( $^{40}\text{K}$ , $^{208}\text{Tl}$ , $^{214}\text{Bi}$ ). . . . .	149
9.2	Naturally occurring potassium-40 concentration throughout the continental United States as mapped by the United State Geological Survey (USGS). . . . .	151
9.3	Naturally occurring thorium-232 concentration throughout the continental United States as mapped by the United State Geological Survey (USGS). . . . .	152
9.4	Naturally occurring uranium-238 concentration throughout the continental United States as mapped by the United State Geological Survey (USGS). . . . .	153



9.5	Path of the TMI during the background collect in February 2012. The path of the imager is shown with a red line starting in Washington D.C. and ending this segment near Philadelphia, PA. . . . .	154
9.6	Level diagram for the decay of $^{40}\text{K}$ . The primary decay mode is beta decay to stable $^{40}\text{Ca}$ , however the electron capture decay and transition to stable $^{40}\text{Ar}$ is the source of the gamma-ray background feature at 1460 keV. . . . .	155
9.7	Energy spectrum regions used for component analysis on a 5 second aggregate background total energy spectrum. The three red areas increasing in energy show the energy regions for $^{40}\text{K}$ (1460 keV), $^{214}\text{Bi}$ (1764 keV) and $^{208}\text{Tl}$ (2614 keV), respectively. . . . .	156
9.8	Example fit to background component regions using a Gaussian + exponential fit. The component fractions are characterized by the ratio of the integral of the green (Gaussian only) fit curves to the total integral of the spectrum. . . . .	159
9.9	Results of fitting each 5 second spectrum for the entire 20 hour data set. The $^{40}\text{K}$ fraction versus the $^{214}\text{Bi}$ fraction is shown in the top left, $^{40}\text{K}$ versus $^{208}\text{Tl}$ in the top right and the $^{214}\text{Bi}$ versus $^{208}\text{Tl}$ on the bottom. 160	160
9.10	Example K-means clustering algorithm. . . . .	161
9.11	Results of the K-means clustering analysis of the component fit results. K-means analysis was performed for three dimensions with three centers. The centers of the groups are shown with block points and the groupings are shown in the various colors, group 1 (red), group 2 (green) and group 3 (blue). . . . .	163
9.12	Averaged 5 second energy spectrum for each of the 3 classes of background as derived by the k-means algorithm. Also shown is the number of 5 second spectra in each class; about 7000, 5500, and 400 for groups 1, 2, and 3 respectively. The bottom plot shows the average energy spectrum for each class of background overlaid on each other to show the difference. The green, blue and red lines represent classes 1, 2, and 3 respectively. . . . .	164
9.13	A section of downtown Washington D.C. with the determined background classification denoted by the colors blue, green and red for classes 1, 2, and 3 respectively . . . . .	166
10.1	The path of the TMI (red) around the Washington D.C. area during the background collection efforts in February 2012. . . . .	169

10.2	Graphical example of an injection scenario (not to scale). The simulation starts with the imager at (-100, 0, 0) <i>m</i> and travels straight in the + <i>X</i> direction, past a 1.0 <i>mCi</i> source at (0, 0, 25) <i>m</i> , to (100, 0, 0) <i>m</i> . The total distance of the run is 200 meters and the imager speed and source activity can be adjusted through down sampling. . . . .	172
10.3	Demonstration of simulation downsampling. The simulated source only counts as a function of time (top) and distance (middle) for all counts (Red), DA array (blue), CA array (green) and coincidence (yellow). The bottom plot shows the total energy deposited for all events as a function of time where the <sup>137</sup> Cs source is clearly visible in the middle of the run. The original simulation is shown in the left column and the down sampled simulation is shown in the right column. . . . .	175
10.4	The frequency versus number of events sampled for 1000 down sampled simulation runs (left) where the red line shows the desired number of events. The middle plot shows the fraction of events sampled versus run number (blue dots) for the same set of runs where the desired fraction is shown with the dashed blue line. The right plot shows the fraction of coded aperture (red) and Compton (blue) events as a function of run number with the desired fraction shown with dashed lines. . . . .	177
10.5	Example data extraction. The full length measured run (red) is sampled from +/- 14.91 seconds around the point closest to the known source location (yellow). . . . .	178
10.6	Example industrial nuisance source ( <sup>137</sup> Cs) in one of the preliminary blocks of background data used for algorithm training. . . . .	179
10.7	Results of the validation injection scenario. The top row shows the total energy spectrum (30 seconds) for the source simulation, measured background, injected simulation and corresponding measurement, respectively (left to right). The middle row shows the 2-dimensional energy versus time histograms with the same columns. The third row shows the energy spectrum for the middle 4 seconds of the runs to emphasize the source peak at 662 <i>keV</i> from <sup>137</sup> Cs. . . . .	181
10.8	Comparison of the composition of events from the data injection validation scenario (blue) and a source measurement (red). Both the coded aperture event rate as a function of time (left) and the Compton event rate as a function of time (right) match well against measurements. . . . .	183
10.9	Total energy deposited in the detector system for the middle 4 seconds of data for the data injection scenario (blue) and the corresponding measurement (red). Counts above the 662 <i>keV</i> gamma-ray line from <sup>137</sup> Cs are not simulated and represent actual count rate variations between measurements at the same location. . . . .	184

10.10	Ratio of injected to measured counts as a function of energy ( <i>keV</i> ) for the injection scenario as compared to a measurement in the same location. Data are shown for $\pm 2$ seconds of closest approach to the source. The dashed red line shows the expected ratio of 1.0, indicating a perfect match. Most data points are within the expected uncertainty due to counting statistics. . . . .	185
10.11	Comparison of imaging results for the source measurement (top) and simulated injection run (bottom). Both images have similar image significance; 34.23 measured versus 33.58 injected. Images report a source within 2.2 meters of each other. . . . .	186
10.12	Sample images generated from processing of injection simulations at various activities: background only (top), 0.1, 0.3 0.5, 0.7, 0.9 and 1.0 <i>mCi</i> (bottom). As the source activity increases, the image intensity increases. . . . .	188
10.13	Centroid of the maximum trigger parameter for 240 simulated injection runs as a function of source activity. Spectroscopic region-of-interest (ROI) is shown in blue, imaging (red) and the combination (green). . . . .	189
10.14	Trigger parameter maximum value for ROI (blue), imaging (red) and the combination (green) as a function of injection run number (0-239). The average (centroid) values for each are shown with a solid line of the corresponding color. . . . .	190
11.1	Example maximum classifier frequency distribution (left) for 240 runs of background only (red) and 40 (blue) and 300 $\mu Ci$ (green), $^{137}Cs$ injected source. A Gaussian fit to each of the distributions is shown on the right. . . . .	194
11.2	1-CDF distribution functions for the background only (red), 40 $\mu Ci$ cesium (blue), and 300 $\mu Ci$ cesium (red) sources as a function of classifier threshold. . . . .	195
11.3	Generated ROC curve for a 40 $\mu Ci$ (blue) and 300 $\mu Ci$ (green), $^{137}Cs$ source. The solid lines are the curves generated directly from the measured frequency distributions and the dashed lines are generated from fits to the frequency distributions. . . . .	197
11.4	ROC analysis of the highest image pixel for Compton (blue), coded aperture (red) and hybrid (green), generated using 100 simulated runs past a 1.0 <i>mCi</i> , $^{137}Cs$ source at 100 <i>m</i> DCA and 30 <i>mph</i> . . . . .	199
11.5	Area under the ROC curve as a function of incident gamma-ray energy for Compton (blue), coded aperture (red) and hybrid (green). . . . .	200

11.6	ROC analysis of ROI significance (blue), hybrid CA/CI gamma-ray imaging (red) and the combination (green). This curve was generated using 240 injected source runs past a 75 $\mu Ci$ , $^{137}Cs$ source at 25 $m$ DCA and 15 $mph$ . . . . .	202
11.7	ROC analysis of ROI significance (blue), hybrid CA/CI gamma-ray imaging (red) and the combination (green) showing the region of very low probability of false alarm in more detail. . . . .	203
11.8	ROC curves generated for 240 runs past a $^{137}Cs$ source at 25 $m$ DCA and 15 $mph$ for 0.04, 0.05, 0.075, 0.1, 0.2, and 0.3 $mCi$ for the ROI algorithm. . . . .	204
11.9	Source activity ( $mCi$ ) as a function of probability of detection assuming a false alarm probability of 0.10. . . . .	206
11.10	ROC curves for the combined analysis. A $^{137}Cs$ source at various activities was injected onto NORM background group 1. The source was located at 25 $m$ DCA and the TMI speed was 15 $mph$ . . . . .	209
11.11	ROC curves for the combined analysis. A $^{137}Cs$ source at various activities was injected onto NORM background group 2. The source was located at 25 $m$ DCA and the TMI speed was 15 $mph$ . . . . .	210
11.12	ROC curves for the combined analysis. A $^{137}Cs$ source at various activities was injected onto NORM background group 3. The source was located at 25 $m$ DCA and the TMI speed was 15 $mph$ . . . . .	211
12.1	Hybrid CA/CI image of the 0.5 $mCi$ , $^{137}Cs$ source used for consistency checking. The source in the image was reported to have an uncertainty of 5.2 $m$ . The actual source location was 1.1 $m$ from the reported location. . . . .	214
12.2	Source images for $^{137}Cs$ (top) and $^{88}Y$ (bottom) co-located at 50 $m$ DCA. The TMI correctly detects, identifies and locates both sources simultaneously. . . . .	215
12.3	Example shielding scenario tested with the TMI. A 10 $mCi$ , $^{137}Cs$ source was located 72.5 $m$ from the roadside with large concrete barriers between the source and detector. The TMI detects the source in the scenario 18/18 times within $1.7 \pm 1.1$ meters of ground truth. . . . .	217
12.4	Example set of testing runs past a 1 $mCi$ , $^{131}I$ source located behind the FOV of the imaging system. The ROI algorithms detect and identify the source even though it is not visible to the imaging system. . . . .	219
12.5	Source images for a run past a 1.0 $mCi$ , $^{137}Cs$ source (top), 1.0 $mCi$ , $^{60}Co$ (middle) and 2.0 $mCi$ , $^{57}Co$ (bottom). Each source was elevated 0.35 $rad$ from the center of the imager. . . . .	221

12.6 Measured $^{131}\text{I}$ (top) and $^{99m}\text{Tc}$ (bottom) sources. Each source was 2.0 $mCi$ located at 25 $m$ DCA. The speed of the TMI during the measurement was 15 $mph$ . . . . .	222
12.7 Source images for a run past a 10.0 $mCi$ , $^{137}\text{Cs}$ source at 25 $m$ DCA for 30 $mph$ (top), 40 $mph$ (middle) and 50 $mph$ (bottom). . . . .	223

# List of Tables

3.1	Physical and environmental specifications for the CNS-5000 navigational subsystem. . . . .	31
3.2	List of checked parameters and acceptable ranges for GPS/INS navigational data. . . . .	34
3.3	Broad agency announcement requirements for the SORDS detector. .	35
3.4	Polynomial DA bar calibration parameters and acceptable ADC channel range . . . . .	53
4.1	Radioisotope composition of soil used for the simulation model. . . .	71
4.2	Elemental composition of soil used for the simulation model. . . . .	72
6.1	The three data segmentation criteria used for coded aperture data. .	94
9.1	Background component peak regions used during the background component analysis. . . . .	155
9.2	Geometric centers as calculated by the K-means clustering algorithm.	162
11.1	Areas under the ROC curves for each ROI, CA/CI, and the combination (TOT) generated using 240 runs of injection data for groups 1 and 2, and 20 for group 3. The source injected was a $^{137}\text{Cs}$ source at 25 <i>m</i> DCA. The TMI speed for each run was 15 <i>mph</i> . . . . .	207
12.1	Summary of distant source testing performed with the TMI. . . . .	214
12.2	Results of multiple source testing performed with the TMI for both imaging and Region-of-Interest (ROI) algorithms. In this table $N$ is the number of detections over the number of tests performed and $\Delta R$ is the average distance to the known location of the source in <i>m</i> . . . .	216
12.3	Summary of all shielding tests performed with the TMI at SRNL. . .	218
12.4	Summary of all backside tests performed with the TMI at SRNL where $\Delta R$ is the distance between the reported and known source location. .	220

12.5 Summary of several elevated source (Partially Coded Field-of-View (PCFOV)) tests performed with the TMI during field trials. . . . .	220
12.6 Summary of several medial isotope tests performed with the TMI at SRNL. . . . .	221
12.7 Summary of all high-speed tests performed with the TMI at SRNL. . . . .	223

# Chapter 1

## INTRODUCTION

In many scenarios related to homeland security, it is not only desirable to detect the presence of a radioactive source but also to identify and localize the source of the radiation. It is also desirable to do so as quickly as possible with high confidence and low probability of false alarm. In the simplest of scenarios stationary counting detectors may be able to detect anomalies in count rates from a single location. However, in dynamic scenarios where the detector is in motion, count rates can vary erratically over both position and time making detection difficult. Figure 1.1 shows the measured count rate from Naturally Occurring Radioactive Material (NORM) as a function of data segment along a 3.2 km stretch of road in Lexington Massachusetts. The measured count rate varies by as much as a factor of two over this small stretch of road with an average count rate of approximately 30 kHz (dashed line) over all energies integrated up to 3 MeV.

Additionally, NORM background can vary over time and as a function of weather for the same location. Figure 1.2 demonstrates the fluctuation in measured count rate as a function of position (latitude) for the same stretch of road taken just 24 hours apart. Deviations in the background rate vary by up to 10 percent.



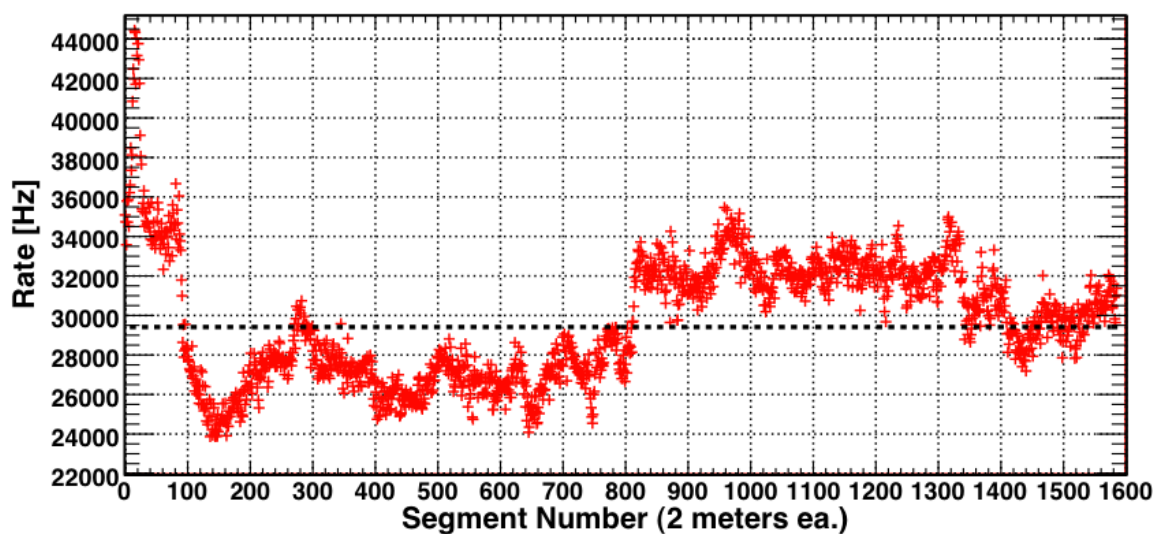


Figure 1.1: Total count rate as a function of sequential data segment for a 3.2 km stretch of road in Lexington, MA. Count rates vary from 24 to 44 kHz depending on location.

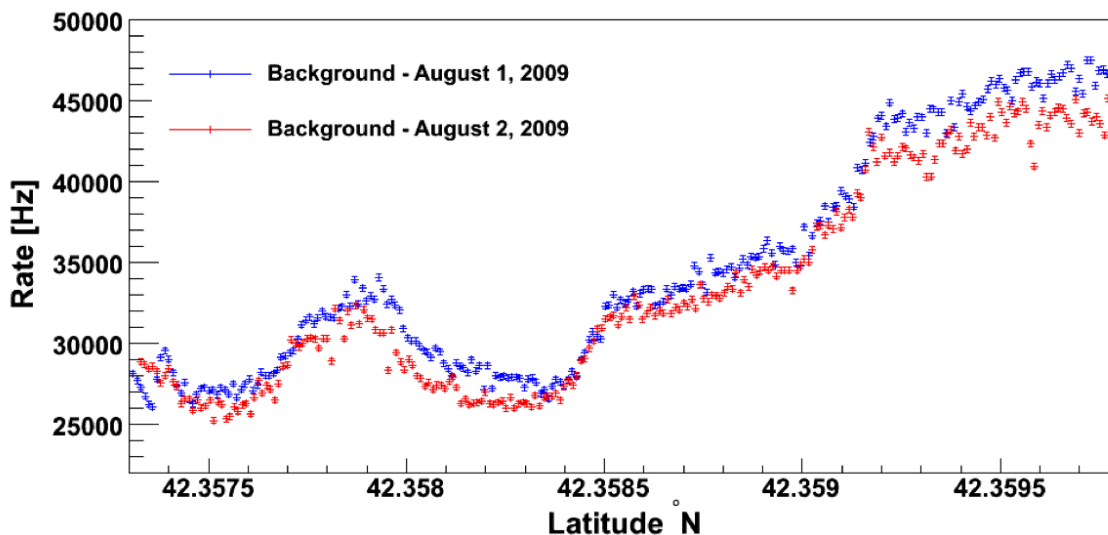


Figure 1.2: Total count rate as a function of latitude along a north bound section of road. Shown here are data from 1 August 2009 (blue) and 2 August 2009 (red). Background rates vary by up to 10% along an identical stretch of road when measured only 24 hours apart.

NORM background is a large contribution to all measured gamma-ray flux and represents the dominant obstacle for detection of other sources of radiation. Additionally, weak sources in the presence of large, rapidly changing NORM backgrounds become increasingly difficult to detect due to attenuation in the surrounding medium and low photon flux, potentially buried within expected variations in the background.

In order to address these challenges, a robust detection system which takes full advantage of all available information is desired. The Department of Homeland Security's Domestic Nuclear Detection Office (DNDO) has expressed interest in a mobile gamma-ray detector system. To meet the global detection challenge a sensitive mobile instrument must be designed to detect, identify and localize radiological threats at distances up to 100 meters. The system must do so over a wide range of gamma-ray energies while providing the necessary sensitivity to true sources through background rejection while maintaining very low false alarm rates. Furthermore, it must be compact, low cost and lightweight.

Currently, no single detector technology has been fully optimized in the desired energy range, weight, size, cost, resolution and sensitivity to meet this challenge. However, the challenge can be met by combining the best features of multiple existing proven detection technologies. With a careful hardware design, detector configuration and sophisticated processing, it is conceivable to construct a detector system capable of performing both coded aperture imaging and Compton scatter imaging along with enhanced spectroscopic detection simultaneously. The Raytheon-SORDS Tri-Modal Imager (TMI) has been constructed as a unique and innovative approach to mobile gamma-ray detection that exploits the advantages of all of these detection technologies.



Figure 1.3: The TMI prototype system with the side panel removed to allow visibility into the detector system.

The TMI incorporates both imaging and non-imaging technologies, specifically a coded aperture imager, a Compton scatter imager, and a large-area spectroscopic detector. Together, these technologies are integrated into a powerful system capable of effectively detecting, identifying and locating radioactive sources of interest from a moving platform. Moreover, the design is capable of being scaled to meet deployment requirements and adapted to aerial and maritime platforms. Figure 1.3 shows the TMI prototype system with the side panel removed to allow visibility into the detector system.

It should be noted that coded aperture and Compton scatter gamma-ray imaging methods have complementary energy regions where they perform well. Coded aperture imaging is typically best for gamma rays with low to mid-range energies ( $<1 \text{ MeV}$ )

and has a large Field-of-View (FOV). Compton imaging excels in the region of medium to high gamma-ray energy ( $>0.5 \text{ MeV}$ ) and has a potential  $4\pi$  FOV. Due to the large area of the scintillator detectors on the TMI, there are statistical advantages to spectroscopic algorithms as well. While non-imaging algorithms are not capable of fine source localization they have potential to determine proximity or likely region where a potential source may exist. Through intelligent placement of detector materials a system has been constructed to allow for multiple simultaneous gamma-ray imaging techniques to be performed along with spectroscopic detection methods to improve the overall performance of the system.

## 1.1 Coded Aperture Imaging

Coded aperture imaging is a method of gamma-ray imaging that uses a position sensitive detector array, shadowed by a dense, sparse mask, in order to cast a coded shadow onto the array [1–6]. The measured coded shadow can then be decoded to reconstruct an image of the source. The advantage of coded aperture gamma-ray imaging comes from the fact that the modulation pattern of background events reconstruct into a randomly filled image while source events reconstruct to a common location. Figure 1.4 shows an example of the coded aperture concept.

## 1.2 Compton Imaging

Compton imaging is another method of gamma-ray imaging that uses multiple position and energy measurements in coincidence to reconstruct the probable origin of the gamma-ray photon. When gamma-ray photons are emitted from a source, they can Compton scatter in a scattering detector, and deposit the remaining energy in

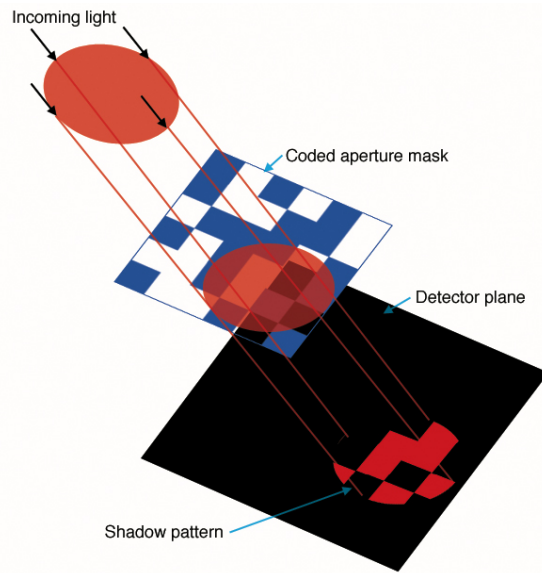


Figure 1.4: Example of incident photons casting a coded shadow onto a detector array. The coded pattern can be unscrambled to reconstruct the source image [7].

the absorbing detector. If this interaction can be precisely measured, the kinematics of Compton scattering can be used to reconstruct the event, where the location of the source can be confined to a point on the cone. The location of a source cannot be determined from a single event cone, however the reconstruction of many cones will overlap at the true location of the source. Figure 1.5 shows several example simulated Compton scattering events, the intersection of the three cones reveals the true source location.

### 1.3 Overview of Thesis

This thesis will present background information on gamma-ray imaging and spectroscopic techniques. Additionally, physics processes common to detector systems will be presented such as radioactive decay and gamma-ray photon interaction mechanisms.

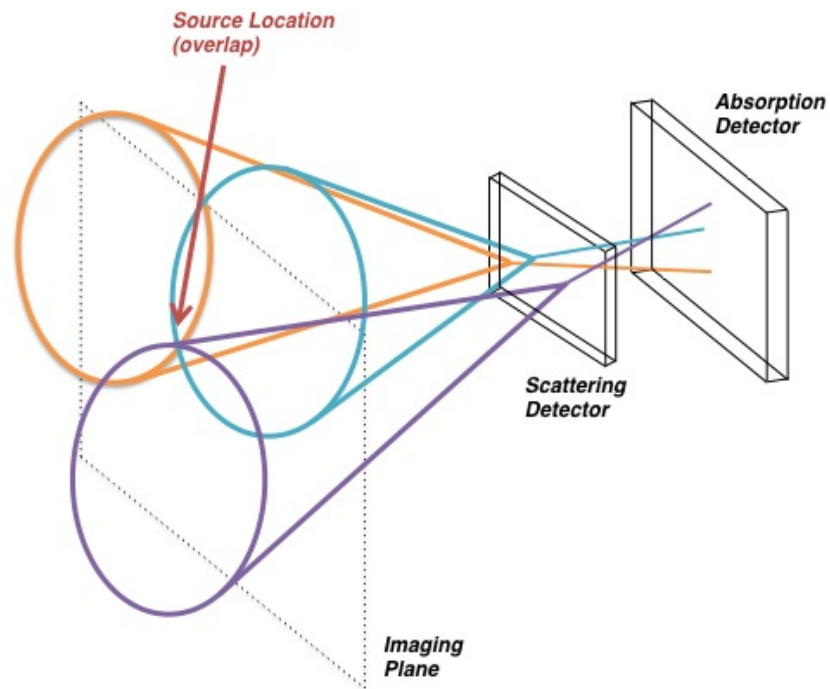


Figure 1.5: Example of three Compton scattering events that overlap at the correct source location.

The next few chapters will present the specifics of the implemented hardware on the TMI prototype and simulation and modeling efforts performed.

Details of the non-imaging spectroscopic algorithms will be presented as well as the details of the implemented coded aperture and Compton gamma-ray imaging algorithms. Techniques for fusion of all imaging and non-imaging modalities as well as methods for co-registration of images and data will be presented. Additionally a chapter is devoted to the methods of analysis for performance metrics is included.

Since NORM background plays a major role in the detection sensitivity there is a chapter devoted to the study and understanding of the principle components of the background. Once characterized, background can be processed through the implemented algorithms using data injection techniques and analysis methods to assess performance under various conditions and assumptions. Finally, results of the prototype systems and analysis of the results will be presented and future work will be discussed.

# Chapter 2

## BACKGROUND

### 2.1 Survey of Technology

Gamma-ray imaging is widely used as a tool in nuclear medicine research and procedures as well as astrophysics research. Additionally, research in the use of gamma-ray imaging for waste monitoring and nuclear nonproliferation began in the 1990s. Since then, efforts to develop better detection technologies has gained increased attention, in particular, imaging technologies suitable for homeland security applications. Imaging and spectroscopic technologies are desirable because they allow for passive systems to detect, identify and localize sources while rejecting background and minimizing false alarm probabilities without complicated active interrogation systems. This capability would provide the improved sensitivity needed to rapidly sense radioactive materials from stand-off distances. Two common gamma-ray imaging techniques are coded aperture and Compton scatter imaging.

#### 2.1.1 Coded Aperture Imaging

Coded aperture imaging has been used for many years, mostly in the fields of X-ray and gamma-ray astronomy [1, 8]. Coded aperture imaging is an attractive solution



because of its maturity and capability to provide accurate images of nuclear material from meters to many light years away depending on the application. The principle of a coded aperture imager is simple. A dense screen (aperture) with random holes is placed in front of a position sensitive detector array. Gamma-ray photons from a source cast an image of the screen onto the array. The screen image can then be unscrambled to reconstruct the source image [8].

R.H. Dicke at Princeton University proposed a scatter-hole camera for X-ray and gamma-rays in 1968 [8]. It was suspected that this technology would have applications in astronomy as well as the medical industry. It was also conceived that Dicke's proposed system would be capable of generating radiographic images or detailed internal images through the use of radioactive tracers in the body. Today coded aperture imaging has been recognized to have applications to homeland security.

In the field of astrophysics, Allen *et al.* constructed protoEXIST [4], a prototype coded aperture hard X-ray telescope. It features a 4.5 m<sup>2</sup> Cadmium-Zinc-Telluride (CZT) detector plane with 4096 pixels, and a wide 90x70 degree FOV. This was the primary instrument on the Energetic X-ray Imaging Survey Telescope (EXIST) mission [6]. EXIST is a large area, space based, coded aperture telescope tasked with surveying Active Galactic Nuclei (AGN), searching for black holes and studying Gamma Ray Bursts (GRBs) and other transient events. Other coded aperture detectors used in astrophysics include the Imager on-board the Integral Satellite (IBIS) [5] and the Burst Alert Telescope (BAT) on the *Swift* mission [7].

The International Gamma-Ray Astrophysics Laboratory (INTEGRAL) incorporates coded aperture imaging technology on both the IBIS and the spectrometer aboard INTEGRAL (SPI). The imagers are used to get directional information on

the incoming gamma-ray radiation [9]. The SPI imager consists of 19 hexagonal germanium detectors shadowed by 63 tungsten alloy elements 30 *mm* thick. Germanium was chosen to deliver high-resolution energy spectra to the SPI (2.2 *keV* Full-Width at Half-Maximum (FWHM) at 1.33 *MeV*).

The IBIS imager is optimized for high angular resolution in order to scan the gamma-ray sky from 3 *keV* to 10 *MeV* [10]. The coded aperture used on IBIS was approximately 1 *m*<sup>2</sup>, 16 *mm* thick tungsten. The detection plane employed for low energy (<150 *keV*) consisted of a 128x128 (2600 *cm*<sup>2</sup>) multi-layer Cadmium-Telluride (CdTe) detector. These detectors were applied to the low energy range because of their thickness (2 *mm*). At 150 *keV*, the efficiency is already down to 50% [10, 11]. On the high energy range a 64x64 Cesium-Iodide (CsI) array was used with photodiode readout. CsI was selected due for its high gamma-ray stopping power. The sensitive area of the CsI array was approximately 2890 *cm*<sup>2</sup>. Additionally the IBIS imager was used as a Compton imaging system. The separation between the low energy CdTe and high energy CsI arrays was approximately 94 *mm*. This allowed for simultaneous capture of coincident interactions in the two arrays allowing for Compton scatter reconstruction and background suppression.

The BAT aboard the SWIFT mission, launched in 2004, included a CZT coded aperture imager [7]. BAT is one of three instruments on the Swift spacecraft, part of the National Aeronautics and Space Administration (NASA) Medium Explorer Program (MIDEX). The purpose of the BAT imager is to study GRBs with location accuracy of 1-4 arcmin. The detector plane consists of 32,768 (4x4x2 *mm*<sup>3</sup>) CZT crystals with an energy range from 15 to 150 *keV* and energy resolution of approximately 7 *keV*. The coded mask is comprised on 52,000 pieces of lead (5x5x1 *mm*<sup>3</sup>).

The mask/detector separation distance is 1 meter. The combination of a large, fine-grained mask and high position/energy resolution detectors are what give the BAT its sensitivity and excellent resolution.

Unrelated to astrophysics, Smith *et al.* at the University of Michigan in 1999 proposed a novel hybrid collimation technique for gamma-ray imaging called the Hybrid Portable Gamma Camera (HPGC) [12]. This team proposed a system that combines the mechanical collimation of a coded aperture imager with the electronic collimation of a Compton camera. Advantages of this system included increased efficiency and improved energy range (50-2000 *keV*). The HPGC used a 2x2 mosaic of a basic 5x5 multiplexed, uniformly redundant array (MURA) [2] passive coded mask made of 5 *mm* thick lead. The detection array was a 100x100x10 *mm*<sup>3</sup> Thallium Doped Sodium-Iodide (NaI(Tl)) read out by four Photomultiplier Tubes (PMTs) using Anger-logic for position sensitivity. Additionally a third detector plane (70x70x30 *mm*<sup>3</sup>) of Sodium Doped Cesium-Iodide (CsI(Na)) with 9x9x30 *mm*<sup>3</sup> pixels was positioned behind the sodium iodide (NaI) array. The passive mask and NaI array acted as a coded aperture imager and the NaI and CsI arrays formed a Compton scatter camera. Results from the HPGC imager demonstrated hybrid collimation was superior to either mechanical or electronic alone.

For homeland security, the Naval Research Laboratory (NRL) in 2008 constructed the Mobile Imaging and Spectroscopic Threat Identification (MISTI) system [13–15]. The MISTI system was developed as a mobile gamma-ray imaging and spectroscopy system. They recognized the value of coded aperture imaging for localization of detected materials using a high-resolution spectroscopic system with applications in homeland security. Threats are identified using 28, 8.5 *cm* diameter, 6.5 *cm* long,

cylindrical High-Purity Germanium (HPGe) detectors with an average relative efficiency of 110% (compared to a 3x3 inch NaI) and 2 keV FWHM energy resolution at 1333 keV. Once identified by the HPGe, threats are imaged, for localization, using a NaI/lead coded aperture system. The imager on MISTI consists of a 10x10 element array of NaI tiles (10x10x5 cm<sup>3</sup>) for energy deposition and position sensitivity. The passive coded mask is constructed from a 12x18 random array, 50% filled with 10x10x2.3 cm<sup>3</sup> lead tiles. The mask and detection array are separated by 40 cm. The reported angular resolution of the imager is 0.25 radians in both the horizontal and vertical dimensions.

Also related to homeland security, Ziock *et al.* at Oak Ridge National Laboratory report the use of a mobile one-dimensional coded aperture imaging system for orphan source searching [16]. Potential improvements include the ability to suppress background through imaging, extending the range of detection for milliCurie class sources by up to 50 meters and beyond. The imager is mounted in a 4.9 m long trailer that can be towed by a large personal vehicle. Sources are localized in both the direction of travel and range. The imager is a 27 element CsI(Na) detector array. Each of the elements is a 4.2x4.2x40 cm<sup>3</sup> CsI bar read out by a single PMT. A feature of this system is the capability to perform imaging on both sides of the trailer. This is accomplished by constructing masks on either side of the central CsI array. Masks on opposing sides of the array are inverses of each other to allow for simultaneous imaging on both sides. The passive mask is constructed from a dense metal alloy to improve opacity and image contrast.

### 2.1.2 Compton Scatter Imaging

Compton imaging has been recognized as an imaging technique with potential applications for homeland security. It is based on the Compton scattering interaction and preserves information about the direction and energy of incident gamma rays if the scattering by-products can be precisely measured.

Various Compton imaging designs have been studied for use in many fields including homeland security and counterterrorism. One such effort was carried out by the Naval Research Laboratory along with the University of California at Berkeley based on their astrophysics expertise. This effort focused on the development of Compton imagers that used thick, position sensitive, solid-state detectors [17]. Efforts by Lawrence Livermore National Laboratory (along with collaborators) included development of the spectroscopic imager for gamma rays, SPEIR [18], Compton imaging with position sensitive silicon and germanium detectors [19], and coaxial germanium detectors [20]. There are many situations applicable to homeland security where it is necessary to both detect and localize an unknown source. Applications include passive searching of areas where nuclear material may be present, cargo screening, where it is inefficient and costly to open containers to search for nuclear material or screening the contents of suspicious objects while maintaining a safe distance.

While Compton imaging is not a new technique, recent advances in material fabrication and signal processing capabilities make building a Compton imaging device more efficient. Also, Compton imaging is one choice for a gamma-ray imaging system capable of performing three-dimensional imaging and provides the means to image gamma rays without the use of a mechanical collimator. Eliminating heavy collimators has the advantage of reducing the overall weight of the system, which is an important

factor when considering a fieldable device, especially in mobile, airborne and space applications. Compton imaging also increases the limited FOV of collimated detectors to potential  $4\pi$  imaging. There are some drawbacks however, including the medium to high cost.

Compton imaging has been of interest to researchers in both the medical imaging and astrophysics communities since the early 1980's. More recently, the potential value of Compton imaging for homeland security applications has been recognized. Currently there are several efforts underway examining how new detector technologies can be applied to Compton imaging as well as utilizing advanced algorithms to improve the detection capabilities of current systems.

Wulf *et al.* [21] at the Naval Research Laboratory (NRL) report the application of germanium strip detectors for the construction of a Compton telescope. As gamma ray energy increases, more material is required to stop it. If detectors with good position and energy resolution are thick enough to have multiple Compton scatters then the photon does not need to be fully absorbed. Thicker detectors require depth resolution or a large separation between detectors to accurately determine the scattering angle. Unfortunately, a large separation between detectors reduces the efficiency of the instrument. Wulf proposed a detector system capable of both stopping low energy gamma rays completely and using multiple Compton scatters for high-energy gamma rays, however this requires expensive electronics and complex event reconstruction algorithms.

Similarly, Vetter *et al.* [22] while at Lawrence Livermore National Laboratory (LLNL) developed an imaging system using position-sensitive HPGe and lithium drifted silicon detectors (Si(Li)) [23]. This system should allow for imaging of gamma

ray sources with higher sensitivity than collimator based systems with the use of advanced 3D gamma ray tracking techniques. They have implemented a Compton camera built of a single double-sided strip HPGe detector with a strip pitch of 2 mm. They report three dimensional position resolution of 0.5 mm at 122 keV using simple pulse shape analysis techniques.

Sullivan, *et al.* [24–27] at Los Alamos National Laboratory have developed the Prototype Compton Imager (PCI) a silicon/CsI prototype Compton scatter camera. This system provided three thin silicon scattering planes followed by an array of CsI(Tl) crystals for collection of scattered photons. Each silicon plane consisted of 320 (16x20) pixels, each 0.3 cm x 0.3 cm x 280  $\mu$ M. In principle, the multiple layers of thin silicon could potentially allow for tracking of recoil electrons, improving reconstruction. The absorption plane consisted of a 6x7 array of 1.2x1.4x1.0 cm<sup>3</sup> CsI(Tl) elements read out by silicon PIN diode.

For space applications, Tanaka *et al.* [28] at the Institute of Space and Astronautical Science (JAXA) have developed a Si/CdTe semiconductor Compton telescope. This effort was aimed at developing a Compton telescope based on high resolution silicon and CdTe imaging devices in order to obtain a high sensitivity astrophysical observation in the sub-MeV gamma-ray region. The Compton telescope consists of a double-sided silicon strip detector surrounded by CdTe pixel detectors. Similar to the PCI, Tanaka uses silicon as a scattering detector but uses CdTe as absorbing detectors rather than CsI.

In 2004 Xu *et al.* of the University of Michigan proposed a unique method of Compton imaging [29,30]. In their method, the use of a single CZT semi-conductor detector with 3D position resolution, as well as energy information of each interaction,

is used to perform Compton imaging. The detector used is a single  $15 \times 15 \times 10 \text{ mm}^3$  CZT crystal. Since any point within the crystal can be the scatter position, it allows them to do  $4\pi$  imaging in the near-field. This is a novel approach because it is the first semiconductor based  $4\pi$  Compton imaging system. They also worked to improve on the algorithms used in Compton imaging, attempting to reconstruct images using filtered back-projection and maximum likelihood techniques.

Aprile from Columbia University and collaborators developed a Compton telescope for space applications called LXeGRIT [31]. LXeGRIT was the first Compton telescope to perform complete 3D reconstruction of the sequence of interactions of individual gamma rays in a single, position-sensitive, liquid xenon time projection chamber for space applications. Characterization of LXeGRIT included both laboratory and balloon flight missions.

### 2.1.3 Considerations

Each of the examples of coded aperture and Compton imaging given have associated drawbacks. The use of HPGe detectors is costly due to cooling constraints. CZT is still a relatively new and expensive material that is not available in large quantities. Also, commercially available CZT rarely operates as expected due to impurities. In addition, the angular uncertainty associated with measurements taken from the currently available small CZT crystal sizes can be large. Silicon is an excellent room temperature detector but is inefficient at stopping high-energy gamma rays. Additionally, the ruggedness of the material must be considered, silicon would not be a good choice because it is fragile. CsI and NaI are both widely available and relatively inexpensive scintillator materials but have worse energy resolution compared to HPGe. All of



these factors come into play when designing a gamma-ray imager.

## 2.2 Radioactive Decay

Since several of the chapters in this thesis will discuss various forms of radioactive decay it is important to review the fundamentals. Additionally, in order to understand how to detect radioactive material it is important to understand the source of radiation. As its name suggests radioactive decay is the decay of one material to another, in the process releasing radiation, either in the form of charged particles, neutrons, neutrinos, or gamma-ray and X-ray photons. The main modes of decay for an unstable isotope are alpha decay, beta decay and electron capture, all of which can lead to subsequent energetic photon emission.

### 2.2.1 Alpha Decay

Heavy nuclei are energetically unstable against the spontaneous emission of an alpha particle. In an attempt to become more stable the nucleus will eject an alpha particle lowering the atomic number ( $Z$ ) by 2 and the mass number ( $A$ ) by 4. Alpha decay is a quantum tunneling process and is governed by the barrier penetration mechanism [32, 33]. The alpha decay process is shown in Equation 2.1 where  $X$  is the unstable nuclei,  $Y$  is the daughter nuclei and  $\alpha$  is the ejected alpha particle.



Since alpha particles have a relatively large mass, high charge and low ejection velocity they are likely to interact quickly and lose their kinetic energy. As a result the vast majority of alpha particles are stopped shortly after emission. However, alpha

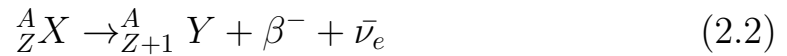
decay usually leaves the decayed nucleus in an excited state. When the nucleus transitions from the excited state energy must be released in the process, or by the daughter atom; usually in the form of energetic photons; *i.e.* X-rays or gamma-rays. These photons have a much longer path length given the probability of interaction in matter, making them easier to detect at a distance.

### 2.2.2 Beta Decay

Beta decay is defined as the process in which an unstable nucleus decays altering the atomic number while leaving the mass number unchanged [33, 35]. This occurs through the release of an energetic electron/anti-neutrino pair or a positron/neutrino pair. The kinetic energy released is split between the electron and neutrino up to some finite value called the end-point energy or Q-value. The Q-value is determined by the mass difference between the decay and daughter nuclei.

As with alpha decay the primary products are not as interesting, because of their short range (electrons), or very small interaction probability (neutrinos). Instead, secondary gamma-ray photons produced as daughter nuclei decay to ground are observable up to many meters away.

Beta minus decay is observed in unstable, neutron rich nuclei. In beta minus decay the atomic number is increased by one as a neutron transitions to a proton, ejecting an electron in the process [35]. Equation 2.2 shows the beta minus decay process.



Beta plus decay is observed in unstable, proton rich nuclei. In beta plus decay the atomic number is reduced by one as a proton transitions to a neutron, ejecting

a positron in the process [33, 35]. Equation 2.3 shows the beta plus decay process. Secondary gamma-ray radiation from beta plus decay includes 511 *keV* annihilation photons produced when the positron annihilates with an electron. Beta plus decay is only possible when the Q-value is greater than  $2m_e c^2$ , where  $m_e$  is the mass of an electron and  $c$  is the speed of light.



### 2.2.3 Electron Capture

A proton rich nucleus can also decrease the atomic number by one, while maintaining the mass number through the capture of an orbital electron. When the electron is captured into the nucleus a proton transitions to a neutron and a neutrino is ejected. Electron capture is a competing process to beta plus decay and is more probable at lower Q-value decays ( $< 2m_e c^2$ ). Equation 2.4 shows the electron capture decay process.



## 2.3 Interaction Processes

Prior to a discussion of gamma-ray detection and imaging it is important to understand the physics of photon interaction mechanisms. Understanding the relevant interaction processes is a necessary step towards being able to detect and reconstruct photon information using coded aperture or Compton imaging techniques.

The three major interactions relevant to the TMI are photoelectric absorption, Compton scattering and pair production. Each of the three processes has an interac-

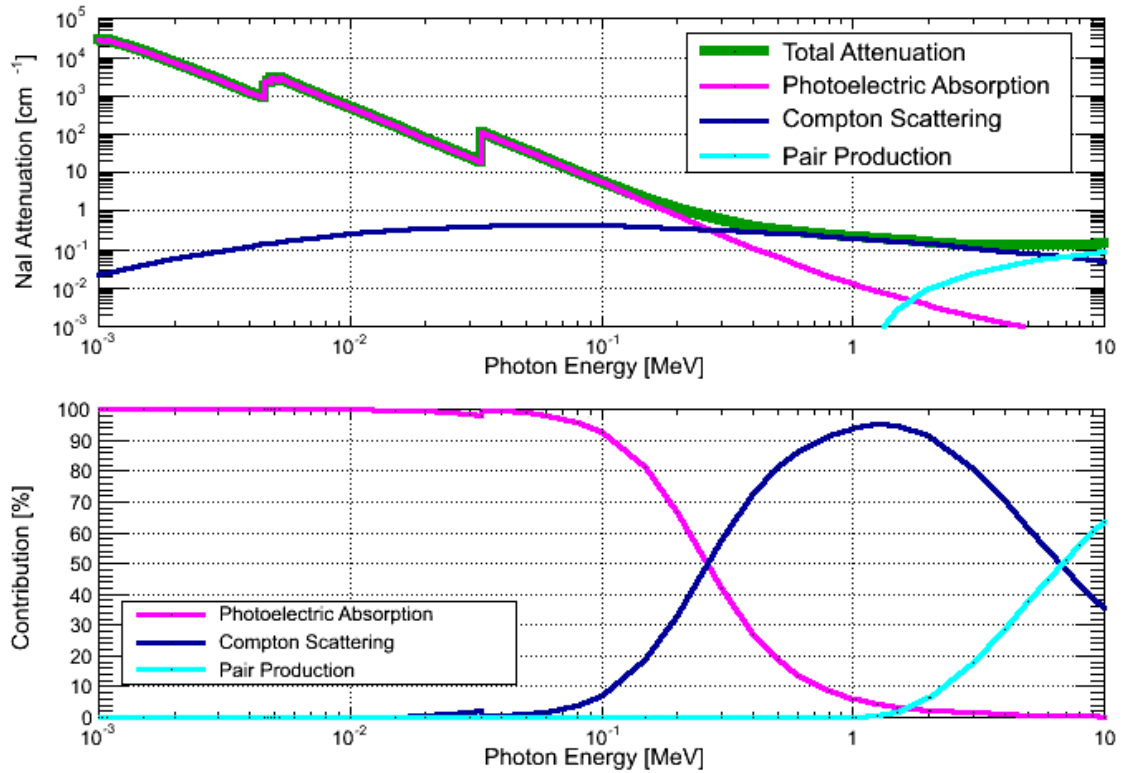


Figure 2.1: Photon attenuation values ( $cm^{-1}$ ) for NaI (top) and the contribution to total attenuation (bottom).

tion probability which depends on photon energy and the material. Figure 2.1 plots the attenuation values ( $cm^{-1}$ ) for NaI (top) and the contribution to the total attenuation (bottom) [36]. It can be seen that photoelectric absorption is the dominant interaction mechanism for gamma-ray photons up to 260 keV in NaI. Compton scattering is the dominant mechanism from 260 keV up to 6.7 MeV where pair production takes over. The contributions from the various processes is important to detection and will be discussed further in chapter 3.

### 2.3.1 Photoelectric Absorption

Photoelectric absorption is a process in which photons interact with bound electrons in an absorber atom, usually tightly bound  $K$ -shell electrons. Following absorption, the incident photon produces a photoelectron. The photoelectron emerges with energy  $E_e$ , as described by equation 2.5, where  $E_\gamma$  is the gamma ray energy and  $E_b$  is the binding energy of the photoelectron, or the energy required to remove it from its shell [37]. Photoelectric absorption is the dominant interaction mechanism for low-energy gamma rays.

$$E_e = E_\gamma - E_b \quad (2.5)$$

### 2.3.2 Compton Scattering

Compton, or incoherent scattering, was first explained by Arthur Compton in 1923 [38]. It was a significant discovery and earned him the Nobel prize in Physics. A key reason for giving him the Nobel prize was his recognition of the fact that a photon could behave like a particle in some circumstances. Compton scattering is an interaction process by which there is a decrease in energy, or increase in wavelength, of an incident photon when it elastically scatters off an electron in matter. The interaction between the photon and an electron in the scattering material results in a portion of the initial photon energy being imparted to the electron, causing it to recoil. The photon then continues on in a direction different from the original direction. Figure 2.2 shows a schematic of the Compton interaction where  $E_\gamma$  is the incident photon energy,  $E'_\gamma$  is the scattered photon energy,  $E'_e$  is the energy of the recoil electron,  $\theta_\gamma$  is the photon scattering angle and  $\phi_e$  is the recoil electron scattering angle.

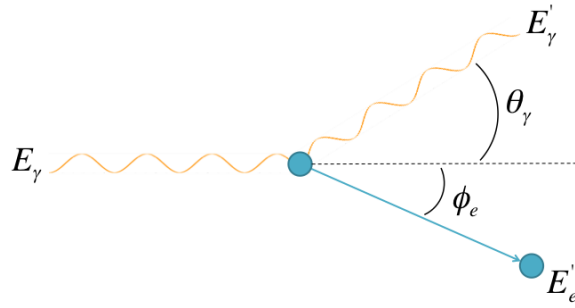


Figure 2.2: The Compton scattering interaction.

The change in direction of the photon is proportional to the energy imparted to the electron and can be calculated. Compton scattering is the dominant interaction mechanism for medium energy photons (0.5 to 3.5  $MeV$ ) in most materials. The kinematics of Compton scattering can be derived using conservation of energy (2.6) and momentum. Although the target electron does have non-zero initial momentum, its initial momentum is not known. As a result, the initial total energy of the electron is assumed to be its rest energy (0.511  $MeV$ ) and its momentum 0. Taking these assumptions into account, conservation of momentum can be expressed in the form of (2.7).

$$E_{\gamma} + E_e = E'_{\gamma} + E'_e \quad (2.6)$$

$$\vec{P}_{\gamma} = \vec{P}'_{\gamma} + \vec{P}'_e \quad (2.7)$$

Solving equations 2.6 and 2.7, the relationship between photon energy and scattering angle can be obtained and is known as the Compton scattering equation [38]. The Compton scattering formula is shown in Eq. 2.8.

$$\cos \theta_\gamma = 1 + \frac{m_e c^2}{E'_e + E'_\gamma} - \frac{m_e c^2}{E'_\gamma} \quad (2.8)$$

### 2.3.3 Pair Production

Another process to be considered in a Compton camera system is pair production. Pair production is the creation of an electron/positron pair from a photon. This process occurs as a result of the interaction of the photon with the electromagnetic field of the nucleus of a target atom. This interaction can also take place with an electron but only at higher energies that are not of interest for Compton imaging. Pair production can only occur when the amount of energy available is greater than or equal to the rest mass energy of the pair ( $2m_e c^2 = 1.022 \text{ MeV}$ ). Figure 2.3 shows the nuclear pair production interaction where  $\theta$  is the polar angle of both the exiting positron and electron.

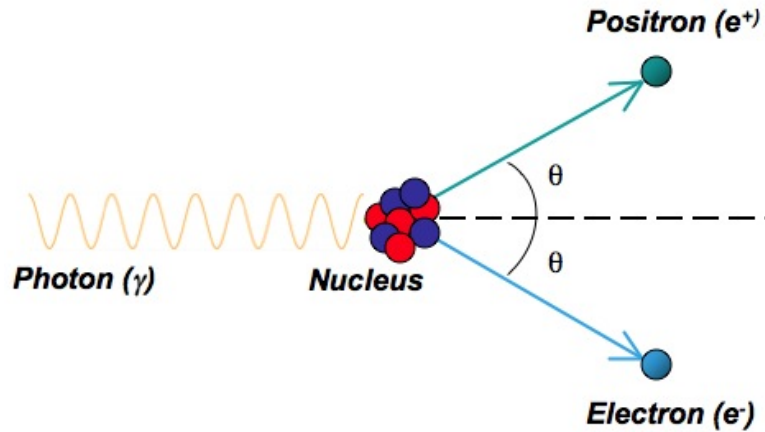


Figure 2.3: The nuclear pair production interaction.

### 2.3.4 Doppler Broadening

Doppler broadening is an effect brought on by the electrons involved in the Compton scatter interaction. Equation 2.8 is based on the assumption that the electrons are initially free or unbound. The electrons, however, are neither free nor at rest, but in motion and bound to a nucleus [39]. This has several effects on the kinematics of the Compton scatter. First, the total scattering probability changes as defined by the Klein-Nishina scattering cross-section [40]. Second, the scattering angle distribution changes, and finally the energy distribution between the electron and the gamma ray changes. All of these consequences give rise to a fundamental, lower limit for the angular resolution of a Compton camera. It is safe to assume that in the case of the TMI (and any other detector) this effect is uncorrectable. Generally, doppler broadening is dominant in systems with very good energy resolution (*e.g.* semi-conductor detectors). In the case of the TMI however, the effect is generally masked by the moderate energy and position resolution of the NaI detectors. Also, the effect is most pronounced at low-energy ( $<150 \text{ keV}$ ). Since the effect of Doppler broadening is inherent to a material, as the atomic number ( $Z$ ) of a material increases so does the effect. This is an important consideration when designing a Compton camera.

## 2.4 Summary

In this chapter a summary of current technology has been presented for a variety of gamma-ray detection systems. Also the source of gamma-ray radiation has been discussed as well as the mechanisms with which energetic photons interact in matter. With this information, it is possible to begin the discussion of the TMI and understand the need and applicability of a hybrid detection system. A system prototype



has been constructed which incorporates some or all aspects of current detection platforms in order to improve the performance of the system overall within cost, size and weight constraints – important considerations of a mobile system. Both coded aperture and Compton imaging have proven useful technologies in a wide variety of fields. Additionally, several of the examples combined multiple detection modes to improve performance. This work aims to combine the power of both imaging and non-imaging detection methods as well as implement the novel approach of image fusion through the use of an active coded aperture mask.

## Chapter 3

# THE RAYTHEON-SORDS TRI-MODAL IMAGER

The TMI is a mobile, coded aperture and Compton scatter imager with enhanced hybrid imaging and spectroscopic capability. The TMI uses a conventional coded aperture imager with a non-conventional active mask to provide both veto capability and Compton imaging. The TMI is unique in that it is the first of its kind as both a mobile platform for 3D gamma-ray imaging and a hybrid active coded aperture/Compton imaging system. The goal of a hybrid imaging system is to improve system performance through the combination of multiple imaging modalities.

Coded aperture and Compton imaging are complementary in several ways. First, coded aperture is normally a passive imaging technology that relies on the opacity of the masking elements for image contrast. This makes coded aperture imaging useful for low to medium energy gamma rays. Conversely, Compton imaging is more efficient in the medium to high energy range because it relies on Compton scattering followed by a photoelectric interaction. Combining these two modalities into a single imager is unique because it provides wide energy applicability and increased sensitivity in both the overlap regions of energy as well as the entire energy range. The sensitivity of the

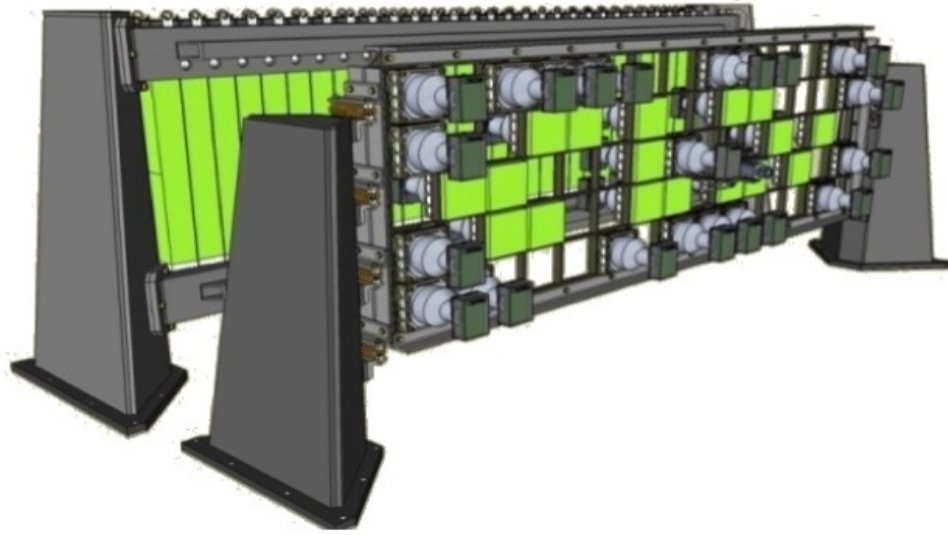


Figure 3.1: The Raytheon-SORDS Tri-Modal Imager. The TMI is a hybrid coded aperture / Compton imager deployed in the back of a truck in order to perform mobile gamma-ray imaging.

TMI increases because the background contribution (dominant) from each modality is large but different, however the source contribution manifests in much the same way. This leads to the ability to reject much of the background in an image and keep only the true source components. Figure 3.1 shows a model of the TMI detector arrays and support hardware.

A system as complex as the TMI requires many hardware (and software) components to work seamlessly in order to take full advantage of the capabilities. This system has many hardware components such as the detector hardware for both the active mask and the absorption array, the navigational system, camera, generator, environmental controls, user interfaces and data processing as well as reach-back capability for remote viewing of the online system. Figure 3.2 shows the top, front and side views of the TMI geometry. The FOV indicated assumes 50% coding, *i.e.* limited

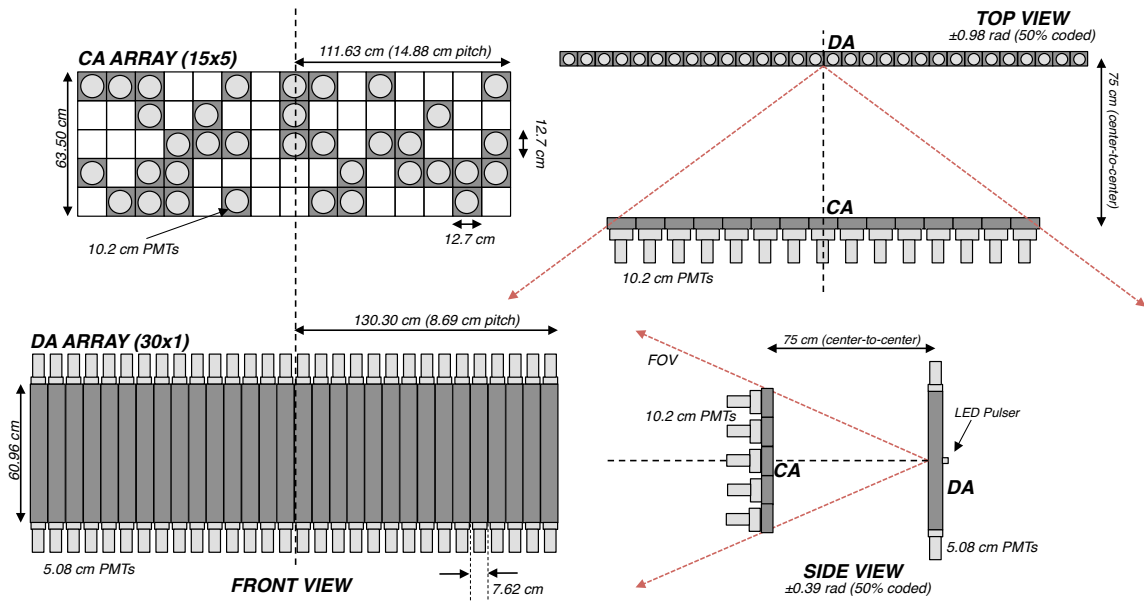


Figure 3.2: Front, side, and top views of the TMI geometry.

to allow for the mask to shadow at least 50% of the detector array from all points.

### 3.1 Navigation Hardware

One of the key components to the TMI is the combined navigational Global Positioning System (GPS) and Inertial Navigation System (INS). The output of the navigation system is both the geographical location of the detector unit (latitude, longitude and altitude) as well as the attitude (roll, pitch and bearing) of the detector. Roll is defined as the port/starboard angle normal to the plane of the earth. Pitch is defined as the fore/aft angle normal to the plane of the earth and bearing is the direction of travel with respect to true north. Additionally, the GPS/INS system can estimate the goodness of the navigational solution based on signal reception and accuracy of the calculated velocity vector.



Figure 3.3: Photo of the KVH Industries Inc. CNS-5000 INS. The system combines an inertial navigation system with a high-accuracy GPS receiver in a single small enclosure.

### 3.1.1 Specifications

The navigational hardware selected for the TMI is a Commercial-Off-The-Shelf (COTS) product from KVH Industries Incorporated [41]. The CNS-5000 inertial navigation system combines the complementary technologies of a fiber optic gyro-based Inertial Measurement Unit (IMU) with a precision GPS receiver in a single enclosure. Figure 3.3 shows an image of the CNS-5000 INS. The physical and environmental specifications of the CNS 5000 are shown in Table 3.1.

Table 3.1: Physical and environmental specifications for the CNS-5000 navigational subsystem.

Specification	Value
Weight	5.2 lbs. (2.36 kg)
Size	6.0" x 6.6" x 3.5"
Power Consumption	15W Max
Operating Temperature	-40°C to +75°C (-40°F to +167°F)
Storage Temperature	-50°C to +80°C (-58°F to +176°F)
Output Rate	100 Hz
Input Voltage	9-16V

Coupling of the GPS and INS systems provides uninterrupted navigation information. This is very important to the operation of the TMI in the event that GPS signal reception is obstructed, or unavailable. This is made possible by the ability to correct for drift in the IMU using the GPS signal when available and the relative position of the IMU provides accurate position readings when GPS is degraded or unavailable. This can be important in urban canyon scenarios where the availability of GPS can be intermittent. The CNS-5000 also uses inertial information to acquire and track the satellite signal in order to improve signal reception and claims to deliver signal acquisition (L1/L2 band lock) in less than 2 seconds compared to 10 seconds for comparable systems [41]. Also, the use of a coupled IMU allows for the data rate to be increased relative to standard GPS. Standard GPS location updates at 5 Hz, however the IMU extrapolates position using data from the accelerometers at 100 Hz. Since data from the gamma-ray imager is highly position sensitive and is measured at rates that can exceed 50,000 events per second this can improve reconstruction capability.

### 3.1.2 GPS/INS Performance

To gauge the performance of the GPS/INS system it is important to look at the deviation in position as a function of time when the imager is at a stand-still. This will allow for measurement of drift in the readings. Shown below in figure 3.4 is the calculation of the Circular Error Probable (CEP) metric. This is a common metric used in assessing the performance of a positioning system [42]. CEP is defined by the smallest radius of a circle, centered at the mean location of all measurements, that will encompass 50% of all measured locations. For this measurement the data set was 82 seconds of 100 *Hz* location information while the imager was stationary. Since the imager is not moving the GPS system should not change the location however, there is some uncertainty and drift in the location calculation. For the purposes of the gamma-ray imaging system the calculated CEP of 3.3 *cm* is more than sufficient.

### 3.1.3 Validation

The first step in making use of the GPS/INS information is to ensure the data is sensible. Checking of navigational information is critical to the reconstruction algorithms to ensure images are placed in the correct location. Table 3.2 shows the criteria used in checking the navigational information. The values in Table 3.2 are first order checks, the fact that a navigation information has a value in range does not imply it is accurate. To this end, data are also checked for deviations between measurements, where an unexpectedly large change in any value over a small time is flagged as invalid. It is also important to check the parameters when interpolating and averaging between measurements within the algorithms to ensure a miscalculation has not been made. Time output from the navigational hardware is presented in milliseconds into

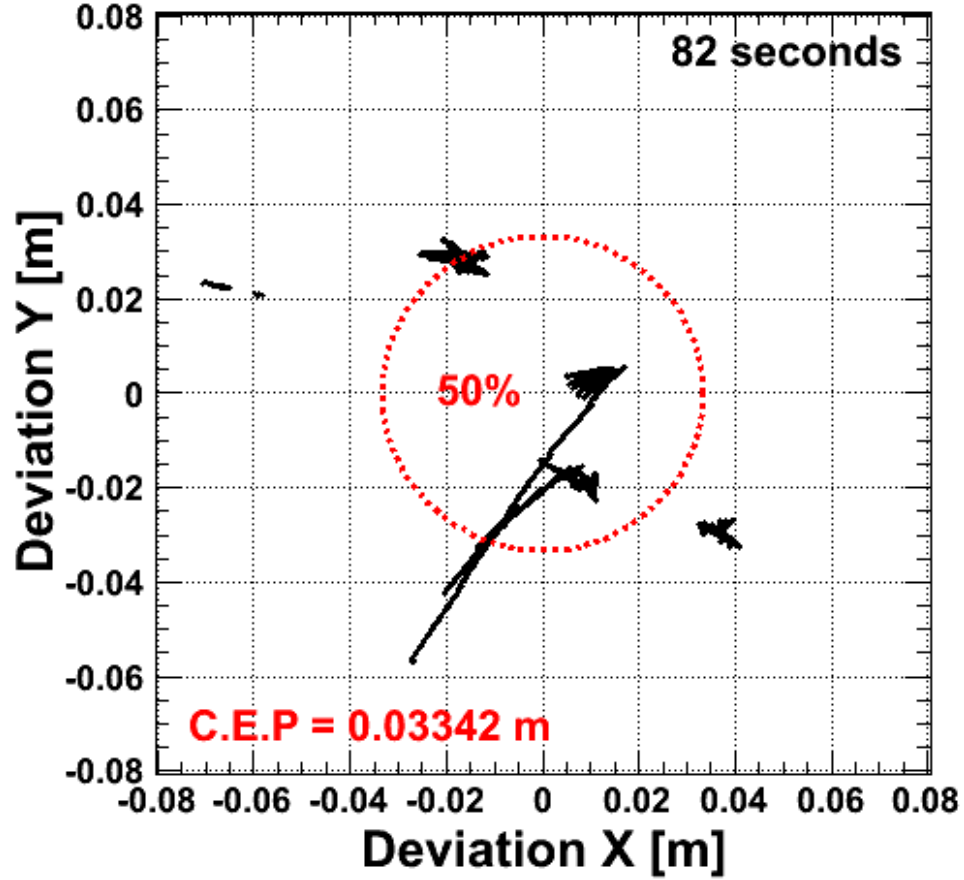


Figure 3.4: Calculation of the CEP resolution for the GPS location shows to be less than 3.4 cm over 82 seconds.

the week. As such, the acceptable range in Table 3.2 is determined by the maximum number of milliseconds in a single week.

### 3.2 Detector Hardware

The heart of the TMI is the detector subsystem. The detector hardware consists of 2 arrays of NaI elements. The first array is an active NaI mask containing 35, 5x5x2  $in^3$  crystals called the CA array. The CA array is used for both attenuation and



Table 3.2: List of checked parameters and acceptable ranges for GPS/INS navigational data.

Segment Parameter	Acceptable Range
Distance from Last	<15 meters
Altitude	-100 meters to 10,000 meters
Latitude	-90 to 90 degrees
Longitude	-180 to 180 degrees
Bearing	0 to 360 degrees
Pitch	-180 to 180 degrees
Roll	-45 to 45 degrees
Velocity	<70 mph (32 m/s)
Time	0 to $6.04 \times 10^8$ ms

scattering of gamma-ray photons. The second is an array of 30,  $2.5 \times 3 \times 24$   $in^3$  position sensitive NaI bars with dual ended readout called the DA array. The purpose of the DA array is to collect both un-scattered and scattered gamma-ray photons. The use of an active coded mask array allows for simultaneous coded aperture and Compton imaging to be performed using the same hardware. The output of the detector arrays is a list-mode (event-by-event) stream of fully digitized data; energy, time, and relative position. A coincidence tag is also included to allow for discrimination between coded aperture events and Compton events. The detectors have been designed to meet the requirements of the broad agency announcement *DNDOBAA07-01* (BAA) from which this program resulted. Table 3.3 summarizes the hardware requirements for the TMI.

### 3.2.1 Active Coded Mask - The CA Array

Coded aperture imaging requires the use of a coded mask array in order to attenuate a fraction of incoming gamma-ray photons such that a shadow pattern is cast onto the rear detector array. In traditional coded aperture systems the mask is constructed

Table 3.3: Broad agency announcement requirements for the SORDS detector.

Criteria	Required Value
Gamma-ray energy range	100-1200 <i>keV</i>
Energy resolution at 662 <i>keV</i>	7.5% FWHM
Energy resolution at 122 <i>keV</i>	17% FWHM
Detected gamma-rays per second in photo peak from 1 mCi <sup>137</sup> Cs at 100 <i>m</i>	15
Field of view in plane of motion	> 2 <i>radians</i>
Field of view normal to motion	> 0.5 <i>radians</i>
Point source angular resolution in plane of motion	< 0.3 <i>radians</i>
Point source angular resolution normal to motion	< 0.3 <i>radians</i>
Total system size †	< 8 <i>m</i> <sup>3</sup>
Total system weight †	1200 <i>kg</i>
Total system power †	< 3 <i>kW</i>
No radioactive sources used in system	Yes

† Includes hardware extraneous to TMI detector arrays.

from dense materials such as lead or tungsten to achieve maximum opacity. The TMI uses an active coded aperture mask, meaning that active NaI tiles are used which can act as both gamma-ray attenuators and scattering detectors for Compton imaging. The thickness of the NaI tiles has been optimized to provide similar opacity to lead at 1.5 *MeV*, given equal mass. Mask elements of lead at 1.64 *cm* thick (3007 *g*) attenuate 61% of 1.5 *MeV* photons while 5.08 *cm* thick NaI elements (3007 *g*) attenuate 58%. The coded aperture array is referred to as the CA array.

The active mask used in the TMI is a 15x5 element grid of NaI tiles. Each element in the array is a 5x5 inch NaI crystal with a thickness of 2 inches. The array is filled in a random pattern with 35 active tiles, leaving 40 open grid locations. This translates to a 46.66% fill factor.

The CA array is mounted in a lightweight, rigid and movable structure that allows

for a wide FOV and easy servicing and reconfiguration. The array structure is 121 inches long and 45 inches high. It has been milled from a single piece of aluminum and is shock mounted to support stands at either end that have been designed not to obstruct the FOV. The array is designed to be easily reconfigurable as the detectors can be mounted in any of the 75 locations in the structure. Each detector element in the array is electrically isolated.

Because the CA array acts as both a gamma-ray attenuator for coded aperture imaging and a scattering plane for Compton imaging the selection of detector size has been carefully considered. The detectors are designed to have good efficiency for low energy gamma-ray absorption and single Compton scatters. Additionally, to meet the off-axis requirements from Table 3.3 the thickness of the detector elements must not occlude the aperture at high incident angles. Each NaI crystal is housed in a 1 *mm* thick aluminum casing.

Each CA array detector element is optically coupled to a 4 inch bialkali PMT on the 5x5 inch face. The 4 inch PMTs are custom built by Hamamatsu specifically for the TMI to achieve similar performance to a 5 inch PMT at 40% of the mass. This is an important consideration since any material in the path of incident gamma-rays can cause scattering or absorption, degrading image reconstruction. Each PMT is housed in an aluminum enclosure to provide shielding from external light and Electromagnetic Interference (EMI). Some of the mass savings comes from the use of 16  $\mu m$  cobalt alloy foil wrapping used for magnetic shielding of the PMT. The magnetic shielding was selected to provide immunity to the Earth's magnetic field to a level of 0.5% maximum gain drift between orientations. The bialkali photocathode material was chosen to achieve the desired sensitivity to the 420 *nm* luminescence wavelength of



Figure 3.5: CA detector element assembly with photomultiplier tube attached.

NaI while meeting BAA requirements and maintaining lower cost. Figure 3.5 shows an assembled CA detector element with PMT.

Optimization was performed using Monte Carlo simulations in order to determine if the PMTs should face out from the front of the detector array or back towards the absorption array. Ultimately it was decided that position does not have an appreciable effect on detection, therefore all PMTs were placed facing out from the front of the detector. This configuration also allows for more room to move about inside the vehicle; reducing the possibility of damaging one of the elements.

Affixed to each PMT is a dedicated, low-profile 4x2 inch circuit card housing High-Voltage (HV) and discrimination electronics. The electronics were custom developed and built by Bubble Technology Industries (BTI). Each circuit card is enclosed in

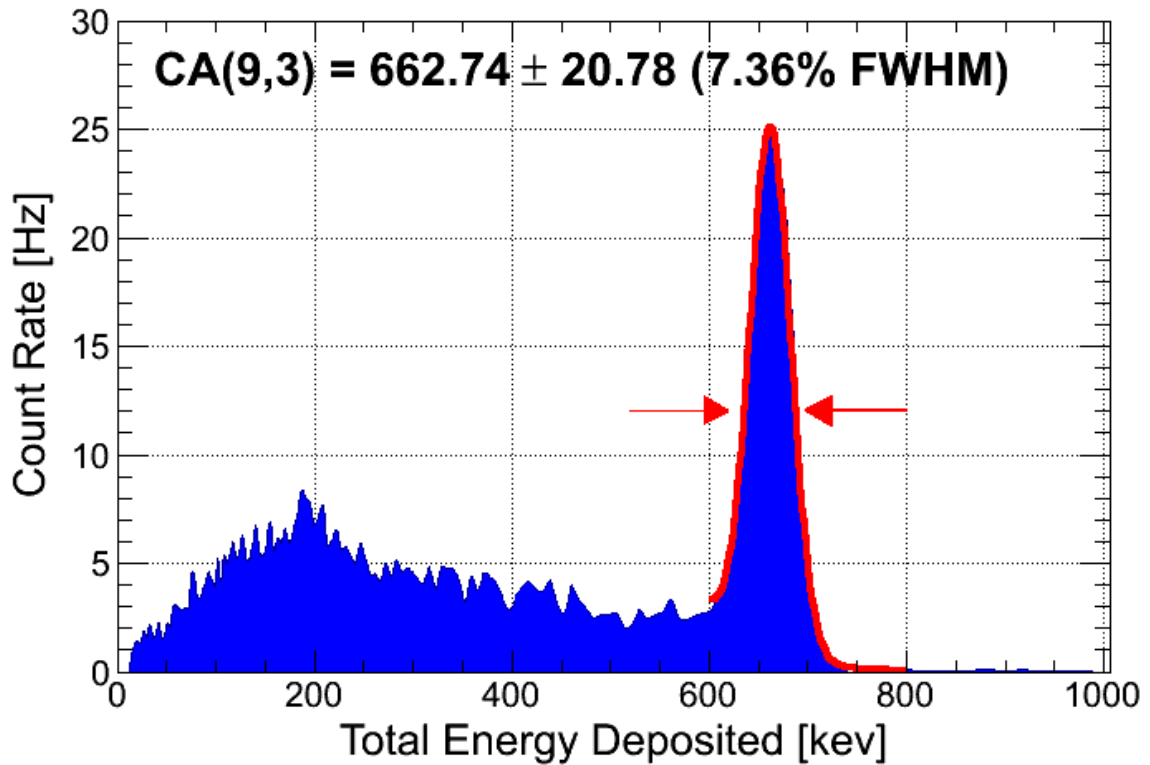


Figure 3.6: Measured energy spectrum from a single CA detector element from a  $^{137}\text{Cs}$  point source taken during field measurements. The FWHM energy resolution at 662 keV is shown to be 7.36%.

an 0.03 inch thick aluminum housing for HV safety and is shielded from EMI. The specifics of the front-end electronics will be given in section 3.6.

The performance of the CA array elements fully meets the specifications in the BAA requirements for energy resolution. Figure 3.6 shows the measured energy resolution from a 1.0 mCi,  $^{137}\text{Cs}$  point source at 25 meters ( $90^\circ$ ) taken during field trials of the system in a single CA element. The demonstrated energy resolution is 7.36% FWHM at 662 keV. Figure 3.6 also exhibits good energy calibration; the 661.59 keV photo peak from  $^{137}\text{Cs}$  is centered at 662.74 keV.

It is also useful to look at the average resolution across the entire CA array. Figure

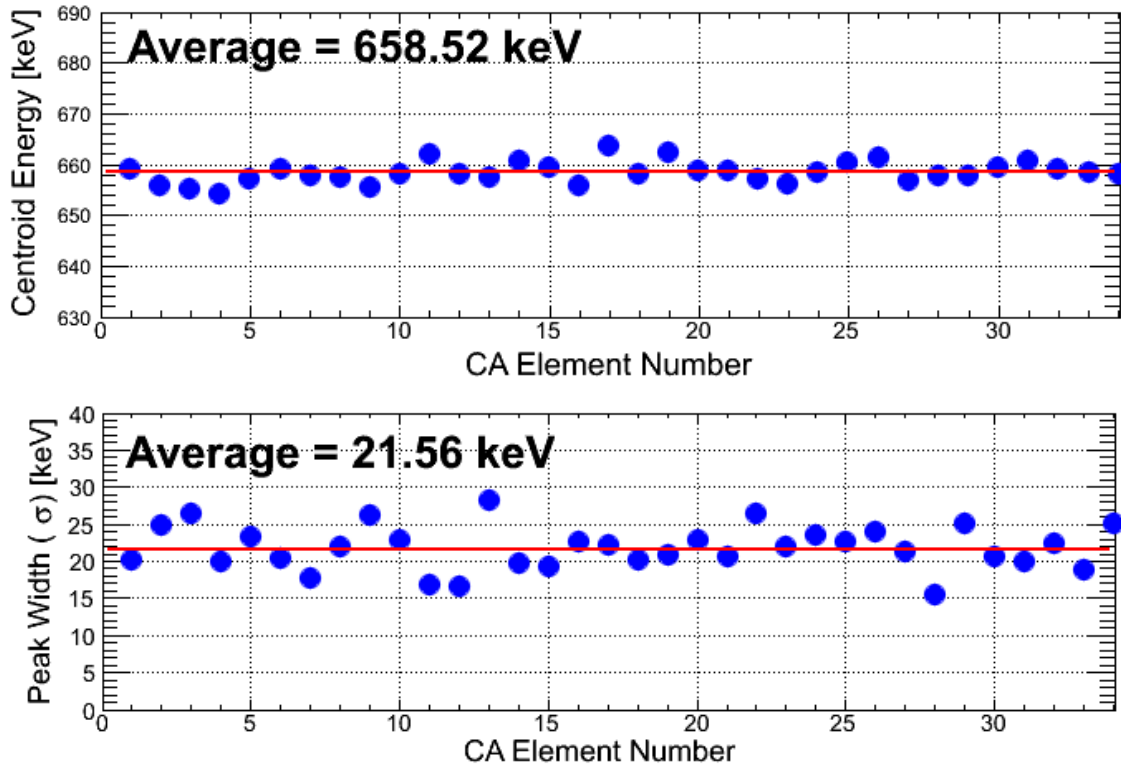


Figure 3.7: Measured centroid (top) and width (bottom) of the <sup>137</sup>Cs photo peak for each of the 35 CA detector elements. The average resolution is  $7.69 \pm 0.2\%$  FWHM.

3.7 shows the <sup>137</sup>Cs photo peak location for each element (top) and the measured width of the photo peak (bottom). From the measurements the average resolution of the CA array is  $7.69 \pm 0.2\%$  FWHM. The average centroid and width are shown with a solid red line.

### 3.2.2 Absorption Elements - The DA Array

For both coded aperture and Compton imaging to function there is a need to absorb the total gamma-ray energy. This functionality is provided by the DA array. This serves coded aperture by measuring the position distribution of gamma rays that have been shadowed by the CA mask array. Also, it serves Compton imaging by

collecting the remaining energy from Compton scattered photons in the CA mask array.

The DA array consists of 30,  $2.5 \times 3 \times 24 \text{ in}^3$ , NaI bars. Similar to the CA array, the DA array is mounted to a rigid, moveable structure comprised of four aluminum beams anchored at the ends by support stands. Each beam has a shock mounted bar attached that acts as the mounting point for the NaI bars. This prevents the bars from moving independently. The array is 127 inches long and 46 inches high. Each of the rear detectors is electrically isolated from the support structure. Figure 3.8 shows two of the NaI bars used in the DA array.

In the design of the DA array it was important to balance multiple factors including efficiency, energy resolution, position resolution, weight and cost of the bars in order to meet BAA specifications. Additionally, all these factors are limited by realistic detector availability from the manufacturer. Energy and position resolution are key to the DA array since it will directly contribute to the angular resolution of the imager.

Bars are read out by 2 inch Super Bialkali (SBA) PMTs at both ends. SBA PMTs were chosen for the rear array, at increased cost, to boost the readout performance due to the length of the bars and the attenuation of light along the length. SBA PMTs have increased quantum efficiency for the emission wavelength of NaI; 32% versus 23% for regular bialkali PMTs. [43].

Position-independent measurements of energy and position can be calculated using the product and ratio of pulse height amplitudes. This calculation can be simplified if the PMTs are gain matched, meaning a burst of light in the center of the bar produces an equal amplitude signal from the PMTs at both ends. The specifics of the

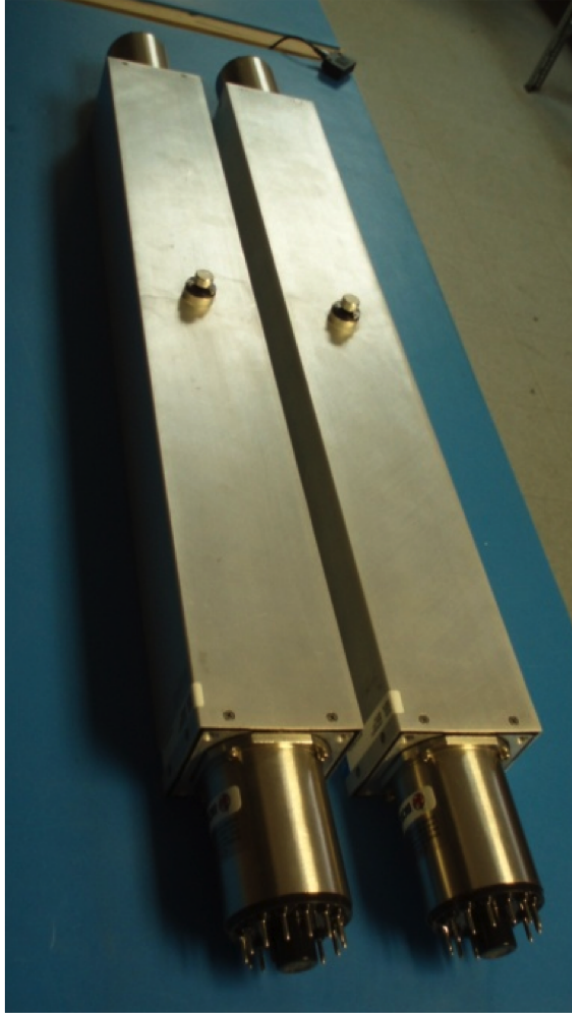


Figure 3.8: Two NaI bars used in the DA array with attached 2" PMTs at both ends and LED pulser port at the center.



gain matching are provided in section 3.3.

Position information is measured by localizing the source of scintillation light. Intensity of light measured at one end of the bar falls exponentially with the origin point of the light within the bar. Equations 3.1 and 3.2 show the calculation of the expected PMT signal at one end of the bar where  $E_\gamma$  is the energy deposited,  $P$  is the probability of an optical photon at one end of the bar reaching the PMT at the other end,  $E_0$  is the energy deposited per optical photon generated, a characteristic of the material, and  $\alpha$  is the light attenuation coefficient in the material,  $y$  is the interaction location along the bar and  $L$  is the length of the bar [33].

$$PMT_1 = \frac{E_\gamma P}{E_0} \exp[-\alpha(L/2 + y)] \quad (3.1)$$

$$PMT_2 = \frac{E_\gamma P}{E_0} \exp[-\alpha(L/2 - y)] \quad (3.2)$$

Dividing the measured signal at both ends of the bar and taking the logarithm as shown in Eq. 3.3 yields a linear indication of the position where the scintillation occurred. Notice from Eq. 3.3 that the calculated position along the bar is independent of energy deposited in the bar and only a function of the ratio of measured signals and fixed material properties.

$$y = \frac{1}{2\alpha} \ln \left( \frac{PMT_2}{PMT_1} \right) \quad (3.3)$$

The total energy deposited in the bar can be calculated by multiplying Eqs. 3.1 and 3.2 and taking the square root as shown in Eq. 3.4. Notice from Eq. 3.4 that the

calculated energy deposited in the bar is position independent and only a function of the measured signals and fixed material properties of the bar.

$$E_{\gamma} = \sqrt{PMT_1 PMT_2} \frac{E_0}{P} \exp[\alpha L/2] \quad (3.4)$$

The performance of the DA array elements fully meet the specifications in the BAA requirements for energy resolution. Figure 3.9 shows the measured energy resolution from a 1.0 *mCi*,  $^{137}\text{Cs}$  point source at 25 meters ( $90^\circ$ ) taken during field trials of the system in DA bar 26. This is the measured energy spectrum, for all interactions, across the entire length of the bar. The demonstrated energy resolution is 7.46% FWHM at 662 *keV*. Figure 3.9 also exhibits good energy calibration; the 661.59 *keV* photo peak from  $^{137}\text{Cs}$  is centered at 663.84 *keV*.

It is also useful to look at the average resolution across the entire DA array. Figure 3.10 shows the  $^{137}\text{Cs}$  photo peak location for each DA bar (top) and the measured width of the photo peak (bottom). From the measurements the average resolution of the DA array is  $7.29 \pm 0.15\%$  FWHM. The average centroid (658.52 *keV*) and width (21.56 *keV*) are shown with a solid red line.

### 3.3 Gain Matching

Gain matching of the PMT readout for a single NaI bar is achieved through automatic high voltage tuning using a reference signal at the center of the detector face. Gain matching is a continuous, automated algorithm that ensures both PMTs register an identical charge output when exposed to the exact same amount of light. Practically, a scintillation event at the center of the detector should read out at each end with

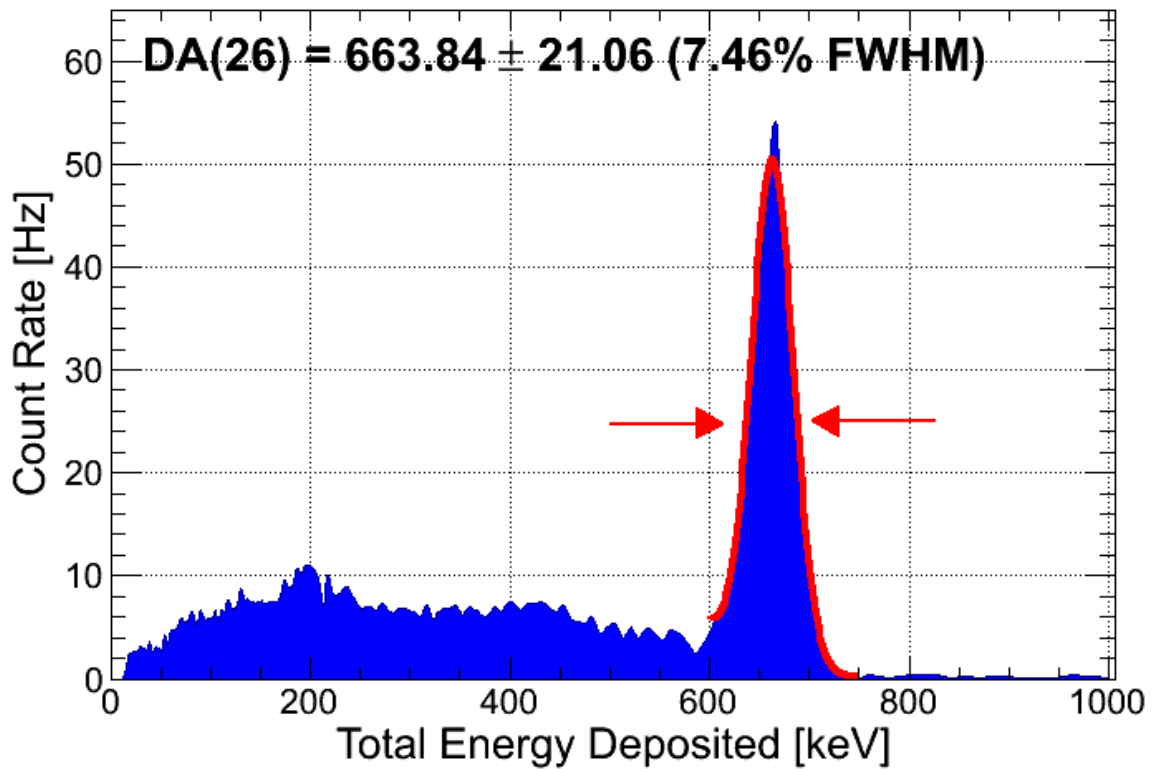


Figure 3.9: Measured energy spectrum from a single DA detector element from a  $^{137}\text{Cs}$  point source taken during field measurements. The FWHM energy resolution at 662 keV is shown to be 7.46% integrating over all energy depositions along the length of the bar.

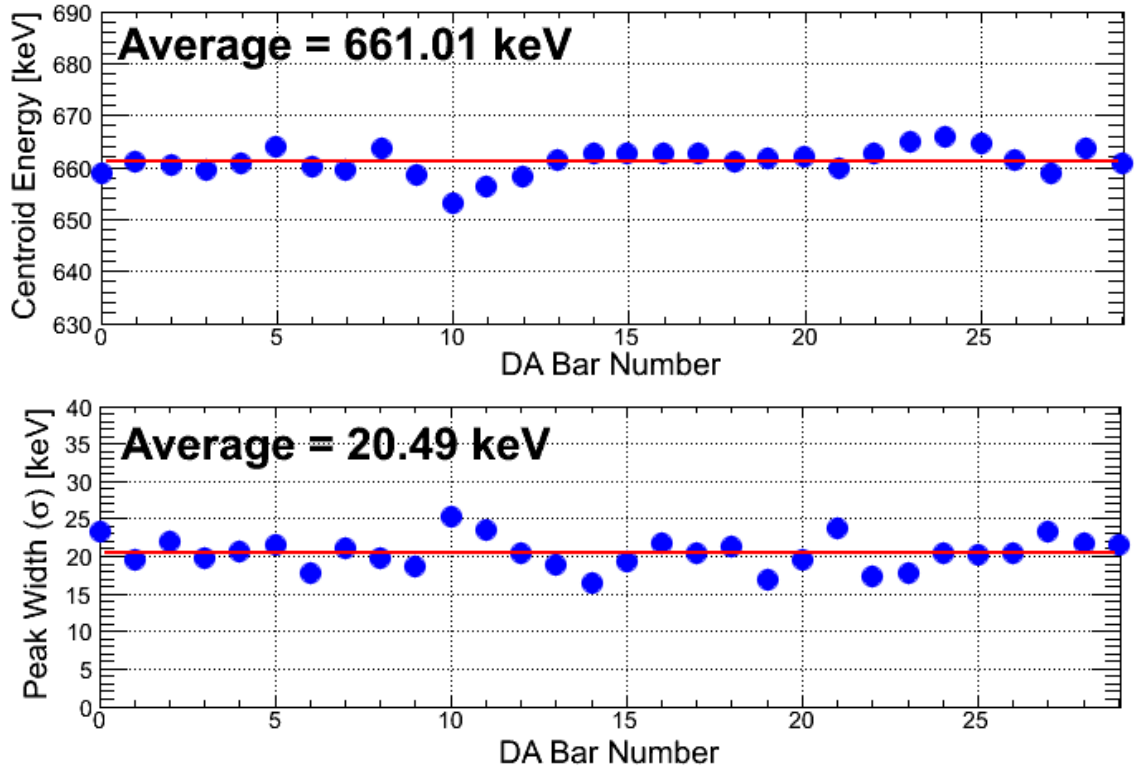


Figure 3.10: Measured centroid (top) and width (bottom) of the  $^{137}\text{Cs}$  photo peak for each of the 30 DA detector elements. The average resolution is  $7.29 \pm 0.15\%$  FWHM.

equal voltage, however differences in the characteristics of the PMTs as well as gain drifts can cause variations in the measurement of the same event at opposite ends of the bars.

Normally, gain matching can be performed in the laboratory fairly easily using a check source centered on the detector element and manually adjusting the gain of the PMTs until an identical signal is measured at each end. This is complicated in the case of the TMI because it must auto-calibrate, track gain drifts and make no use of radioactive sources for calibration purposes to fully meet the system requirements.

In order to overcome this challenge the TMI makes use of a controlled Light Emitting Diode (LED) flash precisely at the center of each NaI bar. Periodically, an LED flashes a brief pulse, several hundred nanoseconds in duration. Light from the LED is piped into the bar via a fiberoptic cable to a port at the geometric center of the 3x24" face of the detector. The port is a hermetically sealed window to the crystal with a SubMiniature version A (SMA) type coaxial connector. Light from the LED emitted into the crystal is diffused evenly between the two ends of the bar, such that light incident on each PMT photocathode will be approximately equal. The pulse from the LED is controlled by the individual detector's Field-Programmable Gate Array (FPGA).

Since the FPGA on the detector electronics also controls both the LED flash and the event classification it can separate calibration from scintillation events. The gain matching algorithm is continuously running for each pair of PMTs on all 30 NaI bars, iteratively changing the voltages as necessary. It must also ensure that the mean voltage provides a good dynamic range for the system in terms of energy calculation. Continuous tracking is used to correct for any gain drifts which would

affect each PMT uniquely. Figure 3.11 shows an event-by-event plot of the measured pulse height amplitude at both ends of a DA array bar. Here, features from the 662  $keV$   $^{137}\text{Cs}$  photo peak, 1461  $keV$  peak from  $^{40}\text{K}$ , the LED pulser and the 2614  $keV$  peak from  $^{208}\text{Tl}$  can be seen.

### 3.4 Energy Calibration

Energy calibration refers to the conversion of the channel value from the Analog-to-Digital Converter (ADC) electronics corresponding to the Pulse Height Amplitude (PHA) measured by the PMT, into a physical value of energy. Similar to the gain matching algorithms, the energy calibration must run continuously and automatically on each detector to account for changes in the PMT gain. The process of energy calibration on the TMI is identical for both CA and DA detector elements with the only exception being that the energy calibration takes place after gain matching in the DA detectors and uses the PHA calculated from Eq. 3.4.

Each calibration is performed using a two-point calibration with the zero-energy channel (pedestal) and the centroid channel of the  $^{40}\text{K}$  peak from NORM background. The zero-energy channel is measured by forcing the ADC electronics to read out when no real trigger is present in the system and taking the centroid of the pedestal. The pedestal has some width defined by the noise in the triggering electronics.

Candidate  $^{40}\text{K}$  peaks are found using an automated searching algorithm. Several tests of peak validation are performed to ensure that the correct peak is selected as  $^{40}\text{K}$ , errors in the searching algorithm could have major effects on the performance of the system, as measurements would be incorrectly converted to energy. Once the  $^{40}\text{K}$  peak is located, detector HV is adjusted such that the peak centroid is appropriate

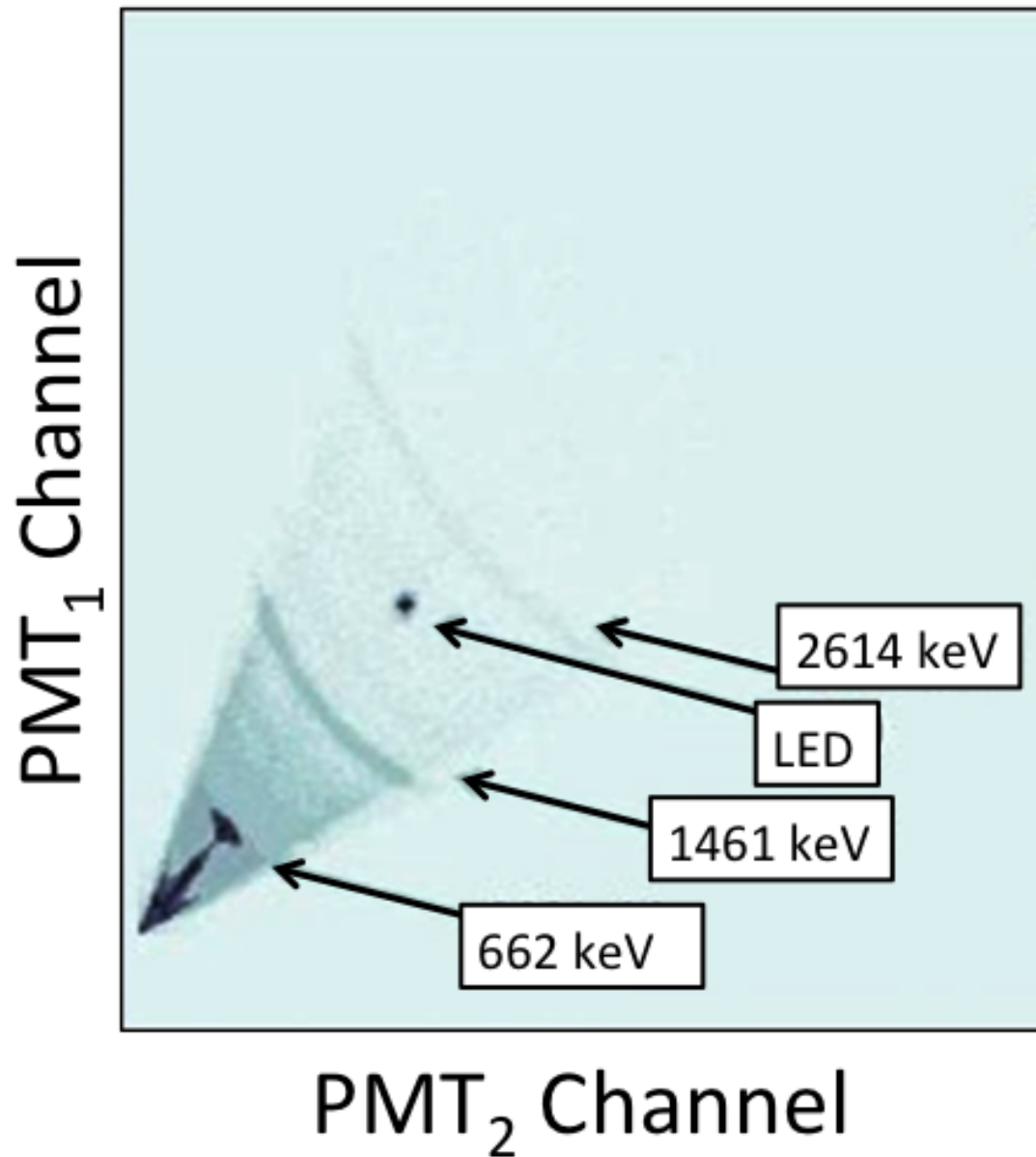


Figure 3.11: Event by event plot of pulse height amplitude as measured by the PMTs at both ends of a single DA array bar [44].

to maintain the dynamic range of the system (up to 3000 keV) and maximize the dispersion at the low-end of the energy spectrum. This translates to roughly 50% of the full range of the ADC.

Event to event variation in the amount of light produced in the crystal results in non-proportional response. Therefore, a final correction to the two-point calibration accounts for the non-proportionality of light output ( $\frac{\gamma}{MeV}$ ), that is characteristic of the NaI crystal [34]. This correction is performed event-by-event using a lookup table generated from interpolated measured data. Once a detector is calibrated it is considered operational and ready to send data to the imaging algorithms for processing. Detector firmware continuously updates the calibration for each element every 2 minutes using the most recent 10 minutes of data collected. The TMI remembers the most recent calibration for each detector to avoid a lengthy calibration period at the beginning of a collection. Any or all detectors can be forced to forget their calibration parameters, putting them into calibration mode. A full initial calibration can take up to 30 minutes to ensure adequate statistics for fitting the  $^{40}\text{K}$  spectral line. This can be expedited by several minutes by placing bags of potassium chloride (KCl), or rock salt, nearby the detector to boost the  $^{40}\text{K}$  peak statistics.

### 3.5 Position Calibration

With properly gain matched PMTs at the top and bottom of the detector the value of  $y$ , or PHA, from Eq. 3.3 is proportional to the position along the length of the bar. In order to make use of the position sensitivity of the bars the PHA must be converted into a physical distance. Additionally, each of the 30 NaI bars, with varying crystal quality, will behave in a slightly different way.



Each of the 30 NaI bars have been manually calibrated using a  $^{137}\text{Cs}$  check source moved along the length of the bar at 15 discrete locations and measured for 30 seconds. By analyzing the measured ADC channel distributions for each bar a calibration curve can be established that will convert the PHA into a physical measurement. Figure 3.12 shows the ADC channel distribution for each of the 15 measurements (top) superimposed with the fit to each (red) and the derived calibration curve (bottom). The observed wide distributions in Fig. (3.12) are a result of two factors. First the check source was placed onto the surface of the bar housing and was not collimated, making the interactions locations essentially a  $2\pi$  distribution. Second, the energy depositions were not windowed around the  $662\text{ keV}$  photo peak from  $^{137}\text{Cs}$  since the calibration could easily be estimated from the centroid of the distribution and includes more photons, reducing the uncertainty.

The derived calibration curves for all 30 bars are shown in Figure 3.13. It can be seen from Fig. 3.13 that there is variation between the bar calibrations, making it necessary to calibrate each bar individually. Fit functions used to generate the calibration curves are  $3^{\text{rd}}$  order polynomials. The equation used is of the form  $y = P_0 + P_1x + P_2x^2 + P_3x^3$ , where  $y$  is the calculated interaction location and  $x$  is the readout ADC value. The parameters of the fits are summarized in Table 3.4. Each of the calibration fits has an acceptable range of ADC channels ( $\text{ADC}_{\min}$  to  $\text{ADC}_{\max}$ ) that will give a measurement location within the physical dimensions of the bar ( $\pm 30.48\text{ cm}$ ).

Measurements taken from the middle region of each bar are generally linear in nature as a function of ADC channel. However at the ends of the bars the functional form takes more of a polynomial shape. This is because a signal near the edge of the

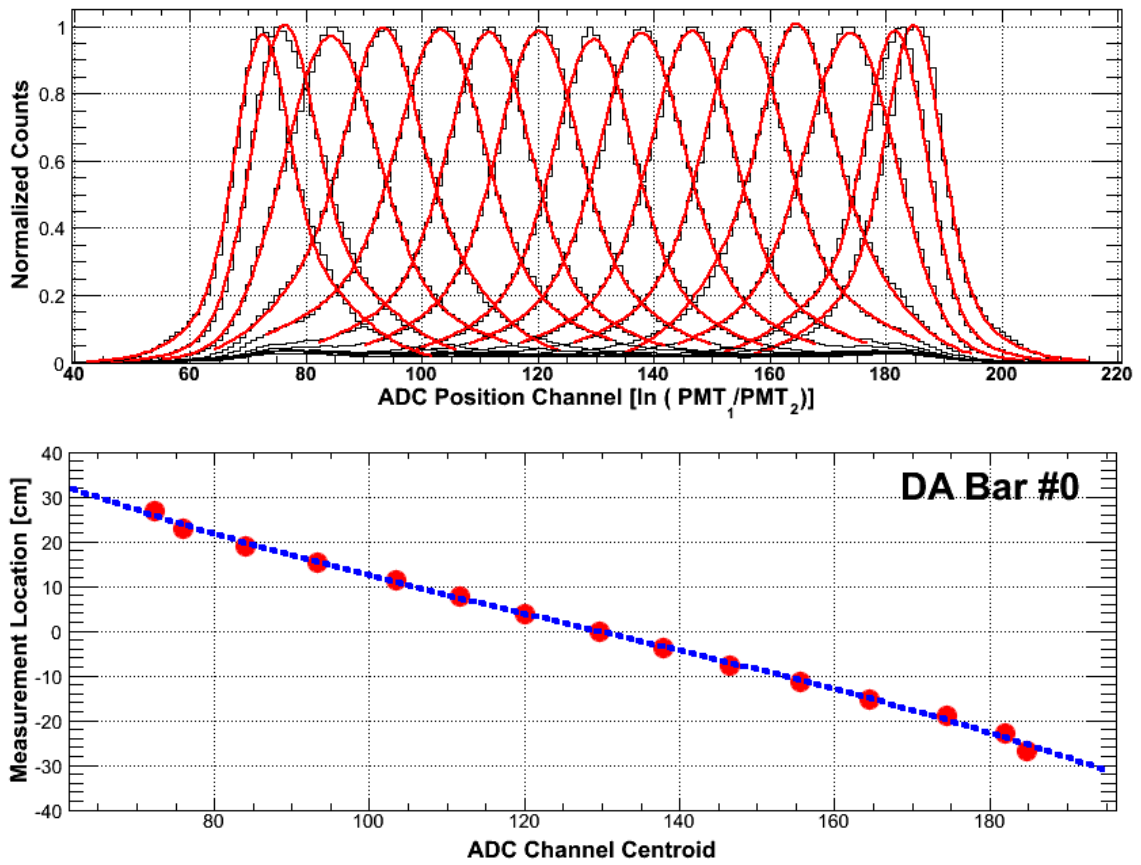


Figure 3.12: Measured ADC channel distribution for 15 points along the face of a single DA detector element (top) and the resulting calibration curve using centroids of the fits to the 15 distributions (bottom).

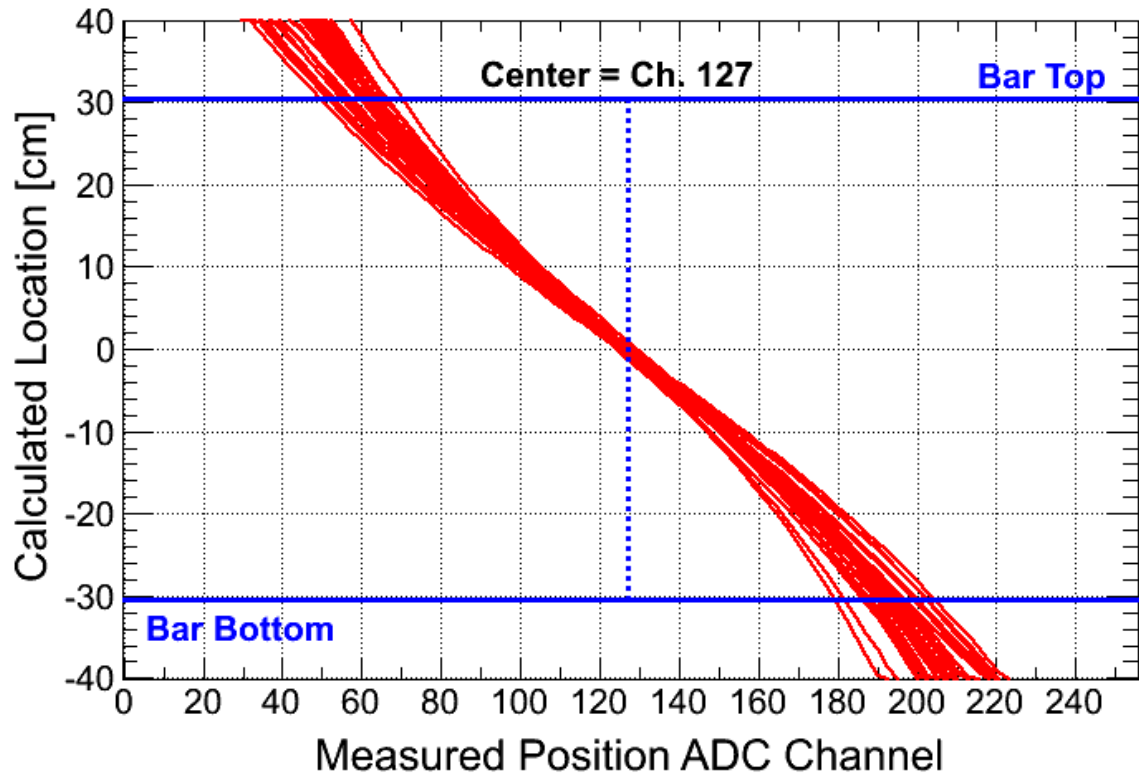


Figure 3.13: Derived position calibration curves for each of the DA detector bars from measured data at 15 points along the each bar.

Table 3.4: Polynomial DA bar calibration parameters and acceptable ADC channel range

Bar ID	$P_0$	$P_1$	$P_2$	$P_3$	$ADC_{min}$	$ADC_{max}$
0	9.4610e+01	-1.5803e+00	1.0359e-02	-3.0321e-05	65	170
1	9.1647e+01	-1.4230e+00	8.2246e-03	-2.1346e-05	68	186
2	8.2253e+01	-1.0988e+00	5.4065e-03	-1.4135e-05	72	184
3	8.6735e+01	-1.2660e+00	7.2257e-03	-2.0943e-05	71	174
4	8.1936e+01	-1.1472e+00	5.9273e-03	-1.5629e-05	69	183
5	1.1339e+02	-1.7825e+00	1.0401e-02	-2.6615e-05	77	180
6	9.4967e+01	-1.4505e+00	8.3877e-03	-2.2570e-05	71	179
7	6.1342e+01	-7.6707e-01	3.2892e-03	-8.7411e-06	59	190
8	6.3696e+01	-7.9162e-01	3.4138e-03	-9.3941e-06	61	185
9	7.3556e+01	-9.4012e-01	4.3139e-03	-1.1642e-05	68	183
10	6.5110e+01	-7.7030e-01	3.0352e-03	-7.8997e-06	64	189
11	9.1031e+01	-1.2785e+00	6.5256e-03	-1.6414e-05	73	184
12	8.9409e+01	-1.2714e+00	6.6185e-03	-1.7052e-05	72	182
13	9.0568e+01	-1.3530e+00	7.5646e-03	-2.0023e-05	70	181
14	6.7990e+01	-8.1944e-01	3.3329e-03	-8.8639e-06	66	185
15	8.8091e+01	-1.2519e+00	6.4908e-03	-1.6614e-05	71	183
16	7.6223e+01	-9.7453e-01	4.3252e-03	-1.0925e-05	69	186
17	7.0382e+01	-9.4281e-01	4.5421e-03	-1.2050e-05	64	186
18	6.6499e+01	-8.8373e-01	4.2454e-03	-1.1097e-05	61	192
19	7.7089e+01	-9.8690e-01	4.4092e-03	-1.1055e-05	70	187
20	8.8316e+01	-1.2155e+00	6.1583e-03	-1.6206e-05	73	180
21	9.5132e+01	-1.3905e+00	7.5954e-03	-1.9965e-05	74	180
22	6.6190e+01	-8.5606e-01	3.9367e-03	-1.0083e-05	62	195
23	6.3197e+01	-7.9118e-01	3.4446e-03	-8.9881e-06	61	192
24	7.3183e+01	-1.0095e+00	5.2007e-03	-1.4109e-05	65	186
25	8.0895e+01	-1.1502e+00	6.0960e-03	-1.6796e-05	67	178
26	6.5410e+01	-6.6501e-01	1.6696e-03	-3.8903e-06	70	186
27	7.7436e+01	-1.0141e+00	4.5734e-03	-1.1060e-05	68	189
28	8.3500e+01	-1.2196e+00	6.6888e-03	-1.7906e-05	68	183
29	6.7714e+01	-8.0412e-01	3.1561e-03	-7.9489e-06	67	189

bar will register a large PHA in the closer PMT while light has to diffuse through the entire length of the crystal to reach the far PMT. Much of the signal is lost along the way distorting the position calculation slightly. By fitting the measurements using a polynomial function this effect can be minimized. It can also be seen from the plot that measurements near the ends of the bars can vary in their reported physical distance much more easily and therefore an effective area of the bar has been established.

If the measured PHA yields a location above or below the limits of the bar, the measurement is discarded in processing because the uncertainty associated with that particular measurement is greater than the benefit of including it in image reconstruction. Since this is a moving system, crystals can shift slightly and optical couplings can degrade. Therefore the calibration should be checked periodically, however should remain consistent as a result of the gain matching.

### **3.6 Front-end Electronics**

Front-end electronics are designed to process individual gamma-ray interactions in the TMI detector arrays. Each detector element must have dedicated electronics for signal processing, high-voltage, and a combined processing unit to correlate events in time. The front-end electronics are separated into three types of Circuit Card Assembly (CCA). The TMI contains 95 High-Voltage Circuit Card Assembly (HVCCA), one for each PMT, 65 sensor CCAs, one for each detector CA element and DA bar, and one Event Characterization Unit (ECU). All front-end electronics were custom designed and built by BTI in Ontario Canada. Figure 3.14 shows the flow of signals and electronics on the TMI. All data are eventually sent to the Data Analysis System (DAS) for parsing, navigational correlation and algorithm processing.

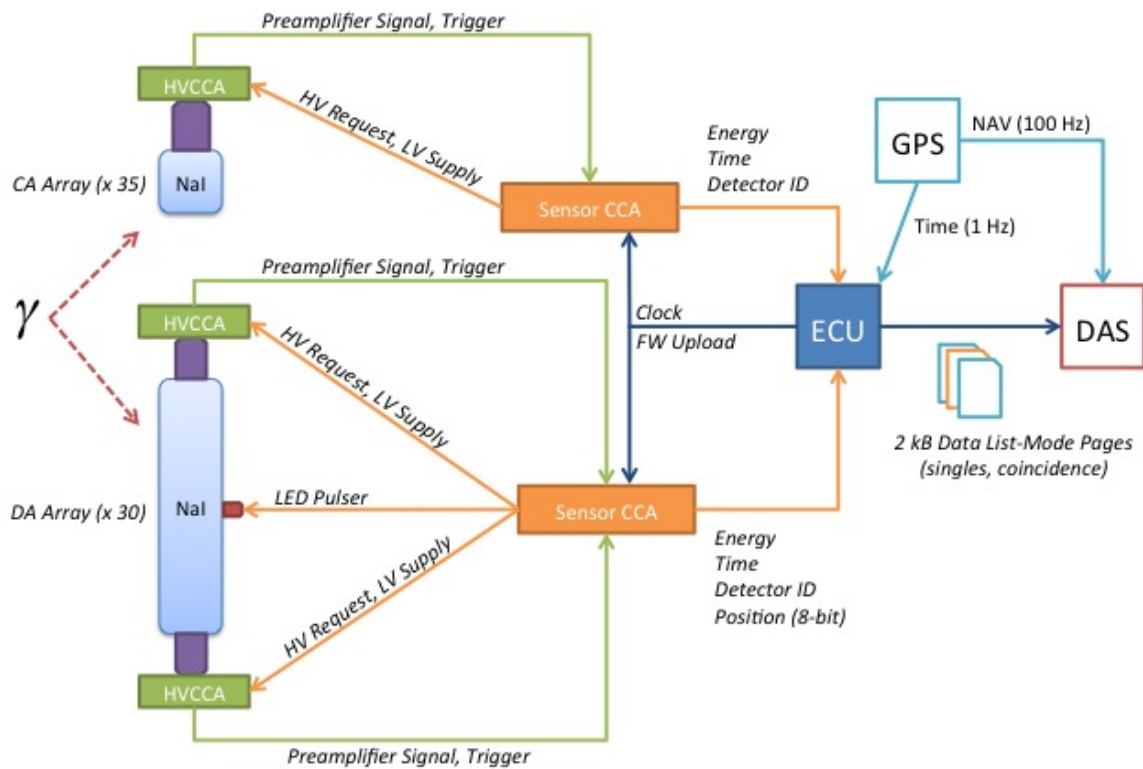


Figure 3.14: The flow of signals and electronics on the TMI. Data is eventually sent to the data analysis system (DAS)

### 3.6.1 Sensor Electronics

There are 65 sensor CCAs, one for each of the CA detector elements and one for each DA array bar. Each sensor card is connected to one or two HVCCA cards for input depending on whether it is connected to a CA element or a dual-ended readout DA bar. The output of the sensor cards is a serial connection to the ECU. Sensor CCAs are rack mounted above the detector arrays and have connections on the front face. Figure 3.15 shows the sensor CCAs for the CA array mounted in a rack prior to integration on the TMI. The red cables are the serial lines to the ECU, input power lines come in from the right-hand side, 20-pin ribbon cables and coaxial lines are also visible. There are also LED lights on each sensor CCA to indicate their current operational status.

Sensor CCAs receive analog and digital signals from the HVCCA card attached to the detector and convert them into data containing measured energy, time, and position of interactions. Positions on the CA array are integer row and column numbers for the CA element that triggered, while positions on the DA array include an integer bar number and an 8-bit (0-256) ADC channel representative of the location of the interaction along the bar from the charge division algorithm. Additionally, each sensor CCA card provides State-of-Health (SOH) information about the detector, for example calibration status and HV settings.

### 3.6.2 High-Voltage Electronics

The HVCCA attached to each PMT is a low profile card that houses a local 1500 V high-voltage supply, the resistive divider chain to support the PMT, and the discriminator circuitry. Analog preamplifier output from each HVCAA is fed to the

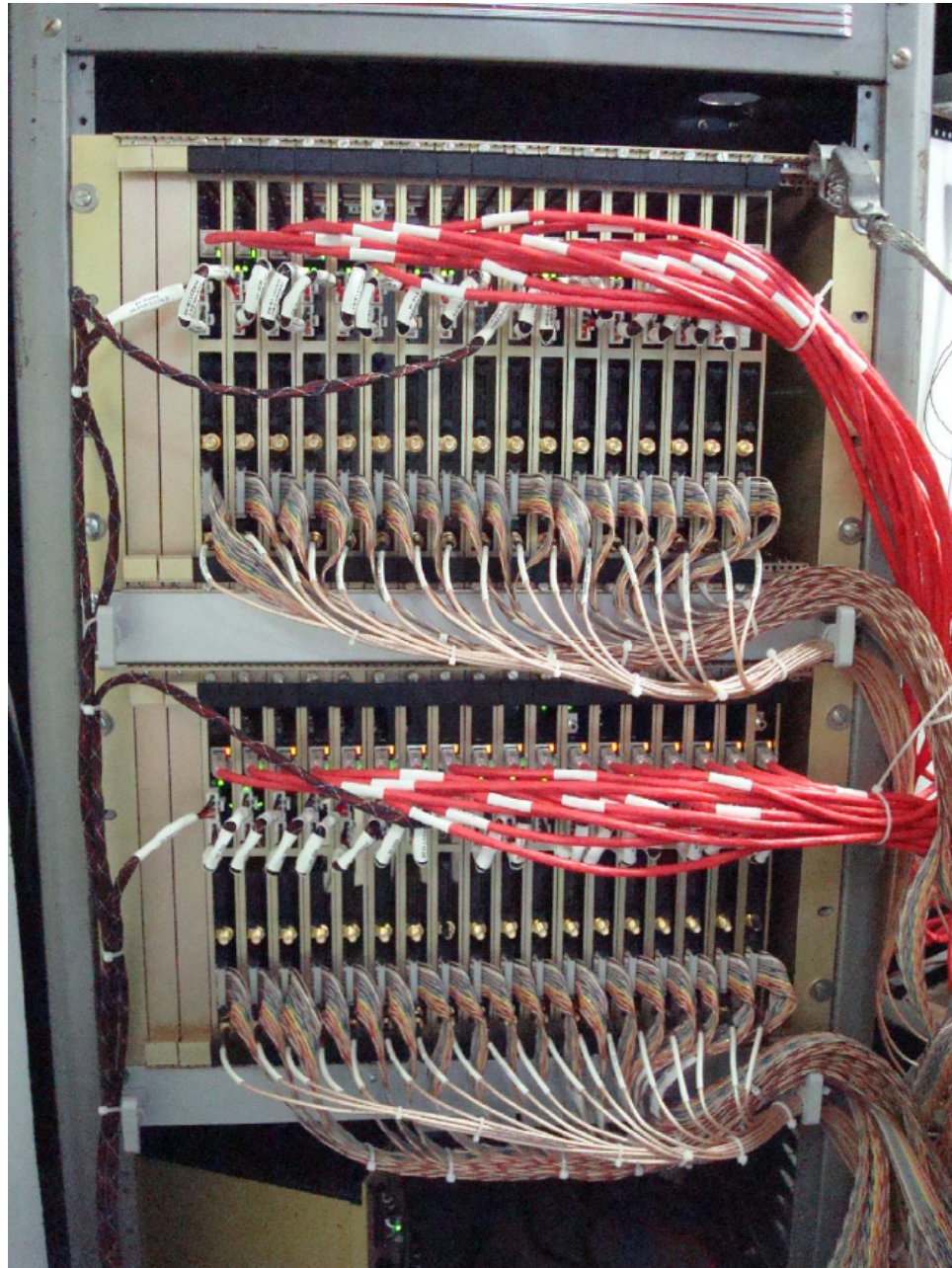


Figure 3.15: Sensor CCAs for the CA array mounted in a rack prior to integration on the TMI.



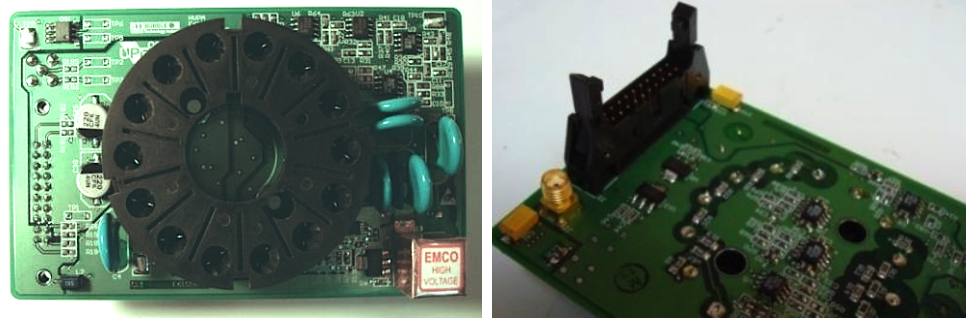


Figure 3.16: Images of a high-voltage circuit card assembly (left) with PMT resistive divider in the center and the HVCCA output connector (right) showing the 20-pin ribbon cable connector.

corresponding sensor CCA via a coaxial cable. Additionally, each HVCCA card is connected to the sensor CCA through a 20-pin ribbon cable. The ribbon cable supplies the low voltage power required by the HVCCA, the voltage request signal and discriminator trigger signals. Voltages on the HVCCA card are determined by the sensor CCA card and communicated over the ribbon cable via a pulse-width modulated signal. Figure 3.16 shows images of a high-voltage circuit card assembly (left) with PMT resistive divider in the center and the HVCCA output connector (right) showing the 20-pin ribbon cable connector on the reverse side of the circuit.

Each HVCCA has two discriminator channels. The first discriminator channel is a fast, low threshold discriminator used to generate fast triggers. The fast threshold is set such that it skims the noise. The second is a confirm discriminator that has a higher threshold and ultimately decides if the detector triggered. If the detector triggered the analog preamplifier signal is sent to the sensor CCA card for analysis.

### 3.6.3 Event Characterization Unit

The ECU is connected, via serial lines, to all 65 sensor CCAs, the navigational subsystem, and the DAS. The DAS is the central processing unit that feeds list-mode event data to the imaging and detection algorithms. The ECU handles time synchronization of all sensor CCAs over the serial connection by providing a master clock sync pulse. It is necessary to maintain time synchronization among all detectors because the relative time between events in different detectors is a crucial piece of information in the coincidence determination. Additionally, events must be synchronized in order to allow for precise correlation with GPS/INS navigational information. The ECU can also be used to perform commanding of the sensor CCA FPGAs. Figure 3.17 shows the ECU with all serial lines from the CA detector array (red) and DA detector array (teal) shown coming in from the top and bottom. Also visible in Fig. 3.17 is the master controller FPGA (center).

#### Event Timing and Synchronization

Pulse amplitudes with a signal above the confirm threshold on the HVCAA generate a timing pulse that is sent to the sensor CCA. Each sensor CCA has a 100 MHz oscillator that is running asynchronously to the ECU and all other sensors and a Time-to-Digital Converter (TDC). The ECU generates a 1 MHz synchronization pulse from the master clock which gets pushed to each sensor CCA card through equal length cabling. The TDC on the sensor CCA measures the phase of the local (asynchronous) clock to the master synchronization clock from the ECU. The sensor CCA now has a Time-of-Arrival (TOA) stamp to sub-nanosecond precision.

The GPS/INS subsystem of the TMI is also connected to the ECU to provide

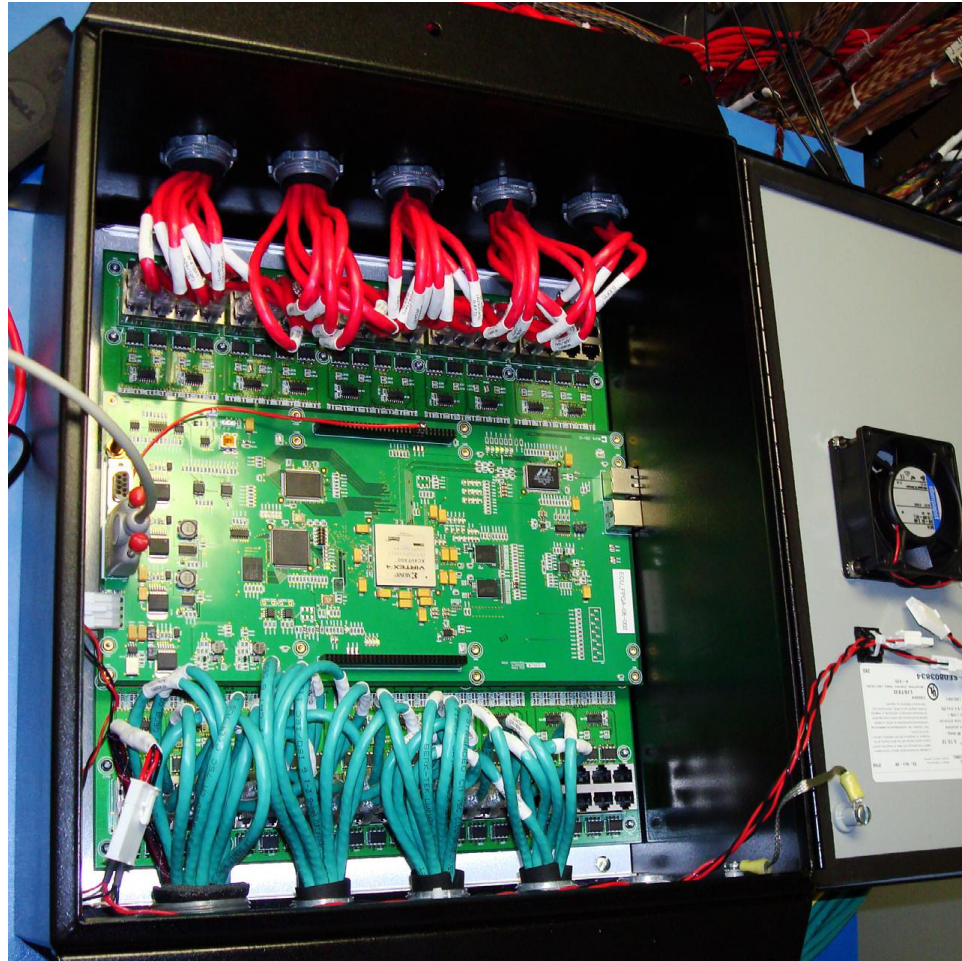


Figure 3.17: Image of the ECU with all serial lines from the CA detector array (red) and the DA detector array (teal) shown coming in from the top and bottom.

coarse timing information ( $1\text{ Hz}$ ). Events measured by the sensor CCAs are stamped with a time calculated as the difference between the TOA and the GPS time. This allows for precise correlation between gamma-ray interactions and the location and attitude of the vehicle. The GPS system is also connected to the data analysis system (DAS) to provide fine timing and location information ( $100\text{ Hz}$ ). Using the timestamp of the measured events, the GPS information can be interpolated to provide the exact location of the detector system for each event.

### **Coincidence Determination**

Since the TMI is both a coded aperture and Compton imaging system, it requires discrimination of the input data to each algorithm. Coded aperture algorithms are only interested in gamma-ray photons that deposit energy in the DA array. Conversely, the Compton imaging algorithms are interested in photons that Compton scattered in the CA array and deposited their remaining energy in the DA array.

In order to separate these event types the ECU makes a coincidence determination based on an acceptable time window. The FPGA in the ECU makes a coincidence determination by examining the timestamps of events that arrive at the ECU within a short window of time. Several factors play a role in the coincidence determination. First, the synchronization between the sensor CCAs must be very accurate. This is handled by the master clock synchronization pulse from the ECU to the sensor cards. Also, there is some time-walk in the HVCCA discriminators due to the pulse amplitude from the PMT, the physical distance between the CA and DA array ( $75\text{ cm}$ ,  $2.5\text{ ns}$ ) and time-walk due to the position the interaction in the DA bar. Each of these effects behaves predictably and is corrected for in the sensor CCA firmware. The coincidence window width implemented on the TMI is on the order of a microsecond,

however it is adjustable.

### 3.7 Data Processing

The final component of the detector system is the processing of event data. In order to make use of the data from a mobile platform, list-mode event data must be associated with the location and attitude of the TMI. Association is achieved in several ways. First, the navigational subsystem has a pulse-per-second ( $1\text{ Hz}$ ) signal that feeds directly into the detector front-end electronics. As gamma-ray interactions are measured, they are stamped with a time relative to the GPS time. This represents the exact time of the interaction. Next, the higher-rate  $100\text{ Hz}$  navigation signal is fed into the DAS. The DAS performs a lookup of the high-rate navigational information according to the event time and stamps each measured interaction with a location and attitude. Once stamped the events can be imaged according to their location as the imager is moving (or not) so that gamma-ray images can be overlaid to produce a source distribution that aggregates counts appropriately. The chapters on the imaging algorithms will discuss how to make use of this information.

### 3.8 Field-of-View

With the detector arrays fully described it is important to calculate the active FOV of the imager. As stated in the BAA requirements the TMI must exhibit a horizontal FOV of  $\pm 1\text{ rad}$  and a vertical FOV of  $\pm 0.25\text{ rad}$ . Measurements have been taken with the TMI at various angles off-axis to determine the FOV in both the horizontal and vertical directions. An  $879\ \mu\text{Ci}$ ,  $^{137}\text{Cs}$  source was used for all measurements. Each measurement is calculated for 20 seconds of integration time. Figure 3.18 shows the

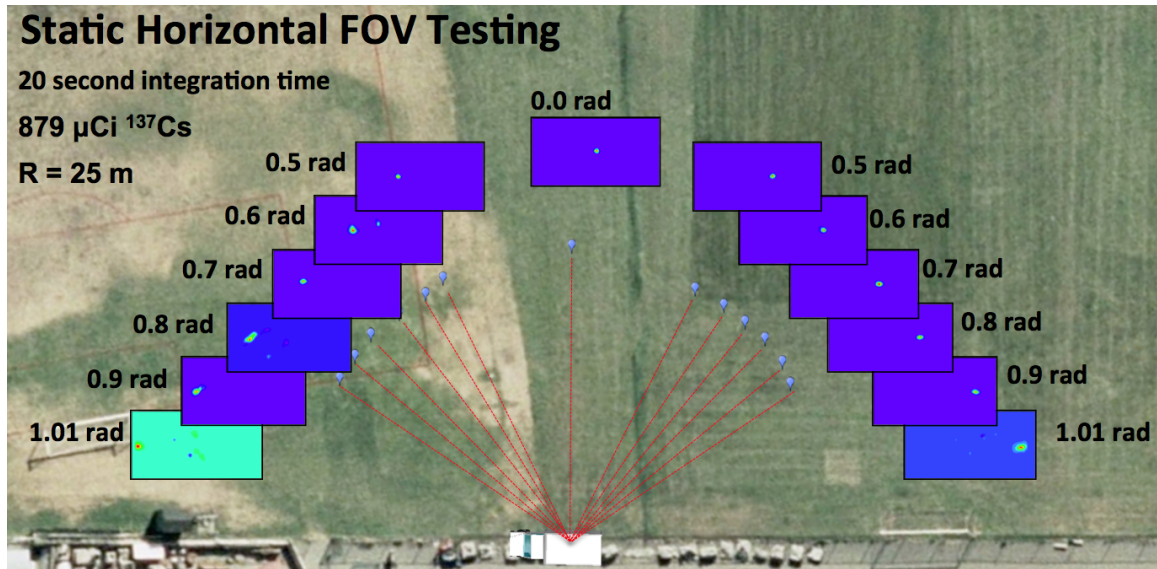


Figure 3.18: Angular measurements taken for TMI horizontal FOV calculations. Each measurement was taken with a  $879 \mu Ci$ ,  $^{137}Cs$  source at a radius of 25 meters, with 20 seconds of integration time. At each location an image from the TMI is shown where the background color (purple) indicates a flat background image.

results of the horizontal FOV calculation for 12 measurements approximately equally spaced by  $0.10 \text{ rad}$ , and a single measurement in the middle. The horizontal FOV is shown to be  $\pm 1.01$  or  $2.02 \text{ rad}$  total. Figure 3.19 shows two measurements with the source located at  $+0.4$  (A) and  $-0.33 \text{ rad}$  (B) off-axis in the vertical direction. This demonstrates a vertical FOV of at least  $0.73 \text{ rad}$ , exceeding the  $0.5$  radian requirement.

### 3.9 Summary

This chapter has given an overview of the components of the TMI that relate to the detection of radiological material in a mobile system. The specifics of the navigation system were presented along with performance characteristics. The detector hardware

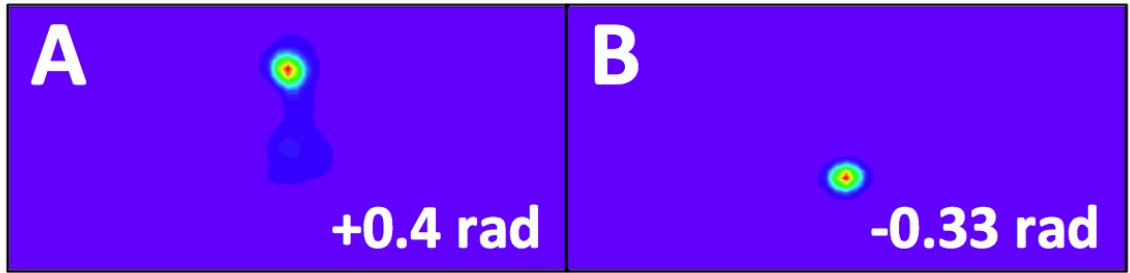


Figure 3.19: Two off-axis (vertical) measurements taken for field-of-view calculations. Each measurement was taken with a  $879 \mu Ci$ ,  $^{137}Cs$  source at a radius of 25 meters, with 20 seconds of integration time. The vertical FOV is shown to be (at least)  $-0.33$  radians (B) to  $+0.4$  radians (A) or  $0.73$  radians total.

of the TMI was presented from all aspects from material, geometry, housing, electronics and readout. Methods for automatic position and energy calibration within the detector elements was presented as well as the flow of data to the detection algorithms. It has been shown that the designed detector system meets BAA requirements and represents a powerful tool for detection of weak radiological sources in the presence of large dynamic NORM backgrounds.

At this point a discussion of the algorithms implemented to maximize the applicability measured data content will be presented. Chapters 5, 6, 7 and 8 will give the details of the spectroscopic, coded aperture imaging, Compton scatter imaging and hybrid detection algorithms respectively.

## Chapter 4

# SIMULATION AND MODELING

Monte Carlo modeling and simulation is extremely valuable for any detector design project. For design and development of the TMI the utility was three-fold. First, it provided a sound method for predicting and optimizing performance of conceptual detector designs such as material selection, detector arrangement and element size. Second, simulation and modeling provided synthetic source and background data to enable both imaging and non-imaging algorithm and code development while detector design was being finalized [45]. Third, once a validated model has been developed it can be applied to other efforts for gamma-ray detection and imaging, for example deployment of alternative systems on modified land, maritime or aerial platforms.

A model of the detector and truck platform was created as shown in Fig 4.1 using the General Response Simulation System (GRESS) [46, 47] Monte Carlo application developed at Los Alamos National Laboratory (LANL), an extension to the Geometry and Tracking Toolkit v4 (GEANT4) [48] package. Outer truck panels have been removed to allow interior visualization. The truck components such as tires, engine, and chassis are rather crude, while the individual detector models are more intricate as they can have a larger effect on performance.



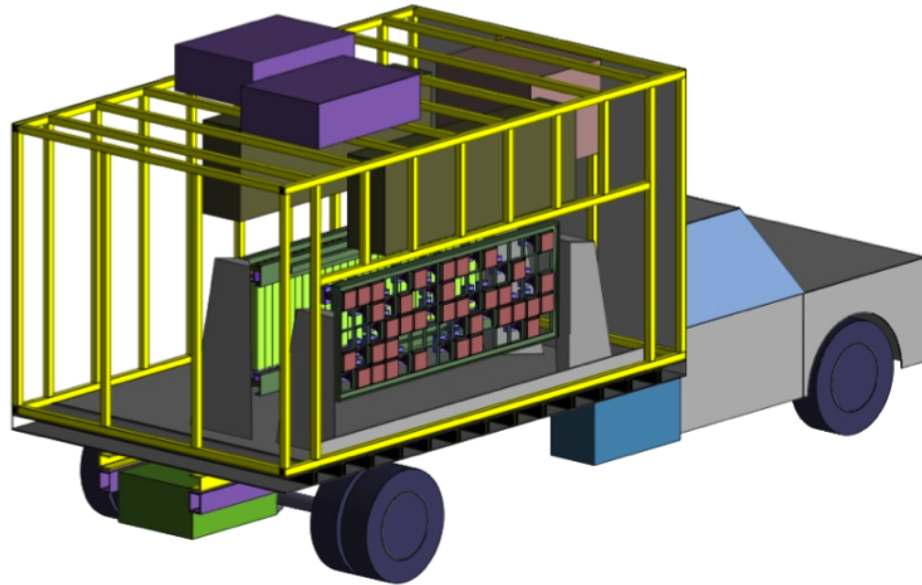


Figure 4.1: GEANT4 model of the SORDS truck platform.

The simulated detector system is intended to accurately predict the response to gamma-ray sources both in a static and moving frame of reference. For motion simulations, sources are moved around a stationary detector geometry, and the detector location is transformed to be the inverse of the source location, thereby simulating detector motion. Motion can be simulated along arbitrary paths to gauge the response to various real-world conditions. Simulated data are reprocessed with estimated or measured energy and position response curves. Reprocessed data can then be provided to detection algorithms as surrogates to measurements. Figure 4.2 shows the reconstructed gamma-ray image from a simulated  $0.5 \text{ mCi}$ ,  $^{137}\text{Cs}$  point source as the model passed the source at  $25 \text{ m}$  traveling at  $15 \text{ mph}$ .

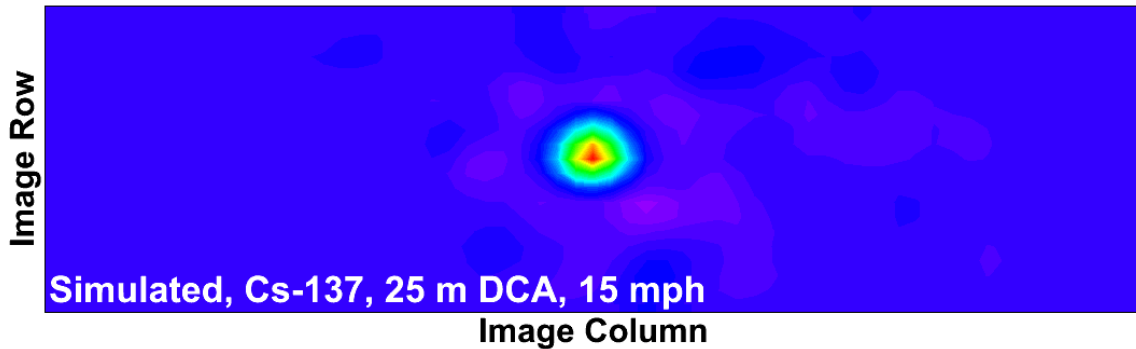


Figure 4.2: Reconstructed image using simulated data of the TMI for a  $0.5 \text{ mCi } ^{137}\text{Cs}$  source at  $15 \text{ mph}$  and minimum approach of 25 meters.

## 4.1 Detector Modeling

The accuracy of SORDS detector simulations must be verified against measured data and selected components. Once available, measurements taken with the prototype detectors were used to validate the simulation output. The ability to reproduce measured data features with simulations lies largely in precise modeling of the detectors. Fig. 4.3 shows a cross-sectional view the simulated model for one of the CA array elements. The model is very detailed including the detector crystal and housing, mounting plates and interface materials, a PMT model and the attached front-end electronics box and HVCCA. A similar model has been constructed for the DA array detectors.

For comparison to data measured in the laboratory, further details were added to the model to account for materials close to the detector during the time of measurement. This included lead bricks supporting the detector, a wooden table, and the concrete floor. Such items are necessary to reproduce the contribution of scattering to the measured data. A comparison between measured and simulated data for a single

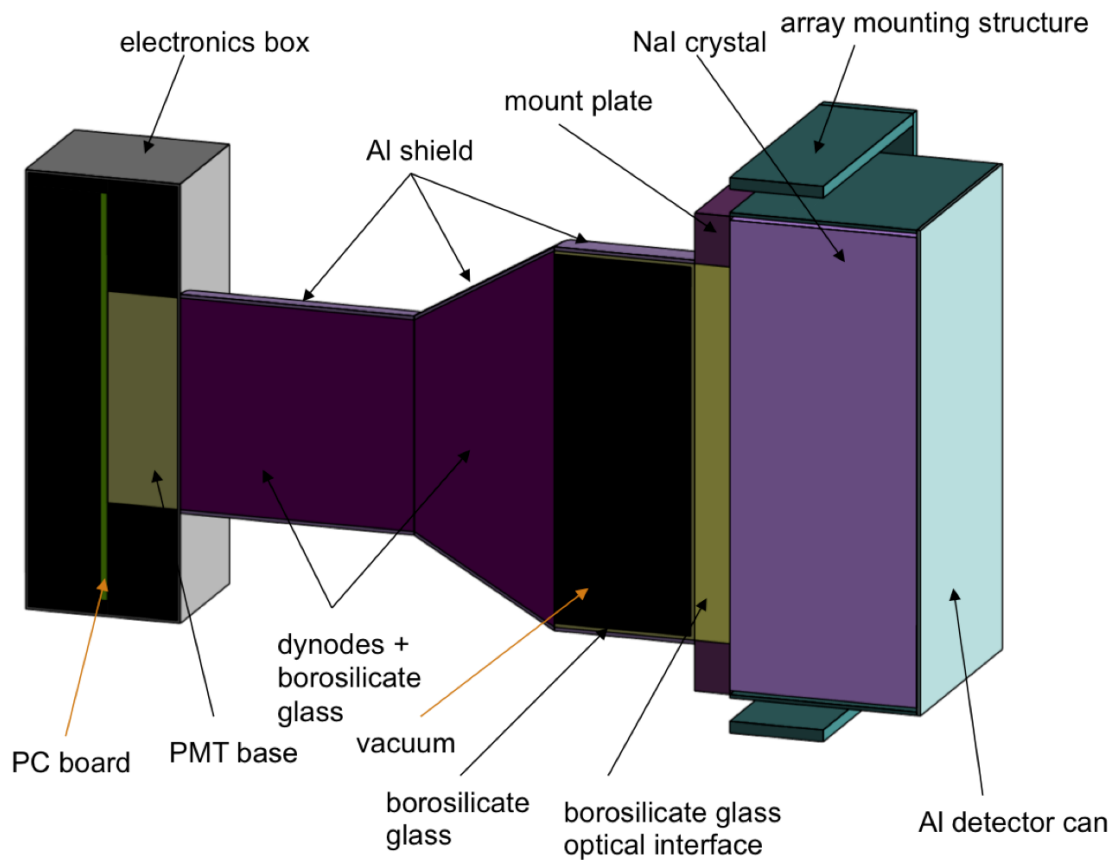


Figure 4.3: Cross-sectional view of the simulated model for one of the 5x5x2 *inch* sodium iodide (NaI) front-plane detectors.

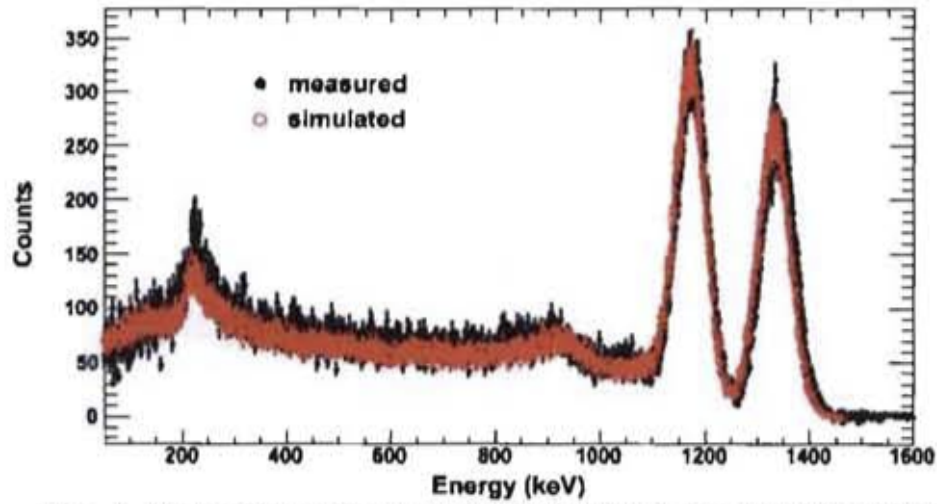


Figure 4.4: Comparison of measured and simulated data for a SORDS 5x5x2  $in^3$  NaI detector exposed to a  $^{60}Co$  source.

CA detector is shown in Fig. 4.4. Data are from a  $^{60}Co$  point source located 10.5 inches from the detector face. Figure 4.5 shows data from the measurement and simulation of one of the DA detector bars. These data were collected with a prototype version of the acquisition hardware that had a large and unknown dead-time. As a result, simulation data is normalized to the measured photo-peak area. The comparisons illustrate that all major spectral features are reproduced. There is some discrepancy in the simulated spectrum at lower energies, where scattered photons dominate. Exhaustive detail, either in the detector model or the surrounding materials (lead bricks, table, floor, walls), would likely improve the low energy response.

## 4.2 Background Modeling

Background from NORM is abundant and will play a major role in the ultimate performance of any large-area system tasked with detection of weak or distant sources.

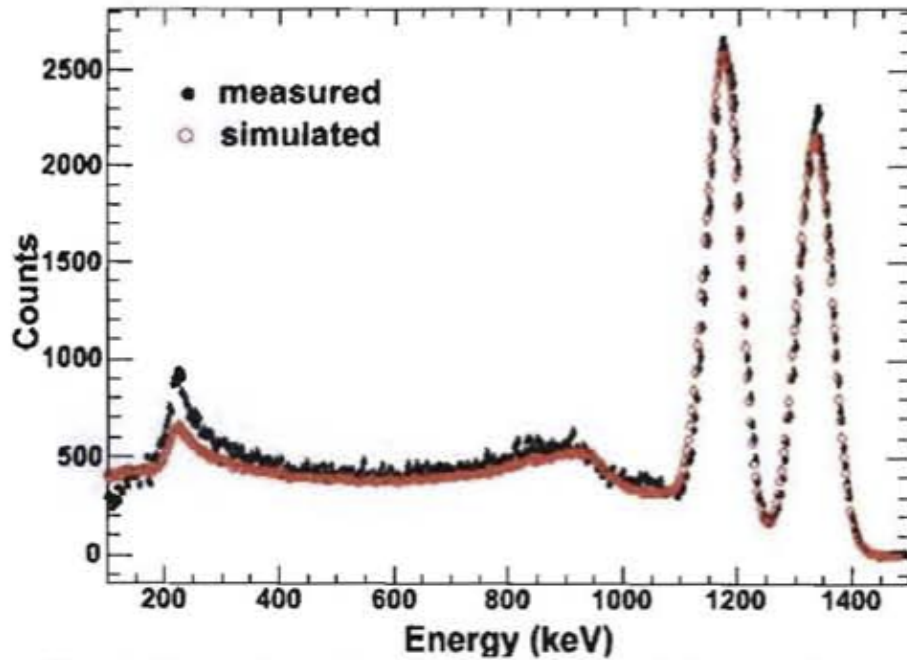


Figure 4.5: Comparison of measured and simulated data for a SORDS 2.5x3x24  $in^3$  NaI detector exposed to a  $^{60}Co$  source.

Radiation is emitted from a variety of primordial and cosmogenic isotopes occurring naturally in soil, rocks, and their by-products. The TMI detector, with its large active area, will observe significant event rates from background sources, on the order of 30 to 100  $kHz$ . Simulation of accurate data for the development of imaging and non-imaging algorithms will therefore require a thorough and well-validated model of the typical background environment. The approach taken was to build the background model starting from the most basic details of soil composition and isotopic distributions. The content of soil has substantial variations depending on location and geography. The assumed radioisotope composition of soil is shown in Table 4.1 [49].

These isotopes and their decay daughters are assumed to be in secular equilibrium and constitute the source of nearly all naturally occurring radiation. For each of the

Table 4.1: Radioisotope composition of soil used for the simulation model.

Isotope	Activity ( $pCi/g$ )
$^{40}K$	9.00
$^{226}Ra$	1.30
$^{232}Th$	0.55
$^{235}U$	0.70
$^{238}U$	0.70
$^{222}Rn$	0.34
$^7Be$	0.27

isotopes in Table 4.1 and their daughters, the specific activity is multiplied by the branching ratio for each gamma-ray emitted, thereby providing the gamma-ray flux per gram of soil for each emitted energy. There are well over a thousand gamma-ray energies produced by these isotopes. For simplicity, the developed model uses the 100 most intense energies. Figure 4.6 shows the calculated gamma-ray emission energies from a sample of soil constructed in the simulation.

The gamma-ray energy spectrum emitted by an extended volume of soil is more complicated than the idealistic representation of many mono-energetic line energies. Some gamma-rays will experience absorption and scattering in the soil itself, stopping some low-energy photons, and producing a continuum of energies from scattering. To reproduce the scattering and absorption effects, a GEANT4 model of soil was constructed, using the chemical composition shown in Table 4.2, with an average density of  $1.5 g/cm^3$ .

The simulated soil model occupied a volume of  $1 \times 1 \times 0.5 m^3$  cube. Gamma-ray energies from Fig. 4.6 were selected at random according to relative intensity and

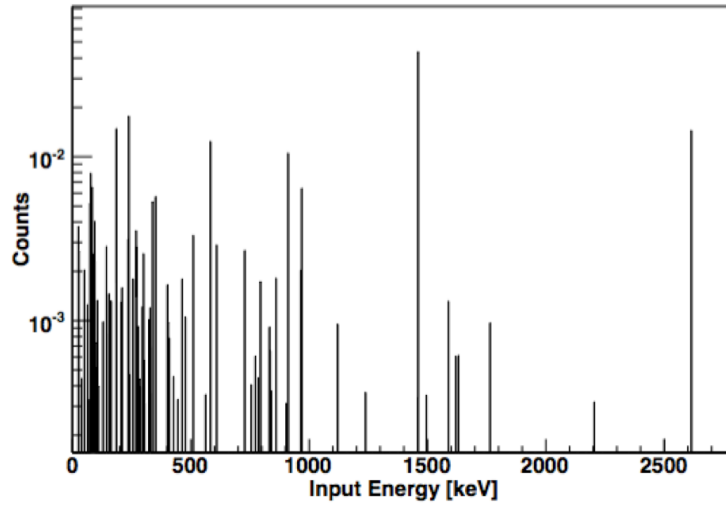


Figure 4.6: 100 most intense gamma-ray emission energies from a sample of soil constructed in the simulation.

Table 4.2: Elemental composition of soil used for the simulation model.

Element	Abundance (%)
Hydrogen	2.1
Carbon	1.6
Oxygen	57.7
Aluminum	5.0
Silicon	27.1
Potassium	1.3
Calcium	4.1
Iron	1.1

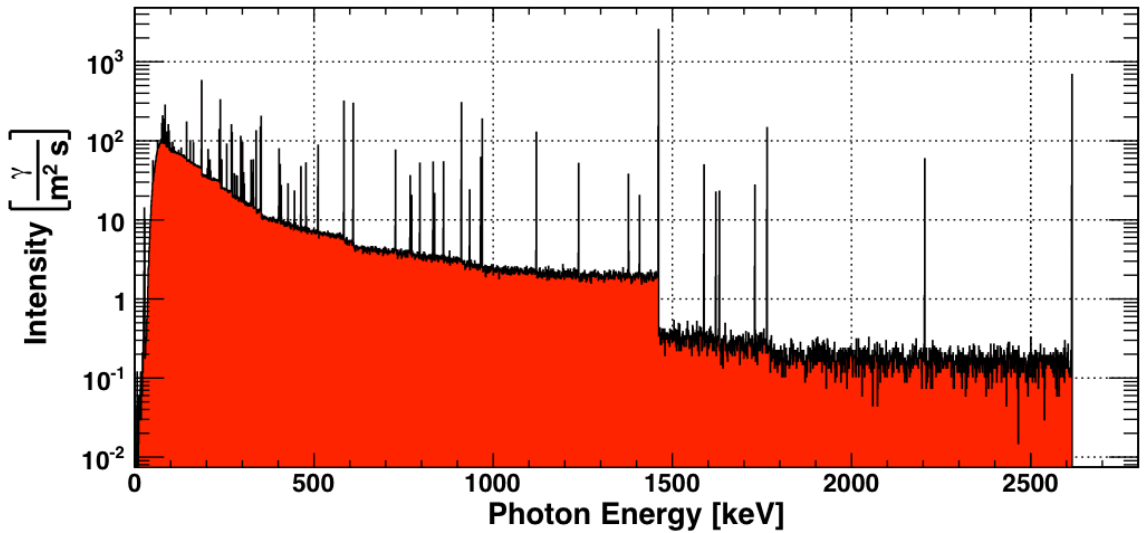


Figure 4.7: Gamma-ray energy spectrum emitted from the simulated soil model. The model includes both self-attenuation effects and scattering within the soil.

emitted in the soil with a random momentum direction. The energy of gamma-rays leaving the surface of the soil was tabulated resulting in the spectrum shown in Figure 4.7. The angular distribution of gamma-rays exiting the soil model was not computed. The output energy spectrum is normalized to gammas per square meter per second so that it can be used to generate the background source term for an arbitrarily large mass of soil.

Since it would be extremely time consuming to simulate interactions in the soil each time we desire to study the response of a detector, the energy spectrum of Fig. 4.7 is used as a source term. That is, photon energies for background studies can be picked randomly from the spectrum when performing detector simulations. Figure 4.8 shows a comparison of background data collected with the TMI (black) and the simulated NORM background (red) using the background model and the truck model discussed previously. Energy spectra are shown for detector front-plane



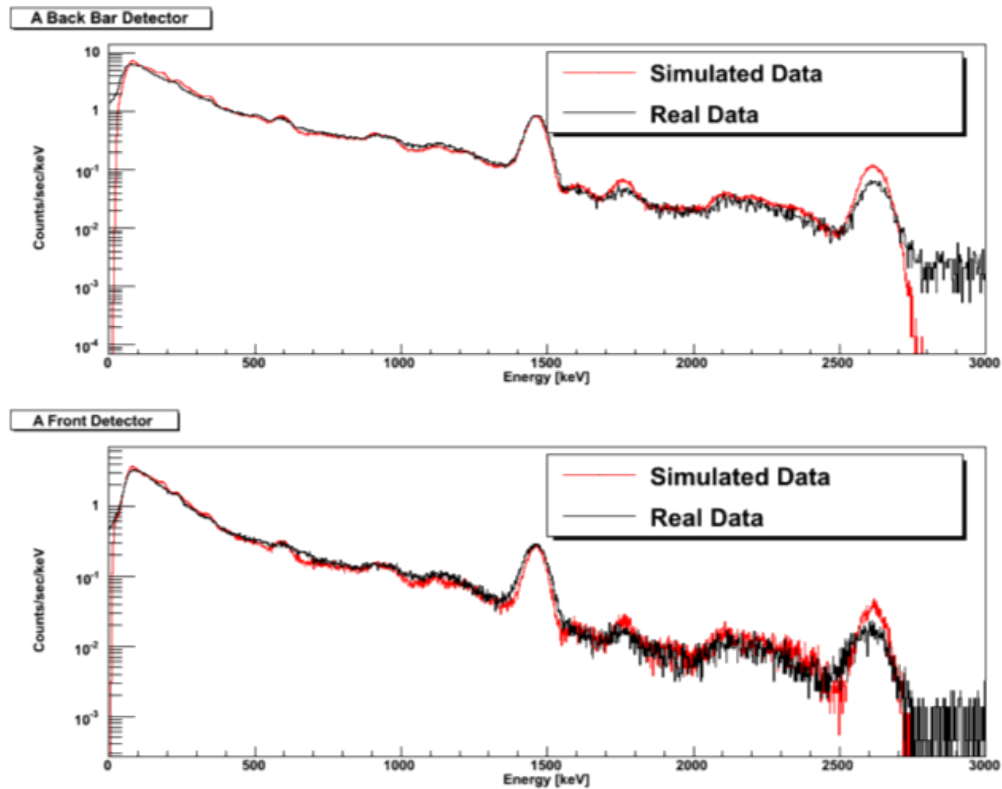


Figure 4.8: Comparison between measured data with the TMI arrays (black) and simulated data (red) for the DA detector elements (top) and the CA detector elements (bottom).

single hit events (bottom), back-plane single hit events (top). The ground was modeled as a plane beneath the truck with dimensions of  $20 \times 20 \text{ m}^2$ . The simulation data is normalized to the measurement live-time. The comparison is generally good with some over-prediction of the  $1460 \text{ keV}$  and  $2614 \text{ keV}$  lines. The ratio of counts in the measured spectrum to the simulated spectrum is 0.85 for front-plane events, 0.96 for back-plane events, and 1.3 for coincidence events, well within the substantial variations known to exist for background intensity.

A truly accurate simulation of background would require the simulation of an infinite plane to replicate the surface of the earth. The simulations performed used a 400  $m^2$  plane because it was more computationally feasible. The total fraction of detected background events that would be expected to originate within a radius of 10 meters has been evaluated. This was accomplished by generating photons from a series of annular rings of width 1 meter at multiple radii. As shown in Figure 4.9, the rate drops off quite rapidly with increasing radius, however the total integral is substantial. Through this calculation it is estimated that about a third of total background photons observed in the detector would be expected to originate within a 10 meter radius. Also shown in Figure 4.9 (bottom) is the simulated origin of gamma-ray photons that interact in the detector, here it can be seen that a large fraction of detected events come from the soil directly in front of the TMI.

The observed agreement between the measured and simulated data using only a 400  $m^2$  ground plane suggests the activity values of the soil constituents in Table 4.1 are too intense for an infinitely large plane. However, the assumed activity values are appropriately normalized if one uses a 400 square meter ground plane. It should also be noted that significant variations in NORM background intensity are not uncommon.

Figure 4.10 shows the comparison of this soil model with data measured from various locations around North America measured with Advanced Spectroscopic Portal (ASP) monitors [50]. A simple model of the detector was constructed in GRESS and simulated with the 400  $m^2$  background plane [45]. It can be seen that the simulated model produces a response in the ASP model (black) that is close to the average of all measurements.

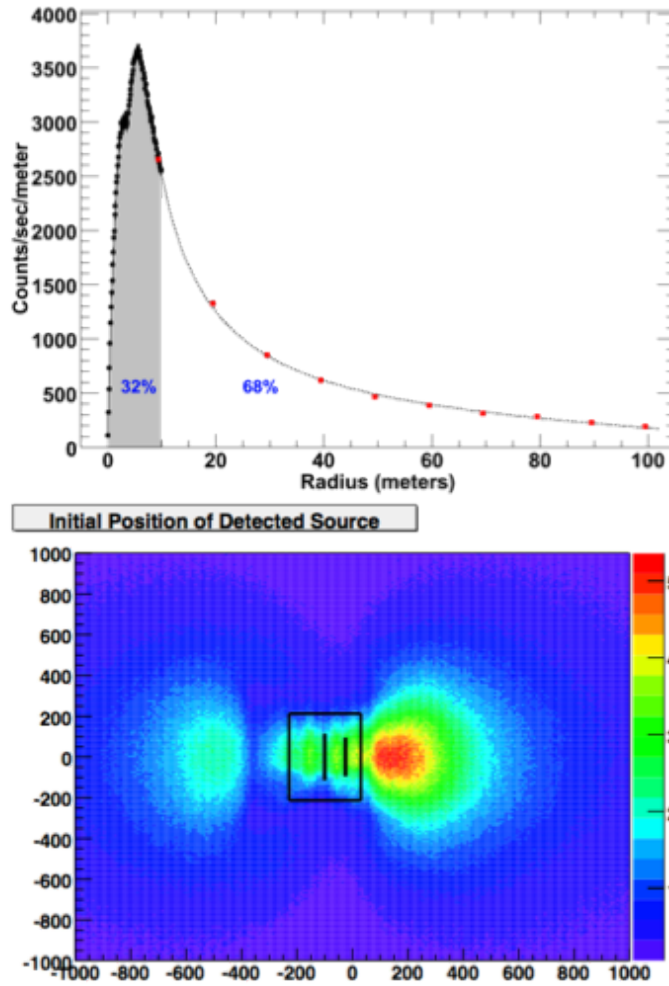


Figure 4.9: Decline of simulated count rate as a function of ground plane radius (top) and the gamma-ray photon origin point for all simulated energy depositions in the TMI above a  $20 \times 20 \text{ m}^2$  ground plane.

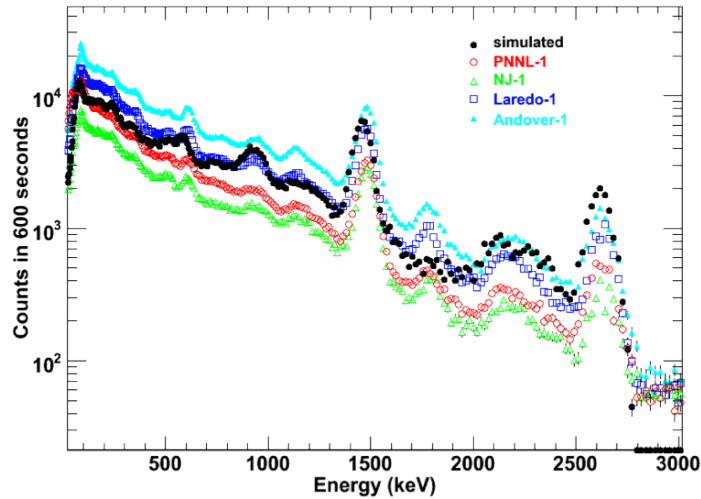


Figure 4.10: Comparison of the simple ASP detector response to the constructed soil model.

### 4.3 Summary

In this chapter a method for design and optimization of a prototype detector for detection, imaging, and identification of gamma-ray sources from a mobile platform was presented. Additionally, the GEANT4 simulation toolkit as well as GRESS were used to guide detector design and produce synthetic data for the development of imaging algorithms and code while detector hardware was being constructed. Significant detail was incorporated into the detector level models. Simulations of individual detectors and of the entire truck assembly were validated against measured data. Terrestrial background radiation is significant for our large-area detector, necessitating a detailed simulation to evaluate the resulting detector signature. A background model was built from first principles and compared well to measured data in several instances. Detector validation will be useful for future research and development of gamma-ray

detection systems and the background model will be useful for any future projects where background contributions are expected to be significant.

# Chapter 5

## SPECTROSCOPIC ALGORITHMS

Since the primary goal of the TMI is detection of threats, at a minimum a simple method for detecting the presence of radioactive material is needed. Spectroscopic algorithms can provide sensitive detection of materials without fine localization information. Additionally, overall system sensitivity can be improved by combining non-imaging spectroscopic algorithms with gamma-ray imaging information.

### 5.1 Data Segmentation

In order for spectroscopic algorithms to provide proximity localization of suspected sources of interest, data must be combined with navigational information and segmented into discrete blocks for analysis. The size of the blocks must be balanced with the need for adequate statistics in the measured energy spectrum and desired location sensitivity.

Data measured by the TMI are segmented into 2 second energy spectra (configurable). Each spectra is associated with an average location provided by the navigational subsystem. Since the average count rate of the system is on the order of 50

$kHz$  including both the CA and DA arrays, as well as coincidence events between the two, an integration time of 2 seconds provides adequate statistics for peak fitting analysis.

Figure 5.1 shows the path of the TMI with a colored block showing the total count rate from a 2 second integration of all measured events (up to  $MeV$ ) within the time range. Each block is color coded to correspond to the total count rate of the system where green is lower and red is higher. The run presented in Fig. (5.1) is a measured run past at  $0.5\ mCi$ ,  $^{137}Cs$  point source (left to right) located at  $25\ m$  Distance of Closest Approach (DCA) from the road. Here, the actual source location is not shown to emphasize the fact that it is not clear from the total count rate where the source is located. There are 3 likely locations: at the first road crossing, just past the road crossing and toward the end of the measurement. In order to increase the sensitivity of detection a method for energy windowing is needed.

## 5.2 Energy Windowing

Energy deposition from gamma-rays originating from NORM background are distributed throughout the energy spectrum, whereas gamma-ray point sources emit energetic photons at specific energies. It is advantageous to the Signal-to-Noise Ratio (SNR) to select only those photons that would have come from a source of interest – more specifically, the photo peak.

Gamma-ray lines emitted by isotopes are mono-energetic and could be approximated using a delta function however, due to the limited energy resolution of NaI, multiple measurements of a single photon result in a Gaussian distribution about the actual energy. This fact makes it necessary to accept all photons within a window of

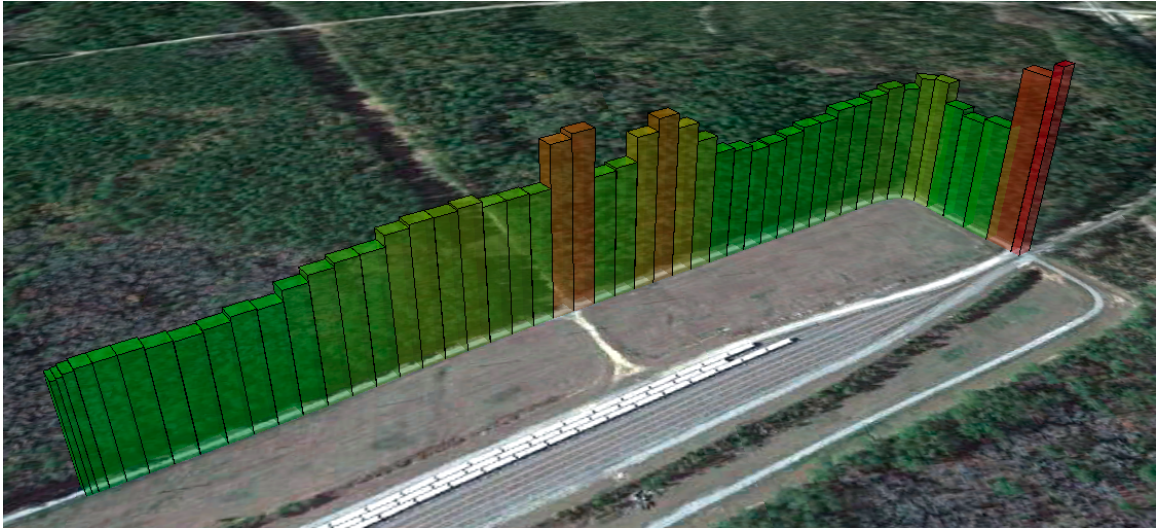


Figure 5.1: Sample measurement past a  $0.5 \text{ mCi}$ ,  $^{137}\text{Cs}$  point source. The total count rate in the TMI is indicated by the height and color of the bars. Each bar represents the integration of total energy deposited in a 2.0 second interval. The location of the source is not easily located due to fluctuations in the total count rate.

energies rather than a single specific photon energy. This method will also be applied to coded aperture and Compton gamma-ray imaging reconstruction in chapters 6 and 7 respectively.

Figure 5.2 shows the energy region of interest for several gamma-ray sources overlaid on the NORM background spectrum. The measured energy spectrum from NORM background is shown in blue and the energy windows used for imaging of  $^{137}\text{Ca}$ ,  $^{22}\text{Na}$ ,  $^{131}\text{I}$ , and  $^{235}\text{U}$  are shown in red, blue, yellow and green respectively. Some isotopes have multiple gamma-ray lines and therefore have multiple energy windows. For example,  $^{22}\text{Na}$  has two energy windows around the photo peak regions at 511 and 1275  $\text{keV}$ .

The width of each energy window is defined using multiples of the known energy resolution as a function of deposited energy. The energy resolution of the detector



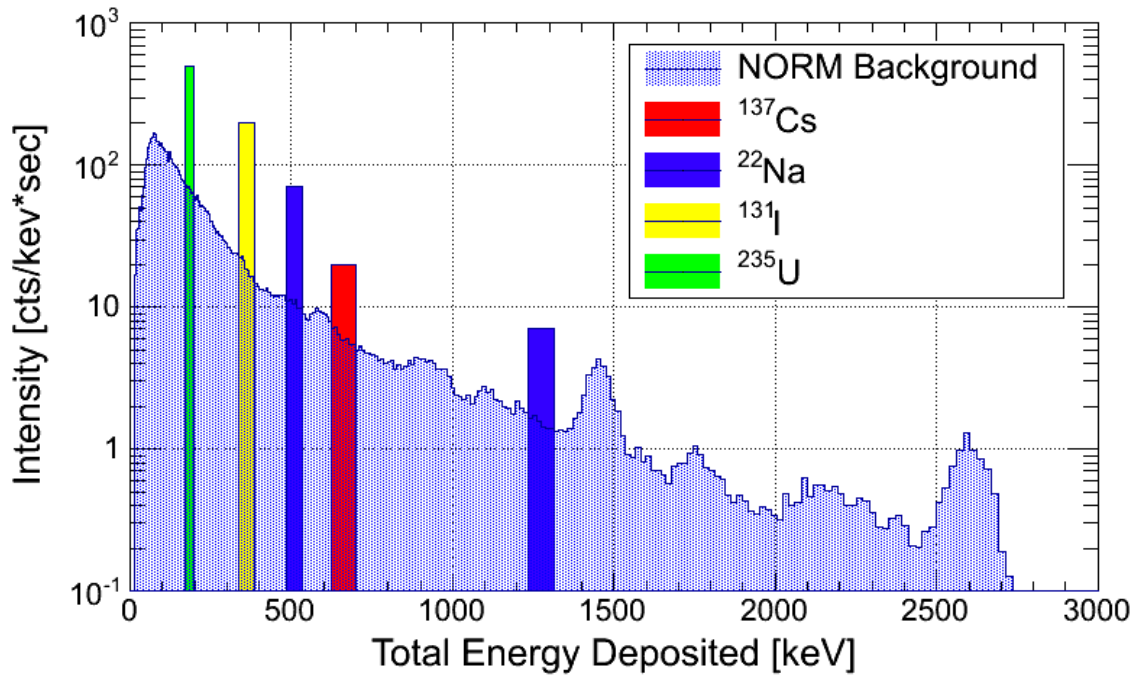


Figure 5.2: Example of the NORM background as well as the energy windows applied for several gamma-ray sources.

elements has been characterized using a  $^{137}\text{Cs}$  check source and approximately follows the  $1/\sqrt{E}$  functional form shown in Figure 5.3. The function in Fig. 5.3 is scaled by the laboratory measured 7.5% FWHM energy resolution at 662 keV from  $^{137}\text{Cs}$ .

In order to increase the sensitivity of detection measured events are segmented into subsets of spectra pertaining to a single isotope as shown in Fig. 5.2. This has several advantages, first it will increase the sensitivity of the algorithms by reducing the total background in the spectrum relative to a potential signal and second will allow for simultaneous detection and identification of threats. If the SNR calculated for a given isotope spectrum is above threshold it will alarm the system providing detection of a source and also identify the source based on the isotope definition that alarmed. Figure 5.4 shows the same run as Fig. (5.1) but shows only the total count

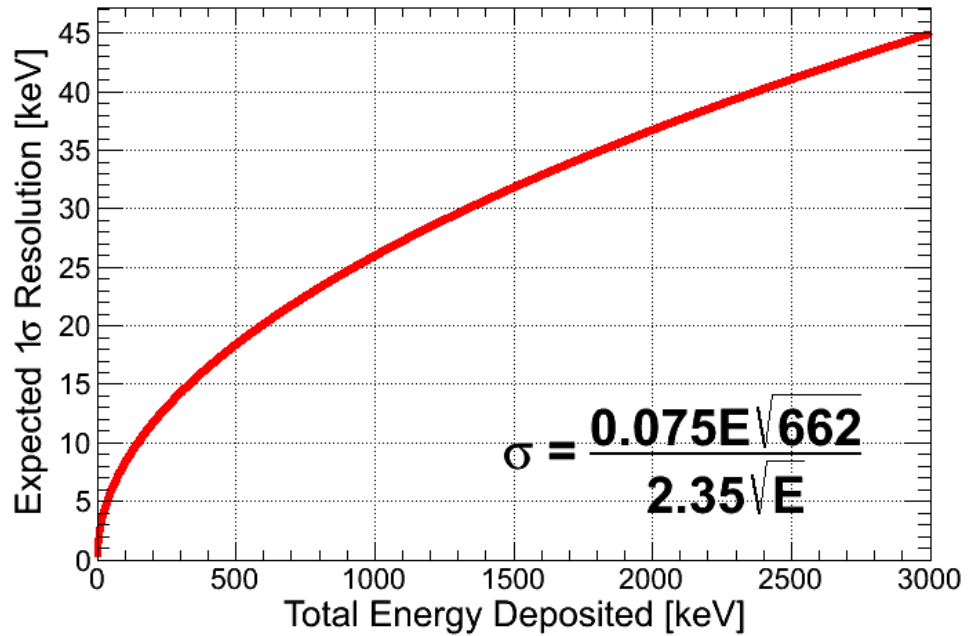


Figure 5.3: Expected energy resolution of the DA detector array ( $\sigma$ ) as a function of total energy deposited in the NaI.

rate within the  $^{137}\text{Cs}$  energy window. Here, the location of the source becomes more easily located as the point just past the road crossing.

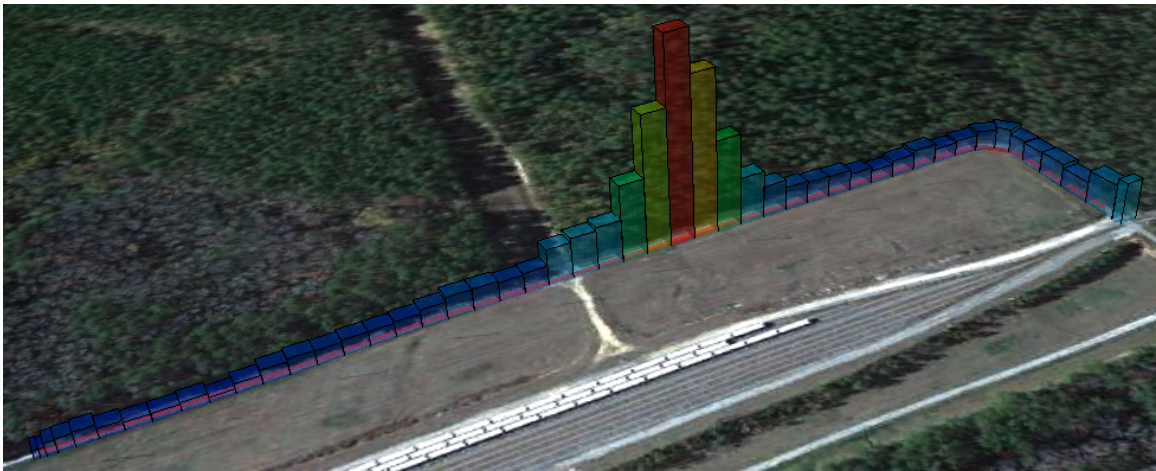


Figure 5.4: Count rate as a function of location for all measured events within the  $^{137}\text{Cs}$  energy window. The location of the source is now clearly visible.

Additionally it can be seen that fluctuations in the total  $^{137}\text{Cs}$  rate are less affected by variation in other parts of the energy spectrum. However, increased count rates in the gamma-ray lines above the energy of the photo-peak(s) of interest can contaminate the energy window with continuum energies. As a result it will be advantageous to the sensitivity to devise a method to estimate the background intensity within the energy window. One simple method for account for background is the Region-of-Interest (ROI) algorithm.

### 5.3 Region-of-Interest

Spectroscopic ROI is a method of background estimation within an energy window. This background estimation is based on the observed counts to the low and high end of the energy window to estimate the background counts within the window. Once the background count rate is estimated a value for the SNR can be calculated. This will be the basis of triggering in the ROI algorithm.

The region of interest for a particular isotope is broken up into three regions. The first region is the background window ( $B_1$ ) of total energy deposited at the low end of the photo-peak ( $e_0$  to  $e_1$ ). The second is the background window ( $B_2$ ) located at the high end of the photo-peak ( $e_2$  to  $e_3$ ). The third peak region ( $S + B$ ) is the photo-peak signal region ( $e_1$  to  $e_2$ ). Equations 5.1, 5.2 and 5.3 show the calculation of  $B_1$ , ( $S + B$ ), and  $B_2$  respectively where  $S(E, T)$  is the measured energy spectrum in all detector elements as a function of energy and time,  $E_i$  is the  $i^{th}$  energy bin in the spectrum,  $N_i$  is the number of energy bins in the summation, and  $t_0$  and  $t_1$  are the limits of the time range for the integration. It should be noted that binned data have been normalized to counts per  $keV$  per second, therefore the width of the bins

is already accounted for in these calculations.

$$B_1 = \frac{\sum_{i=e_1}^{e_2} S(E_i, T)|_{t_0}^{t_1}}{N_{B_1}} \quad (5.1)$$

$$(S + B) = \frac{\sum_{i=e_2}^{e_3} S(E_i, T)|_{t_0}^{t_1}}{N_{(S+B)}} \quad (5.2)$$

$$B_2 = \frac{\sum_{i=e_3}^{e_4} S(E_i, T)|_{t_0}^{t_1}}{N_{B_2}} \quad (5.3)$$

Background is estimated as the average of counts in the measured total energy spectrum between times  $t_0$  and  $t_1$ , for the low and high energy windows. The signal is estimated as the average counts over the same time interval for the photo-peak region minus the background estimation ( $\bar{B}$ ). To calculate the SNR of the peak the signal is divided by the uncertainty in the background estimation ( $\bar{B}$ ). Equation 5.4 shows the calculation of the background estimation for an energy spectrum and Eq. 5.5 shows the calculation of the signal-to-noise ratio from the ROI algorithm.

$$\bar{B} = \frac{B_1 + B_2}{2} \quad (5.4)$$

$$SNR = \frac{(S + B) - \bar{B}}{\sqrt{\bar{B}}} \quad (5.5)$$

Figure 5.5 shows an example measured energy spectrum (blue) with a 2 second integration time in the  $^{137}\text{Cs}$  energy window. The signal and background regions are indicated with the black lines and the red regions show the calculated background estimation in all three regions. The estimated signal in the peak is shown in green.

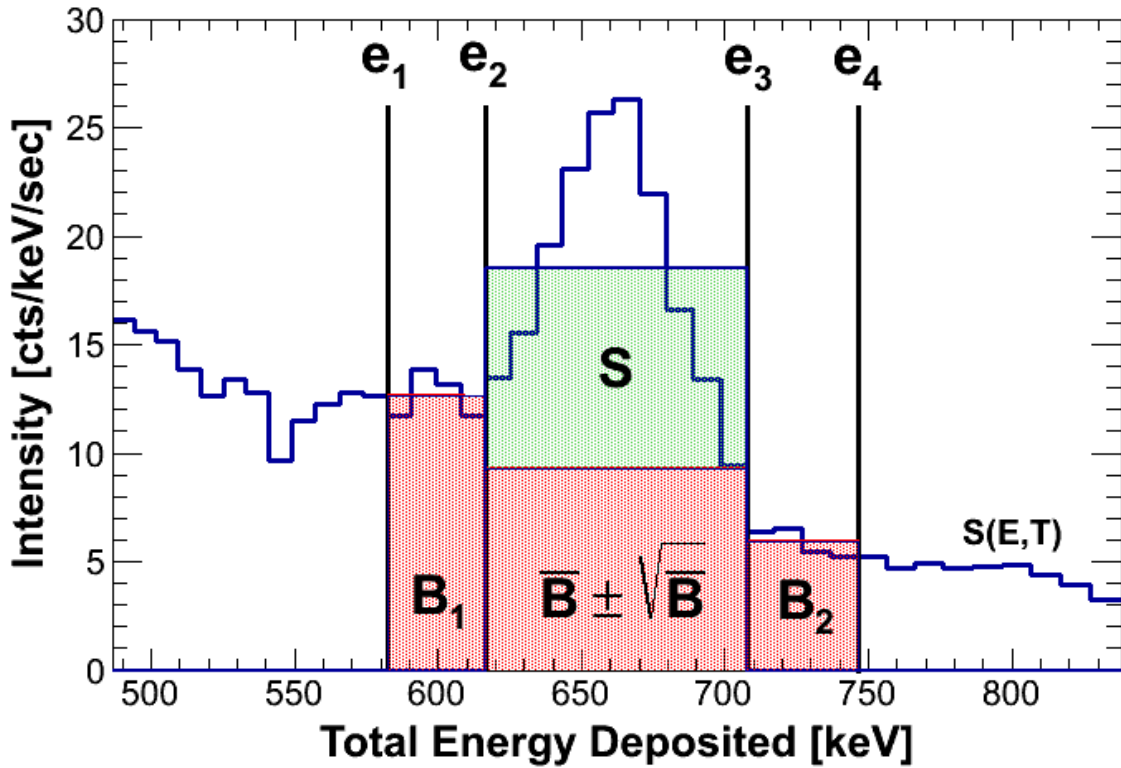


Figure 5.5: Example measured energy spectrum (blue) with a 2.0 second integration time in the  $^{137}\text{Cs}$  energy window with energy regions and estimations shown.

Figure 5.6 shows the calculated ROI SNR as a function of location along a measured run past a  $0.5 \text{ mCi } ^{137}\text{Cs}$  source at 25 meters for each 2 second integration time. Fluctuations in the SNR are not affected as much by variation in the NORM background and the source location is easily located just past the road crossing.

Figure 5.7 shows the result of alarming on the source from the SNR calculation in

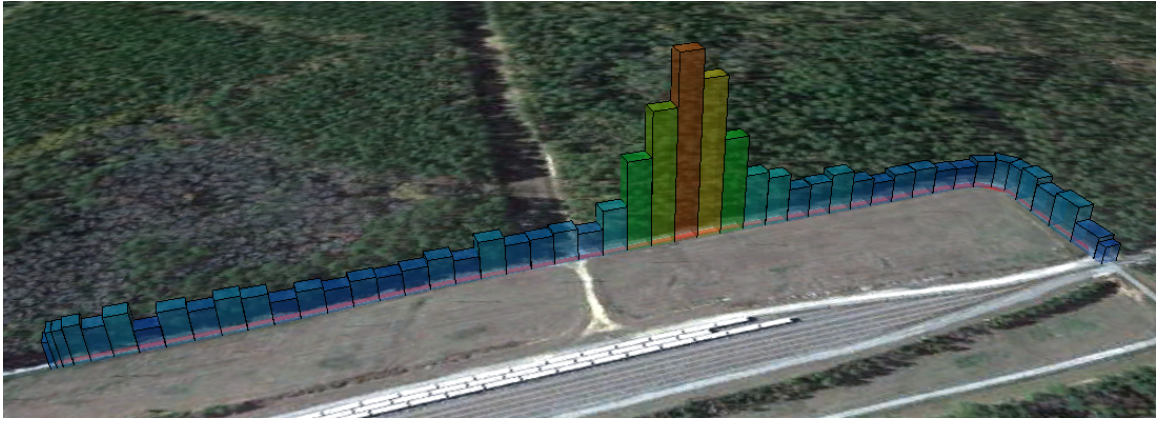


Figure 5.6: Signal-to-noise ratio as a function of location as a result of the ROI algorithm applied to the  $^{137}$  isotope spectra. The location of the source is now clearly visible and background is stable at all other locations.

the ROI algorithm. The red arrow shows the location of the TMI at the time the alarm was generated and the green ring of radius 50 m shows an estimated area where the source could be located. The ground truth location of the source is contained within the ring.

## 5.4 Supplemental Algorithms

In addition to the simple ROI algorithm described here, Bubble Technology Industries has implemented a proprietary isotope identification and detection algorithm which is executed in parallel. Results from the BTI algorithms are also combined with imaging algorithms to improve detection sensitivity of the TMI.

## 5.5 Summary

In this chapter it has been shown that simple spectroscopic methods are considerably sensitive for the detection of radioactive sources in a dynamically changing environ-

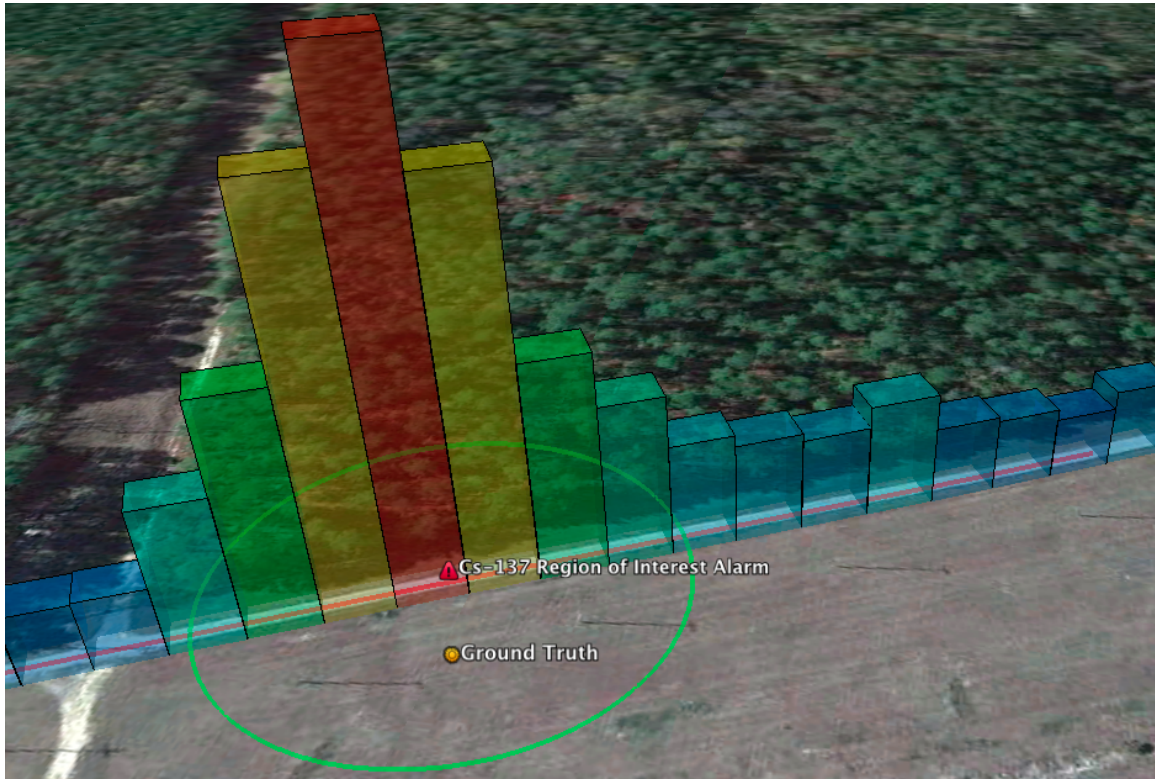


Figure 5.7: ROI alarm for a measured run past a  $0.5 \text{ mCi}$ ,  $^{137}\text{Cs}$  source at  $25 \text{ m}$ . The alarm was generated by the TMI at the location of the red arrow and the estimated area of possible source locations is shown with a green ring. The ground truth location of the source shown to be within the ring.

ment. Through energy windowing techniques the SNR can be increased, resulting in improved sensitivity. Additionally, by analyzing measured energy spectra in order to estimate the background within an energy window triggering and alarming can be performed allowing for isotope detection and identification, as well as crude proximity localization. The energy windowing method in this chapter will be applied to imaging algorithms as well. Improvements in sensitivity can also be observed when combining the results of the ROI algorithm with coded aperture and Compton gamma-ray imaging algorithms.

## Chapter 6

# CODED APERTURE IMAGING ALGORITHMS

Coded aperture imaging is a method of gamma-ray imaging that uses a position sensitive detector array, shadowed by a dense, sparse mask, in order to cast a coded shadow onto the array [1–6]. The TMI detection array consists of 30 position sensitive NaI bars,  $3 \times 24 \times 2.5 \text{ in}^3$  each, to collect gamma-ray energy and position measurements. This is collectively referred to as the DA array. The DA array is shadowed by 35,  $5 \times 5 \times 2 \text{ in}^3$ , NaI tiles in a random  $15 \times 5$  element grid, with approximately 50 percent fill factor called the CA array [51].

The advantage of coded aperture gamma-ray imaging is evident when reconstructing background events and source events. Imaging of pure background counts will modulate on the detector array in a different way than if a source is present in the FOV of the imager. This chapter will present the details of the coded aperture algorithm implemented for the TMI, including methods of data segmentation, registration using navigational information, background suppression, imaging decoding through back projection, and uncertainty compensation. Figure 6.1 shows a sketch of the coded aperture imager integrated into the TMI. Photons from a source pass through



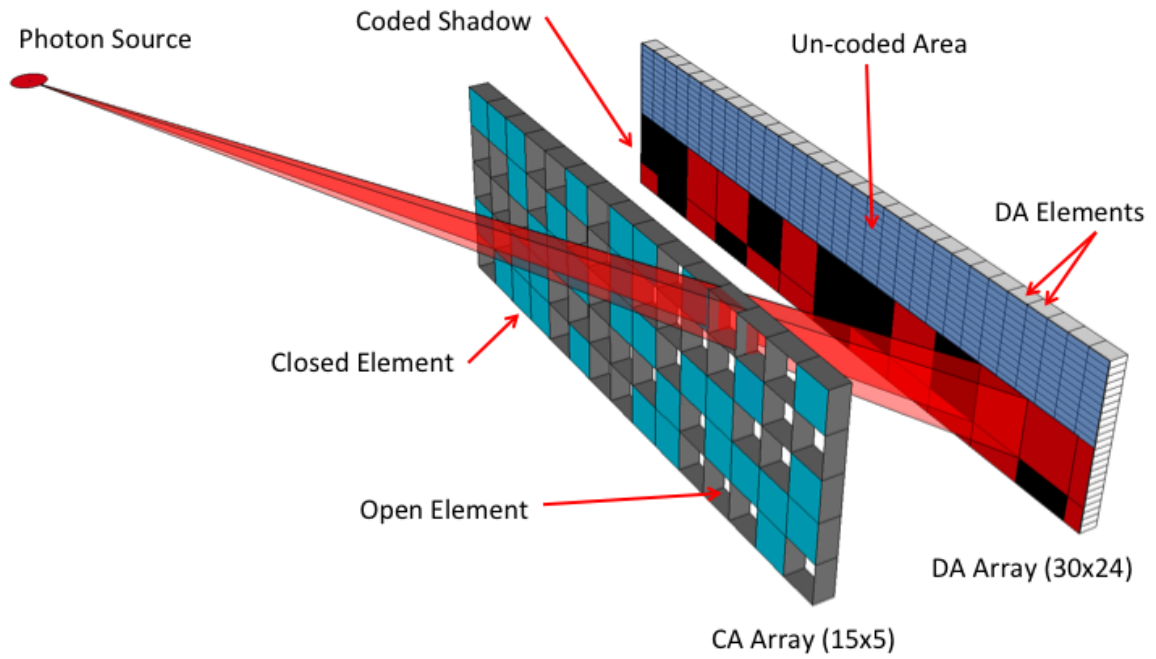


Figure 6.1: Diagram of the coded aperture imager integrated into the TMI.

the open coded mask elements casting a shadow pattern on the detection array. The coded imager is designed to face out the curb side of the vehicle where the positive  $x$  and  $y$  directions point toward the front and top of the vehicle respectively.

A coded aperture event is defined as a single energy deposition in the DA detector array. It excludes multiple DA interactions and coincident interactions in the CA array elements. Given that the coded mask is comprised of active NaI crystals, an interaction in a CA element in coincidence with an interaction in a DA array can be rejected to provide background veto capability.

Each coded aperture event has a discrete  $x$  location based on the NaI bar that triggered and a  $y$  position along the bar. Additionally, each interaction is accompanied by a measurement of the energy deposited in the bar. Segments of events are represented as a distribution of interaction locations  $(x,y)$  on the DA array within a

well defined time and energy windows. Events are carefully segmented based on certain conditions depending on the mode of operation. Segments of event distributions will be referred to as DA array snapshots. Event segments are parsed into multiple isotope snapshots through energy windowing in order to improve the SNR.

## 6.1 Energy Windowing

A method of gamma-ray energy windowing was described in section 5.2. Similar to the spectroscopic algorithms, it is advantageous to the coded aperture SNR to reconstruct only those photons that would have come from a source of interest rather than producing a single image using all measured photons in the detector array. By looking at the reconstruction of a point source using all measured photons, and only those in the energy window, the positive effects of energy windowing on image reconstruction can be observed.

Figure 6.2 shows the reconstructed image of a  $0.5 \text{ mCi}$ ,  $^{137}\text{Cs}$  source from a  $15 \text{ mph}$  drive by at  $25 \text{ m}$  DCA. The images are reconstructed with the coded aperture algorithm using all measured events (top) and only those within  $\pm 1.5\sigma$  of the  $662 \text{ keV}$  cesium photo peak (bottom). It can be observed from both images that the source is present. However, the non-windowed image contains more clutter than the windowed image due to the inclusion of many more background photons. This has a detrimental effect on the performance of the algorithms, lowering the sensitivity of the system and raising the Minimum Detectable Activity (MDA) of a source of interest. The calculated significance of the non-windowed image is  $5.80$  compared to  $11.27$  for the energy windowed image. Also, the uncertainty in location and Time-to-Detect (TTD) are improved;  $\pm 2.40 \text{ m}$  in  $9.52 \text{ s}$  (top) versus  $\pm 2.37 \text{ m}$  in  $7.46 \text{ s}$

(bottom). The method used for calculating significance is given in section 8.5.

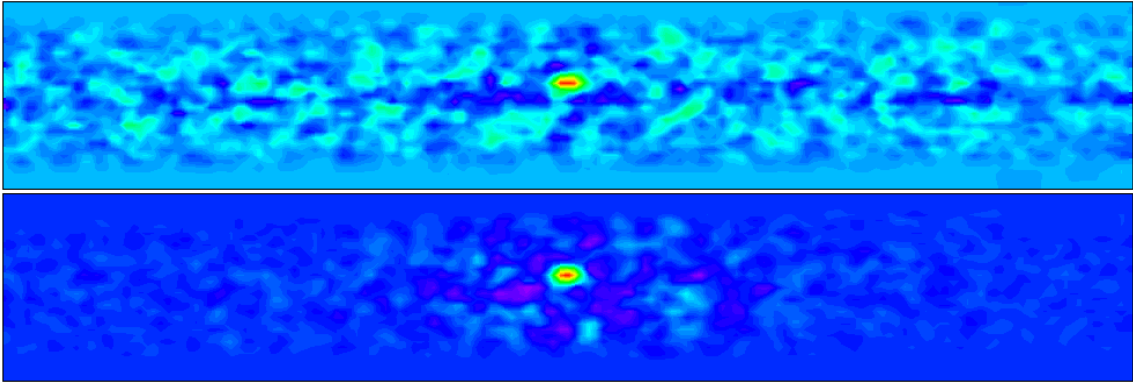


Figure 6.2: Reconstructed coded aperture images using all measured photons (top) and only those that have a total energy deposited within the  $^{137}\text{Cs}$  energy window (bottom). The non-windowed image has a calculated significance of 5.80 with location accuracy of  $\pm 2.40\text{ m}$  and was detected in 9.52 seconds. The windowed image has a calculated significance of 11.27 with location accuracy of  $\pm 2.37\text{ m}$  and was detected in 7.46 seconds.

The width of the energy window has been optimized by analyzing the image significance as a function of window width. The value of  $1.5\sigma$  has been chosen to optimize the SNR in the image based on the results of the analysis shown in Figure 6.3.

## 6.2 Data Segmentation

The coded aperture algorithm aggregates all valid interactions on the DA array during a specified interval and decodes the distribution into an image at a distance. Since the TMI is a mobile system, a method for segmentation of measured data is required to ensure that images are projected to the correct location without introducing distortion from movement of the detector. In a static imaging scenario the selection of interval

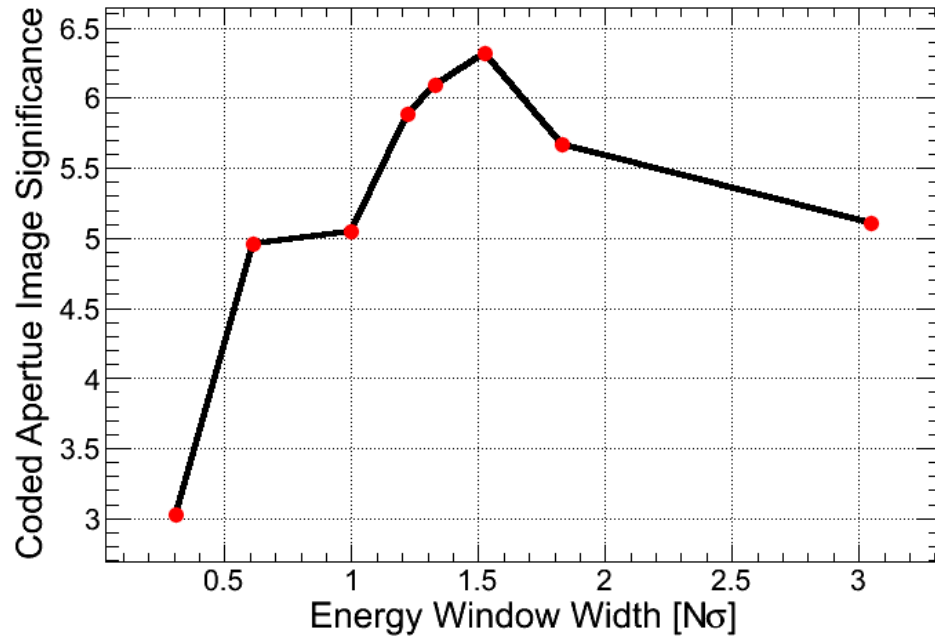


Figure 6.3: Optimization of the energy window width. A width of  $1.5\sigma$  corresponds to the highest significance in the coded aperture image.

is only dependent on the ability to detect a moving source within the FOV, making elapsed time the most important factor.

In a moving scenario the quality of the back projected images depends on the motion of the imager. The imager should not traverse more than a single imaging pixel for a given data segment. Therefore three criteria have been selected to define the intervals at which measured data are packaged and sent to the coded aperture algorithms. These criteria make it possible for the imaging system to function in both stationary and mobile detection scenarios.

Data are segmented according to the first of three criteria; time elapsed, distance traveled, or number of photons collected. When any one of these criteria have met the threshold value, the event segment is sent to the coded aperture imaging algorithm

Table 6.1: The three data segmentation criteria used for coded aperture data.

Criteria	Threshold Value
Time ( $s$ )	1.0
Distance ( $m$ )	2.0
Counts ( $N$ )	100,000

for processing. Table 6.1 summarizes the three criteria.

The selection of the criteria is based on several considerations to the mode of operation. In a static mode, a source in the FOV may be moving and the image must be updated regularly based on time or number of events measured, otherwise the image will blur, lowering the performance of the system. In a moving scenario the distance criteria is the most important. Here, the threshold has been chosen to limit the length of a data segment such that the back projected image does not shift more than a single image pixel for any measurement in the segment.

Each NaI bar is segmented into 24 (1 *in*) virtual elements in the position sensitive  $Y$  dimension (ground to sky). The coded aperture algorithms parse each event segment meeting one of the criteria in Table 6.1 into multiple aggregate matrices of 30 columns and 24 rows for a total of 720 detector elements. These matrices contain the encoded gamma-ray image information and are the basis of the coded aperture reconstruction. A DA detector matrix, constructed from a measured event segment, will be referred to as a snapshot.

Each snapshot represents the distribution of all gamma-ray photons whose total energy deposited in the DA array, in a single interaction, fall into the window of acceptable energies for particular isotope. For example, if the algorithms are configured to produce images for  $N$  isotope definitions, each event segment will be parsed into  $N$

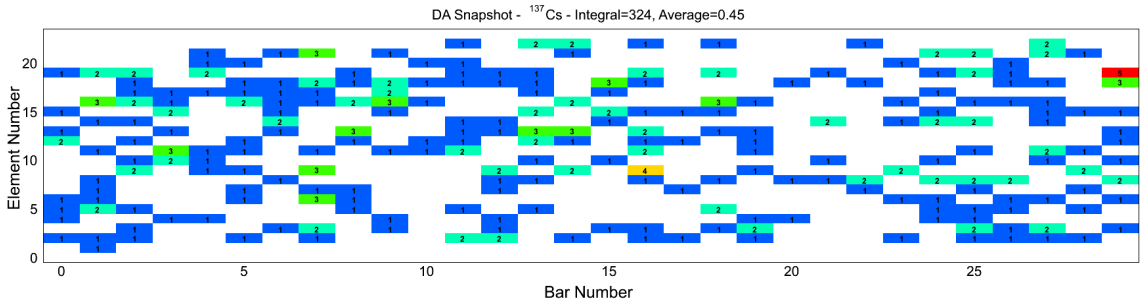


Figure 6.4: Sample DA snapshot (1.46 seconds, 2.00 meters, 324 events) in the  $^{137}\text{Cs}$  energy window.

snapshots, one for each isotope. Each isotope snapshot contains only those photons with an energy in the range of interest for that isotope, however multiple isotope snapshots can contain the same photon.

Figure 6.4 shows an example snapshot, segmented by the distance criteria. The snapshot in Fig. (6.4) is an aggregate of all measured photons (324), valid for the  $^{137}\text{Cs}$  energy window, in 1.46 seconds, traversing 2 meters. The complete event segment had 29,718 measured photons from 0 to 3000  $keV$ . The upper limit of 3000  $keV$  is a result of the dynamic range of the ADC electronics.

Additionally, when performing imaging the average FOV of the imager must be calculated. Figure 6.5 shows the location distribution of 9,438 measured coded aperture events for a single event segment. The average location of the TMI is shown with a red dot and the imaging FOV with red lines. The location of the TMI for each measurement is shown with a blue cross and the corresponding DA element locations (in  $X$  and  $Z$ ) are shown with green marks. For the coded aperture imaging algorithms, all measured photons on the DA array are assumed to be measured on a virtual array located at the average position of the TMI. Obviously this adds uncertainty to the projected image and is handled using the smoothing technique described in section

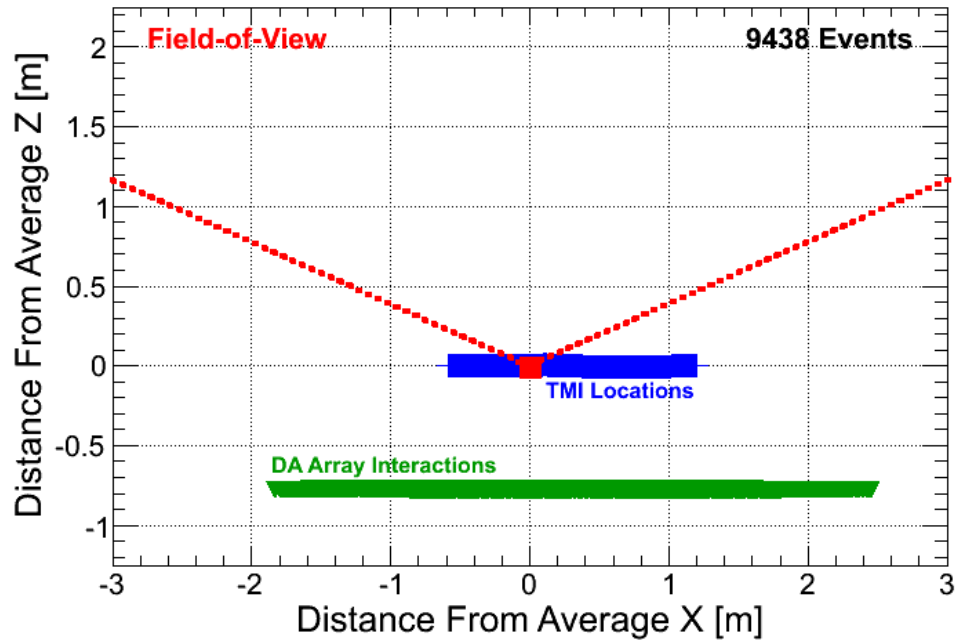


Figure 6.5: Example coded aperture event segment with the average calculated (red square) and the imaging FOV shown (red lines). The location of the TMI for each measurement is shown in blue and the interaction locations are shown in green.

6.4.3. The average location is not directly centered on all the measurements because the speed of the truck can vary as well as the measured count rate as a function of location.

### 6.3 Array Flat Fielding

Energy windowing has been shown to increase sensitivity by reducing background introduced into the coded aperture image. However, there still exists the background within the energy window itself. One method of subtracting background from measured backplane data is to use array flat-fielding [52]. Since photons from NORM background do not have a characteristic emission distribution (usually), it can be assumed that they are incident on the detector plane randomly and that the shape of the ran-

dom distribution should not change, regardless of position or time. Array flat-fielding also has the advantage of removing noisy detector elements or non-uniformities in the array from the image reconstruction.

Flat fielding is the process of taking an estimator of the shape of the distribution of counts on the DA array, scaling it to the observed measurement and subtracting it from the array snapshot. Equation 6.1 shows the calculation of the scaling factor,  $\lambda$ , where  $(S + B)$  is the measurement snapshot array,  $\mathbb{B}$  is the background estimator snapshot, and  $\sigma_i^2$  is the number of counts in the  $i^{th}$  detector element of each. In this equation the background is scaled to the integral counts of the measurement. The scaling factor could also be determined using the elapsed time however that would not accurately compensate for changes in the overall background count rates. Equation 7.21 shows the calculation of the expected source distribution,  $\mathbb{S}$ , after subtracting the scaled background estimator. In the case of purely background counts, the value of  $\mathbb{S}$  should fluctuate normally around zero counts if the value of  $\mathbb{B}$  is an accurate estimator of the background.

$$\lambda = \frac{\sum_{(S+B)_i} \sigma_i^2}{\sum_{\mathbb{B}_i} \sigma_i^2} \quad (6.1)$$

$$\mathbb{S} = (S + B) - \lambda \mathbb{B} \quad (6.2)$$

Figure 6.6 shows the result of subtracting the background estimator from the measurement snapshot. Array flat-fielding can be performed using either historical data or in real-time. The coded aperture algorithms used on the TMI are capable of utilizing both strategies. From Fig. 6.6, the integral number of counts in the snapshot



has been flattened to 0 as expected. Also, the mean of the measured count distribution has been reduced to 0, indicating that  $\mathbb{B}$  is a good estimator of the background, given the fact that no source is present in the FOV.

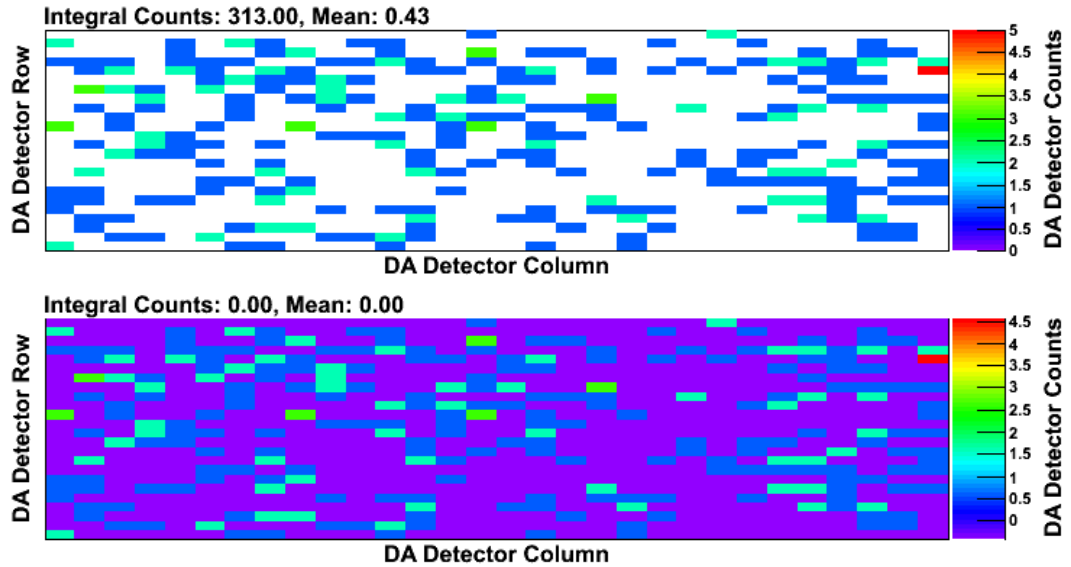


Figure 6.6: Example measured coded aperture backplane data before and after flat-fielding.

Figure 6.7 shows two reconstructions of the same data. The top image shows the reconstruction without array flat fielding enabled and the bottom shows the same reconstruction using array flat fielding. The calculated image significance increased from 4.83 (top) to 8.86 (bottom) while reducing the location uncertainty from  $\pm 4.6$   $m$  (top) to  $\pm 2.2$   $m$  (bottom).

### 6.3.1 Realtime Corrections

Realtime (RT) flat fielding is performed by aggregating counts on the detector plane during a measurement in order to get an estimate of the shape of the distribution. This aggregation can be performed on the basis of time elapsed or gross counts.

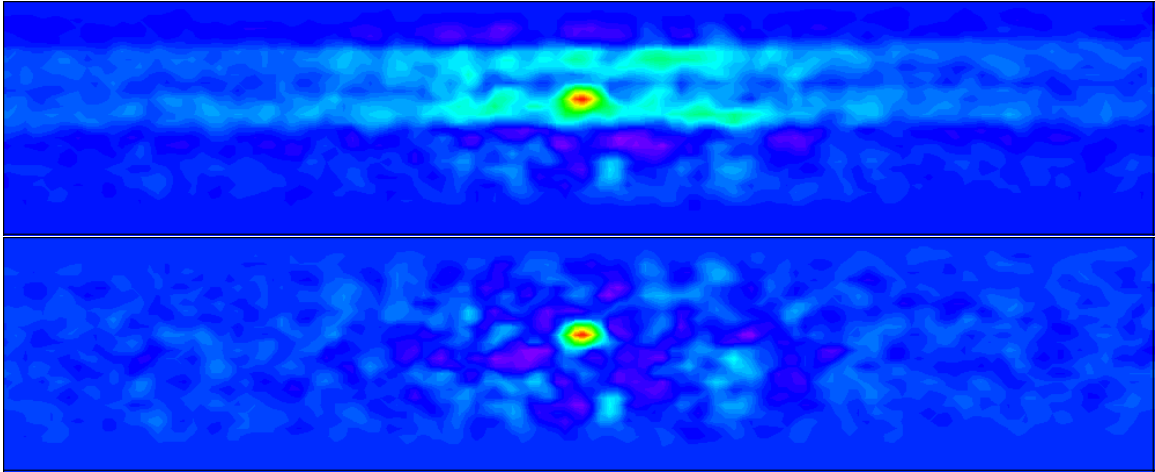


Figure 6.7: Example coded aperture reconstructed images without (top) and with (bottom) array flat fielding enabled.

Once the aggregate detector array has met a certain criteria such as a pre-defined time interval the counts are added to the flat field estimator. Figure 6.8 shows the background estimator as a function of time. The current algorithms update the flat field estimator every 2 seconds when in time-based mode and 13 meters in motion-based mode. The distance criteria is the equivalent distance traveled by the system in 2 seconds at 15 *mph*. The three estimators shown in Fig. (6.8) are after 4.33 (A), 14.30 (B) and 94.7 (C) seconds. After each update the estimate of the background improves.

The advantage of RT flat fielding includes the ability to account for rapid changes to the electronic noise. For example, if a detector element begins to trigger on noise in the middle of a run, the background estimator will incorporate the increased rate of that channel and effectively subtract off the effect. Also, RT corrections are guaranteed to represent the shape of the local background on the DA array. Disadvantages of RT corrections include its susceptibility to the incorporation of real, or nuisance sources,

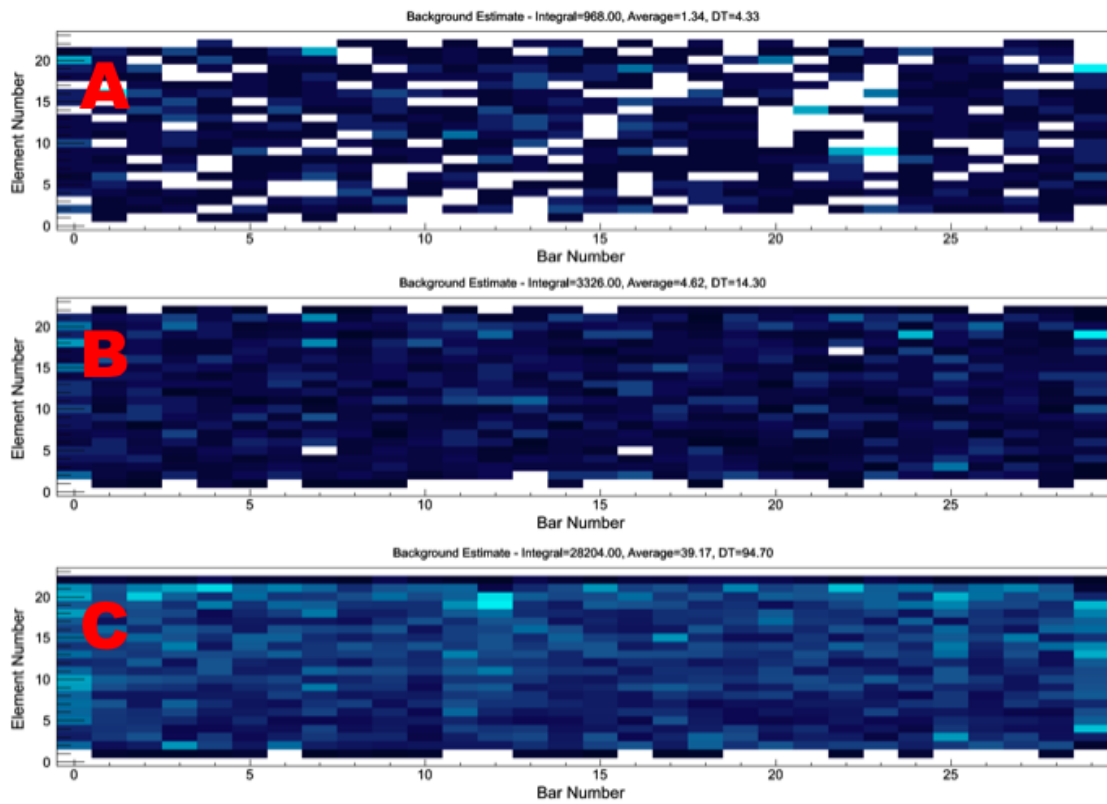


Figure 6.8: Realtime background estimator for  $^{137}\text{Cs}$ . As time progresses the background estimator improves and adjusts to the current sensitivity of the system. The three estimators shown are for 4.33 seconds into the run (A), 14.30 seconds (B) and 94.7 seconds (C).

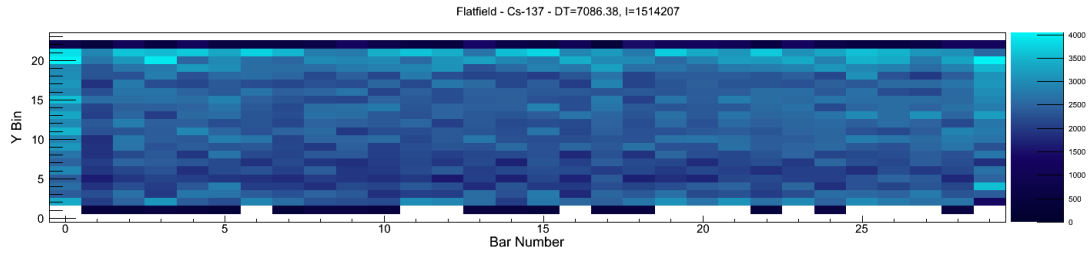


Figure 6.9: Historical flat field estimator for  $^{137}\text{Cs}$ . The flat field history was aggregated over 7086 seconds of background data including 1.5 million measured photons.

in the estimator, reducing the sensitivity of the system. Also, RT corrections cannot be used effectively in a stationary Concept of Operations (CONOPS) because any source in the FOV will potentially become part of the estimator template and get subtracted out of the reconstructed image – making it invisible to the system.

### 6.3.2 Historical Corrections

Another method of array flat fielding is to use historical corrections. This method makes use of an estimator constructed from the combination of array snapshots over the entire period of a background collection, or training set. Additional work is required to ensure that any real or nuisance source are removed from the training set.

When the TMI processes measured snapshots using historical corrections, a new estimator is also aggregated, which can be used to supplement the historical data or form a new background estimator for future scans of the same area. Figure 6.9 shows the historical background estimator for the  $^{137}\text{Cs}$  energy window. This estimator was formed using over 7,000 seconds of background including over 1.5 million measured photons.

It is interesting to observe the pattern formed from the large aggregation on the DA array. Figure 6.9 shows that more counts generally accumulate toward large Y

bins (the bottom of the array) and at the edges of the DA array (*i.e.* bars 0 and 29). This is expected as the side bars have more surface area exposed to the outside world; 3 faces (front, back, and side), rather than 2 (front and back) for internal bars (bars 1 through 28). It is also expected to observe more counts on the bottom of the bar because it acts as a shield to the top of the bar and is closer to the ground plane, where the majority of NORM background originates.

## 6.4 Geometric Pre-calculation

In order to make the back projection calculation fast and efficient many of the commonly used values will be calculated a single time, during initialization, and used repeatedly during reconstruction of images from detector snapshots.

The distance between the detector array (DA) and the coded mask array (CA) will be denoted by  $\Delta_{CA-DA}$  and is calculated using Eq. 6.3; it has a value of 75 *cm* for the configured system. Similarly, the distance between the DA array and the imaging plane (*IM*) is denoted by  $\Delta_{IM-CA}$  and is calculated using Eq. 6.4. The value of  $\Delta_{IM-CA}$  is different depending on the plane for which the pre-calculation is performed (nominally 5000 *cm*).

$$\Delta_{CA-DA} = CA_z - DA_z \quad (6.3)$$

$$\Delta_{IM-CA} = IM_z - CA_z \quad (6.4)$$

One of the most commonly used values in the coded aperture back-projection is the number of image pixels that correspond to a single detector array element,

$\left(\frac{d_{PX}}{d_{DA}}\right)_{x,y}$ . The calculation of  $\left(\frac{d_{PX}}{d_{DA}}\right)_{x,y}$  is given in Eq. 6.5, where  $\hat{D}A_{x,y}$  and  $\hat{P}X_{x,y}$  are the unit size of a DA detector element and image pixel, in  $x$  or  $y$ , respectively.

$$\left(\frac{d_{PX}}{d_{DA}}\right)_{x,y} = - \left[ \frac{\hat{D}A_{x,y} \Delta_{IM-CA}}{\Delta_{CA-DA} \hat{P}X_{x,y}} \right] \quad (6.5)$$

The negative sign comes from the fact that a movement in the  $+(x, y)$  direction on the detector array corresponds to a movement in the opposite direction on the imaging plane if the ray between the points is anchored at a point on the CA array. For example the movement of a single DA detector element in  $+x$  and  $+y$  translates to an equivalent movement of  $-1.73$  and  $-0.504$  image pixels respectively for an imaging plane at  $5000 \text{ cm}$ . The values vary in  $x$  and  $y$  because of the asymmetry of the position determination in the DA detector elements.

Additionally, it is useful to pre-calculate the number of image pixels that correspond to a single coded mask element, when anchored to the DA array,  $\left(\frac{d_{PX}}{d_{CA}}\right)_{x,y}$  as shown in Eq. 6.6. Here,  $\hat{C}A_{x,y}$  is the unit size,  $\text{cm}$ , of a CA detector element in  $x$  or  $y$ . An example movement of a single CA array element  $x$  and  $y$  translates to a movement of 3 image pixels. The values are identical for a movement in either direction because the CA mask elements are square.

$$\left(\frac{d_{PX}}{d_{CA}}\right)_{x,y} = \frac{\hat{C}A_{x,y} \Delta_{IM-CA} + \Delta_{CA-DA}}{\Delta_{CA-DA} \hat{P}X_{x,y}} \quad (6.6)$$

Figure 6.10 is a graphical representation of the detector planes CA and DA as well as the imaging plane (not to scale). In Fig. 6.10 the variables used in the calculation

of  $\left(\frac{d_{PX}}{d_{DA}}\right)_{x,y}$  (top) and  $\left(\frac{d_{PX}}{d_{CA}}\right)_{x,y}$  (bottom) are shown.

Next is the calculation of the image pixel offset from the bore sight for a projection from DA element (0,0) through CA element (0,0), or the bottom corner elements of both arrays;  $PX(0,0)_{x,y}$ . This calculation will be the basis for fast shifting of pre-calculated projections onto the image. This value is also important because it will define the location of projections on the image and contribute to alignment with the Compton imaging algorithm. Equation 6.7 shows the calculation where  $BS_{x,y}$  is the bore sight image pixel, or the pixel closest to the geometric center of the image and  $N_{DA_{x,y}}$  and  $N_{CA_{x,y}}$  are the number of DA and CA array elements in  $X$  and  $Y$  respectively.

$$PX(0,0)_{x,y} = BS_{x,y} - \left[ \left( \frac{d_{PX}}{d_{DA}} \right)_{x,y} \frac{N_{DA_{x,y}}}{2} \right] - \left[ \left( \frac{d_{PX}}{d_{CA}} \right)_{x,y} \frac{N_{CA_{x,y}}}{2} \right] \quad (6.7)$$

#### 6.4.1 Offsets

The calculated offset in pixels from the lower left corner for each of the detector array and mask array elements is also required. This results in a single number that can be referenced, by detector, to shift the projection to the correct location on the imaging plane. When calculating the offset from the DA elements,  $PX(0,0)_{x,y}$  is used to find the lower corner of the projection for that particular element. Calculations for the CA detector elements are with respect to the corner point defined by the DA offset.

$$O_{DA_{i_{x,y}}} = PX(0,0)_{x,y} + DA_{i_{x,y}} \left( \frac{d_{PX}}{d_{DA}} \right)_{x,y} \quad (6.8)$$

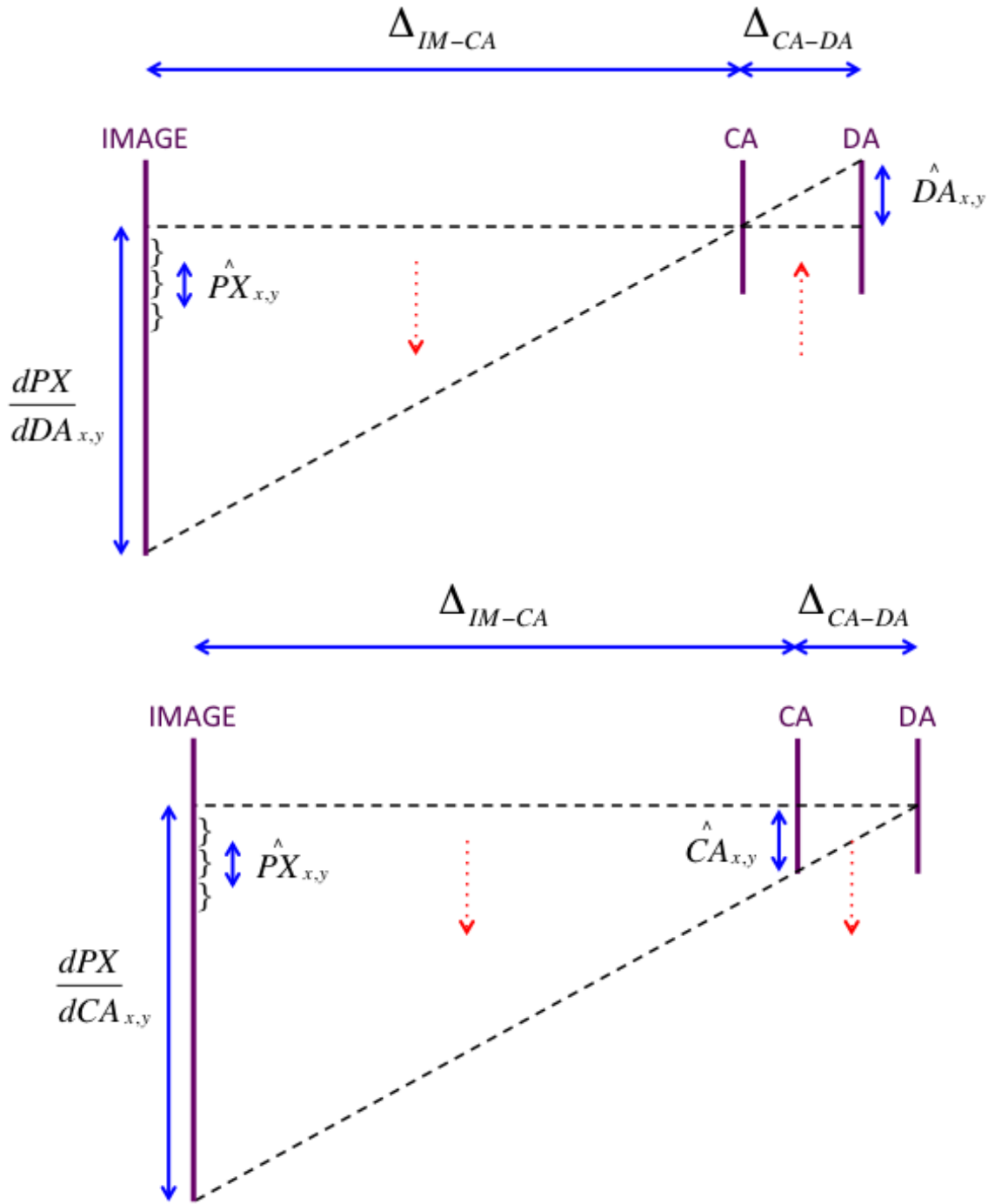


Figure 6.10: Graphical view of the variables used in the calculation of the number of image pixels that correspond to the movement of a single detector element in  $x$  and  $y$  for the DA array (top) and the CA array (bottom).



$$O_{CA_{i_x,y}} = CA_{i_x,y} \left( \frac{d_{PX}}{d_{CA}} \right)_{x,y} \quad (6.9)$$

Once all the offsets have been calculated for each detector and mask element (720x75) we can easily generate the projection from a DA element through any mask element using the offsets. Equation 6.10 shows the simple calculation of the image pixel corresponding to a projection from any DA element through any CA element. The value of the projection is a 1 or -1 depending on whether the mask element is open or closed respectively.

$$IM_{x,y} = O_{DA_{x,y}} + O_{CA_{x,y}} \quad (6.10)$$

## 6.4.2 Pixel Mapping

The last step in the pre-calculation is the calculation of image pixels corresponding to the reference location we specified in Eq. 6.10. In this step the mapping between each open and closed element of the coded mask is generated such that weighting of the image pixels can be performed through a lookup matrix. If a mask element is un-blocked the offset pixel gets added to the open element matrix. If the mask element is blocked it gets added to the closed element matrix. These will be used in the back projection of the DA snapshots to weight the pixel values in the image base on the coding provided by the mask. The pixel indices will be shifted using the pre-calculated offsets of Eq. 6.10.

Figure 6.11 shows 3 sample back projections from the bottom left DA detector element (top plot), the center DA element (middle) and top right element (bottom).

Here, the black pixels indicate a projection through an open mask element and receive a +1 weighting because a source in those image pixels could have produced a count in that detector array element. White pixels indicate a projection through a closed mask element, and receive a weighting of -1 because a source in those images pixel would not likely produce a count in that detector element. All other regions of the image are untouched because there is not sufficient information to provide weights to those pixels.

For each measured snapshot the projections like those in Fig. 6.11 are overlapped for each of the 720 DA detector bins. Figure 6.12 shows the image produced from the overlap of projections from each DA element through each mask element assuming a completely flat distribution. The image is shown for the  $Z = 50$  meter imaging plane. It can be seen from the image in Fig. 6.12 that the projection is grainy and not smooth, this is a result of the fast back projection, which ignores the effects of position resolution, motion, and vignetting. Vignetting is an effect that results in the distortion of a projection due to partial occlusion of mask elements by neighboring elements as well as a softening of the projection edges due to the reduced path length of a photon through the detector.

### 6.4.3 Image Smoothing

Since the back projection algorithm is designed to be as fast as possible, the image quality achieved does not accurately describe the imaging system. It does not account for uncertainty in the measurements and other effects such as vignetting of the detector elements and motion of the detector during the collection of data. In order to account for these uncertainties, back projected images are smoothed using an energy

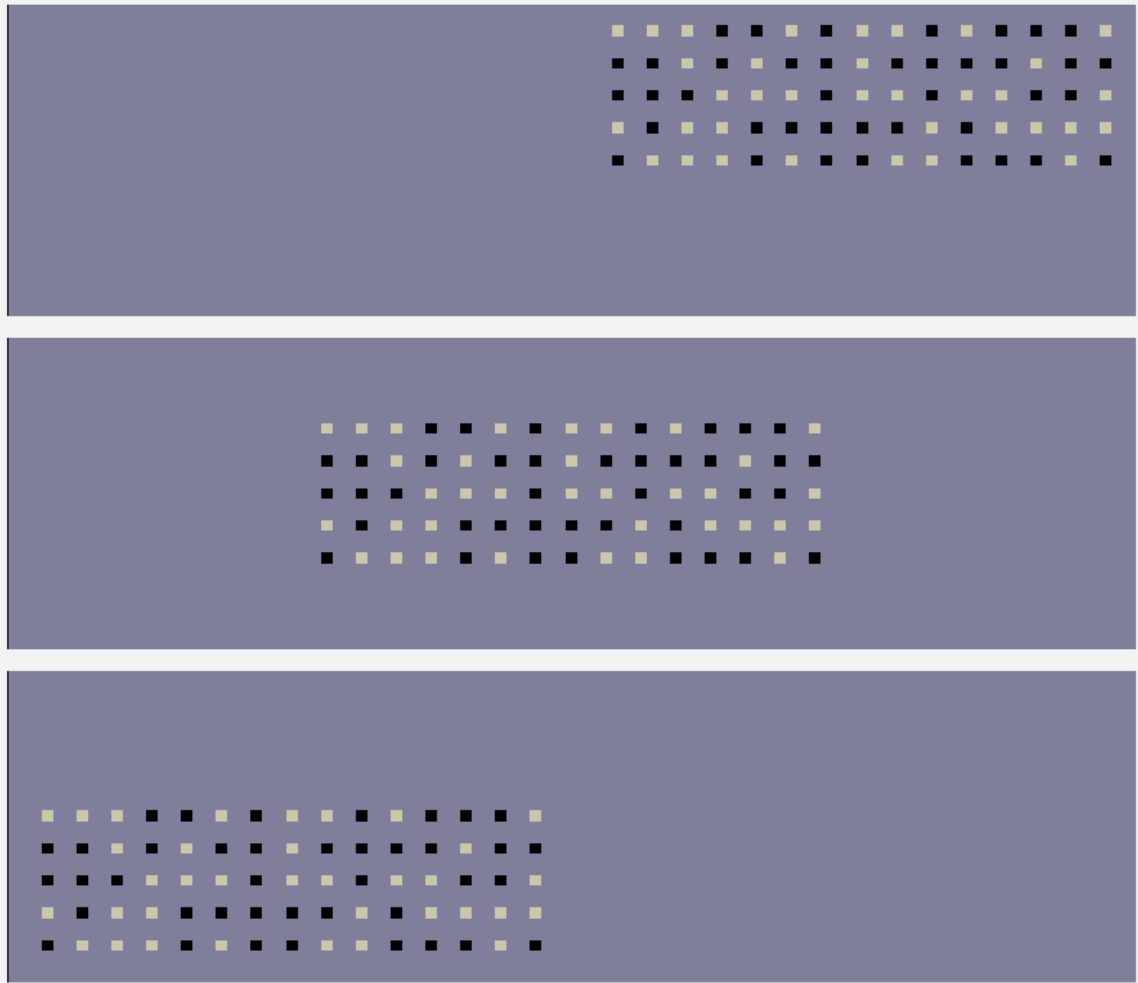


Figure 6.11: Example coded aperture mask projection for 3 individual points on the DA detector array; the lower left element (top), the middle element (middle) and the upper right element (bottom). Black pixels are projections through open mask element (+1), white are projections through closed elements (-1) and grey pixels are zero because no information was available to add to them.

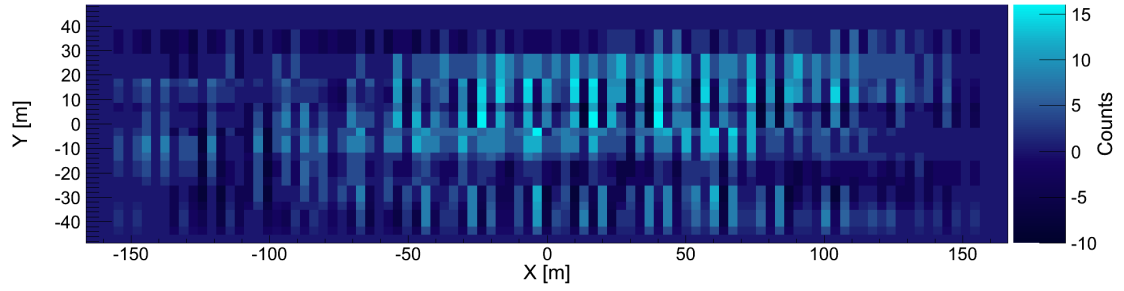


Figure 6.12: Example back-projected coded aperture image formed from the overlap of projections from each of the 720 DA array elements assuming a single count in each of the DA detector elements.

dependent, unit gaussian kernel. Gaussian kernels are pre-calculated for each isotope based on the incident gamma-ray energy and are reused for each projected snapshot.

Gaussian smoothing kernels are constructed using the average energy of the isotope being imaged because the uncertainty in the position of the photon interaction in the DA detector element is energy dependent and therefore effects the reconstruction. The expected energy resolution of the DA elements has been characterized using a collimated  $^{137}\text{Cs}$  source and is assumed to follow a  $1/\sqrt{(E)}$  form. Figure 6.13 shows the expected position uncertainty in the DA elements,  $cm$  as a function of deposited energy,  $keV$ .

Kernels are defined in a range of pixels, not distance. The calculated kernels cover  $\pm 3\sigma$  of the expected value of the uncertainty in each dimension. Uncertainty in the X dimension is assumed to be 3.81 cm (fixed) and the uncertainty in the Y dimension is evaluated using the equation in Fig. 6.13. In order to construct the kernel it is necessary to calculate the number of pixels that correspond to  $1\sigma$  in each dimension. Equation 6.11 shows the calculation of the number of pixels,  $NPX_{x,y}$  corresponding to a  $1\sigma$  movement on the DA array in X or Y, where  $M$  is the magnification factor

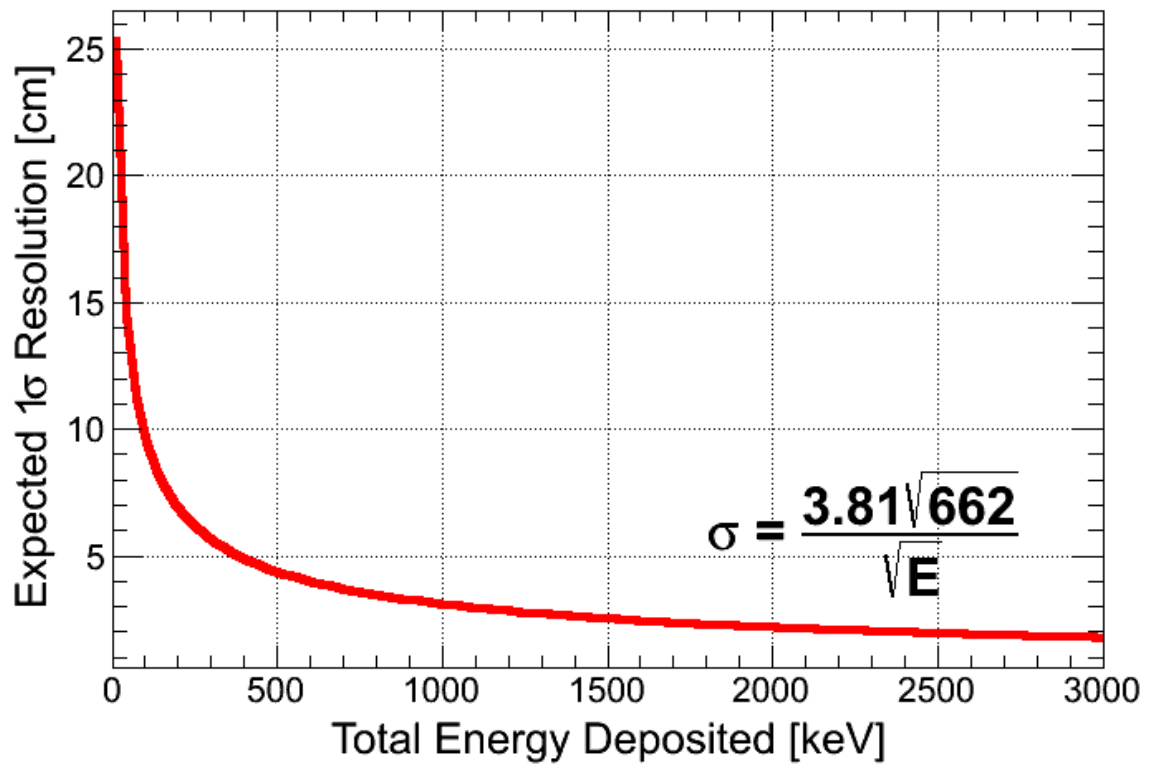


Figure 6.13: The expected 1σ position resolution of the NaI bars as a function of energy deposited.

given the distance to the imaging plane ( $\Delta_{IM-CA}$ ) from Eq. 6.12.

$$NPX_{x,y} = N_{\sigma} \frac{M\sigma_{x,y}}{\hat{P}X_{x,y}} \quad (6.11)$$

$$M = \frac{\Delta_{IM-CA}}{\Delta_{CA-DA}} \quad (6.12)$$

Next, the dimensions of the kernel ( $K_{x,y}$ ) are calculated using Eq. 6.13. Since the desired kernel covers  $\pm 3\sigma$  the calculated value of  $NPX_{x,y}$  is multiplied by 2. Additionally, the kernel should have an odd dimension such that the peak of the Gaussian is centered on an image pixel, so the dimension is increased by 1 pixel.

$$K_{x,y} = 2(NPX_{x,y}) + 1 \quad (6.13)$$

Gaussian kernel values are calculated using an asymmetric two dimensional Gaussian function centered at  $(K_x/2, K_y/2)$ . The calculation of the Gaussian weights is shown Eq. 6.14, where  $W_{x,y}$  is the calculated weight for the  $(x, y)$  pixel and  $NPX_{x,y}$  are the number of pixels corresponding to  $1\sigma$  in  $X$  and  $Y$ .

$$W_{x,y} = \exp \left( -\frac{1}{2} \left[ \frac{x - \frac{K_x}{2}}{NPX_x} + \frac{y - \frac{K_y}{2}}{NPX_y} \right]^2 \right) \quad (6.14)$$

To make a unit kernel, all values of  $W_{x,y}$  are divided by the sum of all the weights. The kernel is normalized to maintain the original number of counts in the image.

Gaussian Kernel - I-131 - 364.00 keV

Gaussian Kernel - Cs-137 - 662.00 keV

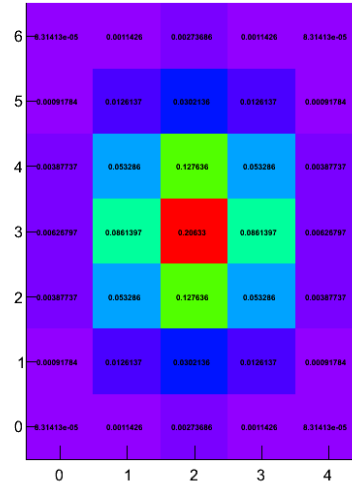
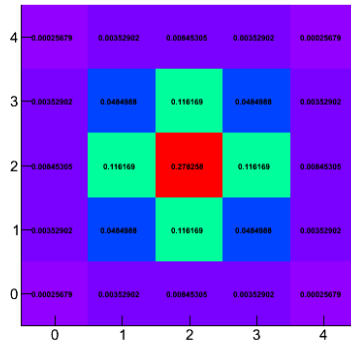


Figure 6.14: Example Gaussian smoothing kernel for  $^{137}\text{Cs}$  (left) and  $^{131}\text{I}$  (right). Since the average energy of  $^{131}\text{I}$  (364 keV) is lower than  $^{137}\text{Cs}$  (662 keV) there is more uncertainty in the Y dimension of the iodine kernel due to the uncertainty in the measured DA element position.

Equation 6.15 shows the calculation of the normalized kernel ( $\hat{W}$ ).

$$\hat{W}_{x,y} = \frac{W_{x,y}}{\sum_{i=0}^{K_x-1} \sum_{j=0}^{K_y-1} (W_{i,j})} \quad (6.15)$$

Figure 6.14 shows two example Gaussian smoothing kernels for the  $^{137}\text{Cs}$  (left) energy window and the  $^{131}\text{I}$  energy window (right). Since the average energy of  $^{131}\text{I}$  (364 keV) is lower than  $^{137}\text{Cs}$  (662 keV) there is more uncertainty in the Y dimension of the iodine kernel due to the uncertainty in the measured DA element position.

Figure 6.15 shows an example mask projection before (top) and after (bottom)

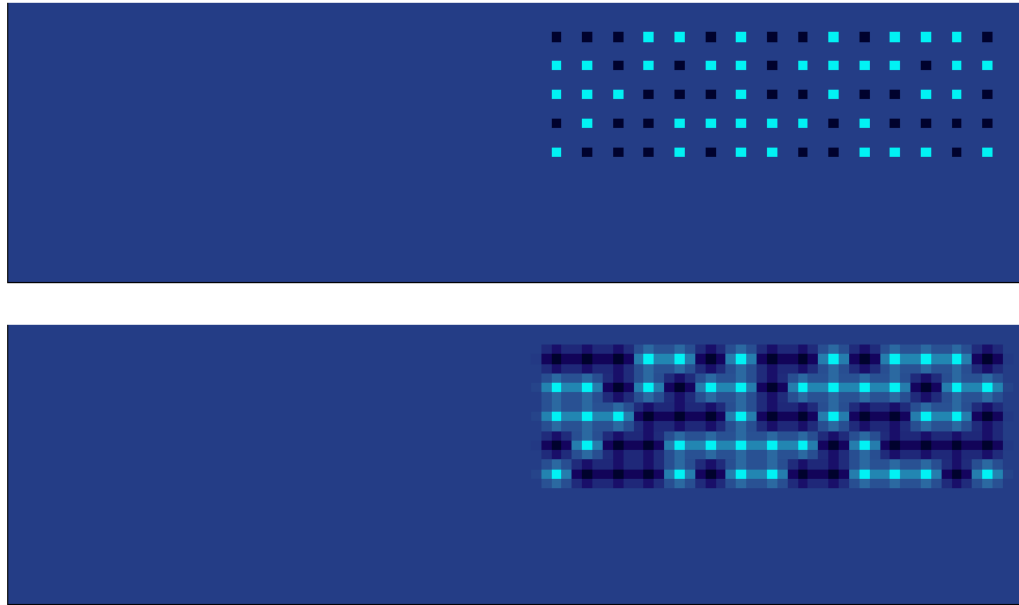


Figure 6.15: A single mask projection before (top) and after (bottom) smoothing using the Gaussian kernel.

smoothing using the Gaussian kernel.

## 6.5 Backprojection

With the pre-calculated projection matrices we can now take a segment of data and back project it quickly into an image. Back projection of coded aperture data is fairly straightforward since much of the work has been pre-calculated in order to save time during the reconstruction.

Back-projection is the process of projecting the ray from each detector element on the DA through each mask element using the pre-computed values described. Open mask elements project onto the imaging plane with a positive weight and closed mask elements project with a negative weight. Weights are determined by the number of



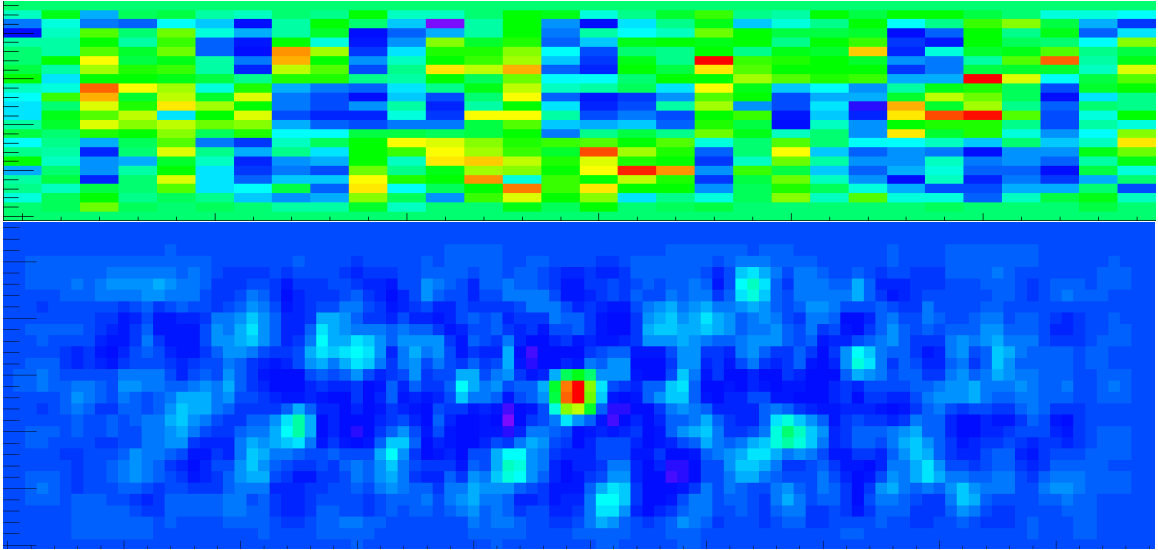


Figure 6.16: Example measured DA snapshot (top) and the associated back-projected coded aperture image (bottom) for a  $10\text{ mCi }^{137}\text{Cs}$  source at  $25\text{ m}$ . The image is formed from the overlap of mask projections from each of the 720 DA array elements. Both historical flat fielding and Gaussian smoothing have been applied to the image.

observed counts in the DA element. For example, if 1 of the 720 array elements has 54 counts, then image pixels get weighted with a value of 54 for open mask elements and -54 for closed mask elements. Figure 6.16 shows a measured DA snapshot (top) for  $^{137}\text{Cs}$  after historical flat fielding has been applied and the associated decoded image (bottom) with Gaussian smoothing applied. The image is for a  $10\text{ mCi }^{137}\text{Cs}$  source at 25 meters distance while the TMI was sitting stationary. Here, the coding is apparent on the array snapshot (top) however it is not until the array is decoded that the source becomes visible.

## 6.6 Summary

This chapter has shown that the TMI is capable of producing coded aperture reconstruction images using measured photon interaction information in the DA array.

Measurements are segmented to account for motion of the imager or source and divided into energy windows to reduce the overall background. Energy windowing was shown to provide an increase in image significance by a factor of 1.94 while reducing TTD by 22% and improving uncertainty in the reported location. Additionally, estimators of the background can be formed using multiple methods to account for the expected background within an energy window. Array flat fielding was shown to improve image significance by a factor of 1.8 while simultaneously reducing the location uncertainty by 53%. A method for fast decoding of measured snapshots was presented as well as a method of smoothing to account for uncertainties in the measurements.

## Chapter 7

# COMPTON IMAGING ALGORITHMS

Compton scatter imaging is a method of gamma-ray imaging that uses multiple position and energy measurements in coincidence to reconstruct the probable origin of the gamma-ray photon. The TMI is capable of Compton scatter imaging through the use of the array of NaI tiles in the CA array and the array of position sensitive NaI bars in the DA array. Unlike coded aperture imaging which requires only a single interaction in the DA array, Compton imaging requires a single interaction in both the CA and DA arrays in coincidence.

Figure 7.1 shows a sketch of the TMI for an example simulated Compton scattering event. Here a gamma-ray photon is emitted from the source, Compton scatters in the CA array and deposits its remaining energy in the DA array. Using the kinematics of Compton scattering the location of the source can be confined to a point on the cone (red). The location of a source on the event cone cannot be determined from a single event however the reconstruction of many cones will overlap at the true location of the source.

Sufficient information to reconstruct the event cone of a single incident gamma ray

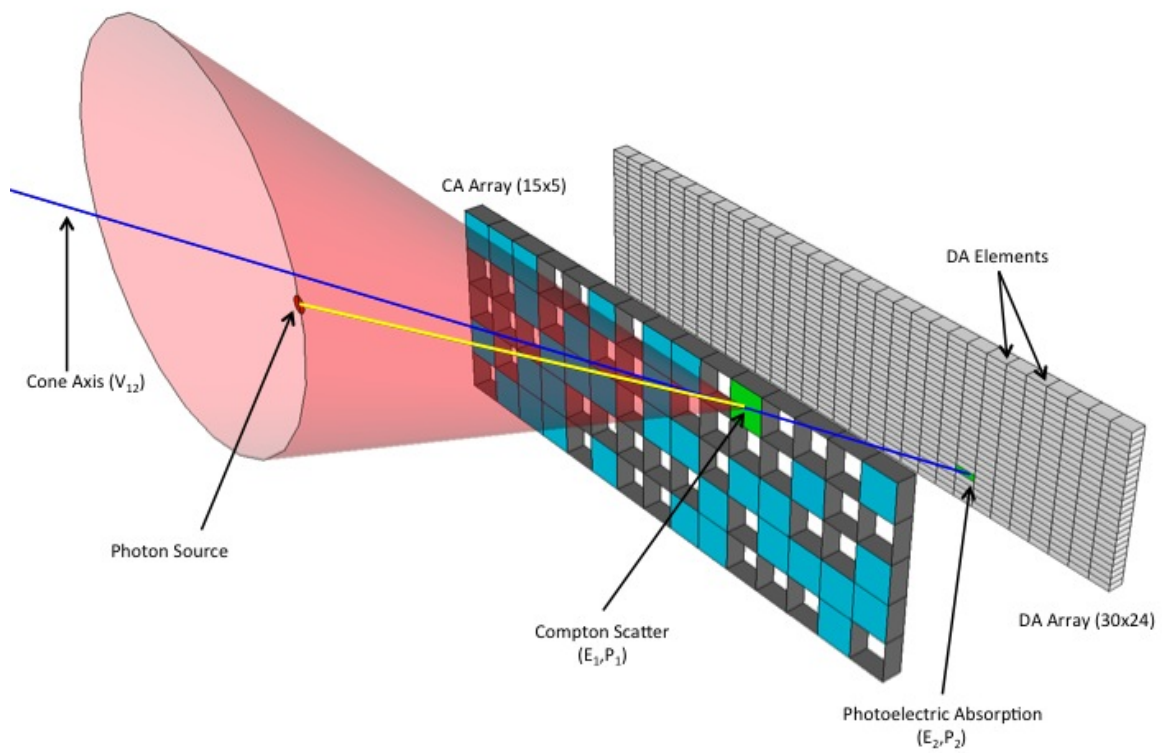


Figure 7.1: Diagram of the Compton imager integrated into the TMI.

can be deduced from a minimum of two position and energy measurements. The next step in the process of reconstruction is to generate an image based on information collected from many measured gamma rays. The measured distribution of a source will be the intersection of many Compton event cones. Imaging is heavily dependent on two factors: fidelity of the measured data and the qualities of the algorithm employed. Since the fidelity of the data is fixed for a given detector and increased fidelity translates to higher cost, improvements in the algorithms and how they are able to reconstruct the data is important.

## 7.1 Energy Windowing

A method of gamma-ray energy windowing was described in section 5.2. Similar to the spectroscopic and coded aperture algorithms, it is advantageous to the SNR to reconstruct an image from only those photons that would have come from a source of interest rather than producing a single image using all measured photons. Discretization of imaging through energy windowing also provides source identification as a source present in the window of a particular isotope definition implies the presence of that isotope.

By looking at a reconstruction of a point source using all measured photons, and only those in the energy window, the positive effects of energy windowing on Compton image reconstruction can be observed. Figure 7.2 shows the reconstructed Compton image without (top) and with (bottom) energy windowing applied around the 662 *keV* photo peak of  $^{137}\text{Cs}$ . The top image has a calculated significance of 2.74 and a location uncertainty of  $\pm 24.7$  *m*. The bottom image has a calculated significance of 3.81 and a location uncertainty of  $\pm 16.7$  *m*. The width of the energy

window has been optimized by analyzing the image significance as a function of window width as described in section 6.1. The value of  $1.5\sigma$  corresponds to the highest image significance by simultaneously reducing the number of background photons and maximizing source photons.

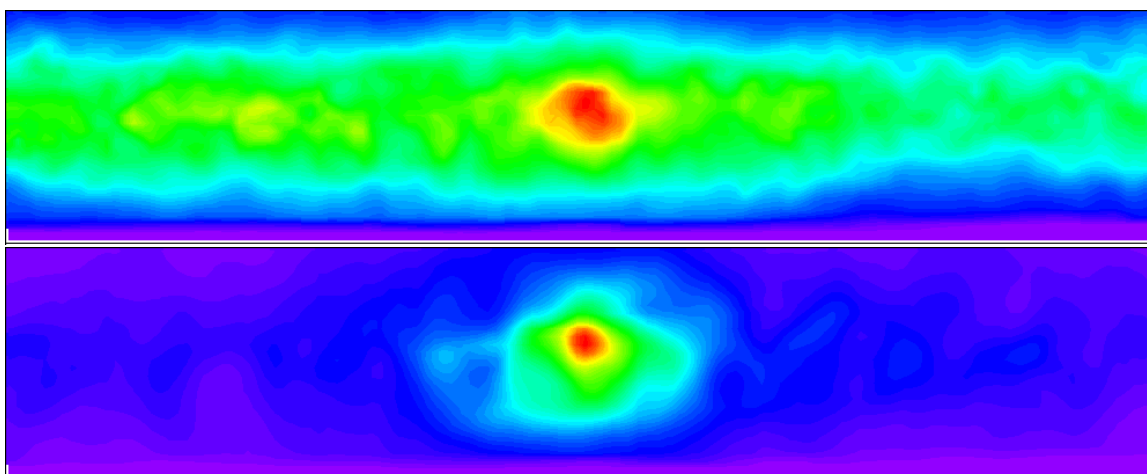


Figure 7.2: Example of energy windowing applied to Compton scatter image reconstruction. The top image does not have energy windowing applied and the bottom image does.

## 7.2 Data Segmentation

Similar to the data segmentation scheme presented for coded aperture in section 6.2, the Compton imaging algorithms aggregate all valid coincident interactions during a specified interval and reconstruct them into a gamma-ray image.

Since the TMI is a mobile system, segmented data must be correlated to the location of the truck. This is accomplished through the navigational subsystem. Each measured photon used in the Compton algorithms has been stamped with the GPS time and navigational information. Reconstruction is centered at the average location

and attitude of the event segment. Each event location is shifted based on the interaction locations within the TMI and the relative location of the truck with respect to the average segment location.

Figure 7.3 shows an example Compton event segment with 6 events. The average location between events is shown as a red square and the imaging FOV shown with red lines. The distance between the event location and the average can be calculated (blue stars) and is used to shift the interaction locations (green). Green lines show the correlation between CA and DA locations. The positive  $X$  direction is always aligned with the bearing of the segment average, as a result imaging planes are aligned parallel to  $X$ .

### 7.3 Back-projection

Back-projection may be performed in several ways, however in this work a geometric method will be presented because it is fast and accurate. Back-projection involves the reconstruction of a single Compton event sequence onto an imaging plane. The combination of many back-projected event sequences results in the formation of an image. In the geometric back-projection method the dot product definition will be used to solve for the intersection points of the event cone and the image pixel.

Begin by supposing that a photon scatters in the CA array at point  $P_1 (x_1, y_1, z_1)$  and photo-absorbs in the DA array at point  $P_2 (x_2, y_2, z_2)$ . Using event reconstruction, the estimated scattering angle  $\theta$  (Eq. 2.8) can be calculated. Also the uncertainty in the scattering angle  $\sigma_\theta$  can be estimated and will be shown in section 7.3.1. The event can then be represented as a cone projected into space from  $P_1$  with its central axis defined by the vector pointing from  $P_2$  to  $P_1$  ( $\vec{V}_{21}$ ) and opening angle described by  $\theta$

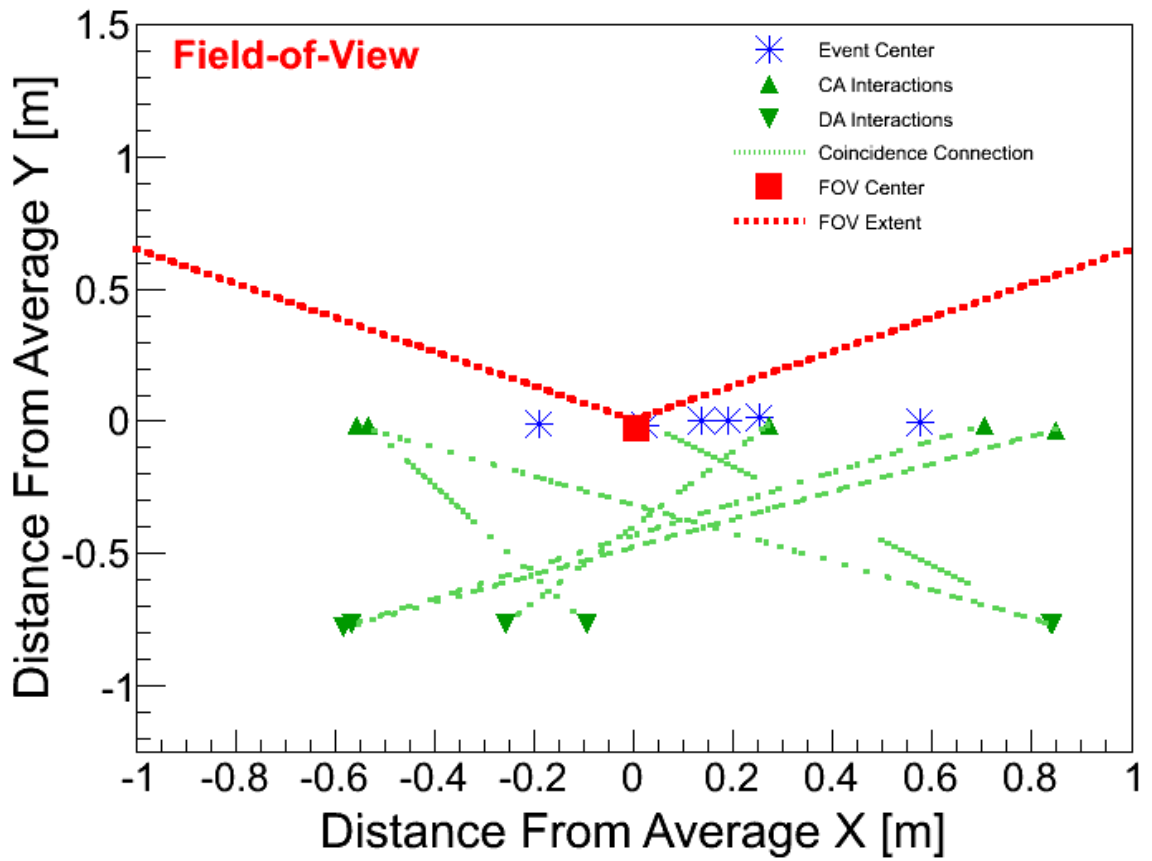


Figure 7.3: Example Compton event segment with the average calculated (red square) and the imaging FOV shown (red lines). The location of the TMI for each event is shown in blue and the interaction locations are shown in green.



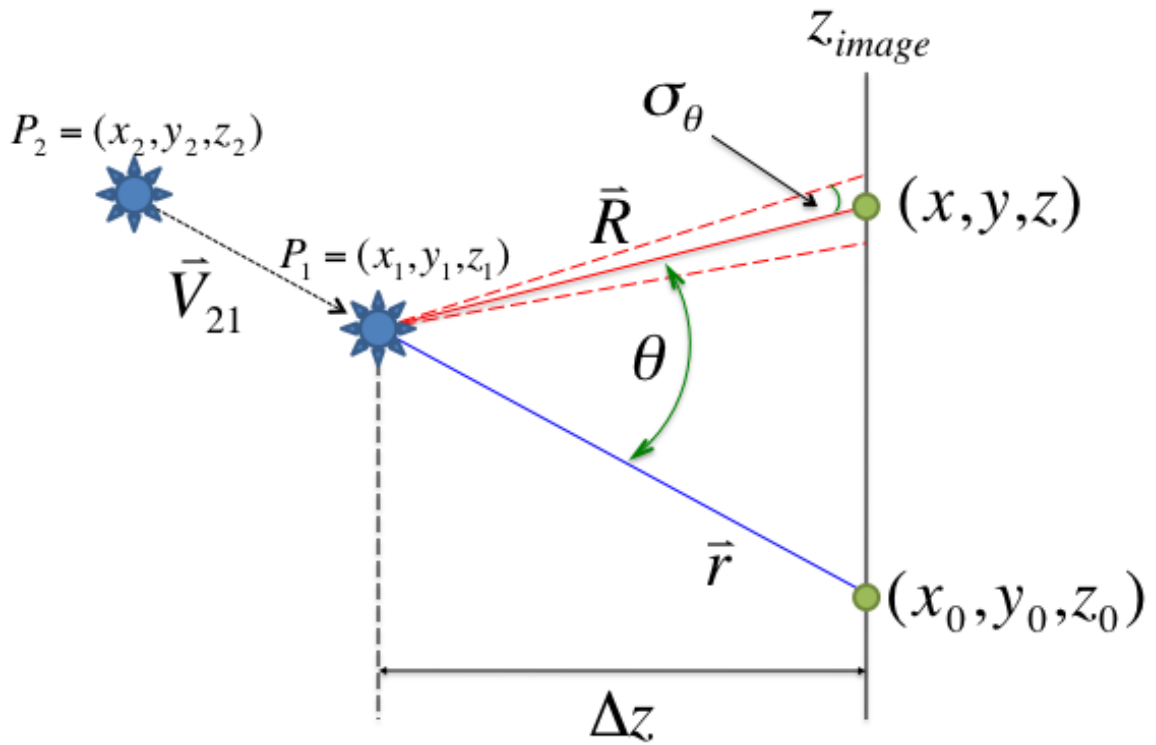


Figure 7.4: Back-projection of a single event sequence.

with a width corresponding to  $\sigma_\theta$ . Let  $\vec{r}$  represent the vector pointing from  $P_1$  along the cone axis to the imaging plane and let  $\vec{R}$  represent the vector pointing from  $P_1$  to the intersection point of the event cone and the imaging plane. Figure 7.4 shows the back-projection of a single Compton event sequence.

In order to define  $\vec{r}(x_0, y_0, z_0)$ , the intersection point of the cone axis and the imaging plane must be calculated. Note that the positions of  $x_0$ ,  $y_0$  and  $z_0$  represent the center of the image pixel. Larger pixel sizes will decrease the resolution of the image but also decrease reconstruction time; an important consideration for realtime processing. The calculation of  $\vec{r}$  is shown in Eqs. 7.1 - 7.3 where all coordinates used are shown in Fig. 7.4.

$$z_0 - z_1 = \Delta z \quad (7.1)$$

$$x_0 - x_1 = \frac{x_1 - x_2}{z_1 - z_2} \Delta z \quad (7.2)$$

$$y_0 - y_1 = \frac{y_1 - y_2}{z_1 - z_2} \Delta z \quad (7.3)$$

The back-projection method described here uses the definition of a dot product (7.4) to solve for the intersection of the reconstructed Compton cone and a point in space. Squaring and transposing (7.4) yields (7.5) where the unknown variables of the intersection points ( $x, y, z$  from Fig. 7.4) for a given event sequence can be obtained by finding the roots.

$$\vec{r} \cdot \vec{R} = |\vec{r}| |\vec{R}| \cos \theta \quad (7.4)$$

$$(\vec{r} \cdot \vec{R})^2 - r^2 R^2 \cos^2 \theta = 0 \quad (7.5)$$

Note from Fig. 7.4 that  $z_0 = z = z_{image}$ . If  $z$  is selected as the imaging plane and  $y$  is known by selecting a row in the image, then  $x$  is the only unknown in the equation. By turning (7.5) into a second order polynomial function of  $x$  (7.6), then  $x$  can be solved using the quadratic formula (7.7). The coefficients of  $x$  are given in Eqs. 7.8 - 7.10. If the discriminant of (7.7) (*i.e.*  $b^2 - 4ac$ ) is less than zero it means the cone does not intersect the imaging plane for the selected values of  $y$  and  $z$ .

$$ax^2 + bx + c = 0 \quad (7.6)$$

$$x = \frac{-b \pm \sqrt{b^2 - 4ac}}{2a} \quad (7.7)$$

$$a = x_0^2 - r^2 \cos^2 \theta \quad (7.8)$$

$$b = 2(x_0 y_0 y + x_0 z^2) \quad (7.9)$$

$$c = y_0^2 y^2 + 2y_0 y z^2 + z^4 - r^2(y^2 + z^2) \cos^2 \theta \quad (7.10)$$

For any given value of  $y$  at a specific  $z$  the outside and inside edges of the cone (in  $x$ ) can be calculated using  $\sigma_\theta$  and  $\theta$ . Pixels between the edges of the cone are filled with weighted values. The result is an event circle scribed onto the imaging plane properly weighted with a width consistent with the limits of the detector.

### 7.3.1 Angular Uncertainty

Calculation of the scattering angle alone leads to a thin cone of probability, however the scattering angle has uncertainty associated with it. By including uncertainty in the scattering angle during event reconstruction the cone is given width. By including the width of the cone in reconstruction, the true source distribution can be more accurately described and the imaging algorithms will have a better chance to reconstruct the data correctly. Angular resolution depends on several factors including Doppler broadening, energy, and position resolution. Doppler broadening represents the lower

limit of angular resolution. Even if the energy and position are known exactly, it is not possible to know the initial momentum of the electron in the scattering medium. Energy and position resolution are known as they are functions of the detector geometry and materials and their contributions to the angular uncertainty can be calculated for each recorded event sequence.

### Energy Contribution

Due to the fact that no detector material has the ability to perfectly resolve the energy deposited, there is uncertainty in calculated scattering angle due to finite energy resolution. As with position uncertainty, the energy resolution of the detector system contributes to the reconstructed event uncertainty. The energy resolution function of NaI was given in Fig. 5.3 from section 5.2. Equations 7.11 through 7.17 show the calculation of the energy resolution contribution to angular uncertainty given the known uncertainty in the energy measurements ( $\sigma_{E_1, E_2}$ ).

$$x = 1 + \frac{m_e c^2}{E_1 + E_2} - \frac{m_e c^2}{E_2} \quad (7.11)$$

$$\theta = \cos^{-1} x \quad (7.12)$$

$$\frac{\partial x}{\partial E_1} = -\frac{m_e c^2}{(E_1 + E_2)^2} \quad (7.13)$$

$$\frac{\partial x}{\partial E_2} = \frac{m_e c^2}{E_2^2} - \frac{m_e c^2}{(E_1 + E_2)^2} \quad (7.14)$$

$$\frac{\partial \theta}{\partial x} = \frac{-1}{\sqrt{1-x^2}} \quad (7.15)$$

$$\frac{\partial \theta}{\partial E_{1,2}} = \frac{\partial \theta}{\partial x} \frac{\partial x}{\partial E_{1,2}} \quad (7.16)$$

$$\sigma_{\theta,energy} = \sqrt{\left(\frac{\partial \theta}{\partial E_1} \sigma_{E_1}\right)^2 + \left(\frac{\partial \theta}{\partial E_2} \sigma_{E_2}\right)^2} \quad (7.17)$$

### 7.3.2 Cone Weighting

The intersection pixels  $j$  of the cone for event  $i$  are weighted based on several factors including the width, circumference and the slant of the cone. Weighting the cones is a way to accurately model the information recorded within the event and serves to smooth the images based on measurements.

In order to account for the width of the cone wall for event  $i$ , each pixel  $j$  intersected by the cone is weighted according to a Gaussian centered at  $\theta_i$  with a width of  $\sigma_{\theta_i}$ . The formula is shown in (7.18) where  $\theta_i$  is the computed Compton scattering angle for event  $i$  and  $\theta_j$  is what the scattering angle would be if the gamma ray originated from pixel  $j$ .

$$W_{ij,width} = \exp\left[-\left(\frac{\theta_i - \theta_j}{2\sigma_{\theta}}\right)^2\right] \quad (7.18)$$

The weight for the circumference of the event circle ( $W_{ij,circ}$ ), is obtained by dividing the weight by  $\theta_i$ . This comes from the fact that larger scattering angles result in greater cone circumferences. The weight due to the slant of the cone ( $W_{ij,slant}$ ), is accounted for by multiplying by  $\cos^3 \theta_{\vec{R}}$  where  $\theta_{\vec{R}}$  is the polar angle of  $\vec{R}$ . One power

of the cosine term comes from the slant angle of the image area with respect to the event cone and two powers come from the inverse square law. The total weight  $W_{ij}$  of each pixel in the reconstructed event cone is given by the product of all the weights for that pixel (7.19). Figure 7.5 shows a single event cone projected onto an imaging plane at 50 m from a Compton scatter interaction in the CA array followed by an absorption in the DA array.

$$W_{ij} = (W_{ij,width})(W_{ij,circ})(W_{ij,slant}) \quad (7.19)$$

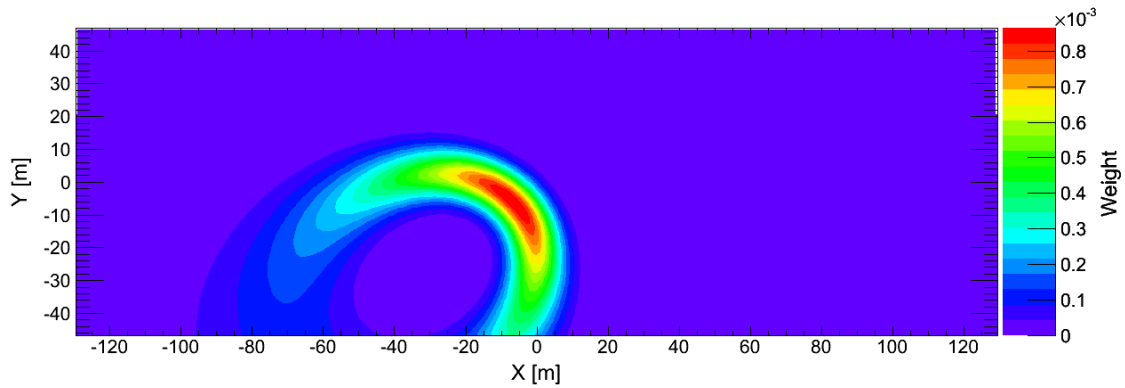


Figure 7.5: A single event cone projected onto the imaging plane at  $z=50m$ .

## 7.4 Background Suppression

It has been shown in section 7.1 that energy windowing can reduce the overall background present in a reconstructed image, however there still exists the background within the energy window itself. Similar to coded aperture array flat fielding, background suppression can be used to approximate and remove the contribution from NORM background in the image. Since NORM background is randomly incident on the detector system the reconstructed image will tend to reproduce the Point Spread

Function (PSF) of the imager. Compton imaging differs from coded aperture imaging in that it acts on the reconstructed image rather than the measured count distribution on the back-plane. As a result an estimator of the background must be calculated for each imaging plane that is being processed.

The suppression algorithm takes an estimator of the shape of the PSF (from measurements), scales it to the counts of the reconstruction and subtracts it from the image. Equation 7.20 shows the calculation of the scaling factor ( $\lambda$ ), where  $(S + B)$  is the reconstructed image (with background),  $\mathbb{B}$  is the expected background image and  $\sigma_i^2$  is the value of the  $i^{th}$  image pixel of each. In this equation the background estimator is scaled to the integral number of counts in each image. The scaling factor may be determined by either image counts (variance) or by the time elapsed, however scaling by time does not accurately account for changes in the background count rates as a function of location.

$$\lambda = \frac{\sum \sigma_i^2}{\sum_{\mathbb{B}_i} \sigma_i^2} \quad (7.20)$$

Equation (7.21) shows the calculation of the expected Compton image,  $\mathbb{S}$ , after subtracting the scaled background estimator. In the case of purely background counts, the value of  $\mathbb{S}$  should fluctuate normally around zero counts if the value of  $\mathbb{B}$  is an accurate estimator of the background.

$$\mathbb{S} = (S + B) - \lambda \mathbb{B} \quad (7.21)$$

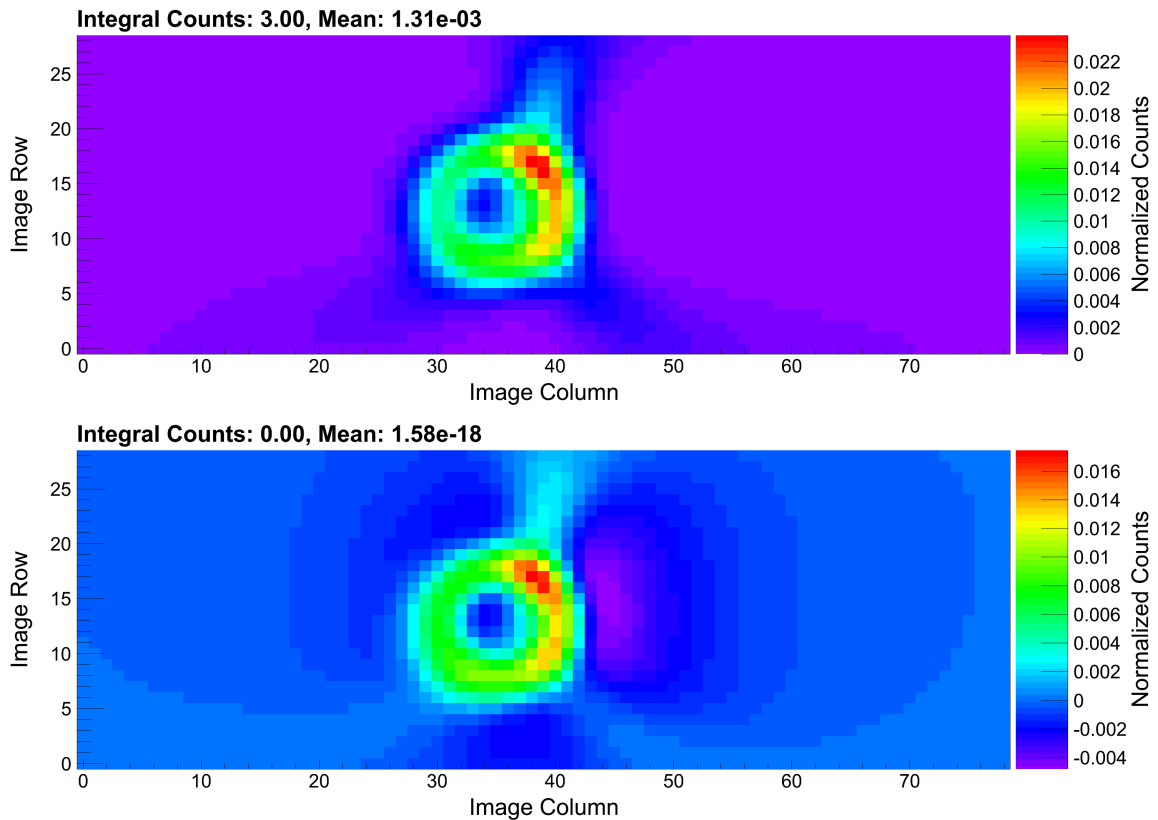


Figure 7.6: Example reconstructed Compton scatter image of 3 events before (top) and after background suppression (bottom). There is no source present in the image.

Figure 7.6 shows the result of subtracting the background estimator from a single reconstructed Compton scatter image at 50  $m$ , formed by 3 measured events. In Fig. 7.6, 2 of the 3 events have a large scattering angle compared to the third so they are less apparent due to cone weighting. Here it can be seen that the estimator is doing a good job, the integral of the image has been reduced to 0 counts as expected and the mean has been reduced to essentially 0 indicating the estimator is describing the PSF well. This method of background suppression can be performed using historical data or in real-time.

Figure 7.7 shows the results of Compton background suppression for a measured



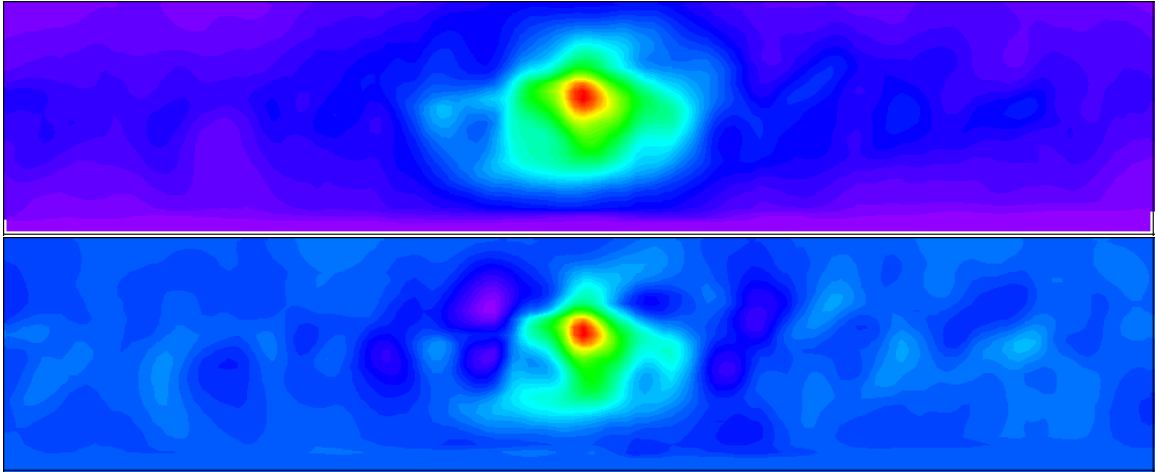


Figure 7.7: Example runs past a source without (top) and with (bottom) background suppression applied.

run past a  $0.5 \text{ mCi}$ ,  $^{137}\text{Cs}$  source at  $25 \text{ m}$  DCA and  $15 \text{ mph}$ . The top image does not have background suppression applied; the calculated significance of the source is  $3.81$  with a location uncertainty of  $\pm 16.7 \text{ m}$ . The bottom image has background suppression applied; the calculated significance of the source is  $4.57$  with a location uncertainty of  $\pm 7.5 \text{ m}$ .

#### 7.4.1 Realtime Corrections

Realtime (RT) background suppression is performed by aggregating image weights during a measurement in each reconstructed Compton image in order to get an estimate of the shape of the distribution or PSF. This aggregation can be performed on the basis of time elapsed or gross counts. Once the aggregate image has met a certain criteria such as a pre-defined time interval the counts are added to the background estimator. Figure 7.8 shows the background estimator as a function of time, at each successive update of the estimator becomes more complete. The current algo-

rithms update the estimator every 2 seconds when in time-based mode and 13 meters in motion-based mode. The three estimators shown in Fig. 7.8 are after 9 (top), 100 (middle) and 131 (bottom) measured events covering approximately 90 seconds. After each update the estimate of the background improves.

The advantage of RT suppression includes the ability to account for rapid changes to the electronic noise. For example, if multiple detector element begins to trigger on noise in the middle of a run and generate false coincidences, the background estimator will incorporate the increased rate of those channel combinations and effectively subtract off the effect. Disadvantages of RT corrections include its susceptibility to the incorporation of real, or nuisance sources, in the estimator, reducing the sensitivity of the system. Also, RT corrections cannot be used effectively in a stationary CONOPS because any source in the FOV will potentially become part of the estimator template and get subtracted out of the reconstructed image – making it invisible to the system.

#### 7.4.2 Historical Corrections

Another method of background estimation is to use historical approximations. This method makes use of an estimator constructed from the combination many reconstructed Compton images over the entire period of a background collection, or training set. Additional work is required to ensure that any real or nuisance source are removed from the training set.

When the TMI processes data using historical corrections, a new estimator is also aggregated, which can be used to supplement the historical data or form a new background estimator for future scans of the same area. Figure 7.9 shows the background history for the  $^{137}\text{Cs}$  energy window. This estimator was formed using over

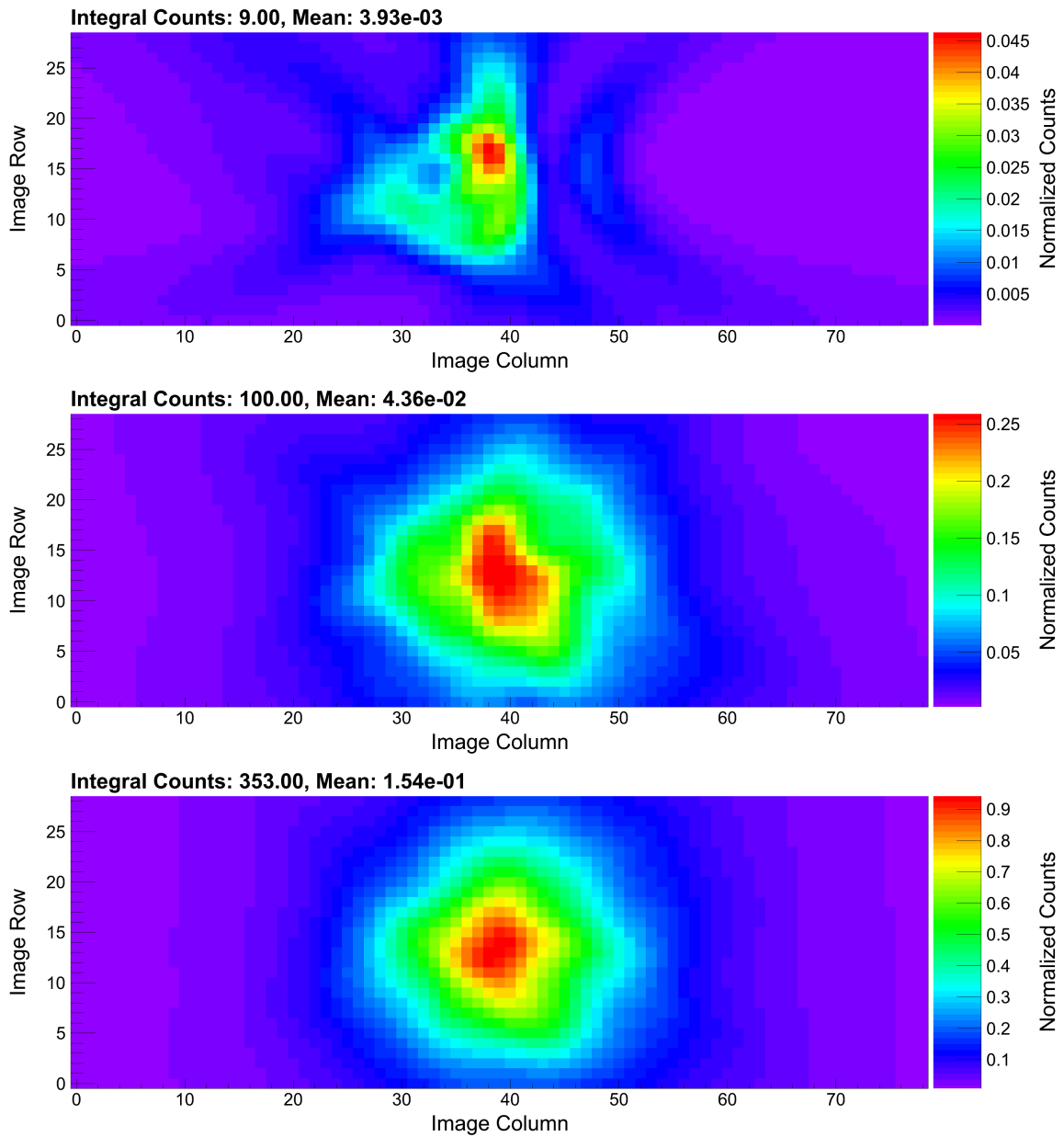


Figure 7.8: On-the-fly Compton flat field estimator for  $^{137}\text{Cs}$ . As time progresses the flat field estimator improves and adjusts to the current sensitivity of the system. The three estimators shown include 9 events (top), 100 events (middle) and 131 events (bottom).

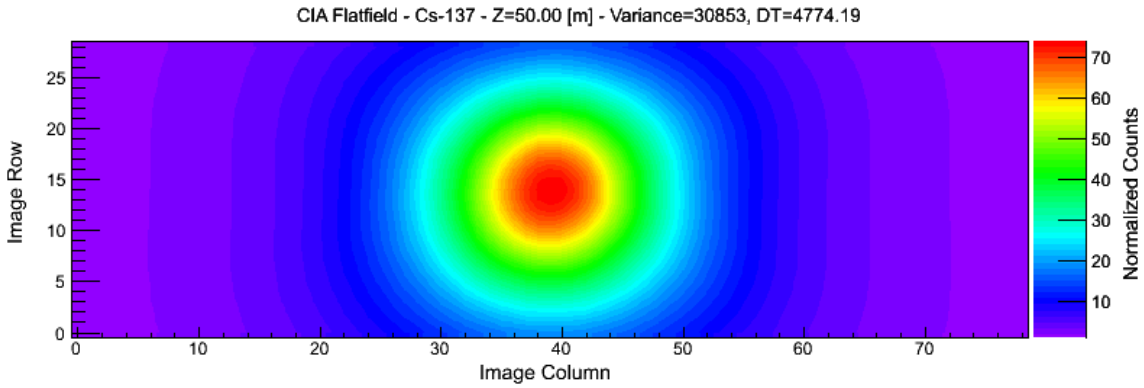


Figure 7.9: Historical background estimator for  $^{137}\text{Cs}$  at 50 meters. The flat field history was aggregated over 4774 seconds of background data including 30,000 measured photons.

4774 seconds of background including over 30,000 measured photons.

The shape of the PSF arises from the angular sensitivity of the imager. Since Compton scattering is more probable at small scattering angles [40], and range to the image for off-axis pixels is increasing, the estimator is approaching a 2D cosine distribution that scales with detection efficiency.

## 7.5 Summary

This chapter has shown that the TMI is capable of producing Compton scatter reconstruction images using measured photon interactions in the CA and DA arrays. A detailed description of the Compton scatter reconstruction algorithm was given as well as calculations to approximate the uncertainty in measurements. Measurements are segmented to account for motion of the imager or source and divided into energy windows to reduce the overall background. Energy windowing has been shown to improve image significance by a factor of 1.4 and reduce localization uncertainty by 32%. Additionally, estimators of the background can be formed using multiple methods to

account for the expected background within an energy window. The background suppression technique demonstrated improvements of a factor of 1.2 in image significance and a 55% reduction in localization uncertainty. By combining energy windowing and background suppression Compton reconstruction significance is improved by a factor of 1.7 while reducing the localization uncertainty by 70%. With the details of the ROI, coded aperture and Compton imaging algorithms complete, the next chapters will describe the current methods used to combine all available data and quantify the performance of the system as a whole.

## Chapter 8

# MOBILE/HYBRID ALGORITHMS

The coded aperture and Compton imaging algorithms implemented on the TMI have been discussed in chapters 6 and 7. Additionally, a simple ROI spectroscopic algorithm was discussed in chapter 5. So far the imaging algorithms have been used to reconstruct gamma-ray images given a set of measured events at a single location. However, since the TMI is a mobile system the imaging algorithms must be adapted to function in a dynamic environment. Also, a robust method to generate hybrid images through fusion of coded aperture and Compton data is needed, as well as a method to combine imaging and non-imaging modalities.

### 8.1 Image Registration

So far imaging algorithms have focused on reconstruction of a gamma-ray image from a single segment of events localized in time and space. A mobile imaging system, such as the TMI, requires means for aggregation of imaging information, shifted by location, such that all individual snapshot images are registered in the same reference frame so they accumulate as the imager moves. Since static reconstructions are geo-

located (from the average navigational information), a method of aggregation has been developed such that a single large image is generated from the overlap of many static images.

Figure 8.1 illustrates the image registration for the coded aperture imaging planes, however the process is identical for all image types. Each image (1-5) has an associated geographic location. The static images are aligned based on pixel size, and distance traveled such that an aggregate image is formed from the overlap of all reconstructed images. The cumulative world image keeps track of multiple pieces of information including the exposure time, pixel locations, and weighted values for each pixel.

The aggregate image continues to expand as incoming data generates additional static images. Aggregate images are capable of handling slight variations in bearing however, once the TMI changes bearing more than 45 degrees (configurable) a new world image is started. Registration and aggregation of image data is performed for each imaging modality (CA/CI) as well as the fusion of both (FUS) at multiple distances, for each isotope definition (energy window).

When searching for sources of interest in the aggregate images, geo-location for pixels of interest is established through information carried along in the world image. Each aggregate image is referenced geographically to the first element inserted. Since image pixel sizes are known, the location of each individual pixel can be calculated. When a pixel has a significance that is above a set threshold, the location of that pixel is calculated and reported as the location of the source in geographic coordinates. Additionally, the image peak is fit with a 2D gaussian function to estimate uncertainty in the location.

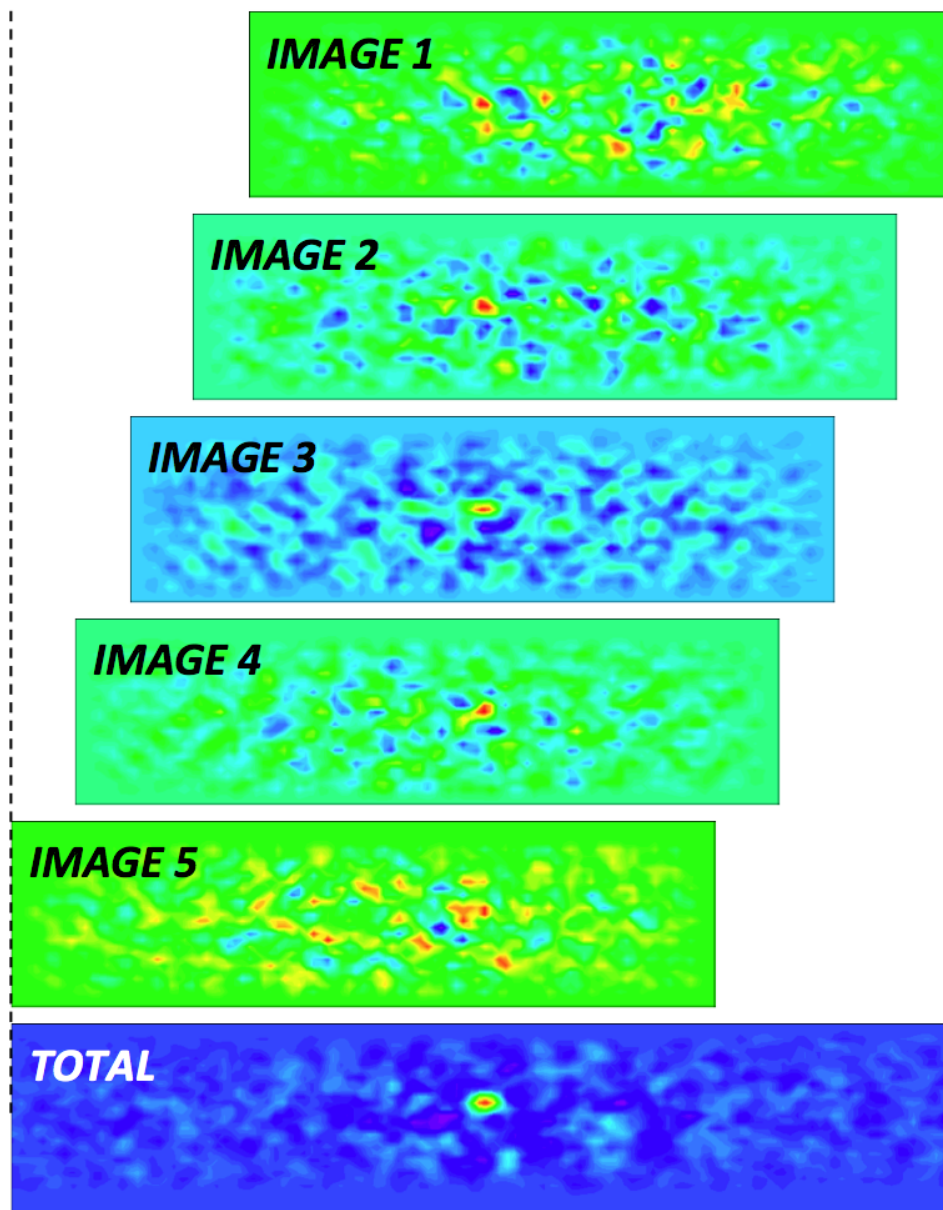


Figure 8.1: Example image registration for the coded aperture imaging planes. Each image has an associated geographic location and can be aligned in the algorithms such that an aggregate image is formed from the overlap of all reconstructed images.



## 8.2 Distance Determination

Aggregate coded aperture, Compton scatter and hybrid images are constructed as described in the previous section for each imaging modality, isotope definition and reconstruction distance. Typically the TMI is operated with 14 imaging planes, from as close as 5 out to 100 *m* and beyond. The TMI also performs imaging simultaneously for over 20 isotope definitions at each imaging distance and for each modality.

As the distance to a source of gamma-ray radiation increases, incident photons become essentially parallel. Sources at farther distances move through the FOV of the imager more slowly than those closer to the detector. This effect, known as parallax, has been used in astronomy to determine the distance to objects in space as viewed from multiple points along Earth's orbit [53]. Since the TMI is a mobile system parallax can be used to determine the location of a source when viewed from several different angles. By moving past a source, multiple snapshot images constructively form a stronger image at the actual distance and blur at incorrect distances. Figure 8.2 illustrates how the TMI is able to localize a source through motion. The dashed lines represent the ray of highest pixel intensity through the image at each point. As the imager moves past a source the rays will intersect in a common region, revealing the source location.

## 8.3 Image Fusion

Hybrid gamma-ray imaging is the combination of multiple modes of imaging. It has already been shown that by using an active mask for the coded aperture array the TMI can capture Compton scatter events and veto background coded aperture events, pro-

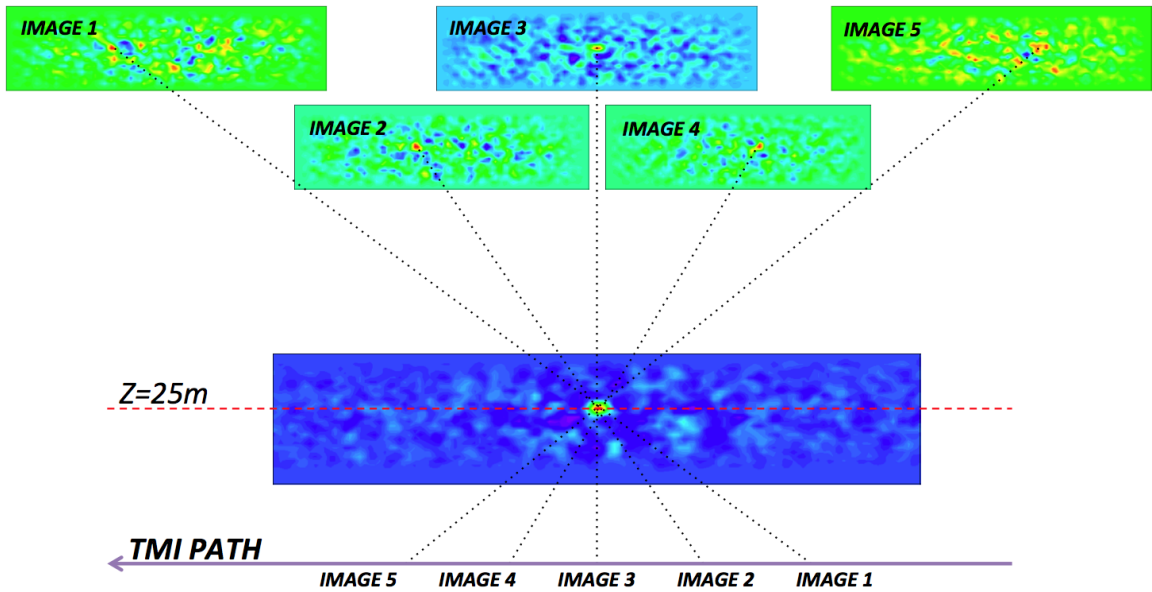


Figure 8.2:

viding multiple orthogonal imaging modalities. Images are combined through a multiplicative fusion of pixel data. Because of the nature of coded aperture and Compton imaging to reconstruct background differently but sources the same, this method acts as an *AND* gate on pixel data. For a pixel in the fused image to be considered significant, there must be increased counts in both reconstructed coded aperture and Compton reconstructions. Equations 8.1-8.3 show the calculations performed during the fusion of modalities where  $\sigma^2(i, j)_{FUS}$  is the total number of measurements contributing to the value of pixel  $(i, j)$  from the coded aperture and Compton scatter images,  $\Delta T(i, j)_{FUS}$  is the average exposure time of fused image pixel  $(i, j)$ ,  $\lambda(i, j)_{CIA_k}$  is the weight in pixel  $(i, j)$  of the Compton scatter image from the  $k^{th}$  Compton snapshot,  $\lambda(i, j)_{CAA_k}$  is the weight in pixel  $(i, j)$  of the coded aperture image from the  $k^{th}$  coded aperture snapshot and  $\lambda(i, j)_{FUS}$  is the fused weight of pixel  $(i, j)$ .

$$\sigma^2(i, j)_{FUS} = \sigma^2(i, j)_{CIA} + \sigma^2(i, j)_{CAA} \quad (8.1)$$

$$\Delta T(i, j)_{FUS} = \left( \frac{T(i, j)_{CIA_{max}} + T(i, j)_{CAA_{max}}}{2} \right) - \left( \frac{T(i, j)_{CIA_{min}} + T(i, j)_{CAA_{max}}}{2} \right) \quad (8.2)$$

$$\lambda(i, j)_{FUS} = \sum_k \lambda(i, j)_{CIA_k} \sum_k \lambda(i, j)_{CAA_k} \quad (8.3)$$

Coded aperture and Compton pixel data can be combined in many different ways using various statistical techniques from scaled addition, maximum likelihood, multiplication, etc. Here, multiplicative fusion has been chosen because it provides the best performance in background rejection over all methods tested. In the chapter on future work (13) there will be a discussion of improvements that could be made to the fusion algorithm.

Figure 8.3 shows an example coded aperture (top), Compton scatter (middle) and hybrid image (bottom) from the reconstruction of a 0.5 *mCi*, <sup>137</sup>Cs source at 25 *m* DCA and 15 *mph*. The coded aperture and Compton images are registered in the same geographic coordinates and can therefore be fused to cancel background and improve source reconstruction. The purple pixels in the image indicate a very low observed count rate and the red pixels (source) indicate a high count rate. The coded aperture image has a calculated significance of 9.51 with localization uncertainty of  $\pm 2.4$  *m*. The Compton scatter image has a calculated significance of 4.57 with localization uncertainty of  $\pm 7.5$  *m*. The hybrid image (bottom) has a much higher calculated

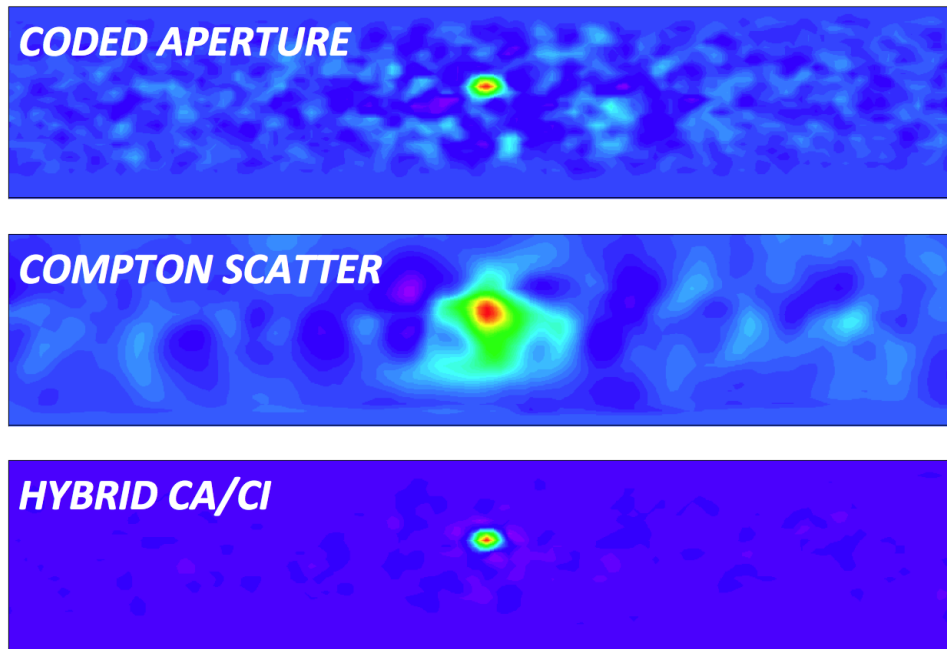


Figure 8.3: Example hybrid CA/CI image of a  $0.5 \text{ mCi}$ ,  $^{137}\text{Cs}$  source at  $25 \text{ m}$  DCA and  $15 \text{ mph}$ . The coded aperture and Compton images are registered in the same geographic coordinates and can therefore be fused to cancel background and improve source reconstruction.

significance of 35.88 with localization uncertainty of  $\pm 2.2 \text{ m}$ .

In Fig. 8.3 both the coded aperture and Compton scatter images demonstrate the source location (red pixels) however there is some residual background noise present in the images even after energy windowing and background suppression. The fused image however takes advantage of the differences in the reconstruction of background for each imaging modality and the agreement of source localization. Source pixels get amplified and background remains small. The resulting hybrid image has a much better SNR and therefore higher probability of detection and lower false alarm rate for the same activity source. Results of the fusion performance will be given in chapter 11.

## 8.4 Non-imaging Fusion

Since the TMI has both imaging and non-imaging capabilities, a method for improving sensitivity using all available information has been implemented. The ROI algorithms in chapter 5 calculate the significance value for each energy spectrum that is analyzed. Additionally, image pixels of interest have an associated significance. The method for combining imaging and non-imaging information is simple, the significances are added together. Candidate image pixels have a calculated significance and know the location of the TMI as a function of time. The non-imaging (ROI) significance calculated is retrieved for the location nearest the candidate image pixel. Equation 8.4 shows the calculation of the total significance ( $I_{TOT}$ ) through the combination of the fused image and the spectroscopic ROI algorithms. This method is effective since a simultaneous rise in the imaging and non-imaging significance is not expected unless there is a true source in the FOV. There are many methods of combining multiple sources of data, however this method was chosen because it makes the largest overall improvement to sensitivity of the TMI.

$$I_{TOT} = I_{ROI} + I_{FUS} \quad (8.4)$$

## 8.5 Alarm Triggering

An alarm trigger calculation is performed whenever new data has been processed by the algorithms and added to the world image. For the ROI algorithm the calculated value of significance is compared to a threshold value for each measured spectrum. If the calculated significance for a particular isotope is above a set threshold (adjustable)

the detection and identification are reported to the operator along with the location of the TMI at the time of the measurement. Reconstructed gamma-ray images are added to the aggregate image for each isotope and distance as the TMI moves along. At the end of processing a particular data segment the triggering algorithm will analyze all pixel data in the world images to calculate the significance of the highest intensity pixels in the image, for each isotope across all distances and modalities (coded aperture, Compton scatter and hybrid).

Selection of intense pixels is based on the measured weights in the image. Candidate trigger pixels (by distance and isotope) are stored for comparison to newly acquired pixels. Each imaging plane (distance, modality, and isotope) can have a single bright pixel in the FOV, per trigger scan. If the location of the newly acquired pixel is within a single pixel of the stored candidate pixel, the persistence time of the candidate peak is incremented, otherwise the newly acquired pixel becomes the candidate peak and the persistence time is reset to zero.

In the event a real source is present in the image it will persist for some length of time, usually across multiple trigger scans, depending on the speed of the TMI. Once the candidate peak list has been updated with the latest information, persistence time is checked to ensure alarming does not occur on a bright pixel that has been in the FOV for a fraction of a second. Persistence time cuts are distance dependent as a source at 100 meters is expected to remain in the FOV for a longer period of time than a source at 10 meters, given a constant velocity. Figure 8.4 shows the minimum time required for a candidate imaging pixel to persist before the triggering system will allow it to generate an alarm.

Once it has been decided by the triggering algorithm that the peak has persisted

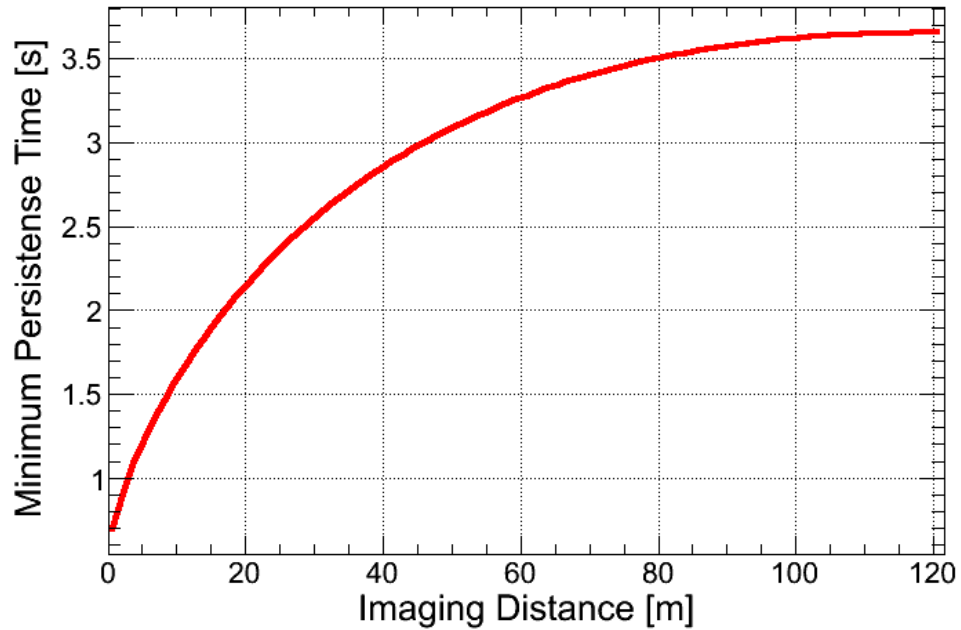


Figure 8.4: Minimum persistence time required as a function of imaging distance for a candidate imaging peak to trigger an alarm.

long enough in the image the significance of that pixel value is calculated. Significance is calculated by looking at the reconstructed signal in the image and how the background fluctuates around it. This provides a uniform and stable method for selecting a trigger threshold. First, the signal region is averaged within  $R = 1.5\sigma$  of the candidate pixel based on the expected shape of a true source distribution. Next, the background region is averaged between  $R = 2\sigma$  and  $R = 9\sigma$  of the candidate pixel and the standard deviation is calculated. The SNR, or significance of the candidate peak is then calculated as shown in Eq. 8.5. Figure 8.5 shows the regions used in a sample trigger calculation. If the calculated significance of any pixel (in all images) using Eq. 8.5 is above threshold an alarm is generated with the isotope identified (by the alarming image plane) and the location of the image pixel in geographic coordinates

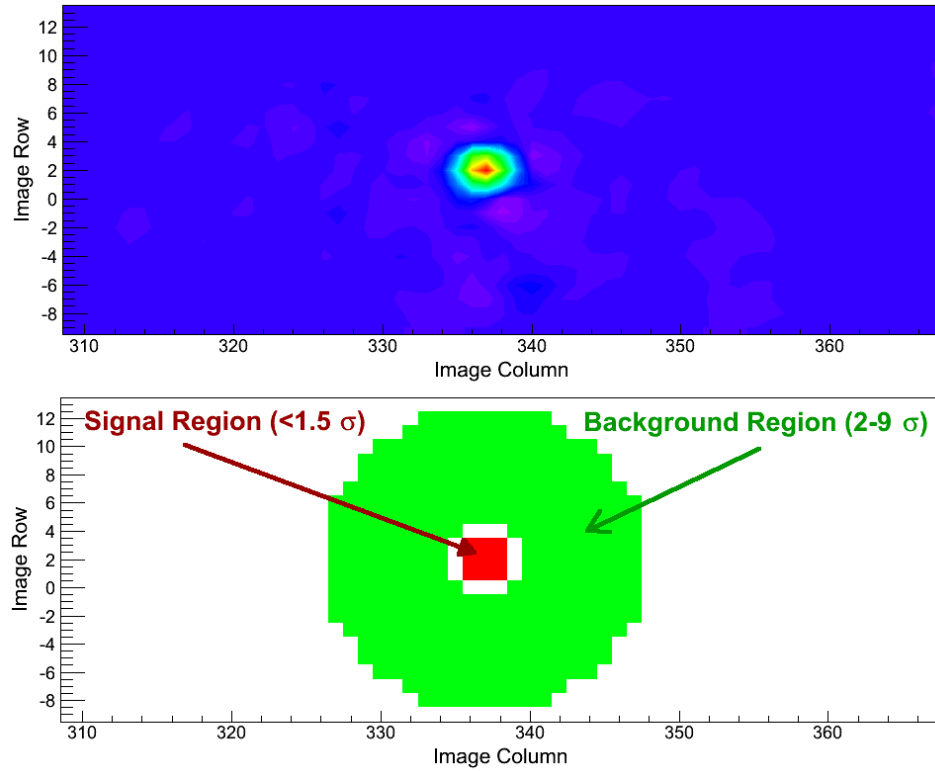


Figure 8.5: Candidate peak (top) and signal (red) and background (green) regions used in the calculation of image significance (bottom).

with uncertainty.

$$SNR = \frac{(S + B)|_0^{1.5\sigma} - \bar{B}|_0^{9\sigma}}{\sigma_B} \quad (8.5)$$

Only pixel data that has changed since the last trigger scan is considered for alarming. Additionally, the triggering rate is controlled by the operator. For example image data is added to the aggregate depending on data segmentation rate, which could happen as often as 5 times per second. It may not be desirable computationally



or realistically to check for an alarm that often. The operator of the system can select the interval on which data are checked, which ties directly into the probability of false alarm by defining the false alarm rate. A discussion of threshold selection will be presented in chapter 11.

## 8.6 Summary

In this chapter a method for handling reconstructed images from a moving platform has been shown such that many static images can be summed into a single aggregate image. The implemented algorithms are capable of creating an arbitrarily long image that contains the sum image of all individual reconstructions. Additionally it was shown that images from coded aperture and Compton scatter reconstructions can be combined in a way that promotes the source intensity while minimizing the background due to the orthogonal nature of the background manifestations. The fusion of coded aperture and Compton data was shown to dramatically increase the SNR for a point source while reducing the reported location uncertainty. Also, a method for combining imaging and non-imaging data has been presented which adds additional suppression of calculated significance to help reduce the false alarm rate and boost the probability of detection overall. Each of the algorithms presented so far can trigger the system independently or combined.

## Chapter 9

# BACKGROUND CHARACTERIZATION

Earth is naturally radioactive including over 60 radionuclides varying from primordial to cosmogenic and human produced. The various contributions are highly variable both in elemental composition and isotopic concentration based on multiple factors including, but not limited to, location, time and weather. It is important to thoroughly characterize the observed background from NORM so that the effect on the detection algorithms can be quantified.

In this chapter a method for qualitative characterization of NORM background based on the derived component fractions of expected materials is presented. Once characterized through this analysis, the background can be grouped by similar components using a clustering algorithm. Measured data falling into each of the defined clusters can then be used to quantify the effect on the detection algorithms. Chapter 10 presents a method of data injection which uses the results of this characterization to produce data to study the effect of varied NORM background on source detection.

## 9.1 Primary Components

There are three dominant components to NORM background in most areas. These components result from the radioactive decay of the primordial nuclides potassium-40 ( $^{40}\text{K}$ ), uranium-238 ( $^{238}\text{U}$ ) and thorium-232 ( $^{232}\text{Th}$ ). The half-life of  $^{40}\text{K}$  is 1.277 billion years with a simple decay scheme producing a single gamma-ray line at 1460.8  $keV$ . Similarly,  $^{238}\text{U}$  and  $^{232}\text{Th}$  have long half-lives, 4.468 and 14.05 billion years respectively, however they exhibit very complex decay schemes with many daughter nuclei which produce a variety of gamma-ray lines as they decay to a stable isotope of lead.

As a result of the emissions from the decay products, the NORM background energy spectrum is cluttered with gamma-ray lines and continuum energies with very few spectral features. In order to characterize background features by exploiting the energy resolution of the detector system, it is necessary to select those features which identify each of the principle components without difficulty. Figure 9.1 shows the complete decay series (chain) from the three principle components  $^{40}\text{K}$  (bottom-left),  $^{238}\text{U}$  (top),  $^{232}\text{Th}$  (bottom-right).

The radioactive decay of  $^{40}\text{K}$  is straightforward and results in a stable isotope of calcium ( $^{40}\text{Ca}$ ) or argon ( $^{40}\text{Ar}$ ) with a single decay (red boxes), however  $^{238}\text{U}$  and  $^{232}\text{Th}$  are complex with many daughter nuclei in the chain before reaching stable lead;  $^{206}\text{Pb}$  and  $^{208}\text{Pb}$  respectively. In Fig. 9.1 alpha decay ( $\alpha$ ) is denoted by a blue arrow, beta decay ( $\beta^-$ ) by a red arrow and electron capture ( $\epsilon$ ) by a green arrow.

Each of the decays shown are usually accompanied by the release of energetic gamma-ray photons (sometimes many). The daughter nuclei with the strongest, relative, gamma-ray branching ratios ( $BR$ ) are shown with blue boxes;  $^{214}\text{Bi}$  (1764.5  $keV$

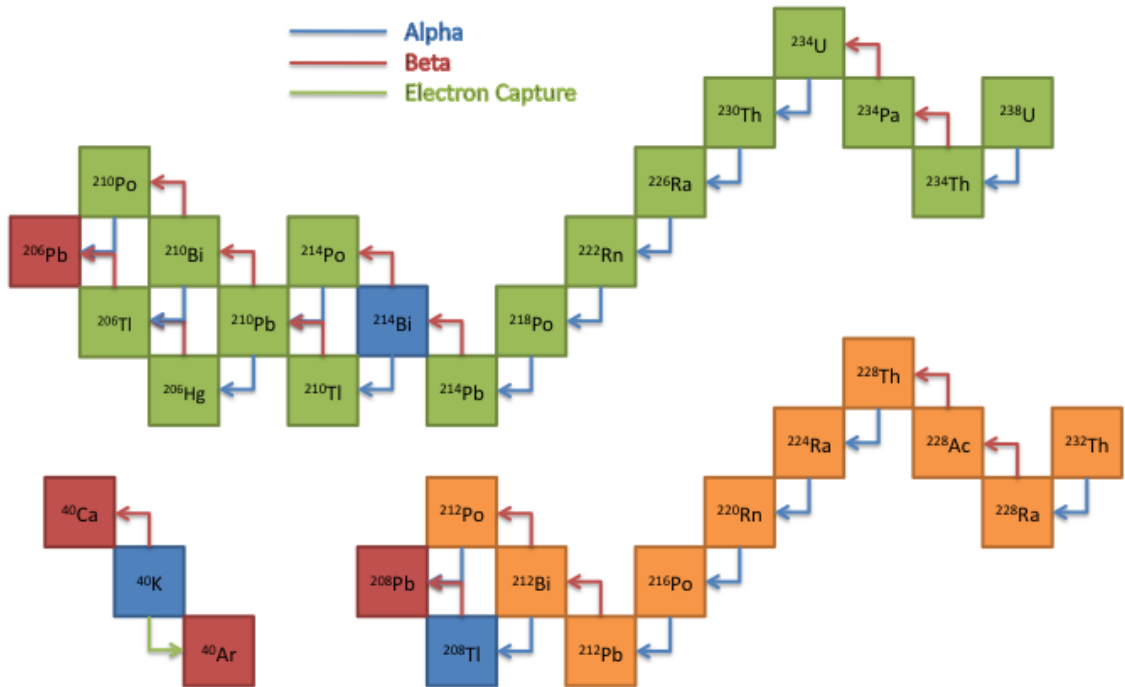


Figure 9.1: Complete decay chains for the principle NORM background components  $^{238}\text{U}$  (top),  $^{232}\text{Th}$  (bottom-right) and  $^{40}\text{K}$  (bottom-left). Alpha decays are shown with blue arrows, beta and electron capture are shown with red and green arrows respectively. The daughter nuclei with the most easily characterizable lines are shown in blue ( $^{40}\text{K}$ ,  $^{208}\text{Tl}$ ,  $^{214}\text{Bi}$ ).

-  $BR=0.15$ ) for the uranium series,  $^{208}\text{Tl}$  ( $2614.5\text{ keV}$  -  $BR=0.14$ ) for the thorium series and  $^{40}\text{K}$  ( $1460.8\text{ keV}$  -  $BR=0.11$ ) for potassium. These are the lines that will be used for the background segmentation and characterization.

## 9.2 NORM Variations

Variations in NORM background are caused by the distribution of radioactive material in the Earth and in surrounding materials. Primordial nuclides include long-lived isotopes such as uranium-238, uranium-235, thorium-232, radium-226, radon-222 and

potassium-40. Cosmogenic sources are those produced by reactions between high energy cosmic particles interacting in Earth's atmosphere. Cosmogenic sources can be short lived and include carbon-14, tritium ( $^3\text{H}$ ) and beryllium-7. Human produced nuclides are those produced for medical treatments, through above ground nuclear weapons testing and by fission power reactors. Figures 9.2, 9.3 and 9.4 show the naturally occurring concentrations for  $^{40}\text{K}$ ,  $^{232}\text{Th}$  and  $^{238}\text{U}$ , respectively throughout the continental United States as mapped by the United States Geological Survey (USGS). In addition to the variable concentration in the soil, construction materials (*e.g.* bricks, concrete, granite, asphalt, and steel) have various amounts of radioactivity due to raw materials used in their production. For example, an urban environment might have granite statues or brick sidewalks, a bridge may be constructed from a certain type of steel or a tunnel may have used a particular type of concrete, each with very different characteristics. Also, changes in weather, such as rain or snow can cause elevated levels of  $^{222}\text{Rn}$  as it gets deposited onto surfaces from the atmosphere, temporarily altering the background profile.

### 9.3 Background Measurements

In order to characterize NORM background, extensive measurements were taken in February of 2012. The TMI surveyed the Washington D.C. area and the route to the Boston, MA area. The primary focus of this collection was to increase the quantity of background data available for characterization purposes. The data collection included many varied background conditions such as urban, rural, suburban, tunnels, and bridges.

Figure 9.5 shows the path of the TMI for a section of the data collection starting in

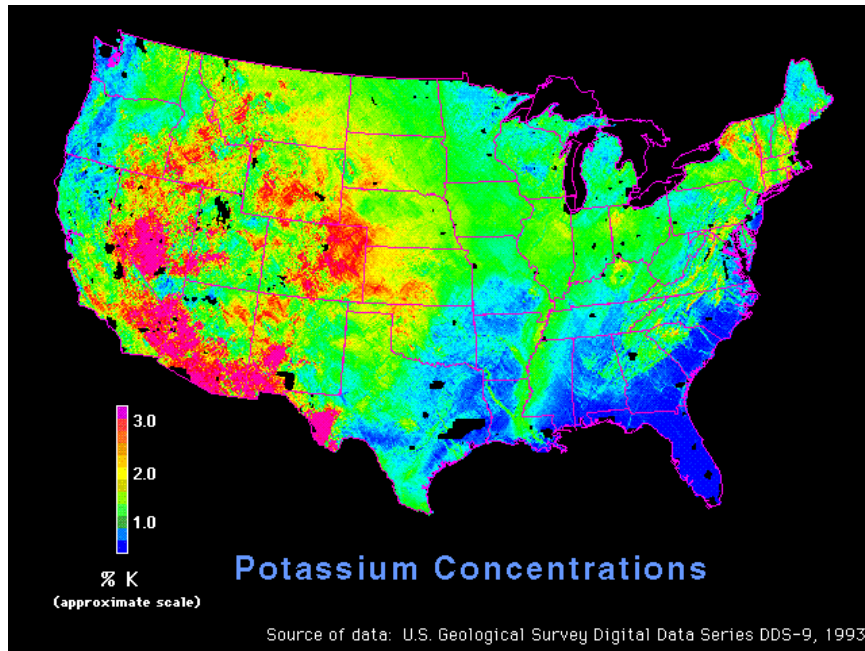


Figure 9.2: Naturally occurring potassium-40 concentration throughout the continental United States as mapped by the United State Geological Survey (USGS).

the Washington D.C. area, ending outside Philadelphia, PA. Background data were collected over four days totaling approximately 20 hours of data. From Fig. 9.5 it can be seen that the TMI covered a wide variety of terrain in order to observe large variations in the background.

NORM background from these regions can vary (or not) substantially both temporally and spatially. This background characterization effort aimed to qualitatively identify several main classifications of background in order to determine the effect on the detection algorithms. Once complete, the background measurements will be segmented into the constituent classes and used to quantify the expected response of the TMI to each.

The first step in this process is to perform component analysis of the representative

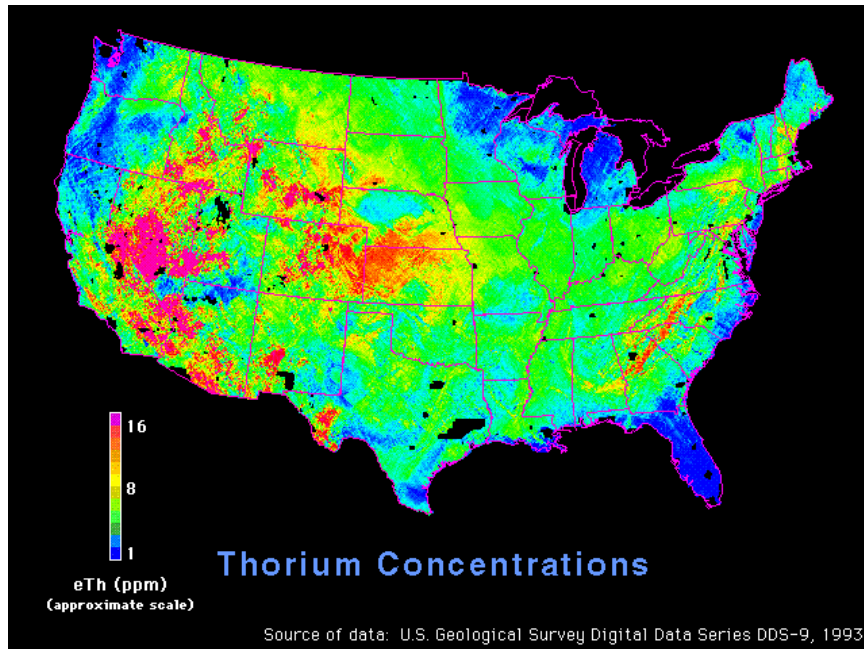


Figure 9.3: Naturally occurring thorium-232 concentration throughout the continental United States as mapped by the United State Geological Survey (USGS).

spectral features observed in NORM background and define the classification scheme.

## 9.4 Component Analysis

There are three main elemental components to NORM background that will be used in this characterization: potassium (K), uranium (U) and thorium (Th). This type of characterization is sometimes referred to as KUT analysis [54]. Background gamma-ray data are sometimes characterized by the relative concentrations of these elements through quantitative analysis of the strongest spectral (energy) lines produced from the decay products of those primary NORM components [49, 55, 56].

The first step in the component analysis process is the selection of commonly observed gamma-ray lines in order to characterize the composition of the local back-

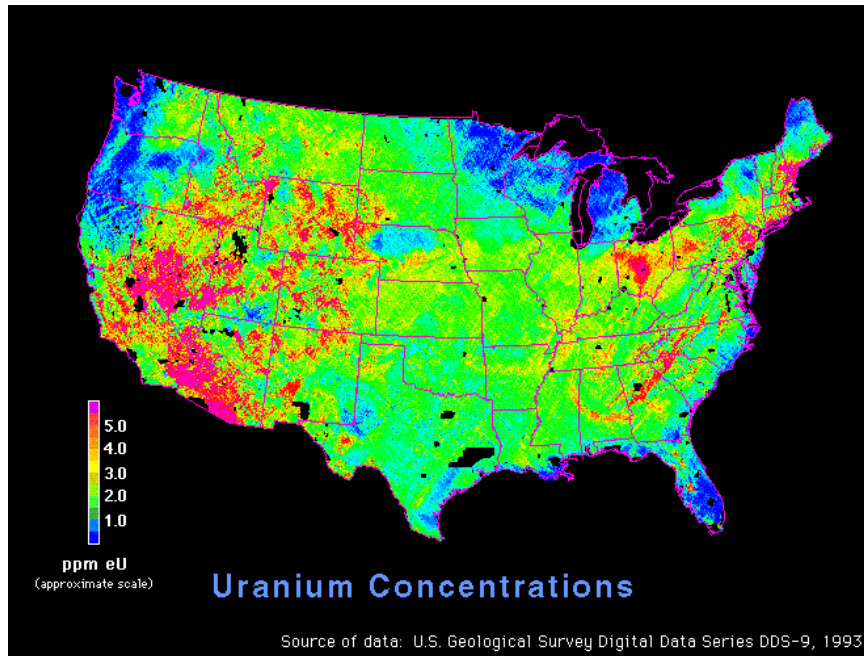


Figure 9.4: Naturally occurring uranium-238 concentration throughout the continental United States as mapped by the United State Geological Survey (USGS).

ground. For example,  $^{40}\text{K}$  has a relatively strong  $1460.8\text{ keV}$  gamma-ray emission resulting from the electron capture ( $\epsilon$ ) decay to  $^{40}\text{Ar}$ . Figure 9.6 shows the complete decay scheme of  $^{40}\text{K}$ . The decay schemes of the other U and Th isotopes have been omitted because they are extremely complex and include thousands of gamma-ray emissions from daughter nuclei, however they result from similar processes. A description of the radioactive decay processes which produce gamma-rays is given in section 2.2.

The  $1460\text{ keV}$  spectral feature of  $^{40}\text{K}$  is a secondary result of the electron capture ( $\epsilon$ ) decay of  $^{40}\text{K}$  to the first excited state of  $^{40}\text{Ar}$  and subsequent gamma-ray emission resulting from the transition to ground state. The primary decay mode for  $^{40}\text{K}$  is beta decay ( $\beta^-$ ) to stable  $^{40}\text{Ca}$  with a branching ratio of 0.8925.





Figure 9.5: Path of the TMI during the background collect in February 2012. The path of the imager is shown with a red line starting in Washington D.C. and ending this segment near Philadelphia, PA.

This decay does not produce any gamma-ray emission, however there is a gamma-ray photon produced in the electron capture decay ( $BR_{\epsilon}=0.1055$ ) to the first excited state ( $E = 1460.8 \text{ keV}$ ) of  $^{40}\text{Ar}$ . When the argon nucleus transitions from the first excited state to the ground state the energy difference between that states is released in the form of an energetic photon; this is the source of the observed background spectral feature.

The prominence of the  $^{40}\text{K}$  line is due to the high emission probability (11%) and the fact that there are no other gamma-ray lines associated with the decay of the potassium component of NORM background. Table 9.1 summarizes the characteristic lines used in the component analysis where the dominant isotope from each decay

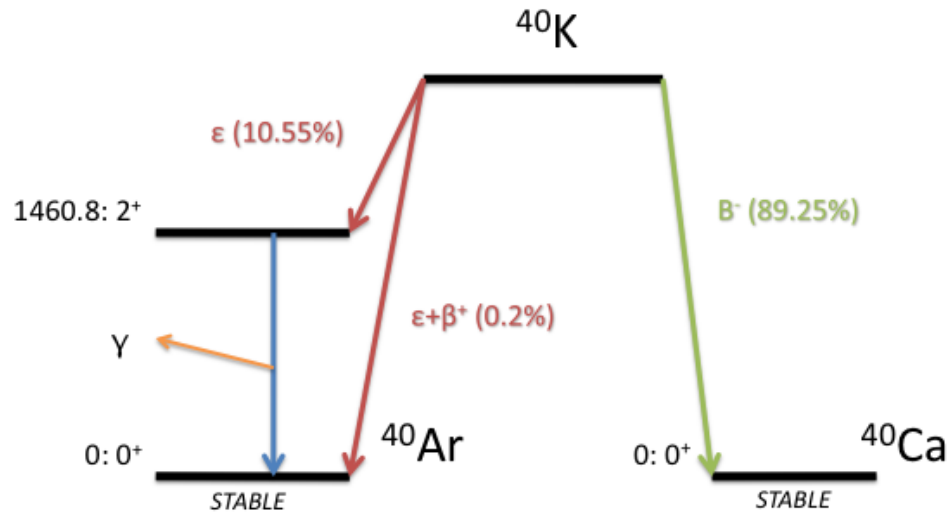


Figure 9.6: Level diagram for the decay of  $^{40}\text{K}$ . The primary decay mode is beta decay to stable  $^{40}\text{Ca}$ , however the electron capture decay and transition to stable  $^{40}\text{Ar}$  is the source of the gamma-ray background feature at 1460 keV.

Table 9.1: Background component peak regions used during the background component analysis.

Component	Identifier	Dominant Isotope	$E_c$ (keV)
$^{40}\text{K}$	K	$^{40}\text{K}$	1460.00
$^{238}\text{U}$	U	$^{214}\text{Bi}$	1764.00
$^{232}\text{Th}$	T	$^{208}\text{Tl}$	2614.00

chain (K/U/T) is shown along with the gamma-ray line centroid ( $E_c$ ) in keV. Figure 9.7 shows the three energy regions from Table 9.1 used for analysis overlaid on a measured energy spectrum.

Measured energy spectra will be fit using a combined Gaussian and exponential parametric fit. The fit uses a least squares minimization to determine the optimal parameters [57].

An exponential fit is used to account for the continuum background measured

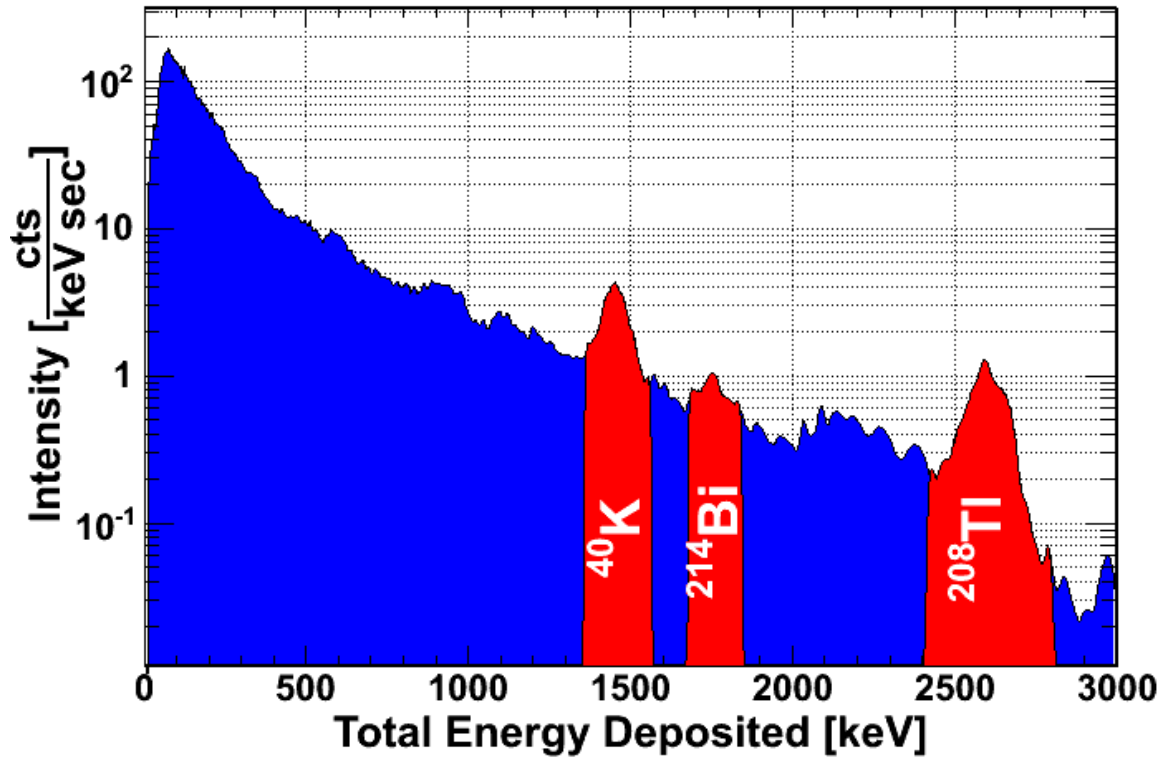


Figure 9.7: Energy spectrum regions used for component analysis on a 5 second aggregate background total energy spectrum. The three red areas increasing in energy show the energy regions for <sup>40</sup>K (1460 keV), <sup>214</sup>Bi (1764 keV) and <sup>208</sup>Tl (2614 keV), respectively.

in the detector from incomplete collection of energy either in the detector material itself or resulting from scattering in ambient materials (*e.g.* soil or concrete). The formula used for the fit is shown in equation 9.1. In the fitting function,  $f(E)$ ,  $P_0$  is the normalized amplitude of the gamma-ray peak ( $\frac{\gamma}{keVsec}$ ),  $P_1$  is the known photon energy in  $keV$ ,  $P_2$  is the expected width of the gamma-ray peak distribution ( $keV$ ) as measured by the detector, and  $P_3$  and  $P_4$  are the amplitude and decay constant of the background continuum.  $E(t)$  is the measured energy spectrum where  $t$  has been evaluated on some interval  $t_0$  to  $t_1$ . This fit is seeded and constrained using prior knowledge of the detector system and the known location (energy) of the peaks in order to ensure accurate fitting.

$$f(E)|_{t_0}^{t_1} = P_0 e^{-\frac{1}{2} \left[ \frac{(E(t)-P_1)}{P_2} \right]^2} + P_3 e^{-P_4 E(t)} \quad (9.1)$$

The respective concentrations will be estimated from the integral counts of the Gaussian only component of the fits. This method assumes that the isotopes have reached an equilibrium state, which is a good assumption since the earth was formed many years ago. Each of the component integrals are divided by the total (numerical) integral of the energy spectrum up to 3000  $keV$  in order to remove the dependence on total count rate.

Equation 9.2 gives the equation for the calculation of the component fraction basis estimators where  $F_{KUT}$  is the estimated fraction of K/U/T,  $t_0$  and  $t_1$  are the upper and lower time limits, in seconds, for the energy spectrum  $S(E, T)$  measured by the detector system.  $P_{0,1,2}$  are the results from the fit obtained from equation 9.1. To ensure adequate statistics for peak fitting the integral duration ( $t_1 - t_0$ ) is

5.0 seconds. This represents a compromise between the ability to distinguish rapid changes in the background characteristics and the ability of the algorithms to fit the defined peaks adequately. Figure 9.8 shows an example fit to measured data of the three selected background features where the fit results from (9.1) are shown with red lines,  $S(E, T)$  is shown in blue for a 5 second aggregation, and the fit results of the photopeak region are shown with green lines.

$$F_{KUT} = \frac{\int_{t_0}^{t_1} \int_0^{3000} P_0 e^{-\frac{1}{2} \left[ \frac{(E(t)-P_1)}{P_2} \right]^2} dEdT}{\int_{t_0}^{t_1} \int_0^{3000} S(E, T) dEdT} \quad (9.2)$$

## 9.5 Clustering Analysis

Once component analysis has been applied to reduce the data down to three dimensions (*i.e.* K/U/T), the next step is to use a clustering algorithm to make unsupervised decisions about the natural grouping of the measured data. This will allow for unbiased, qualitative classification of background characteristics without associating measurements to specific geographic regions or locations. Both manual (by eye) and unsupervised algorithms were tested and it was decided to use an unsupervised K-means clustering algorithm as it is fast and automated producing essentially the same result. A description of the algorithm and the results of the clustering follow in section 9.5.1.

Figure 9.9 shows the component fraction derived from the fits defined for each 5 seconds of data throughout the entire 20 hour data set. The  $^{40}\text{K}$  fraction versus the  $^{214}\text{Bi}$  fraction is shown in the top left,  $^{40}\text{K}$  versus  $^{208}\text{Tl}$  in the top right and the  $^{214}\text{Bi}$  versus  $^{208}\text{Tl}$  on the bottom. It can be seen from this figure that there is variation

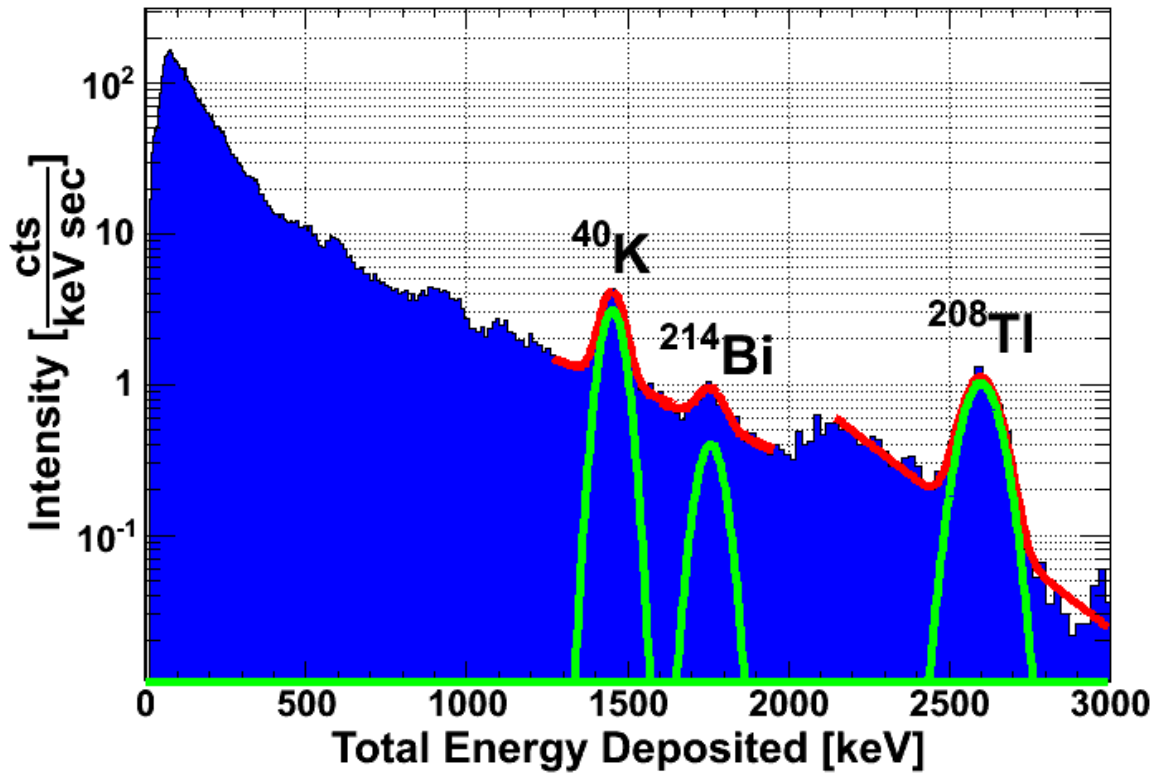


Figure 9.8: Example fit to background component regions using a Gaussian + exponential fit. The component fractions are characterized by the ratio of the integral of the green (Gaussian only) fit curves to the total integral of the spectrum.

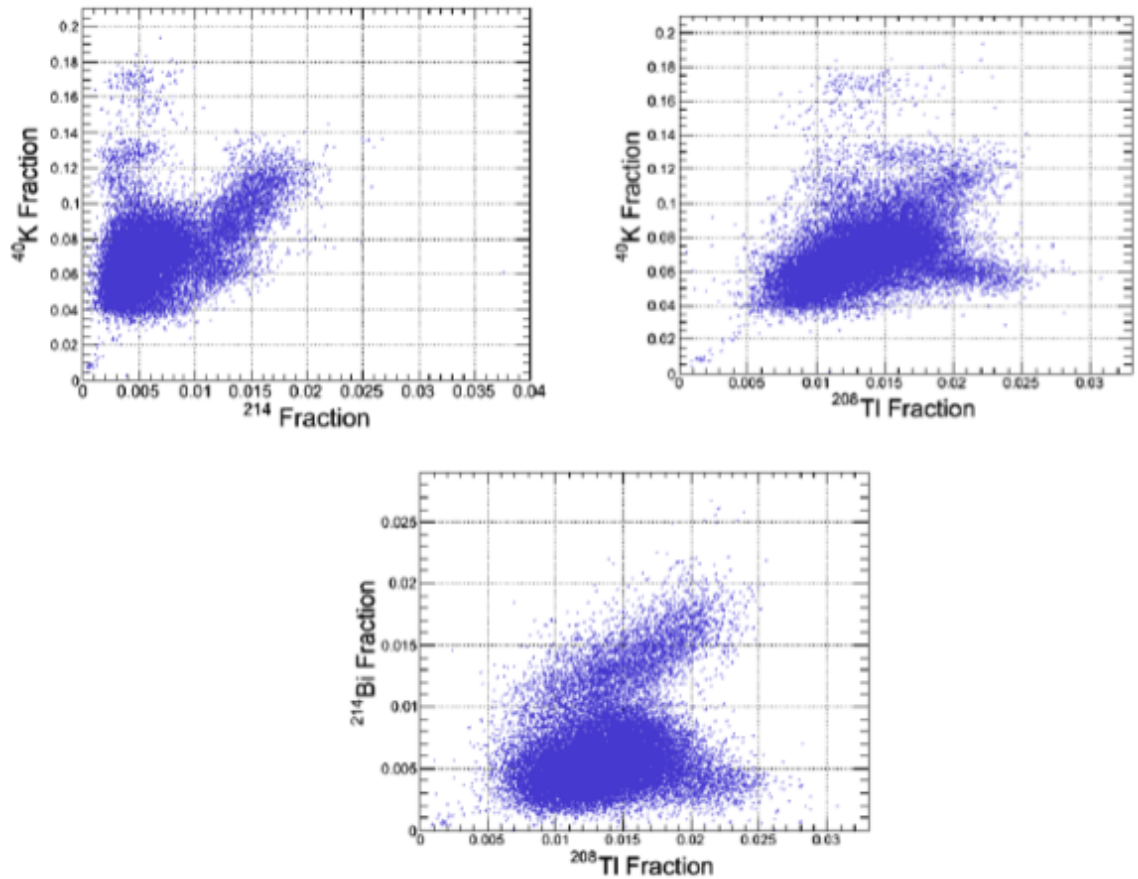


Figure 9.9: Results of fitting each 5 second spectrum for the entire 20 hour data set. The  $^{40}\text{K}$  fraction versus the  $^{214}\text{Bi}$  fraction is shown in the top left,  $^{40}\text{K}$  versus  $^{208}\text{Tl}$  in the top right and the  $^{214}\text{Bi}$  versus  $^{208}\text{Tl}$  on the bottom.

between all three components. The next step in the analysis will be to cluster these data into distinct groups using a K-means clustering algorithm.

### 9.5.1 K-Means Clustering

The algorithm chosen for this effort was a K-means clustering algorithm [58–61]. K-means clustering is a variance based clustering algorithm. Given a set of  $k$  points in about  $d$  centers, the mean squared distance from each data point to the its nearest

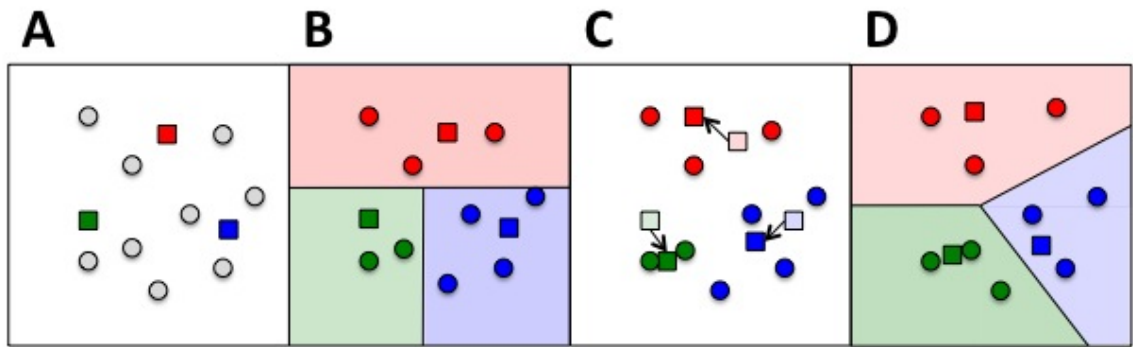


Figure 9.10: Example K-means clustering algorithm.

center is minimized [58]. There are many different algorithms available, in this work a heuristic algorithm (generalized Lloyd's) was chosen for simplicity [59].

Figure 9.10 shows an example of the K-means clustering algorithm. The algorithm starts by selecting random centers, among the data points (A), shown in red, green and blue. Next, each point is associated with the closest center (B). In step C, the centers are re-calculated as the mean of the data points closest to them. Steps B and C repeat until the centers no longer move, or converge. The result of the clustering is shown in (D) where the groupings are different than the original random points.

## 9.6 Results

The clustering algorithm results in a list of geometric cluster centers which minimizes the distance of each point to its closest center. When looking at a measurement, in order to determine the grouping (1, 2, or 3) that best represents it, the distance from each of the cluster centers is calculated. The grouping with the closest center is selected. Figure 9.11 shows the results of the clustering. K-means analysis was performed in three dimensions (K/U/T) with three centers (groupings). The centers



Table 9.2: Geometric centers as calculated by the K-means clustering algorithm.

Group	$f_K$	$f_U$	$f_T$
1	5.556e-2	9.635e-3	4.879e-3
2	7.548e-2	1.202e-2	5.937e-3
3	1.316e-1	1.112e-2	4.291e-3

of the groups are shown with black points and the groupings are shown in the various colors, group 1 (red), group 2 (green) and group 3 (blue). It can be seen from the figure that group 3 was less frequently observed given there are far fewer measurements in that group than the others. This will be discussed in section 9.6.1 when the geographic distribution of the grouping is introduced with qualitative statements about their possible causes. Table 9.6 shows the calculated geometric centers from the K-means clustering algorithm.

It is also beneficial to look at the characteristics of each of the clusters. Figure 9.12 shows the averaged 5 second energy spectrum for each of the 3 groups of background as derived by the K-means algorithm. Group 1 is shown on the top, group 2 in the middle and group 3 on the bottom. Also shown is the number of 5 second spectra in each class; about 7000, 5500, and 400 for groups 1, 2, and 3 respectively. The bottom plot shows the average energy spectrum for each background group overlaid on each other to show the difference. The green, blue and red lines represent classes 1, 2, and 3 respectively.

### 9.6.1 Geographic Distribution

With qualitative, automated classification of the NORM background measured across a variety of terrain it is interesting, and provides some validation, to observe any geo-

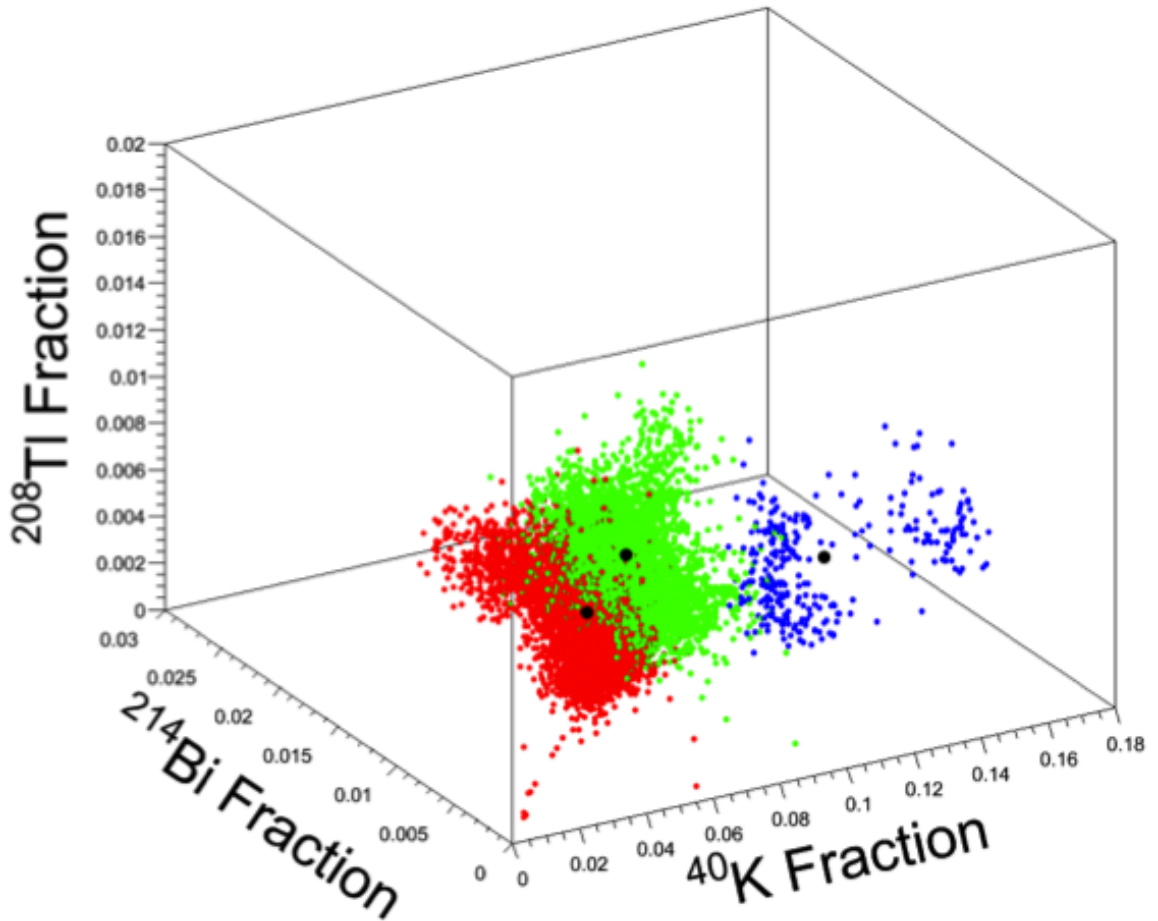


Figure 9.11: Results of the K-means clustering analysis of the component fit results. K-means analysis was performed for three dimensions with three centers. The centers of the groups are shown with block points and the groupings are shown in the various colors, group 1 (red), group 2 (green) and group 3 (blue).

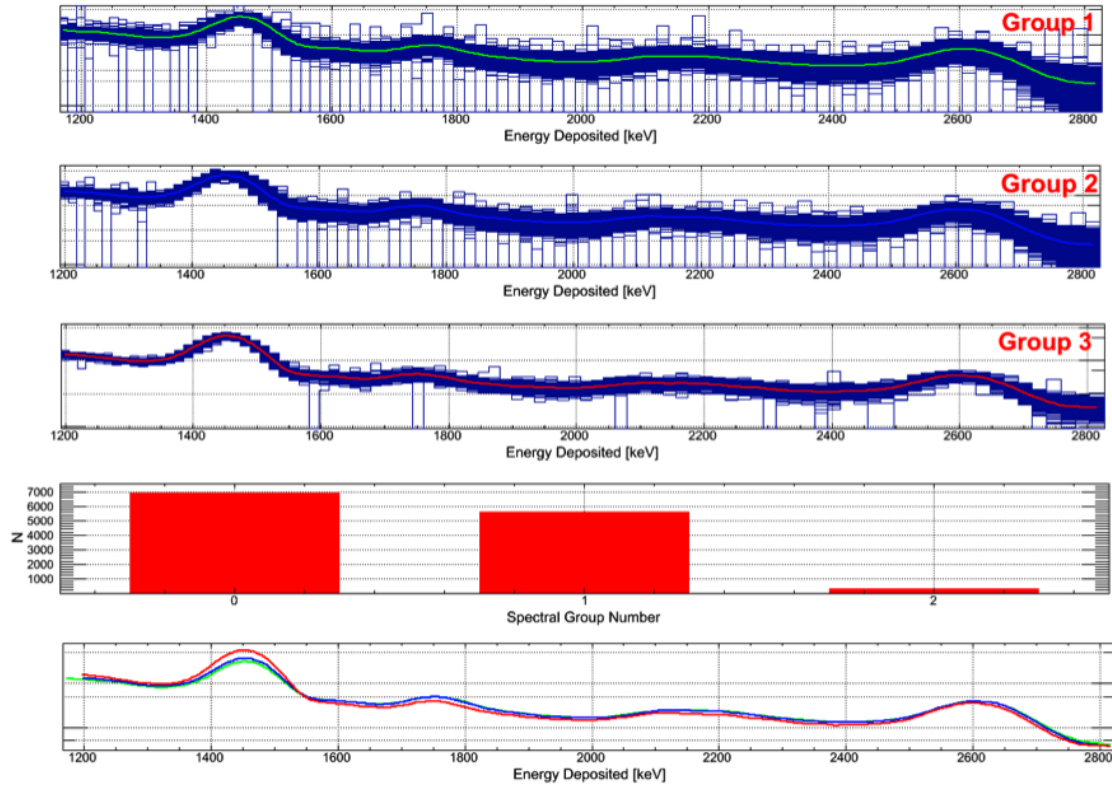


Figure 9.12: Averaged 5 second energy spectrum for each of the 3 classes of background as derived by the k-means algorithm. Also shown is the number of 5 second spectra in each class; about 7000, 5500, and 400 for groups 1, 2, and 3 respectively. The bottom plot shows the average energy spectrum for each class of background overlaid on each other to show the difference. The green, blue and red lines represent classes 1, 2, and 3 respectively.

graphical correlation among the groupings. Figure 9.13 shows a section of downtown Washington D.C. with the determined background classification denoted by the colors blue, green and red for classes 1, 2 and 3 respectively. Each block represents 5 seconds of data. From (9.13) it can be seen that the clustering algorithm is working as expected and classifying the background differently in regions that would be expected to have variations in NORM concentrations.

Group 3 (red) is associated mostly with bridges and group 2 (green) is associated with open areas such as the National Mall. Group 1 (blue) covers most other areas. This is also consistent with data from the rest of the collection. Throughout all data collected group 3 is always nearby water, group 2 is observed in mostly rural or open areas and group 1 is present throughout the collection. Another important observation from Figure 9.13 are regions where the background can change rapidly in areas such as gaps between buildings or highway underpasses. Even with this simple classification using groups, large, frequent variations are observed.

## 9.7 Summary

This chapter presented a method for analysis of NORM background so that it can be qualitatively classified by automated algorithms. The next chapter (10) will describe a method by which measured background will be segmented into blocks of similar characteristics using the result of the clustering such that simulation data can be injected within it. This analysis will require at least 30 seconds of contiguous background data of the same type. Then from those resulting segments, blocks from each group will be extracted for training detection algorithms.

Additionally, blocks for testing the performance of the algorithms will be ex-

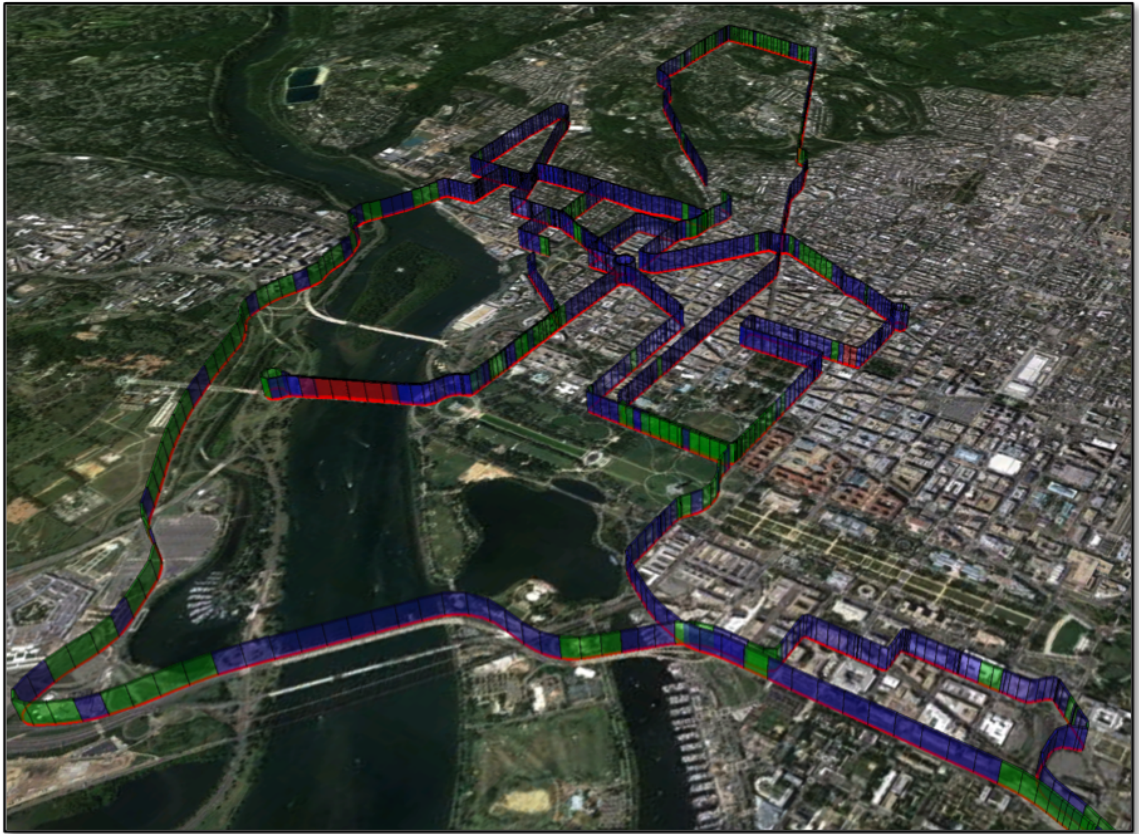


Figure 9.13: A section of downtown Washington D.C. with the determined back-ground classification denoted by the colors blue, green and red for classes 1, 2, and 3 respectively

tracted. Background blocks alone can be used to set alarming thresholds for each algorithm and isotope for a given False Alarm Rate (FAR). Also, simulated source data can be injected into the background blocks to analyze system performance as will be demonstrated in chapter 10.

# Chapter 10

## DATA INJECTION

Complete characterization of any detector system requires a large number of measurements to be statistically significant. This can be prohibitively time consuming and expensive due to source procurement costs. As a result, a limited number of measurements are usually performed in order to characterize the most important aspects of the system. An alternative, or supplemental, method for characterization is the utilization of well validated simulation models combined with measured background. Background measurements are trivial to procure because they are inexpensive and can be acquired anywhere. In this chapter a method in which simulated data can be injected into measured background will be presented and validated. Injected data sets can be processed through analysis software to estimate the performance of the algorithms (*see chapter 11*).

Since the GEANT4 [48] simulation model of the TMI developed and employed during preliminary design stages of the program has been well validated, it can serve to accurately produce the response of the instrument to various sources of interest. Also, approximately 18 hours of background data have been collected across various terrain from the metropolitan Washington D.C. area to Boston, MA. Simulation data

will be injected into measured background after sufficient timing, energy and position resolution (based on measurements) has been convolved into the simulated response. This method is expected to predict the performance of the system since the dominant factor in detection is variation in the NORM background. Figure 10.1 below shows a Google Earth plot of the path of the imager for section of the data around Washington D.C. collected on route to Boston in February of 2012.

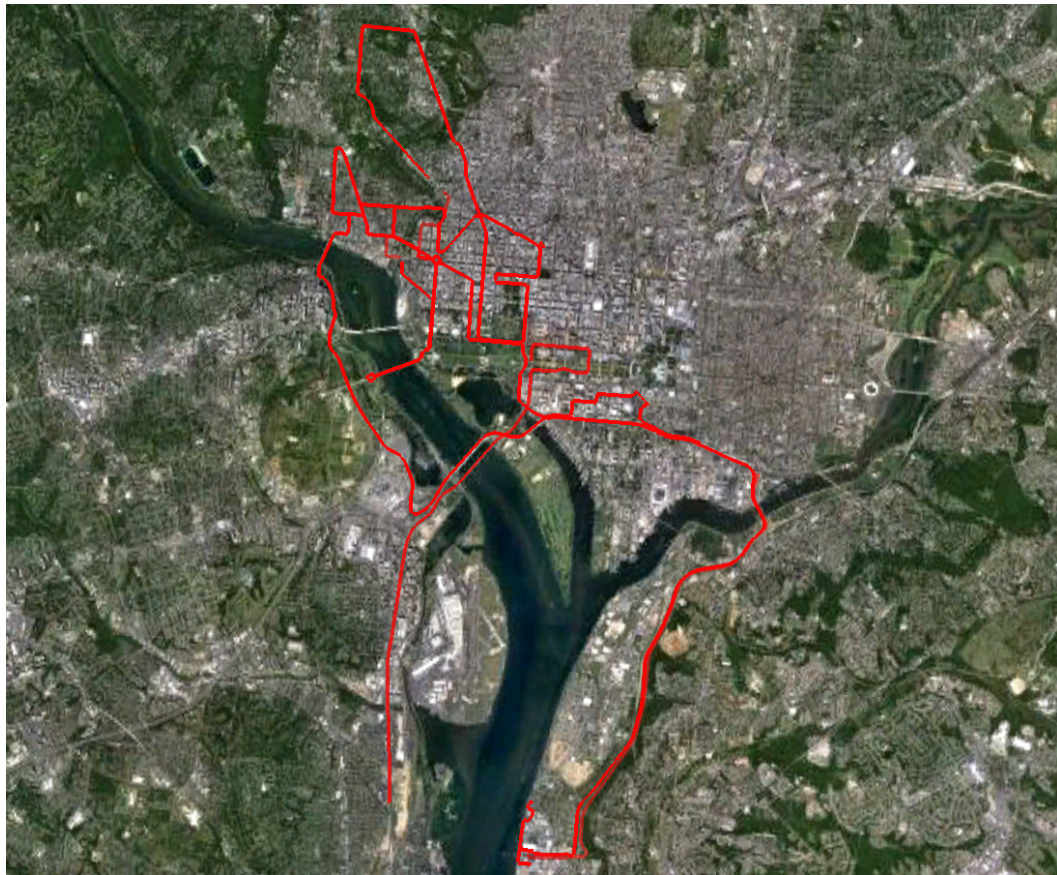


Figure 10.1: The path of the TMI (red) around the Washington D.C. area during the background collection efforts in February 2012.

In order to perform injection of simulated data into measured background there must be a consistent (speed and distance) set of both background data and source



simulations. Additionally, it will be useful to observe the effect of various categories of background on the imaging and spectroscopic algorithms. To address this challenge, a method was developed to take background segments classified by component analysis, extract the background measurements into 30 second sections, and inject 30 seconds of simulated data onto this background. A full description of the background component analysis can be found in Chapter 9.

## 10.1 Source Simulation

The first step in the data injection process is the generation of simulated source data. Depending on the source of radiation this can be a fairly trivial task, or extremely detailed. A few of the simple cases include standard laboratory check sources such as cesium-137, cobalt-60, cobalt-57 or iodine-131. These sources generally have several gamma-ray emission lines with well defined branching ratios, for example  $^{137}\text{Cs}$  can be approximated with a single 661.59 keV gamma-ray line with a branching ratio of approximately 0.851. In the case of more complex sources such as special nuclear material (SNM), *e.g.* plutonium-239 or highly enriched uranium (HEU), spectral features become much more complicated to model due to lengthy decay chains, radioactive daughter nuclei and self-absorption.

In order to reduce the complexity related to the simulation of SNM sources we will use the well validated GADRAS code [62] to generate the source emission models. This has the added benefit of providing a method for direct comparison to other simulation models for other detection systems [63]. Once an emission model is generated, or derived, it can be used in the existing GEANT4 framework to simulate the response of the detector system as a function of activity and position. The gamma-ray flux

at the source is generated by random sampling from the provided emission profile. Detector simulations generate the response to the source only and do not include any NORM background. The resulting list-mode event data is ready to be injected onto background measurements acquired with the detector system. Additionally, realistic resolution effects (energy, position) have been folded into the simulations based on measurements performed with the TMI (see Figs. 5.3 and 6.13)

### 10.1.1 Simulation Geometry

The general geometry configuration of a typical simulation run is a straight line trajectory past a single point source located at a distance off-axis (in  $Z$ ) near the geometric center of the run. Figure 10.2 shows an example scenario for a simulated source run. The TMI travels from  $(-100, 0, 0)$  to  $(100, 0, 0)$   $m$  in the  $+X$  direction for 600 seconds ( $0.333$   $m/s$ ). The source in this example is  $1.0$   $mCi$ ,  $^{137}Cs$  at  $(0, 0, 25)$  meters. In this figure the  $+X$  and  $+Z$  directions indicate the direction of travel and the direction of the FOV of the imager, respectively.

### 10.1.2 Simulation Down Sampling

It is not necessary to simulate every configuration of speed and activity for a given isotope and distance. If a large relatively source at a very slow speed is simulated, that run can be down sampled using Monte Carlo techniques to produce a file that contains a weaker source at the same speed, or a stronger source at a faster speed. The distance to the source ( $Z$ ) is more complicated, due to range and air attenuation effects, therefore only speed and activity are scaled. Runs at various  $Z$  distances will need to be simulated separately for down sampling.

For example, in order to alter the source activity, the original activity is scaled by

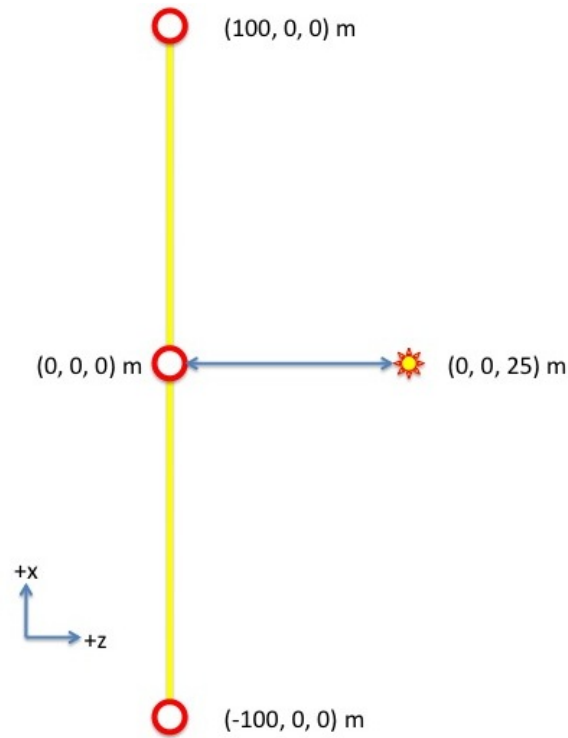


Figure 10.2: Graphical example of an injection scenario (not to scale). The simulation starts with the imager at  $(-100, 0, 0) \text{ m}$  and travels straight in the  $+X$  direction, past a  $1.0 \text{ mCi}$  source at  $(0, 0, 25) \text{ m}$ , to  $(100, 0, 0) \text{ m}$ . The total distance of the run is 200 meters and the imager speed and source activity can be adjusted through down sampling.

the ratio of the desired to simulated activity. Alternatively, to increase the speed of the imager from a simulation, the original activity is scaled by the ratio of speeds. If the speed of a simulation is changed, then displacement of each event must also be compressed, temporally, for each accepted event. Of course both values at the same time may need to be modified simultaneously, which is also possible if there is enough list-mode data in the simulation file to meet the requested parameters. An example is shown in Eqs. 10.1-10.3 for the calculation to scale a  $1.0 \text{ mCi}$ ,  $0.333 \text{ m/s}$  ( $0.745 \text{ mph}$ ) run into a  $0.5 \text{ mCi}$ ,  $15 \text{ mph}$  run. Here  $S_1$  is the scaling factor for the velocity

change in  $mph$ ,  $S_2$  is the scaling factor for the activity change where activity is in  $mCi$ , and  $S$  is the total scaling factor. It should be noted that if  $S$  is greater than 1.0, the original simulation data does not contain a sufficient quantity of events to produce an injection simulation at the requested speed and activity. According to the calculations the down sampled simulation should contain 1 event per 40 simulated events (0.025).

$$S_1 = \frac{v_i}{v_f} = \frac{0.745}{15.0} = 0.05 \quad (10.1)$$

$$S_2 = \frac{A_f}{A_i} = \frac{0.5}{1.0} = 0.50 \quad (10.2)$$

$$S = \prod_{n=1}^2 S_n = 0.025 \quad (10.3)$$

In order to generate the correct sampling of events a Monte Carlo method is used to preserve the ordering of the simulation events and only select the desired fraction of events with a pseudo random number generator [64]. For each simulated source event a pseudo random number  $R$  is generated, uniformly distributed between 0 and 1. If  $R$  is less than the desired fraction of events ( $S$ ) the event is accepted and added to the output array, otherwise it is ignored, as if it was not detected. The random number generator requires the use of a seed value to initialize the random number sequence. Since many runs are generated by sampling from the same base data set, it is crucial that a different set of selected events is chosen for each down

sampled run by selecting a different random number seed. This is handled by choosing to use the Unix (or POSIX) time at the moment the down sampling is performed. The Unix time is defined as the number of seconds that have elapsed since midnight Coordinated Universal Time (UTC), 1 January, 1970, not including leap seconds [65]. Figure 10.3 shows an example down sample simulation from 1.0 to 0.7 *mCi* and 0.745 to 15 *mph*. It can be seen from (10.3) that the time, location and energy information from the original simulation is preserved, while the total strength of the source and the duration of the run is altered.

### 10.1.3 Time Correction

One aspect of the simulation that cannot easily be changed is the distance of travel simply because the interactions measured in the system are at a particular location along the path of travel with respect to the source and cannot easily, or reliably, be changed because they include air attenuation and range effects. Since the original simulation has a defined distance range defined by the speed and starting location (*i.e.* 200 meters from (-100, 0, 0) *m* to (100, 0, 0) *m* at 0.745 *mph*), simply sampling a random number of events may not be sufficient. If the speed of the simulation is increased then the time range of the down sampled simulation will be shorter than the original. As a result, each event must be corrected to the proper time given the starting location and the desired velocity of the truck.

For example, to down sample the original, 200 meter simulation only by activity, the position and time information would remain consistent. If the velocity of the simulation is changed, the detector will move further in the same amount of time, leading to erroneous position information. To address this problem, the simulation

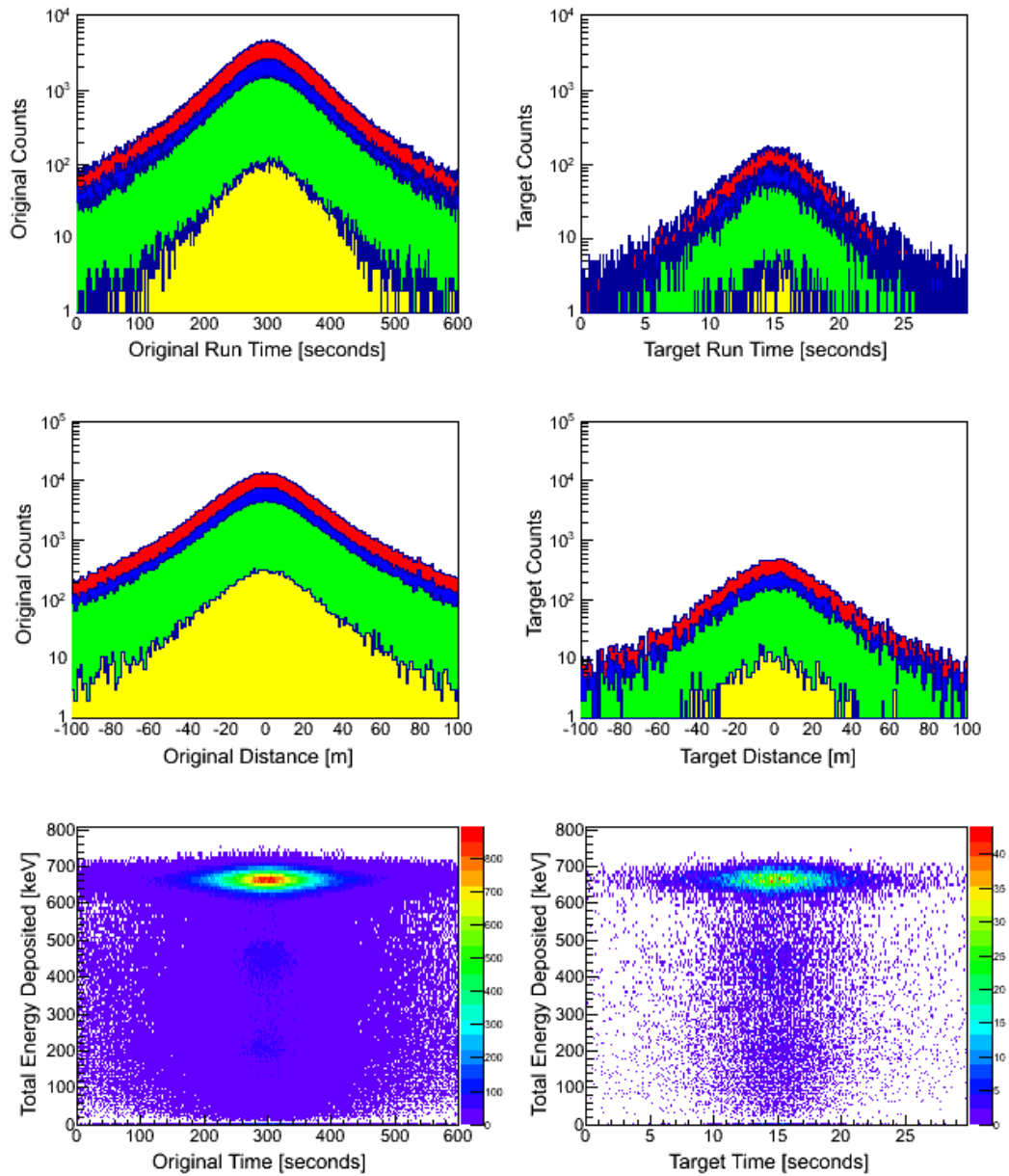


Figure 10.3: Demonstration of simulation downsampling. The simulated source only counts as a function of time (top) and distance (middle) for all counts (Red), DA array (blue), CA array (green) and coincidence (yellow). The bottom plot shows the total energy deposited for all events as a function of time where the  $^{137}\text{Cs}$  source is clearly visible in the middle of the run. The original simulation is shown in the left column and the down sampled simulation is shown in the right column.

must always have a fixed distance of travel. Each down sampled run will still cover 200 meters, however it may take 30 seconds to traverse at 15 *mph* or 600 seconds at 0.745 *mph*. Since the distance of the simulation is fixed, the time of the resulting down sampled simulation is determined by the amount of time that it will take the TMI to traverse the simulation distance at the desired speed.

#### 10.1.4 Down Sampling Validation

The goal of down sampling is to be able to create many small simulated runs from a larger simulation. Through the use of a random number generator we can select a different subset of events each time we process the simulation. This technique has been validated to generate runs that are normally distributed about the desired fraction of events. Figure 10.4 below shows the results of 1,000 down sampled runs. From the plot on the left it can be seen that the total number of accepted events (green) is normally distributed about the desired number of events (red line) with a width consistent with the expected  $\sqrt{N}$  Poisson variation. The middle plot shows the fraction of events for each down sampled simulation (blue dots) where the desired fraction of events is represented by the blue line. The plot on the right shows the fraction of coded aperture (red) and Compton (blue) events as a function of run number.

### 10.2 Background Extraction

Now that a simulated source run with the desired isotope, at a specific distance, speed and activity is available, a background data set that is suitable for injection must be created. There are several methods to achieve this. First, an average background rate can be defined and events randomly selected from a much larger data set. Second,

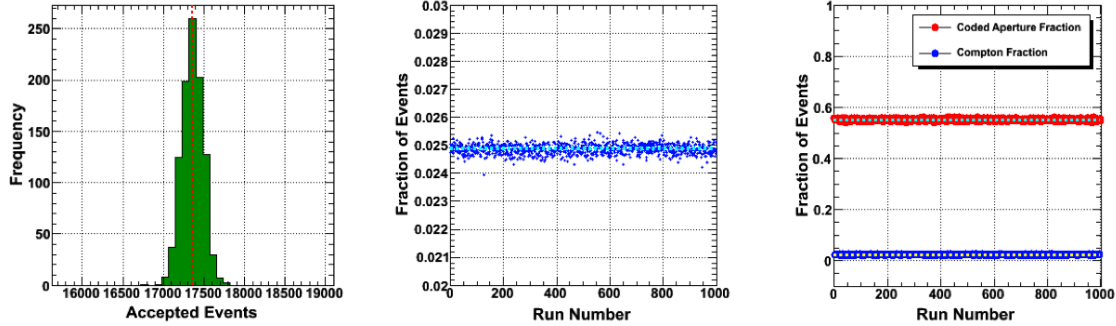


Figure 10.4: The frequency versus number of events sampled for 1000 down sampled simulation runs (left) where the red line shows the desired number of events. The middle plot shows the fraction of events sampled versus run number (blue dots) for the same set of runs where the desired fraction is shown with the dashed blue line. The right plot shows the fraction of coded aperture (red) and Compton (blue) events as a function of run number with the desired fraction shown with dashed lines.

a continuous subset of background can be sampled from a larger set. The later is more representative of normal variations in NORM for both energy and total count rate, where the former can only approximate a change in overall count rate with respect to position and may lead to unphysical, rapid, changes in the rate as well as energy distribution. For comparison and validation a measurement from a section of background will be extracted that can be replicated through injection. Figure 10.5 shows the path of the imager (red) around the rail yard track at the Savannah River Site (SRS) test facility. The speed of the imager for this run (source and background) is approximately 15 *mph*. The path shown is for a background only run, where the location of the source from a corresponding run is indicated with an orange dot. To make this scenario consistent with the simulation data 200 meters of background data need to be extracted such that the source is located in the geometric center of the run (yellow).



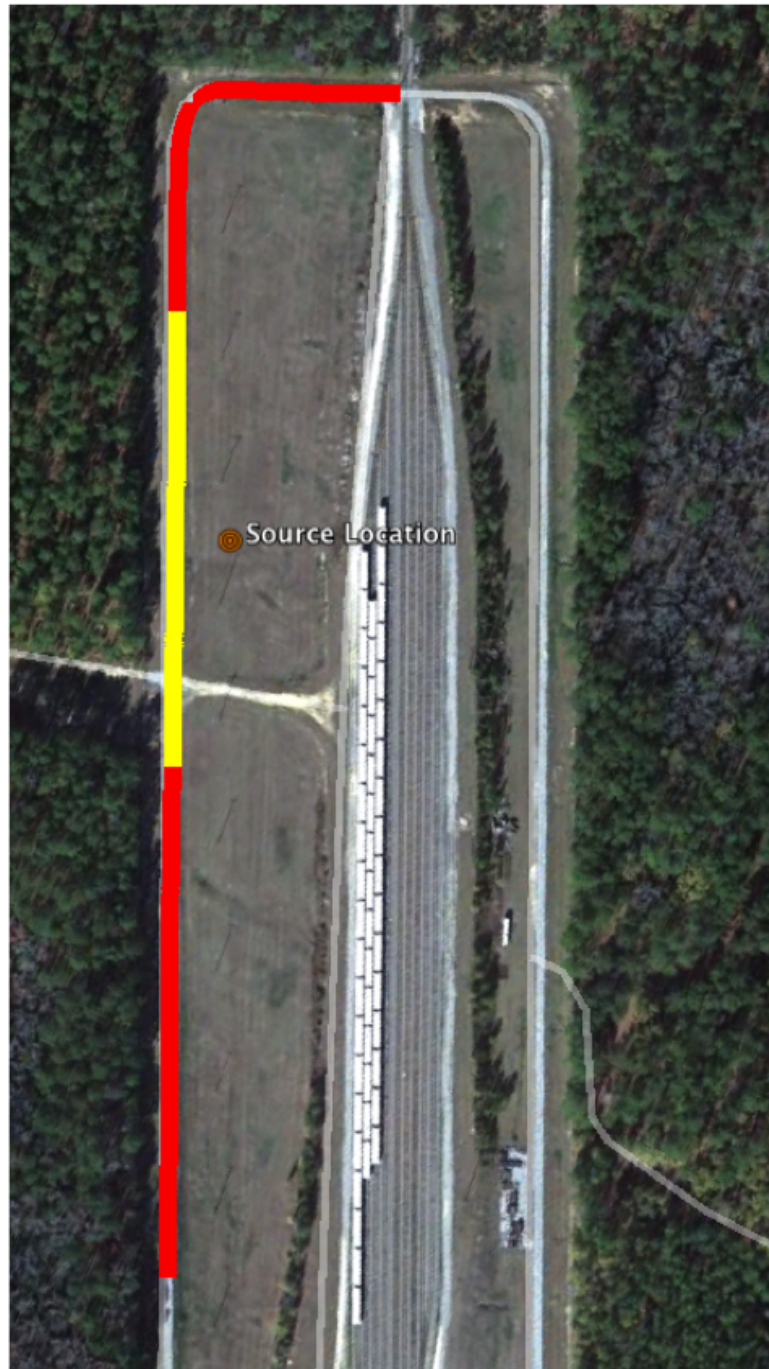


Figure 10.5: Example data extraction. The full length measured run (red) is sampled from +/- 14.91 seconds around the point closest to the known source location (yellow).

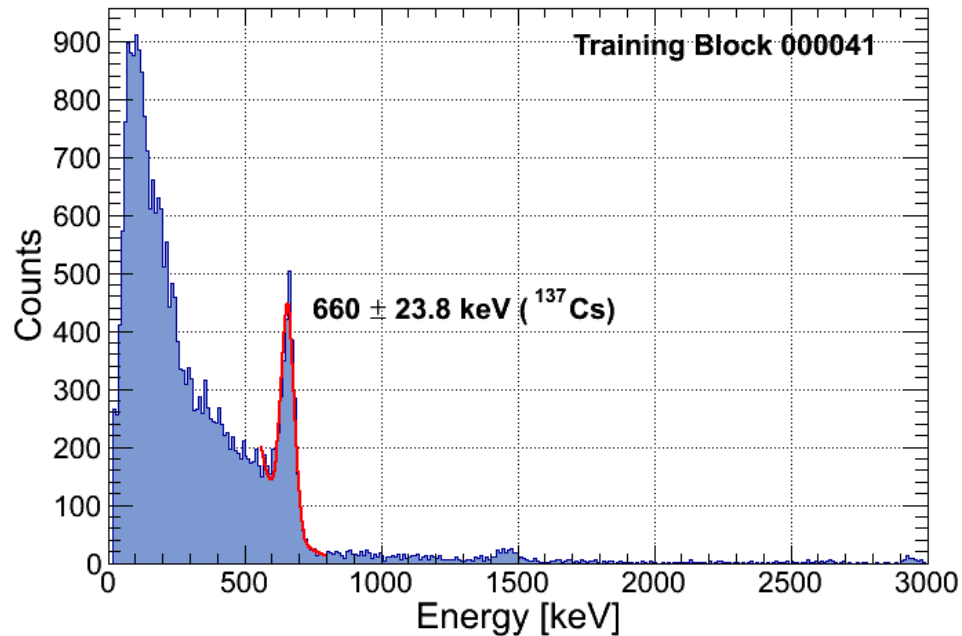


Figure 10.6: Example industrial nuisance source ( $^{137}\text{Cs}$ ) in one of the preliminary blocks of background data used for algorithm training.

### 10.2.1 Nuisance Sources

There is always the chance that an actual source of radiation is present within the detectable range of the system, whether it is an industrial source used by utility companies for pipe maintenance, or a cancer patient that just had a medical treatment. As background data were collected in the Washington DC area in February of 2012 several nuisance sources were observed in the data. These sources included a  $^{137}\text{Cs}$  industrial source and multiple  $^{99m}\text{Tc}$  medical isotopes. Figure 10.6 shows an example of a  $^{137}\text{Cs}$  source located in block 041/239 of the algorithm training set. When selecting background blocks for algorithm testing or training, care must be taken to ensure any nuisance sources of radiation are removed prior to processing and analysis.

## 10.3 Injection

Injection of simulated data into measured background is performed through time comparison. As it was seen in the source simulation and data extraction, there is a comparable set of source and background data, each containing many individual time-tagged interactions. To perform injection, each event from the source and background data sets are examined, deciding which has the next consecutive event time. This process continues until there is no more data thereby producing a simulated source injected into measured background. Figure 10.7 shows the results of a single, down sampled, source simulation injected onto measured background. The top row shows the source only energy spectrum, with the 662 *keV* line from  $^{137}\text{Cs}$  clearly visible (column 1), the background only energy spectrum (column 2), the injected energy spectrum (column 3) and a comparable measurement (column 4). The comparable measurement is a 25 *m* distance of closest approach, 15 *mph*, drive past a 0.5 *mCi*,  $^{137}\text{Cs}$  point source. The middle row shows the time evolution of the energy spectrum for the simulated source (column 1), the measured background (column 2), the injected simulation (column 3), and the measurement (column 4). The bottom row shows the energy spectrum for events that are within 2 seconds of the middle of the run, or where the truck is directly in front of the source. From these plots it can be seen that the injection scheme appears to reproduce the correct time and energy structure of the measurement. The peak in the background spectrum (top-row blue) is the 511 *keV* electron/positron annihilation peak, not the  $^{137}\text{Cs}$  photo peak. All sources are absent from the background spectrum.

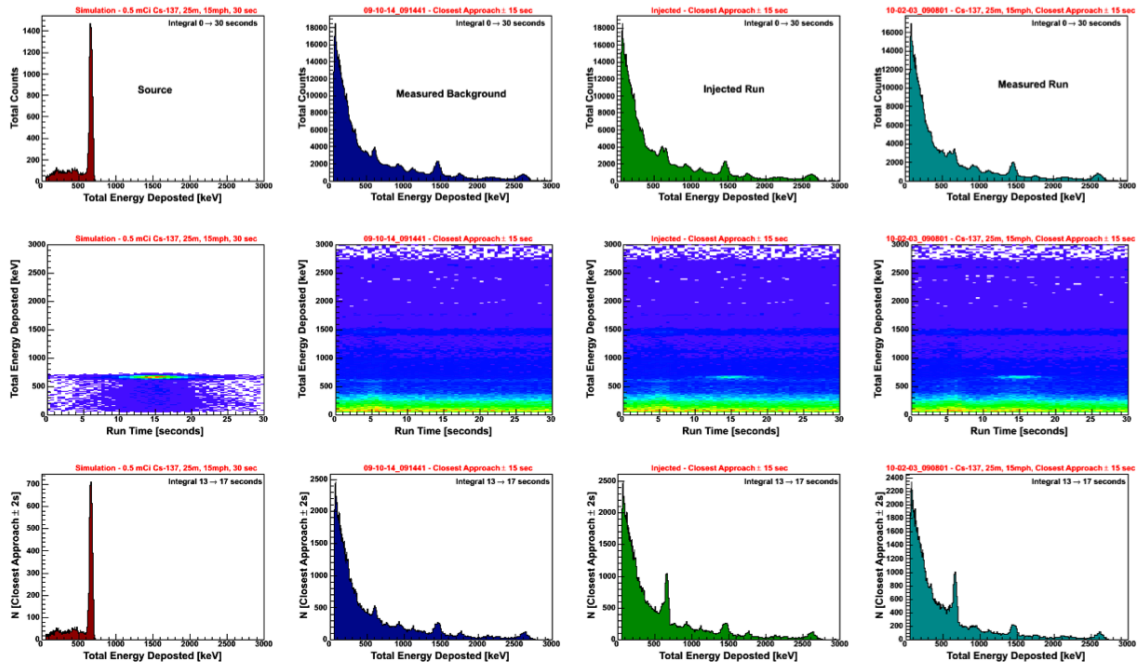


Figure 10.7: Results of the validation injection scenario. The top row shows the total energy spectrum (30 seconds) for the source simulation, measured background, injected simulation and corresponding measurement, respectively (left to right). The middle row shows the 2-dimensional energy versus time histograms with the same columns. The third row shows the energy spectrum for the middle 4 seconds of the runs to emphasize the source peak at  $662\text{ keV}$  from  $^{137}\text{Cs}$ .

## 10.4 Validation

In order to validate this method of data injection a  $0.5 \text{ mCi } ^{137}\text{Cs}$  source with a DCA of 25 meters will be used. This is a convenient run to compare against because there was at least one run of this type taken each day of testing (chapter 12). To make the comparison as close as possible, the 200 meters of data around the source location was extracted. The same distance was extracted from the background only and source runs. It should be noted that the background run count rate will not align exactly with the background rate in the source run, as the variation in NORM is time, as well as position, dependent.

### 10.4.1 Event Composition

The first step in validation of the injection technique is to compare the composition of events in the simulation run and the measurement. The imaging subsystems are only interested in those events used for Compton imaging (*i.e.* coincident interactions) and coded aperture imaging (*i.e.* singles interactions in the DA array). Figure 10.8 shows the coded aperture event rate as a function of time into the run (left) for the injection simulation (blue) and measurement (red). The Compton event rate as a function of time (right) shows the injected simulation (blue) and measurement (red).

It can be seen from the plot that aside from expected fluctuations in the background rate as previously mentioned the coded aperture and Compton scatter event rates are consistent between the measurement and the injection simulation.

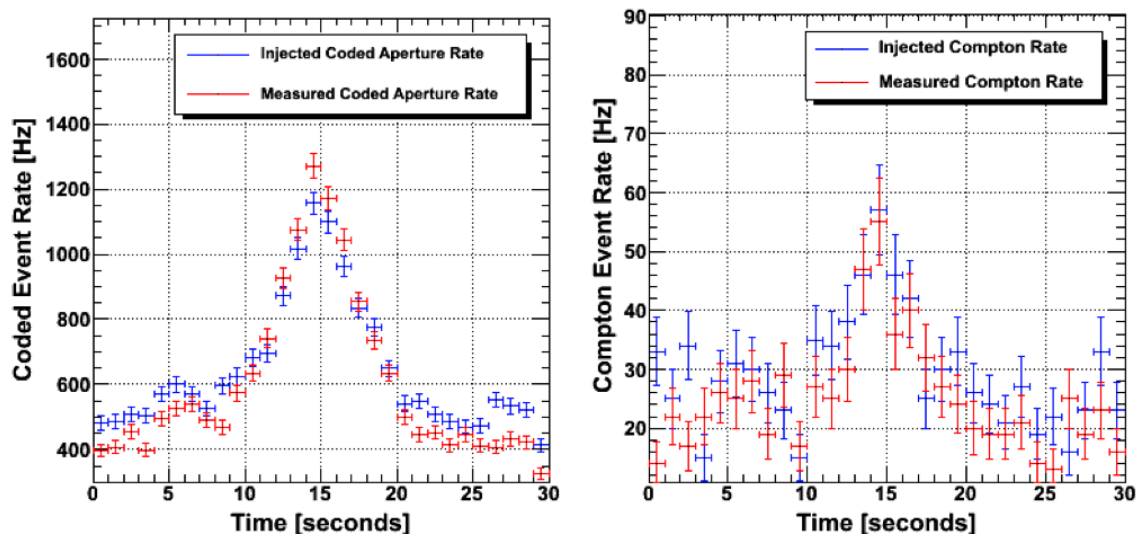


Figure 10.8: Comparison of the composition of events from the data injection validation scenario (blue) and a source measurement (red). Both the coded aperture event rate as a function of time (left) and the Compton event rate as a function of time (right) match well against measurements.

## 10.4.2 Spectroscopy

Since this is both an imaging and spectroscopic system we must ensure that the energy distribution of injected events is consistent with measurements. To perform this validation 4 second snapshots of the energy spectrum at each point in the injection simulation with measurement will be compared. It is expected to observe some deviation in the energy spectrum based on Poisson noise and variation in the NORM background between the background measurement time and the source measurement. Figure 10.9 shows the comparison of the measured counts versus energy in  $keV$  for the 4 seconds closest to the source to show the source emission line. From this plot it can be seen that the injection simulation (blue) is very closely modeling the measurement (red). It can also be seen that the high energy events ( $E > 700 keV$ ) differ between the injection simulation and the measurement. Since this part of the

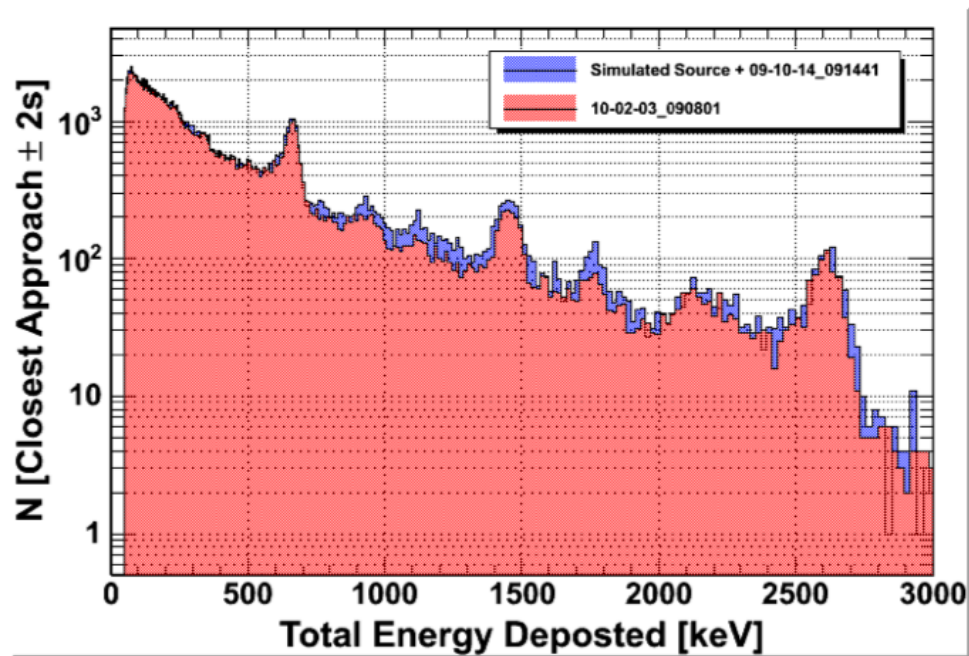


Figure 10.9: Total energy deposited in the detector system for the middle 4 seconds of data for the data injection scenario (blue) and the corresponding measurement (red). Counts above the 662 keV gamma-ray line from  $^{137}\text{Cs}$  are not simulated and represent actual count rate variations between measurements at the same location.

spectrum has not been simulated it represents real fluctuations in the background between the measurements. Additionally, Figure 10.10 shows the ratio of injected counts to measurement for the same 4 second slice. From this it can be seen that for the energy range of the source injection ( $E < 700\text{keV}$ ) the deviation is entirely within the expected uncertainty of photon counting statistics.

### 10.4.3 Imaging

In order to fully validate the functionality of the injection method it is necessary to test the imaging algorithms. If the injection method is working correctly, sources having similar intensity in the injection simulation and the measurement should be equiva-

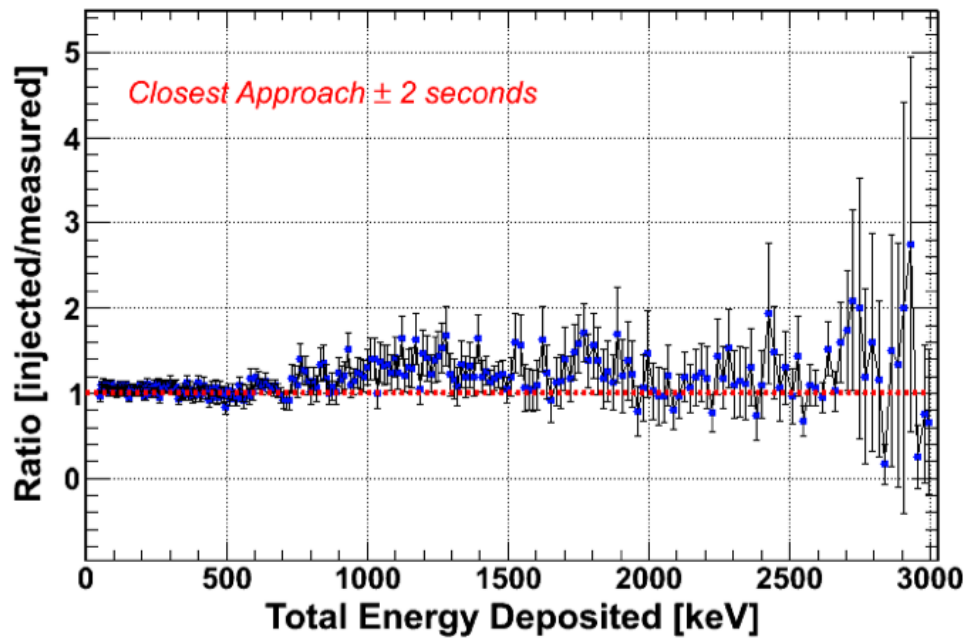


Figure 10.10: Ratio of injected to measured counts as a function of energy ( $keV$ ) for the injection scenario as compared to a measurement in the same location. Data are shown for  $\pm 2$  seconds of closest approach to the source. The dashed red line shows the expected ratio of 1.0, indicating a perfect match. Most data points are within the expected uncertainty due to counting statistics.



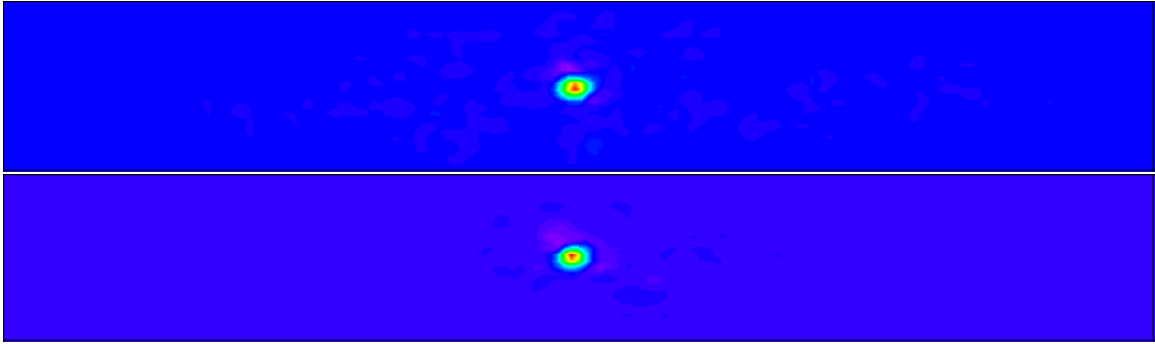


Figure 10.11: Comparison of imaging results for the source measurement (top) and simulated injection run (bottom). Both images have similar image significance; 34.23 measured versus 33.58 injected. Images report a source within 2.2 meters of each other.

lent. Also, reconstructed images should have similar shapes if the resolution folding of the simulation is correctly applying position uncertainty. Figure 10.11 shows the comparison of the measured source image (top) and the injection simulation (bottom) for the same source location and intensity. The measured image has a calculated significance of 34.23 versus 33.58 for the injected source. Both images are aligned in the same location and report an alarm within 2.2 *m* of each other. Also, both images have similar localization uncertainty;  $\pm 4.88$  and  $\pm 5.58$  *m* for the measured and injected sources respectively. Replay of all 60 similar measured runs (*see chapter 12*) the mean significance calculated was  $34.62 \pm 7.82$  versus  $29.5 \pm 5.15$  for the injection data. Also, the reported uncertainty was on average  $3.76 \pm 1.64$  *m* for measurements versus  $2.10 \pm 1.32$  *m* for injected data. There were 60 measurements and 240 injection runs compared. The agreement between the runs is reasonable considering that the actual speed, distance, and source activity used in measurements are not exact. Injected source runs are fixed at 25 *m* DCA, 15 *mph*, and 0.5 *mCi*.

## 10.5 Injection Analysis

The method of data injection has been well validated. Simulated sources can be injected over measured background and analyzed to determine the performance of the system for both spectroscopy and imaging. Using the 18 hours of data collected on the trip from Washington D.C. to Boston, we can extract many basis background sets and perform injection into those sets. An example of the analysis is the injection of various activities of  $^{137}\text{Cs}$ . In this case a set of 1000 unique background blocks (30 seconds each) were extracted from measurements according to the groupings determined in chapter 9. Each group consists of 240 background blocks for algorithm training and 240 for algorithm testing, with the exception of group 2, which only had data to generate 40 unique blocks. Source simulations were then down sampled to various activities and injected into those blocks using the method from this chapter.

Figure 10.12 shows several sample images from the algorithms for background only (top) and 0.1, 0.3, 0.5, 0.7, 0.9 and 1.0  $mCi$  as the images go down. The color scale of the image has been modified such that they are on the same scale for comparison. It can easily be seen that as injected source activity increases so does the image intensity.

Given a large number of runs for a specific isotope, distance and speed combination (*e.g.*  $^{137}\text{Cs}$ , 25 *m*, 15 *mph*) for multiple source strengths performance of the algorithms can be gauged as a function of source activity. Analysis includes performance of the gamma-ray imaging algorithms, spectroscopic algorithms and the combination of both.

To perform analysis, each of the 240 injected runs at each activity is processed through the algorithms. For each activity, the mean and standard deviation of the

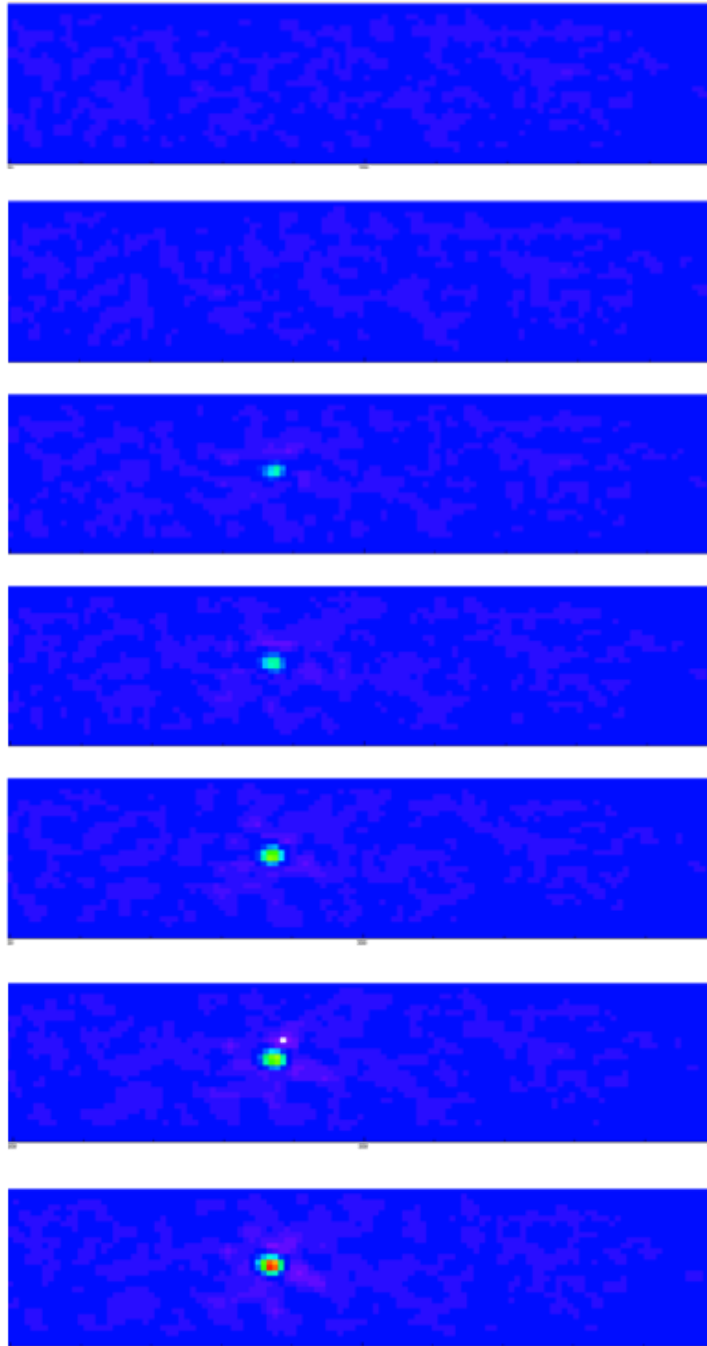


Figure 10.12: Sample images generated from processing of injection simulations at various activities: background only (top), 0.1, 0.3 0.5, 0.7, 0.9 and 1.0  $mCi$  (bottom). As the source activity increases, the image intensity increases.

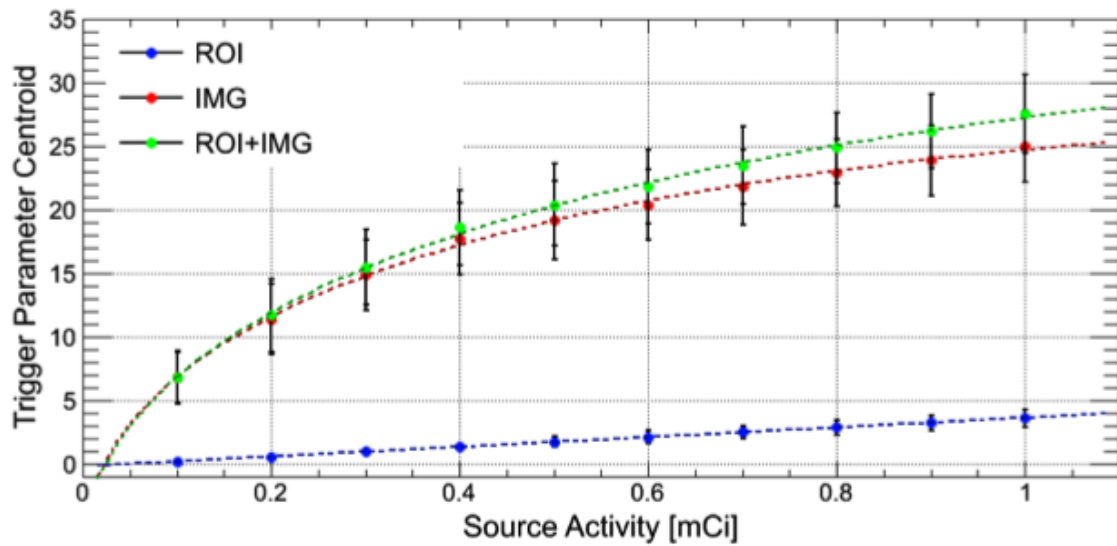


Figure 10.13: Centroid of the maximum trigger parameter for 240 simulated injection runs as a function of source activity. Spectroscopic region-of-interest (ROI) is shown in blue, imaging (red) and the combination (green).

maximum image pixel significance (trigger parameter) frequency distribution is calculated. Figure 10.13 shows the triggering parameter centroid as a function of activity. As the source activity increases, the mean value of the trigger parameter increases for each of the algorithms, region-of-interest (ROI), imaging (IMG) and the combined (IMG+ROI).

Also, the mean and standard deviation of the 240 background blocks is calculated. This demonstrates how the significance calculation in the images fluctuates in the absence of a source. Analysis of the background only data allows for determination of triggering thresholds. Figure 10.14 shows the maximum calculated trigger parameter value for the various algorithms for the background blocks. It should be noted that each set of data is independent and the lower value for ROI (blue) does not indicate smaller background or better sensitivity.

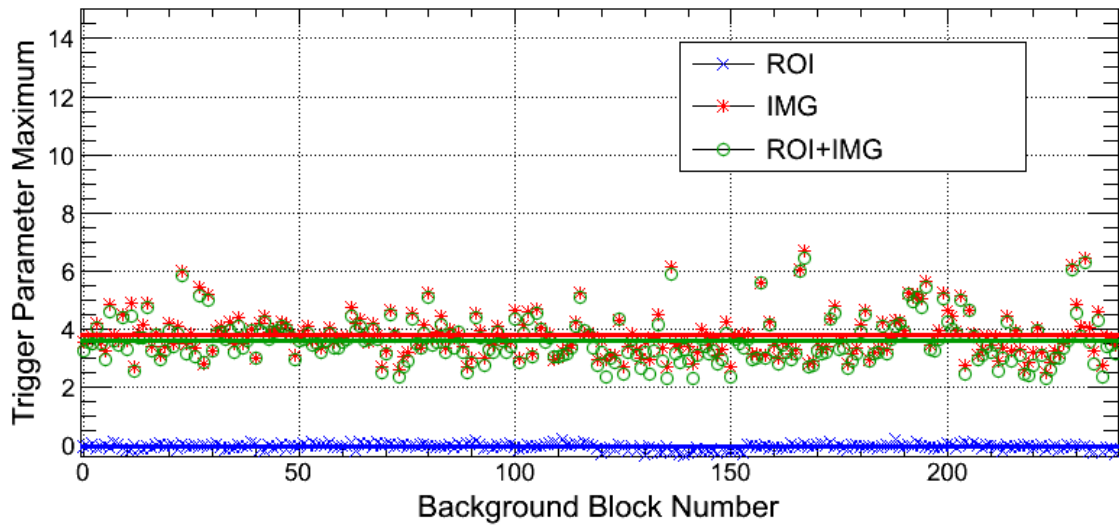


Figure 10.14: Trigger parameter maximum value for ROI (blue), imaging (red) and the combination (green) as a function of injection run number (0-239). The average (centroid) values for each are shown with a solid line of the corresponding color.

This analysis also allows for identification of blocks of background that have substantially higher trigger values. These blocks can be examined in more detail and provide insight into potential improvements to the algorithms that would further reduce the background significance and fluctuation.

## 10.6 Summary

This chapter has presented a method for injection of simulated source terms into measured background. Background blocks have been segmented into groups according to the analysis performed in chapter 9. Each set of background data has a unique source injected into it for a given activity, speed and distance. This method of injection has been shown to reproduce measurements with very good agreement. This method allows for analysis of many injected source runs over realistic backgrounds to gauge the

performance of the algorithms without making thousands of field measurements. Data produced using this method have been processed through the detection algorithms in order to calculate sensitivity. Sensitivity will be quantified using Receiver-Operator Characteristic (ROC) analysis; the details of this analysis are presented in chapter 11.

# Chapter 11

## PERFORMANCE RESULTS

In order to quantify strengths of each detection modality, individually and combined, a uniform method of analysis is required. It is advantageous to use a standardized approach to performance analysis such that information is presented clearly and understandably. Also, using a standardized method of analysis, performance of multiple algorithms and detector systems can be compared and contrasted on equal footing.

A common method for the quantification of detection algorithms is ROC analysis. In this chapter the details and results of the ROC analysis technique will be given. ROC analysis will be used to compare the various modes of detection for the TMI. The binary classifier used will be the single most effective measure of detection fidelity for each algorithm. For imaging algorithms the classifier is the maximum significance in the world image while for spectroscopic algorithms it is the maximum significance calculated by the ROI algorithm.

### 11.1 Receiver Operator Characteristic Analysis

ROC analysis was first employed in World War II for the analysis of radar signals. Following the attack on Pearl Harbor in 1941, the United States Army began new

research to increase the prediction of correctly detected Japanese aircraft from their radar signals [66–68]. ROC analysis is a method in signal detection theory that estimates the performance of a system through the use of a binary classifier. The classifier is observed as a function of discrimination threshold [69]. For the TMI the binary classifier is true if the measured significance of the data point is above the threshold value for detection and false if it was not. ROC curves are a graphical representation of the true probability of detection (sensitivity) versus the probability of false alarming (1-specificity).

### 11.1.1 Binary Classifier

Through data injection methods presented in chapter 10 many pseudo-synthetic runs can be generated for both background only and multiple activities for a source of interest. The first step in generating an ROC curve is to gather the maximum value of the classifier for each run. Figure 11.1 shows an example plot of three ROI classifier frequency distributions (left) for background only (red), background with a  $40 \mu Ci$  source (blue) and background with a  $300 \mu Ci$  source (green). Additionally a Gaussian fit to the data is shown on the right of Fig. 11.1, where each distribution has been normalized the same intensity. These data represent the maximum classifier value determined by the ROI algorithm for each of the 240, group 1 background blocks (chapter 9) with a  $^{137}Cs$  source injected into them (chapter 10) at 2 different activities (40 and  $300 \mu Ci$ ). For each of the injected runs the source was located at 25 m DCA in the middle of a 30 second pass at 15 mph.

For each of the 240 runs the maximum value of the ROI significance calculation is plotted. As expected the maximum value of the classifier increases with source ac-



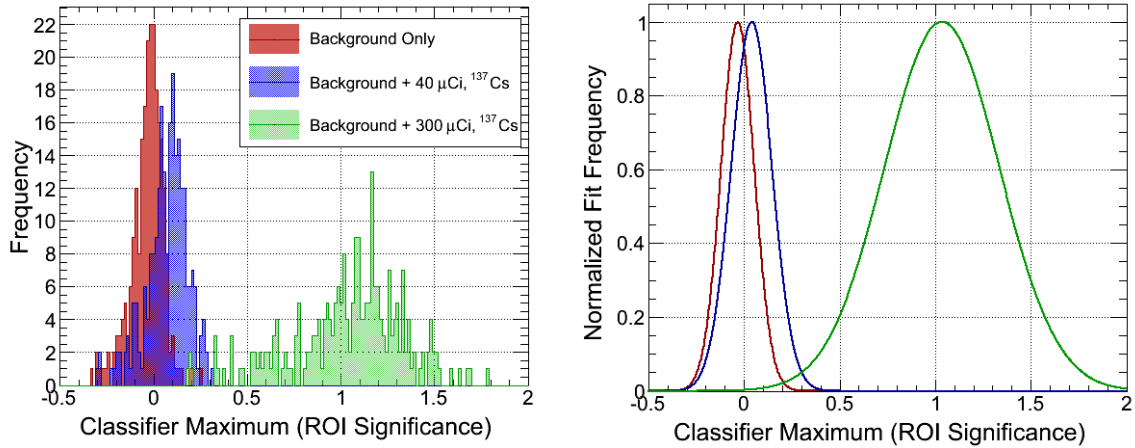


Figure 11.1: Example maximum classifier frequency distribution (left) for 240 runs of background only (red) and 40 (blue) and 300  $\mu Ci$  (green),  $^{137}Cs$  injected source. A Gaussian fit to each of the distributions is shown on the right.

tivity (with some spread). The Gaussian fits to the data are a good approximation to the functional form of the frequency distribution given the Poisson nature of photon counting statistics. Fitting the frequency distribution may allow for estimates of performance in regions with a very low probability of false alarm where it would become prohibitively time consuming to take the actual number of measurement required. For example, to measure 1000, 30 second runs past a source would likely consume a minimum of 83 hours.

### 11.1.2 Cumulative Distribution Functions

In order to make an estimate of the probability of detection or probability of false alarm, frequency distributions are integrated as a function of threshold on the classifier value. The Cumulative Distribution Function (CDF) represents the fraction of measurements with a classifier value below the threshold. The probabilities of false alarm and detection are calculated as the ratio of measurements above the threshold

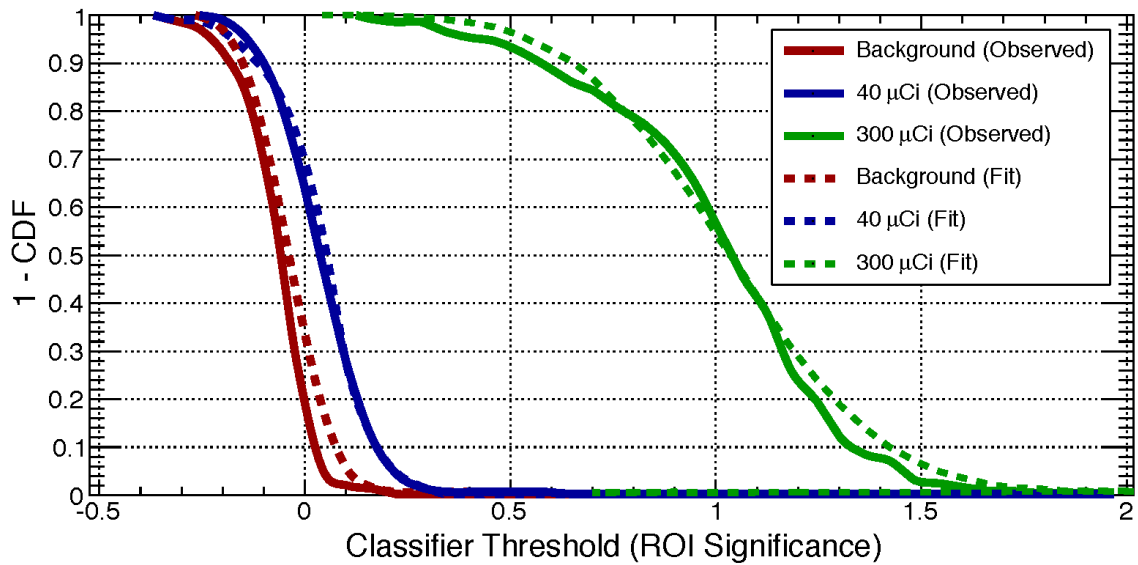


Figure 11.2: 1-CDF distribution functions for the background only (red),  $40 \mu Ci$  cesium (blue), and  $300 \mu Ci$  cesium (red) sources as a function of classifier threshold.

to all measurements for the background and source distributions respectively. By calculating the cumulative number of measurements with a value below the threshold, the value above threshold is simply one minus the fraction of measurements below threshold (1-CDF). Figure 11.2 shows the 1-CDF functions for the background and source frequency distributions from Fig. 11.1. As the threshold on classifier value increases the probabilities of false alarm and detection are reduced as expected.

Additionally, the 1-CDF distributions are used to set triggering thresholds. For example, reading from Fig. 11.2, if the operator was willing to accept a false alarm probability of 20%, the classifier threshold could be set at around 0.0. This would give a probability of detection of about 60% for the  $40 \mu Ci$  source and 100% for the  $300 \mu Ci$  source.

### 11.1.3 Generating the Curve

Generating ROC curves is performed by scanning the 1-CDF distributions along the discrimination threshold. At each threshold point the estimated probability of detection is equivalent to the value of 1-CDF for the source distribution and the probability of false alarm is the value of 1-CDF for the background only distribution. Figure 11.3 shows the associated ROC curve generated from the data in Fig. 11.2.

From Fig. 11.3 it can be seen that fit to the distributions produces nearly the same result and can be used as an estimated ROC area in the case where limited run statistics are available, assuming the fit function is a good descriptor of the data. Each ROC curve shown in Fig. 11.3 also has an Area Under the Curve (AUC) value associated with it. AUC values can be used to quantify the overall sensitivity of the system to a particular source.

### 11.1.4 Area Under the ROC Curve

Sensitivity can be characterized by the area under the ROC curve. It is a measure of the overall discrimination power of a detector. The maximum value of AUC is 1.0 and the minimum value is 0.5, representing unambiguous discrimination and random detection respectively [67].

AUC is a convenient metric because it does not rely on any particular portion of the ROC plot but the complete curve. The interpretation of the area implies that a randomly selected run with a source present has a probability equivalent to the area of having a test value larger than a randomly selected run without a source present. For example if the area under the ROC curve is 0.92, a randomly selected run with a source present has a 92% probability of having a larger test value than a run without

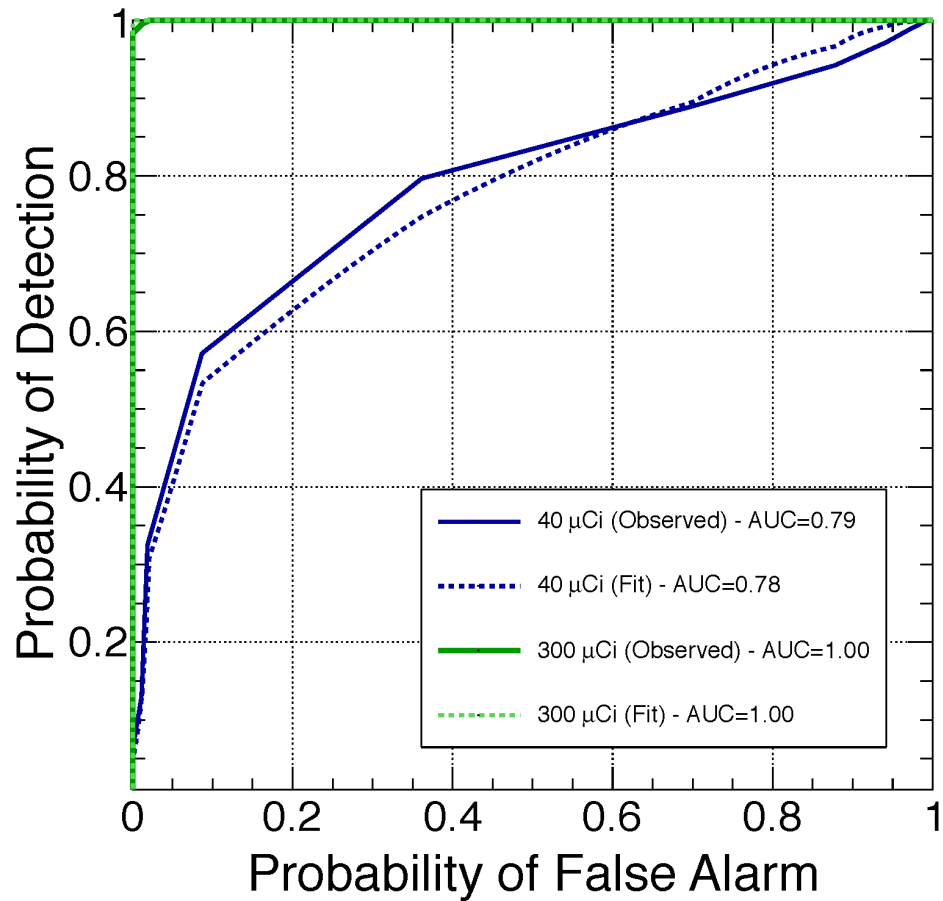


Figure 11.3: Generated ROC curve for a 40  $\mu Ci$  (blue) and 300  $\mu Ci$  (green),  $^{137}Cs$  source. The solid lines are the curves generated directly from the measured frequency distributions and the dashed lines are generated from fits to the frequency distributions.

a source present. The area does not imply that a source is detected 92% of the time or that a true alarm is associated with a run with a source present 92% of the time.

## 11.2 Imaging Modality Fusion

Since the TMI is a hybrid imaging system, each modality has different performance characteristics as well as a different effective energy range. In order to verify that the fusion of multiple imaging modalities improves sensitivity, ROC analysis can be performed on each modality for the same set of data and compared. Figure 11.4 shows the calculated ROC curves for the Compton imaging (CI), coded aperture (CA), and the fusion of the two (CA/CI). These curves were generated from 100 simulated source and background runs at 30 *mph* past a 1.0 *mCi*,  $^{137}\text{Cs}$  source located at 100 meters DCA. Here, it can be seen that in this scenario Compton imaging is not very sensitive, and provides nearly random detection (AUC=0.515). Coded aperture imaging is more sensitive than Compton (AUC=0.696), however the combination of CA/CI is shown to be superior to both at this energy (662 *keV*) with an AUC of 0.843.

Another aspect of hybrid imaging is the ability to improve sensitivity over a broad range of energies. Figure 11.5 shows the AUC metric for CI (blue), CA (red), and CI/CA (green) as a function of source energy for 100 simulated runs past a 1 *mCi*,  $^{137}\text{Cs}$  source at 100 *m* DCA and 30 *mph*. As expected the CI algorithm does not perform as well as coded aperture at low energy and coded aperture does not perform as well as Compton at high energy. Also, as expected the fusion of CA and CI improves sensitivity across the range of energies proving that hybrid coded aperture/Compton imaging is a powerful tool in detection of weak sources at a distance in the presence of large backgrounds. Additionally, a large improvement (as observed) is expected

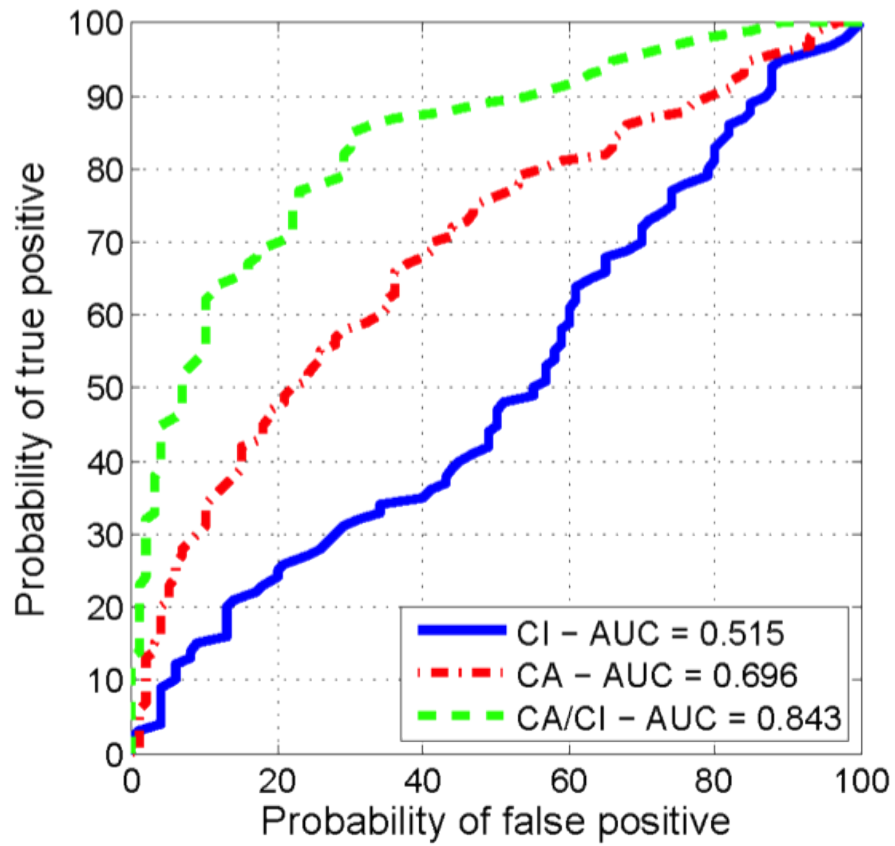


Figure 11.4: ROC analysis of the highest image pixel for Compton (blue), coded aperture (red) and hybrid (green), generated using 100 simulated runs past a 1.0  $mCi$ ,  $^{137}Cs$  source at 100  $m$  DCA and 30  $mph$ .

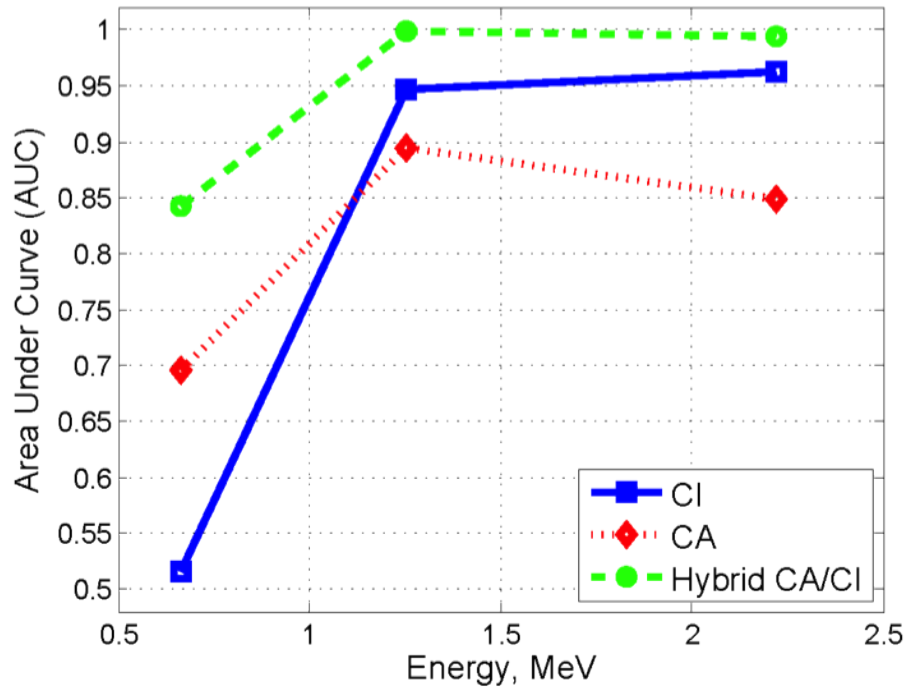


Figure 11.5: Area under the ROC curve as a function of incident gamma-ray energy for Compton (blue), coded aperture (red) and hybrid (green).

because the data used in the coded aperture and Compton imaging algorithms are orthogonal with very different background characteristics.

### 11.3 Imaging/Non-Imaging Modality Fusion

Since the TMI is also a large-area spectroscopic detector it is important to show the applicability of fusing imaging and non-imaging modalities. Figure 11.6 shows the ROC curves generated from 240 runs past a  $75 \mu Ci$ ,  $^{137}Cs$  source at 25 m DCA and 15 mph for ROI (blue), CA/CI imaging (red) and ROI/CA/CI (green). The area under the curves for the spectroscopic algorithms and the imaging algorithms are similar, 0.885 and 0.906 respectively. However, the combination of both leads

to improved sensitivity (AUC=0.914) over either alone. The overall improvement in area is small but expected since the majority of measured events are used by all algorithms (DA singles, CA/DA coincidence), the only difference for ROI being CA singles interactions.

So far the ROC curves have focused mainly on the region of the curve with a high probability of false alarm, mostly because the examples so far have large observable differences in this range. Even though the area under the ROC curve has been shown to be slightly better for the fusion of imaging and non-imaging algorithms, at more realistic false alarm probabilities ( $< 10^{-3}$ ) a larger difference can be observed. Figure 11.7 shows the same ROC curves as Fig. 11.6 with a logarithmic Probability of False Alarm (PFA) scale to show very low probabilities of false alarm. Here it can be seen that the relatively small difference in AUC translates to a large improvement in detection probability.

## 11.4 Minimum Detectable Activity

ROC curves can also be used to estimate the smallest source the TMI is capable of detecting, or the MDA. MDA values are derived based on two criteria from the ROC curve, probability of false alarm and probability of detection. The choice of these criteria can be based on many factors related to the CONOPS. If the operator of the detector is performing a routine scan of an area they may be unwilling to accept a high probability of false alarm. Other scenarios may be based on some form of intelligence that a source is suspected to be present in a specific area. In this case it may be acceptable to trade false alarm probability for detection probability. Figure 11.8 shows ROC curves for a  $^{137}\text{Cs}$  source located at 25 *m* DCA, for 240 runs at 15



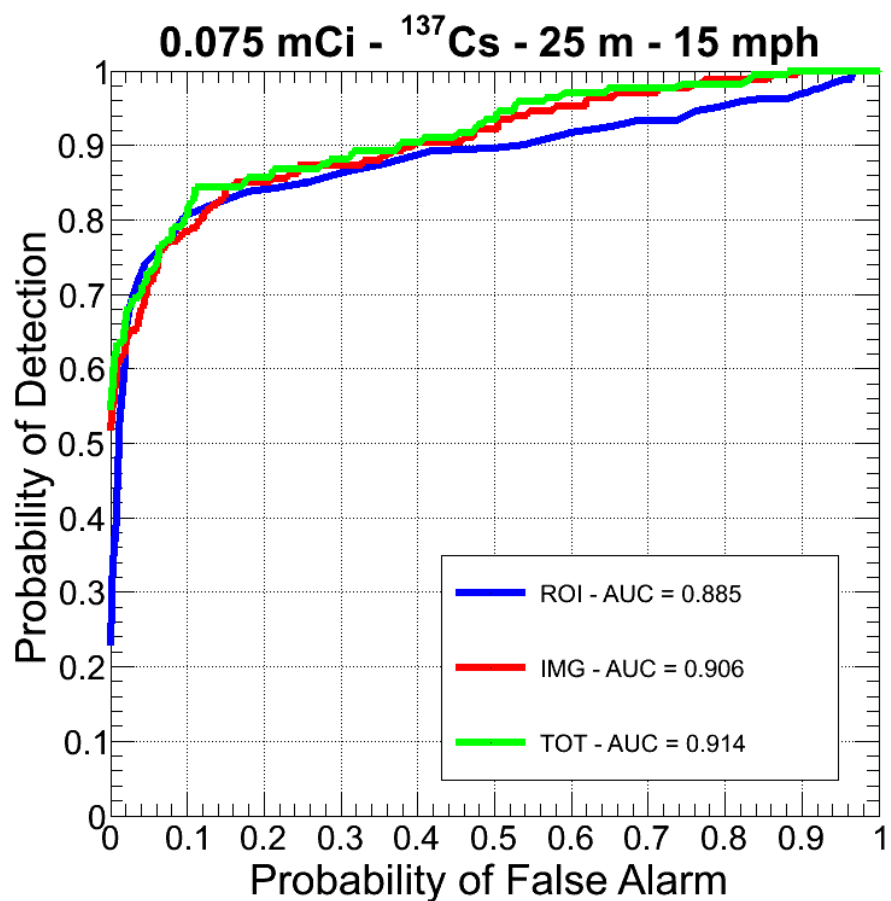


Figure 11.6: ROC analysis of ROI significance (blue), hybrid CA/CI gamma-ray imaging (red) and the combination (green). This curve was generated using 240 injected source runs past a  $75 \mu\text{Ci}$ ,  $^{137}\text{Cs}$  source at 25 m DCA and 15 mph.

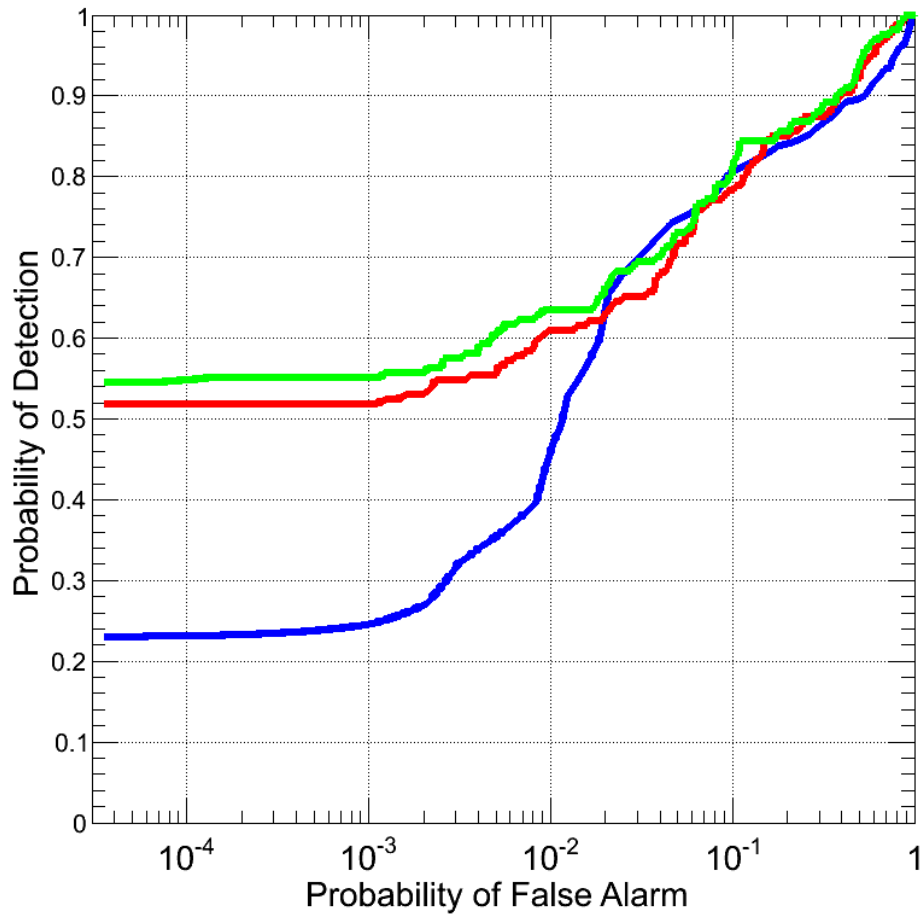


Figure 11.7: ROC analysis of ROI significance (blue), hybrid CA/CI gamma-ray imaging (red) and the combination (green) showing the region of very low probability of false alarm in more detail.

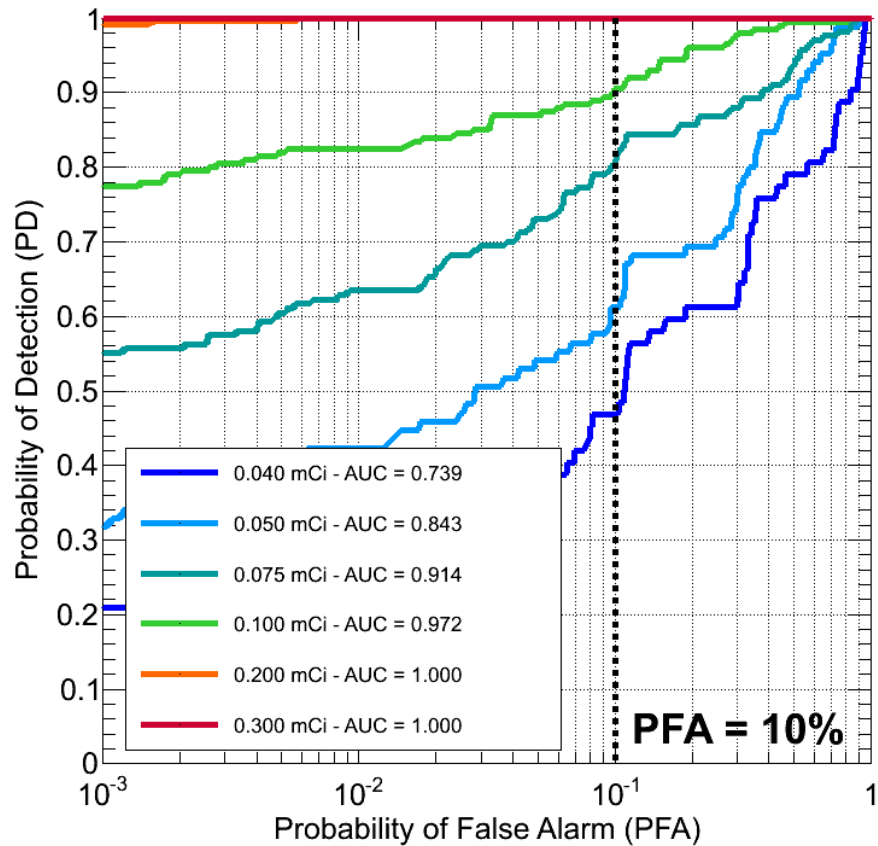


Figure 11.8: ROC curves generated for 240 runs past a  $^{137}\text{Cs}$  source at 25 *m* DCA and 15 *mph* for 0.04, 0.05, 0.075, 0.1, 0.2, and 0.3 *mCi* for the ROI algorithm.

*mph*. Each line represents a different source activity including 0.04, 0.05, 0.075, 0.1, 0.2, and 0.3 *mCi*.

For example, if the operator is willing to tolerate a PFA of 10%. By using the ROC curves in Fig. 11.8 the Probability of Detection (PD) for each activity can be determined for the selected PFA, shown with a dashed black line. By correlating source activity versus PD at a prescribed PFA data points can be interpolated to estimate the MDA. Figure 11.9 shows the source activity as a function of PD for

the arbitrary selected PFA of 10%. Now say the operator, in addition to accepting a PFA of 10%, wishes to detect with probability 90%. By interpolating the plot in Fig. 11.9 for a PD of 0.90, the hypothetical MDA is estimated to be 0.1 *mCi*. (black lines). There is no single number for MDA because of the nature of detection, it relies heavily on the selection of false alarm probability. As PFA goes to 1, MDA goes to 0, since every point in space will be determined to have a source, eventually the source location will be identified. Conversely, if PFA is strictly 0, MDA effectively goes to infinity because the threshold would need to be set so high that even large sources would never trigger an alarm.

## 11.5 Injection Results

In chapter 10 a method for simulated source injection into measured background was presented. Additionally, chapter 9 classified measured background into various groupings based on the principle NORM components. Data produced through injection methods have been analyzed as a function of both grouping and activity for  $^{137}\text{Cs}$  at 25 *m* DCA and 15 *mph*. Since NORM background is the dominant factor in detection sensitivity and the spectral characteristics of NORM change as a function of time and location it is interesting to observe the effect of various groupings on the detection algorithms. Figures 11.10, 11.11 and 11.12 show the derived ROC curves for the injection studies performed for  $^{137}\text{Cs}$  at 25 *m* DCA and 15 *mph* for 0.04, 0.05, 0.075, 0.1, 0.2 and 0.3 *mCi*. Table 11.1 below summarizes the results of the ROC analysis for each algorithm, activity and background grouping.

From Table 11.1 it can be seen that the area under the curves increases as a function of activity, as expected. Also, in most scenarios the combination of imaging

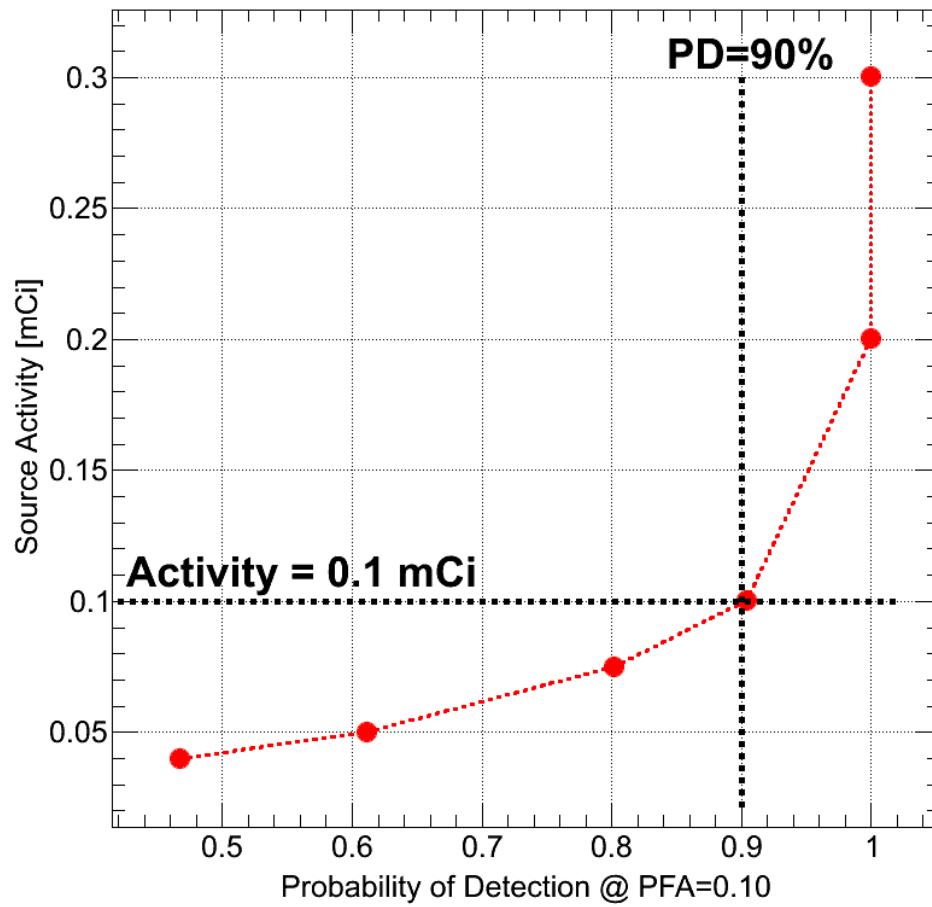


Figure 11.9: Source activity ( $mCi$ ) as a function of probability of detection assuming a false alarm probability of 0.10.

Table 11.1: Areas under the ROC curves for each ROI, CA/CI, and the combination (TOT) generated using 240 runs of injection data for groups 1 and 2, and 20 for group 3. The source injected was a  $^{137}\text{Cs}$  source at 25 m DCA. The TMI speed for each run was 15 mph.

Activity	ROI <sub>1</sub>	IMG <sub>1</sub>	TOT <sub>1</sub>	ROI <sub>2</sub>	IMG <sub>2</sub>	TOT <sub>2</sub>	ROI <sub>3</sub>	IMG <sub>3</sub>	TOT <sub>3</sub>
0.040	0.729	0.724	0.725	0.644	0.698	0.690	0.843	0.546	0.552
0.050	0.769	0.807	0.828	0.615	0.699	0.705	0.966	0.660	0.704
0.075	0.877	0.907	0.913	0.722	0.858	0.868	0.995	0.697	0.724
0.100	0.930	0.971	0.975	0.804	0.927	0.940	1.000	0.946	0.961
0.200	0.993	1.000	1.000	0.974	0.997	0.997	1.000	1.000	1.000
0.300	1.000	1.000	1.000	0.997	1.000	1.000	1.000	1.000	1.000

and ROI improves sensitivity. The results of group 3 indicate superior sensitivity from ROI, however there are limited statistics for background conforming to group 3. It is conceivable that ROI is more sensitive because of the observed characteristics of the group 3 spectrum. Generally, these regions are near water or over bridges where the background rate is significantly decreased. This should allow for easier detection of small signals. Imaging algorithms rely on accurate estimators of the background, ROI does not. Due to the limited statistics in group 3, poor background estimators seem to be causing degraded performance.

## 11.6 Summary

In this chapter a method for analyzing the performance of the detection algorithms implemented on the TMI has been presented. Additionally, it has been shown in previous chapters that, through thoughtful detector design a system can be constructed that combines multiple independent data sets to improve the detector sensitivity over any individual modality alone, over the entire energy range. Fusion of coded

aperture and Compton scatter imaging has been shown to improve AUC (sensitivity) by as much as 64% over Compton imaging alone and 21% over coded aperture alone. Moreover, methods shown in this chapter demonstrate multiple non-imaging and imaging detection modes can be fused to improve the overall sensitivity and lower false alarm rates. Using the methods described in this chapter allow for the calculation of thresholds and minimum detectable activity estimates depending on the concept of operations. Overall the TMI is a powerful tool for detection of weak sources at a distance through the combination of multiple imaging and non-imaging modalities. It gains strength in the combination of these modalities while exploiting the advantages and capabilities of each individually.

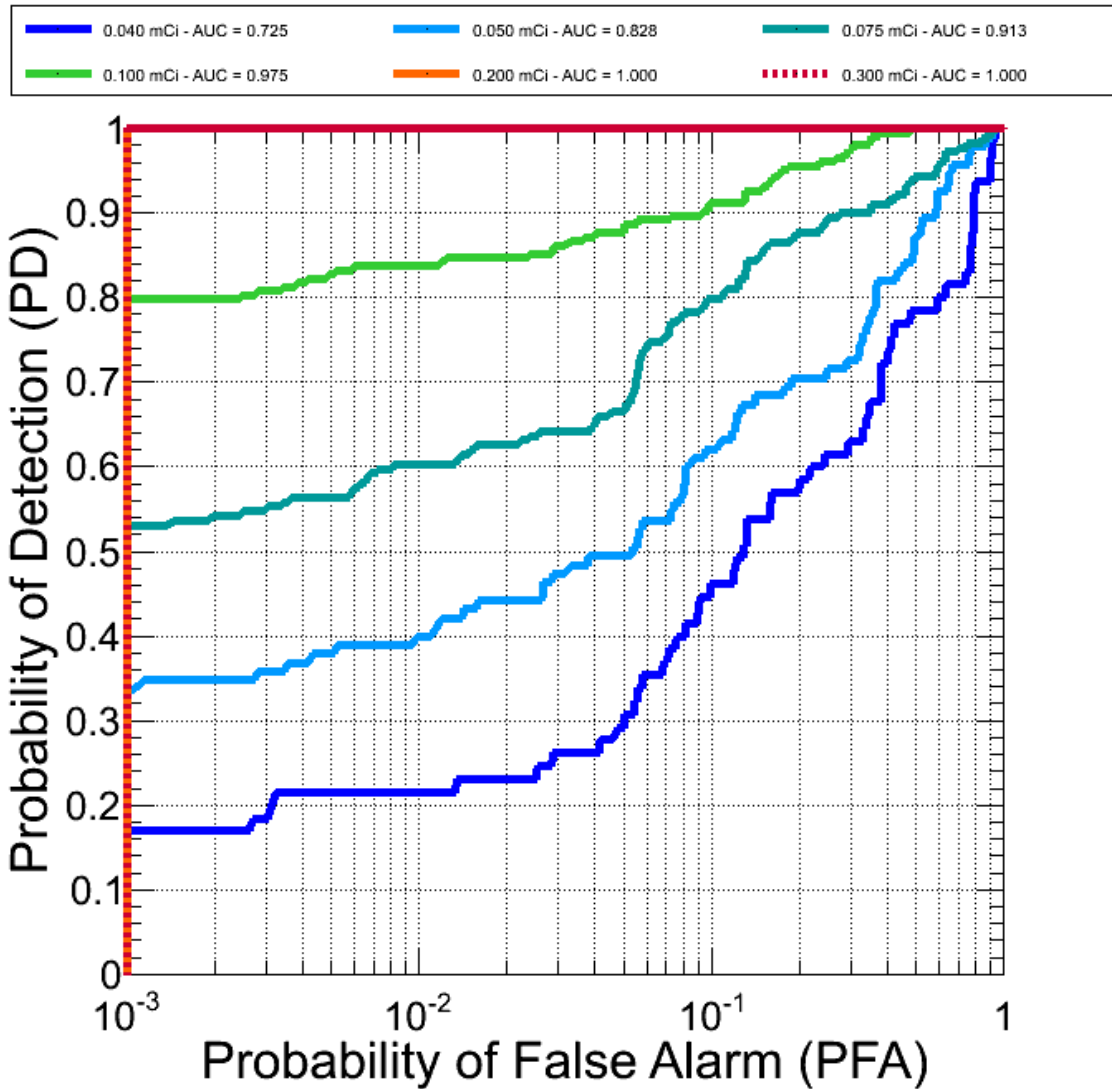


Figure 11.10: ROC curves for the combined analysis. A  $^{137}\text{Cs}$  source at various activities was injected onto NORM background group 1. The source was located at 25 m DCA and the TMI speed was 15 mph.



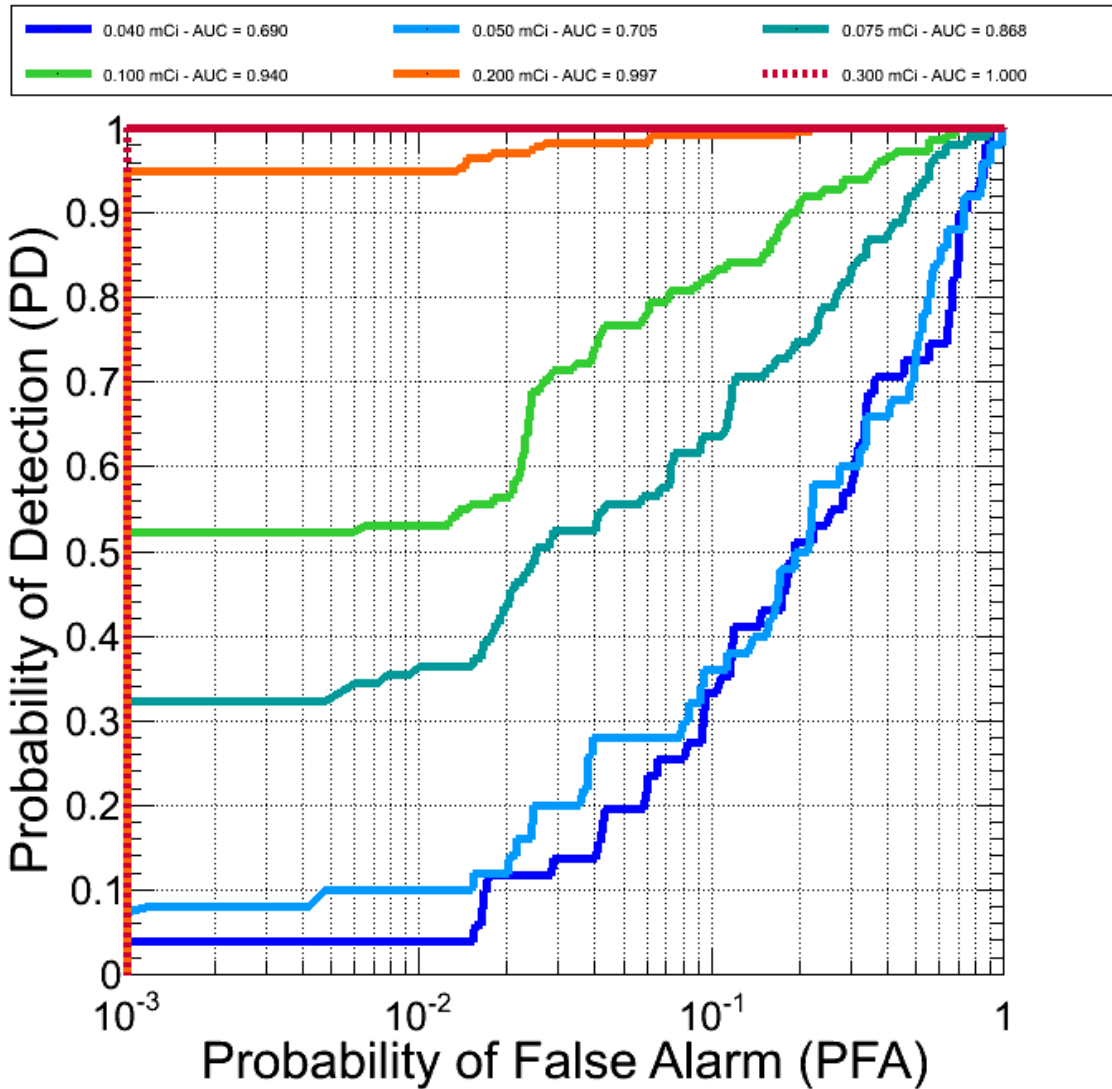


Figure 11.11: ROC curves for the combined analysis. A  $^{137}\text{Cs}$  source at various activities was injected onto NORM background group 2. The source was located at 25 m DCA and the TMI speed was 15 mph.

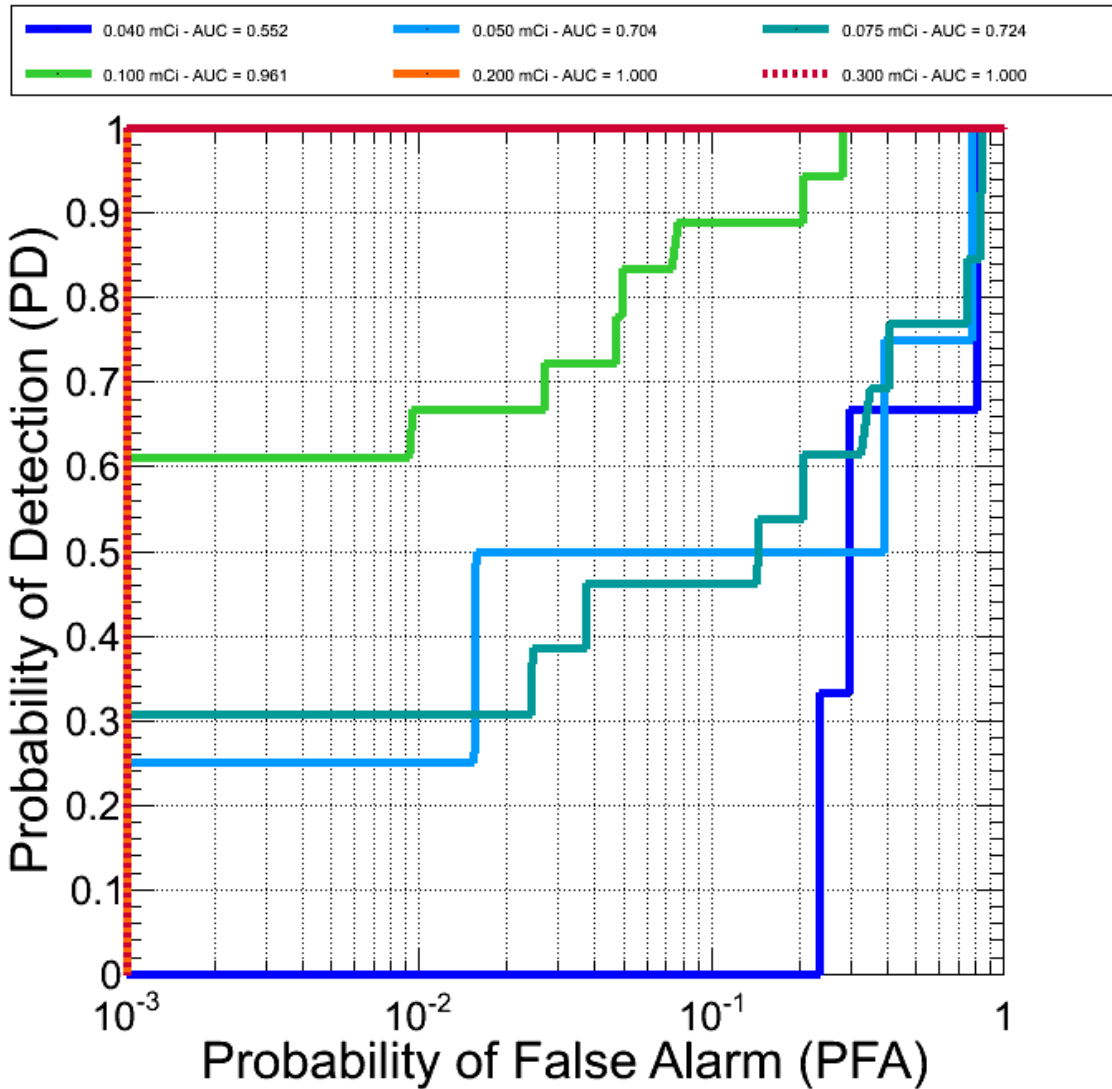


Figure 11.12: ROC curves for the combined analysis. A  $^{137}\text{Cs}$  source at various activities was injected onto NORM background group 3. The source was located at 25 m DCA and the TMI speed was 15 mph.

# Chapter 12

## FIELD TESTING

Once constructed the TMI was delivered for field testing in the fall of 2009. Testing covered a range of scenarios to gauge the applicability and performance of such a system. The results of some of the field tests will be presented in this chapter. Testing of the TMI was conducted over a period from October of 2009 to February of 2010. Data collected during the testing phase of the program have been instrumental in developing the analysis results of chapter 11 as well as providing a large set of measurements to be used for improvement of the algorithms using off-line replay tools. System characterization was conducted at the Department of Energy's SRS facility in Aiken, SC. This facility provided the sources, locations and expertise to perform the characterization uniformly across multiple systems and scenarios. Each of the examples given in this chapter will present the performance of the algorithms to the replay of data recorded during testing using the most recent version of the algorithms. A source that is located or detected is defined as having the maximum significance of all points in the FOV during a run, independent of threshold. Point source localizations must have reported a location within  $\pm 0.2$  radians of ground truth to be considered true. ROI algorithms must report the detection of a source within 50 *m* of the point

of closest approach to the source to be considered true.

## 12.1 Consistency Checking

In order to ensure consistency during testing, each morning a system check was performed. This check consisted of a moving run (15 *mph*) past a 0.5 *mCi*,  $^{137}\text{Cs}$  source at 25 *m* DCA. Figure 12.1 shows an example detection of the source. The source was localized to (33.228168°N, -81.555054°W) with a reported uncertainty of 4.33 meters in the horizontal direction and 2.83 meters in the vertical direction. Ground truth for the source location was (33.228178°N, -81.555054°W), a distance of 1.1 *m* from the alarmed location; well within the reported uncertainty. During this 90 second run the TMI came no closer than 24 *m* from the source according to GPS/INS data. Over the course of the testing campaign the scenario in Fig. 12.1 was repeated 60 times. Replay of recorded TMI data shows the distance of the reported source to ground truth was on average  $3.8 \pm 1.6$  meters with a calculated significance of  $34.62 \pm 7.82$ . The TMI correctly detects, identifies and localizes the source for each of the 60 runs.

## 12.2 Distant Sources

Since the TMI was designed to be a stand-off detection system, testing included measurements to verify the sensitivity to sources at large distances. The general scenario is a point source located at a fixed distance aligned to the center of the detector array. The TMI then drove past the source at 15 *mph* and attempted to detect, identify and localize the source. Table 12.1 summarizes the results of the distance testing where  $\Delta R$  is the average radial distance of the reported maximum significance to the known location of the source.

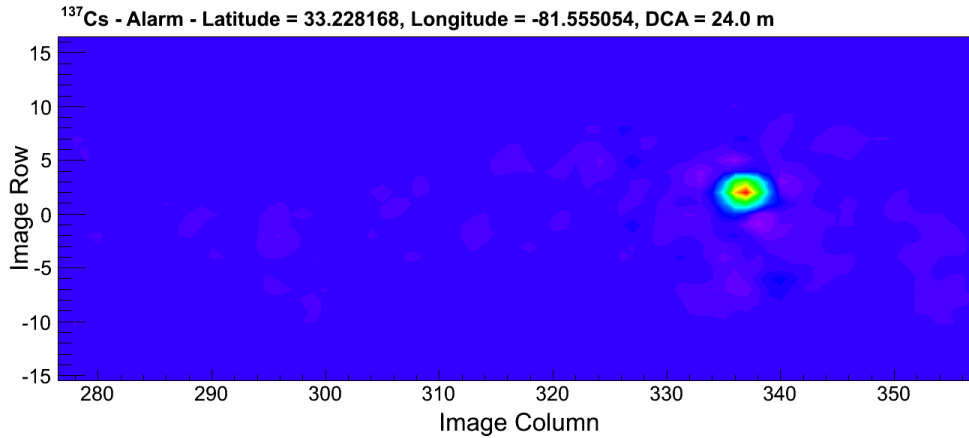


Figure 12.1: Hybrid CA/CI image of the 0.5 *mCi*, <sup>137</sup>Cs source used for consistency checking. The source in the image was reported to have an uncertainty of 5.2 *m*. The actual source location was 1.1 *m* from the reported location.

Table 12.1: Summary of distant source testing performed with the TMI.

Source	Activity [mCi]	Distance [m]	Runs	Located	$\Delta R$ [m]
<sup>137</sup> Cs	10	100	8	8	$7.1 \pm 1.8$
<sup>137</sup> Cs	1	100	18	8	$16.7 \pm 15.1$
<sup>137</sup> Cs	1	50	4	4	$3.5 \pm 0.5$
<sup>68</sup> Ge	4	25	32	32	$3.2 \pm 1.0$

## 12.3 Multiple Sources

In addition to a single gamma-ray point source in the FOV of the detector system it is interesting to evaluate the ability of the system to distinguish multiple point sources. Figure 12.2 shows the results of a run past a <sup>137</sup>Cs source co-located with a <sup>88</sup>Y source at 50 *m* DCA. The TMI correctly detected, identified and localized both sources simultaneously 10 out of 10 times, to within an average of 4.2 meters from ground truth. The ROI algorithms also detected and identified both sources simultaneously

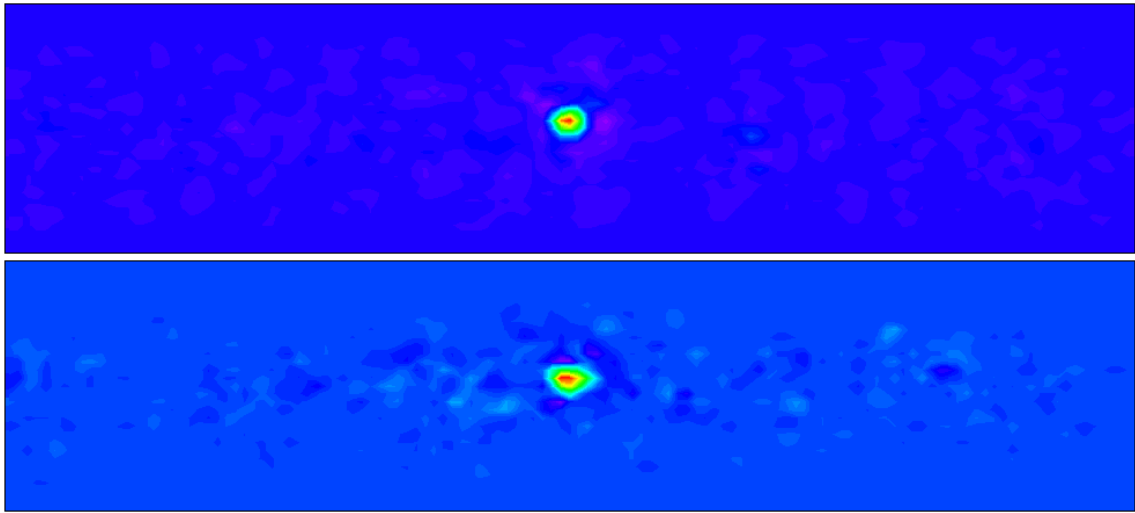


Figure 12.2: Source images for  $^{137}\text{Cs}$  (top) and  $^{88}\text{Y}$  (bottom) co-located at 50 *m* DCA. The TMI correctly detects, identifies and locates both sources simultaneously.

for each run. The calculated significance for the  $^{137}\text{Cs}$  source was 29.02 with a location uncertainty of  $\pm 4.34$  *m*. The calculated significance of the  $^{88}\text{Y}$  source was 24.08 with a location uncertainty of  $\pm 4.30$  *m*. The ROI algorithms calculated a significance of 0.71 for cesium and 0.96 for yttrium.

Results of several of the multiple source tests performed are shown in Table 12.2 below. The orientation specifies the placement of the sources. Co-located means the sources were in the same location, separated refers to a 20 meter distance between the two sources on the same side (curb-side) of the TMI. Opposite runs featured the  $^{137}\text{Cs}$  source on the curb-side of the TMI at 50 *m* DCA and the  $^{88}\text{Y}$  source on the driver side (outside the imager FOV) close to the road. It can be seen from Table 12.2 that the TMI correctly identifies both sources in each of the runs and is able to simultaneously detect sources using non-imaging and imaging modalities. The average distance to the source is not specified for the  $^{88}\text{Y}$  runs when the source was located on

the backside of the TMI because the actual location of the source was not recorded. However, all ROI detections occur within  $\pm 1.9$   $m$  across all 13 runs and are assumed to be correct detections.

Table 12.2: Results of multiple source testing performed with the TMI for both imaging and ROI algorithms. In this table  $N$  is the number of detections over the number of tests performed and  $\Delta R$  is the average distance to the known location of the source in  $m$ .

Algorithm	Orientation	$N_{ss\gamma}$	$\Delta R_{ss\gamma}$	$N_{137Cs}$	$\Delta R_{137Cs}$
Region-of-Interest	co-located	10/10	$52.6 \pm 2.5$	10/10	$54.7 \pm 3.1$
Imaging	co-located	10/10	$4.6 \pm 1.4$	10/10	$4.2 \pm 1.0$
Region-of-Interest	separated	16/16	$52.7 \pm 3.3$	16/16	$53.6 \pm 3.8$
Imaging	separated	16/16	$5.2 \pm 1.8$	16/16	$3.0 \pm 1.5$
Region-of-Interest	opposite	13/13	$\pm 1.9$	13/13	$54.2 \pm 3.2$
Imaging	opposite	0/13	N/A	13/13	$5.4 \pm 2.1$

## 12.4 Shielded Sources

Some scenarios in gamma-ray detection likely include the presence of shielding material. Shielding may be intentional, as in the use of high- $Z$  materials such as lead, or unintentional, through occlusion by objects in the environment. Shielding changes both the intensity and average energy of gamma-rays escaping the shielding, softening the measured energy spectrum. Figure 12.3 shows the results of 18 passes by a 10  $mCi$ ,  $^{137}Cs$  source at 72.5  $m$  DCA. The speed of the truck for these runs was 15  $mph$ . Approximately halfway between the detector and the source there are a series of concrete pylons (yellow box). The pylons were several meters tall and act as a shield of photons emitted from the source. The TMI algorithms accurately detect, identify and localize the source for each of the 18 runs. The average reported distance to the

known location of the source was 1.67 meters. Table 12.3 summarizes several of the results of shielding tests performed at SRNL.

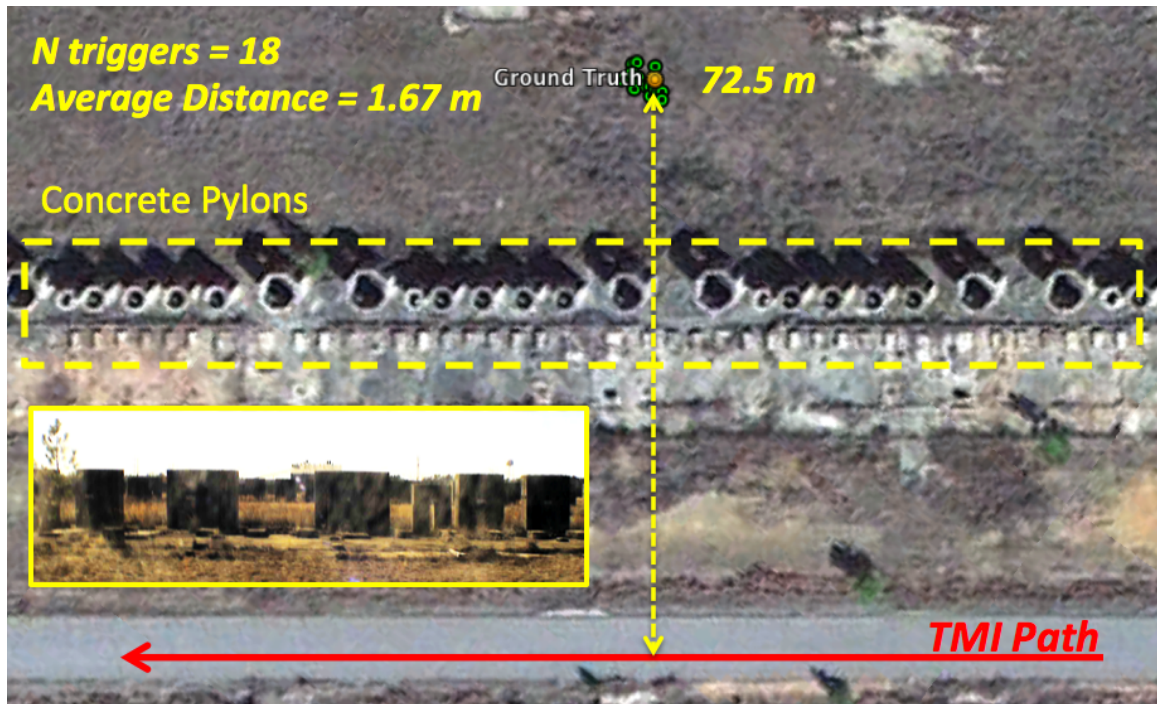


Figure 12.3: Example shielding scenario tested with the TMI. A  $10\text{ mCi}$ ,  $^{137}\text{Cs}$  source was located  $72.5\text{ m}$  from the roadside with large concrete barriers between the source and detector. The TMI detects the source in the scenario 18/18 times within  $1.7 \pm 1.1$  meters of ground truth.

## 12.5 Backside Sources

The TMI has been designed to perform gamma-ray imaging out the curb-side of the vehicle, however it is important to know if a source outside the FOV of the imaging system is present. This is where the spectroscopic detection system is extremely valuable. Figure 12.4 shows the results from 12 runs past a  $1\text{ mCi}$ ,  $^{113}\text{Sn}$  source located at  $25\text{ m}$  DCA on the backside of the TMI. Since the FOV of the imaging system is not



Table 12.3: Summary of all shielding tests performed with the TMI at SRNL.

Source	Activity [mCi]	Distance [m]	Material	Runs	Detects	$\Delta R$ [m]
$^{60}\text{Co}$	1.0	25.0	Lead	8	8	$2.3 \pm 1.0$
$^{60}\text{Co}$	1.0	25.0	Lead	10	5	$3.5 \pm 0.6$
$^{60}\text{Co}$	1.0	10.0	Lead	18	18	$2.0 \pm 0.8$
$^{137}\text{Cs}$	10.0	50.0	Concrete	21	21	$6.9 \pm 1.2$
$^{137}\text{Cs}$	1.0	10.0	Lead	5	5	$3.9 \pm 0.4$
$^{137}\text{Cs}$	10.0	25.0	Lead	2	2	$2.1 \pm 1.3$
$^{60}\text{Co}$	1.0	50.0	Concrete	21	18	$4.4 \pm 1.7$
$^{137}\text{Cs}$	10.0	72.5	Concrete	18	18	$1.7 \pm 1.1$
$^{60}\text{Co}$	1.0	72.5	Concrete	14	12	$7.4 \pm 4.1$

facing the source it does not reconstruct an image and therefore cannot alarm. Since the spectroscopic detection system is independent of direction it is able to detect an increase in SNR in the region around the source and alarm the system. In Fig. 12.4 the green rings show a 50 meter radius around the TMI at the time of the alarm and the red triangle shows the direction of the imaging FOV. The ROI algorithm detected, identified the  $^{113}\text{Sn}$  source correctly as well as localized the proximity for all runs. Table 12.4 summarizes all of the backside tests performed with the TMI during field trials. If the ROI algorithm detects the strong presence of a source and the imaging system does not it is an indication that a source is likely present outside the FOV. To localize the source the imager could be repositioned/retasked until the source is located.

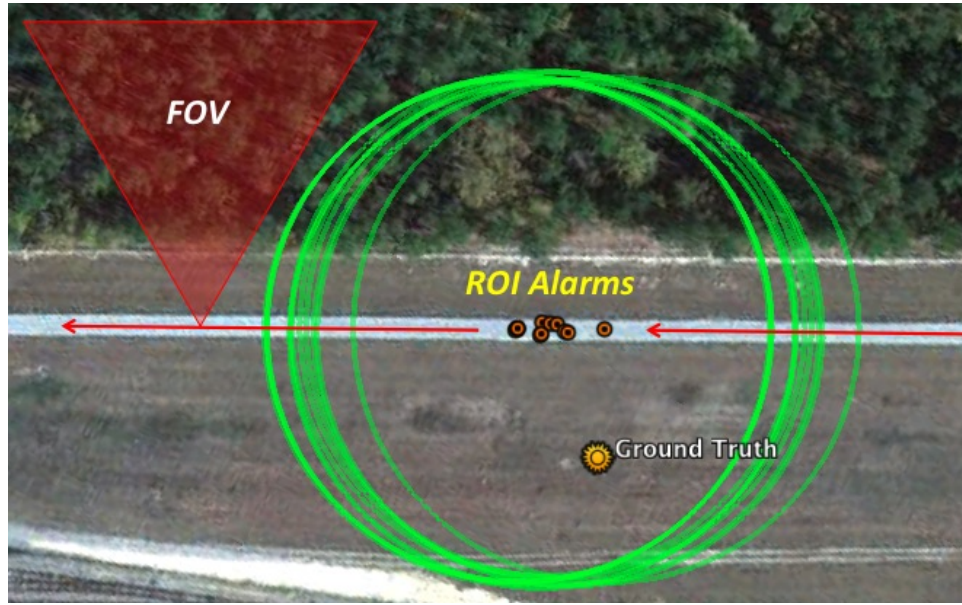


Figure 12.4: Example set of testing runs past a 1  $mCi$ ,  $^{131}I$  source located behind the FOV of the imaging system. The ROI algorithms detect and identify the source even though it is not visible to the imaging system.

## 12.6 Elevated Sources

The location of a source may not always be directly centered on the vertical plane of the imager as in the tests presented so far. As such, testing was performed that included elevated sources. Partially Coded Field-of-View (PCFOV) tests were performed by elevating sources such that only a portion of the DA array was coded (e.g. 50% PCFOV). Figure 12.5 shows three example PCFOV images; 1.0  $mCi$ ,  $^{137}Cs$  (top), 1.0  $mCi$ ,  $^{60}Co$  (middle) and 2.0  $mCi$ ,  $^{57}Co$  (bottom). Each source was elevated 0.35 radians vertically. The calculated significance of the cesium source was 21.10 with a width of 5.2  $m$  FWHM and reported an elevation of  $0.32 \pm 0.06$  radians. The calculated significance of the  $^{60}Co$  source was 19.79 with a width of 4.84  $m$  FWHM and reported an elevation of  $0.34 \pm 0.06$  radians. The calculated significance of the

Table 12.4: Summary of all backside tests performed with the TMI at SRNL where  $\Delta R$  is the distance between the reported and known source location.

Source	Activity [mCi]	Speed [mph]	Distance [m]	Runs	Detects	$\Delta R$ [m]
$^{113}\text{Sn}$	1.0	15.0	-25.0	12	12	$31.4 \pm 1.6$
$^{137}\text{Cs}$	1.0	15.0	-25.0	12	12	$29.1 \pm 2.1$

$^{57}\text{Co}$  source was 9.32 with a width of 5.2 *m* FWHM and reported an elevation of 0.36  $\pm$  0.06 radians. The  $^{57}\text{Co}$  reconstruction is formed using coded aperture only since the energy (122 *keV*) is too low for Compton imaging to be used. Results of additional elevated tests are given in Table 12.5.

Table 12.5: Summary of several elevated source (PCFOV) tests performed with the TMI during field trials.

Source	Activity [mCi]	Distance [m]	Elevation [rad]	Detect	$\Delta R$ [m]
$^{137}\text{Cs}$	1.0	25	0.35	5/5	$3.5 \pm 0.4$
$^{60}\text{Co}$	1.0	25	0.35	10/10	$3.3 \pm 1.0$
$^{57}\text{Co}$	3.0	25	0.35	11/11	$3.4 \pm 0.8$

## 12.7 Medical Sources

During the course of testing several scenarios involving medical sources were characterized. Medical sources are often a source of nuisance alarms for detection systems. The TMI is capable of detecting medicals and classifying them correctly as such. Figure 12.6 shows an example  $^{131}\text{I}$  (top) and  $^{99m}\text{Tc}$  detection (bottom). The iodine source has a calculated hybrid image significance of 26.94 and width of 5.75 *m* FWHM.

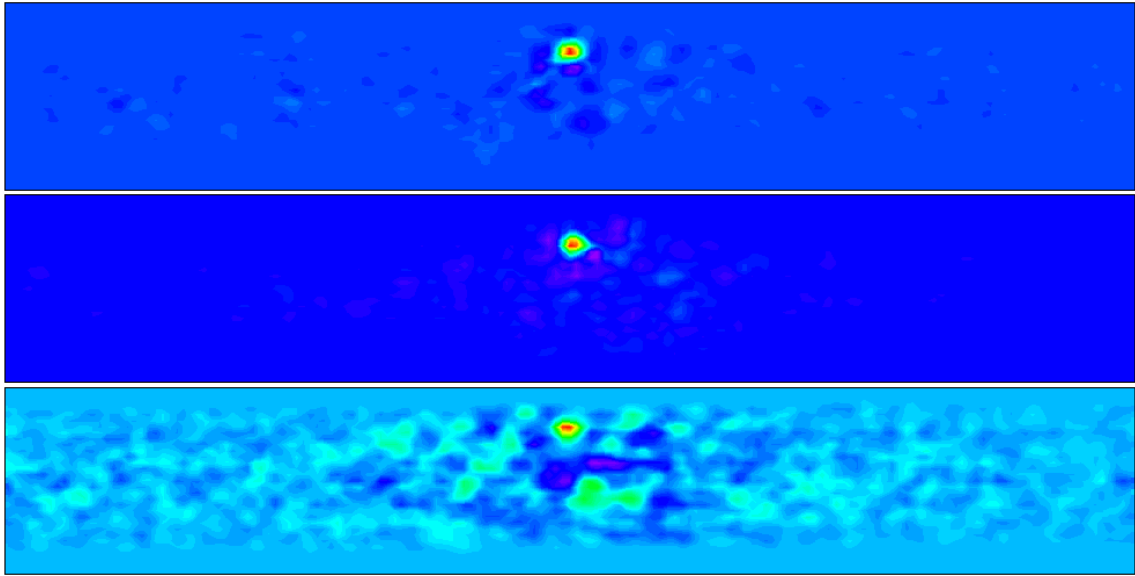


Figure 12.5: Source images for a run past a 1.0 *mCi*,  $^{137}\text{Cs}$  source (top), 1.0 *mCi*,  $^{60}\text{Co}$  (middle) and 2.0 *mCi*,  $^{57}\text{Co}$  (bottom). Each source was elevated 0.35 *rad* from the center of the imager.

The technetium source has a calculated coded aperture image significance of 9.86 and width of 6.58 *m* FWHM. The 140 *keV* gamma-ray line from  $^{99m}\text{Tc}$  is too low in energy for Compton scattering to be used, therefore only coded aperture is included in the result. Table 12.6 summarizes the results of the medical isotope testing.

Table 12.6: Summary of several medial isotope tests performed with the TMI at SRNL.

Source	Activity [mCi]	Distance [m]	Speed [mph]	Detect	$\Delta R$ [m]
$^{99m}\text{Tc}$	2.0	25	15	20/20	$4.5 \pm 1.1$
$^{131}\text{I}$	2.0	25	15	19/19	$3.9 \pm 0.5$

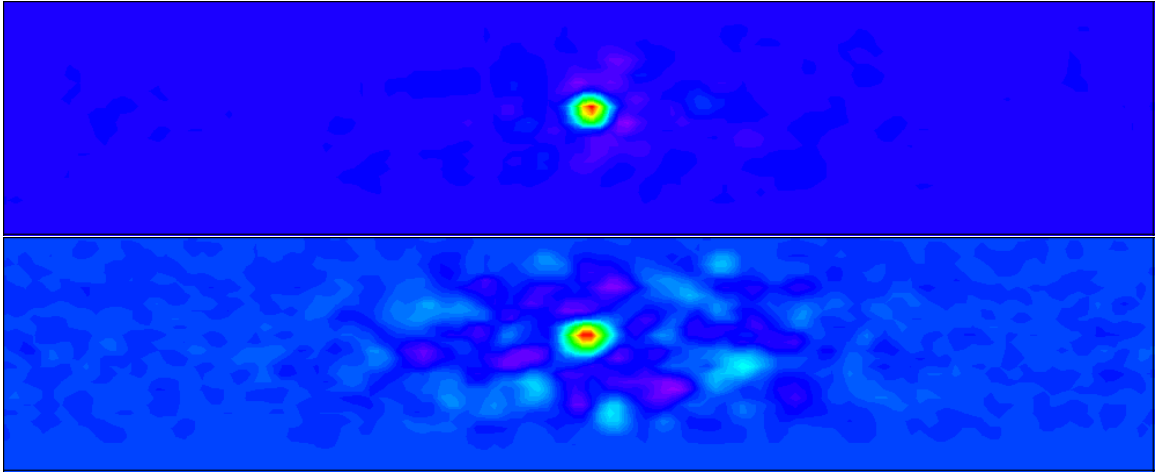


Figure 12.6: Measured  $^{131}\text{I}$  (top) and  $^{99m}\text{Tc}$  (bottom) sources. Each source was 2.0  $m\text{Ci}$  located at 25  $m$  DCA. The speed of the TMI during the measurement was 15  $mph$ .

## 12.8 High Speed Detection

Depending on the CONOPS the TMI may be required to operate at high speed. Tests were performed to verify the response of the system to a source at high speed. A 10  $m\text{Ci}$ ,  $^{137}\text{Cs}$  source was placed at 25  $m$  DCA and the TMI made up to 10 runs at 30, 40, and 50  $mph$  each. Results of the high-speed testing are shown in Table 12.7. Performance may be improved in this scenario by adjusting algorithm parameters for increased speed, for example the peak persistence time. Figure 12.7 shows the reconstructed images for 3 runs past a 10  $m\text{Ci}$ ,  $^{137}\text{Cs}$  source at 25  $m$  DCA and 30 (top), 40 (middle) and 50 (bottom)  $mph$ . The calculated significance for the 30, 40, and 50  $mph$  runs were 52.48, 41.38 and 40.90 respectively. The uncertainty in location reported for the 30, 40, and 50  $mph$  runs was 5.3, 5.4, and 5.8  $m$  FWHM respectively. It can be seen from Fig. 12.7 that the source reconstruction does get slightly wider

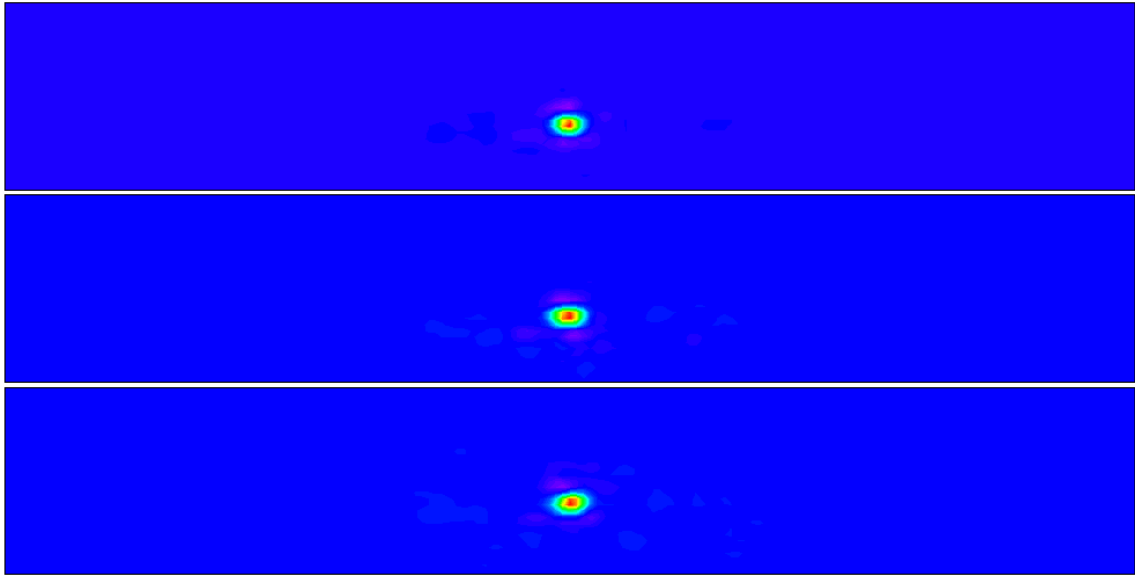


Figure 12.7: Source images for a run past a 10.0  $mCi$ ,  $^{137}\text{Cs}$  source at 25  $m$  DCA for 30  $mph$  (top), 40  $mph$  (middle) and 50  $mph$  (bottom).

as a function of speed however the algorithms are adjusting the segmentation of data on the fly in order to ensure precise reconstruction. The source was slightly below the center of the imager for these runs ( $-0.3$   $rad$ ).

Table 12.7: Summary of all high-speed tests performed with the TMI at SRNL.

Speed [mph]	Runs	Detects	Mean Alarm Distance [m]
30	10	9	$7.9 \pm 0.8$
40	9	6	$9.8 \pm 0.7$
50	10	5	$12.9 \pm 0.7$

## 12.9 Summary

In this chapter it has been shown that the TMI performs well in a range of scenarios related to detection of sources in the real-world. Additionally, the TMI takes advantage of multiple detection modalities to ensure detection of radioactive material at a minimum. In most cases however the sources are detected, identified and localized within expected limits, taking full advantage of the sensitivity gains from the combination of all available data.

# Chapter 13

## FUTURE WORK

A project as extensive as the TMI has many valuable applications. However, a system this complex has areas for potential improvement through algorithm development and additional sensor integration. Much of the future work will involve improvements to currently implemented algorithms as well as study of CONOPS to determine the most useful environments to deploy the system.

### 13.1 SORDS Spiral Development

After the successful characterization campaign at SRS the government team, led by Lawrence Berkeley National Laboratory (LBNL) performed detailed analysis of the TMI and came to the conclusion that it would perform at increased capacity with several changes and modifications to the algorithms. DNDO took this advice and decided to allocate a period of time to make improvements to the TMI. The goal of the improvements is to improve sensitivity and increase the Technology Readiness Level (TRL) of the TMI bringing it closer to a production ready system. To date the team has been actively engaged with DNDO to complete improvements to the system and have shown substantial gains in sensitivity for both imaging algorithms



and isotope identification. Spiral development will culminate in additional limited testing phase to verify performance gains.

## 13.2 Background Modeling

An additional improvement to the TMI is careful treatment of the background. Since the testing campaign we have collected additional data sets that can be used to improve the basis templates used by the imager. This includes characterizing the background among varied environments *e.g.* urban, rural and maritime. Fitting algorithms can be used to compare measurements to the basis templates to both estimate which current environment and how best to best handle the process data based on that information. Using the vast collection of background data and the simulation model of the TMI, algorithms can be written to fuse prior knowledge of detector response with measurements to enhance background suppression.

## 13.3 Sensor Fusion

Technology and algorithms developed for the TMI demonstrate enhanced detection when combining multiple gamma-ray detection methods. Additional gains can be realized through incorporation of additional, non-nuclear, sensors to augment gamma-ray detectors and algorithms in much the same way. Also, given lessons learned on the Stand-off Radiation Detection System (SORDS) program to date, technologies can be improved and migrated to platforms. One such platform is an aerial gamma-ray detection. Aerial radiation monitoring and mapping technology has not changed much since the 1970's and could improve emergency responder's capability to answer actionable intelligence and routine monitoring of areas.

This thesis has shown that multiple gamma-ray detection and imaging modalities can be fused to improve sensitivity. Additional gains in performance can be achieved through non-nuclear peripheral sensors. Research into the applicability of target tracking through radar, lidar, electro-optical and infrared may improve detection. This will allow for improved sensitivity through a reduction in threat space. Also, incorporation of weather sensors could improve detection by providing realtime information to algorithms to better anticipate background levels. Hyperspectral imaging may also provide improved background handling capability by identifying materials in the FOV of the system. Much research has already gone into many of these technologies making them mature and ready for integration with radiation detection systems.

# Chapter 14

## CLOSING REMARKS

This thesis has presented a novel approach to hybrid imaging from a mobile platform. The widely used and complementary methods of coded aperture and Compton scatter imaging have been combined through the use of an active coded mask. It has been shown that the combination of these imaging technologies is superior to either modality alone and sensitivity is increased over a wide range of energies. Additionally it has been shown that non-imaging spectroscopic methods can be combined with imaging methods to further improve sensitivity and extend the range of the system beyond the field-of-view of the imager. It has been shown that simulation and modeling is a valuable tool in the development of any detector system and can allow for algorithm development prior to a realized system. Also, simulation and modeling, once validated, can be used to predict the response of hypothetical systems and provide data to supplement algorithm development. The TMI has been a very successful program whereby a novel detector concept was brought from the drawing board to field testing in just under 2 years. Since then it has continued to improve with the goal of production in the near future. The TMI continues to be fully functional and operate as designed; a considerable feat considering the prototype nature of the sys-

tem. Testing and development will continue on this and similar projects with the goal of continuous improvement to detection of weak sources in the presence of large, dynamic backgrounds.

## Chapter 15

# ACKNOWLEDGEMENTS

I would like to thank the Department of Homeland Security's Domestic Nuclear Detection Office for funding this research. I would also like to thank all of our collaborators from Raytheon Integrated Defense Systems; Michael V. Hynes, Maurice Toolin, Michael King, John McElroy, Bruce Chignola, Bernard Harris and the rest of the Raytheon team. I would like to thank our collaborators at Bubble Technology Industries, Daniel Wakeford, Liane Ing, Martin Smith and Nicholas Hartmaan and the rest of the BTI team. And finally the members of the Los Alamos National Laboratory team, Mark Wallace, David Palmer, Andrew Hoover, Larry Schultz, Mark Galassi and Michal Mocko.

I would also like to thank my dissertation committee from the University of New Mexico; Adam Hecht, Gary Cooper, Douglas Fields and John Sullivan. A special thank you to John Sullivan, Mohini Rawool-Sullivan and Mark Wallace at Los Alamos National Laboratory for mentoring me throughout this program and being a part of my professional development, your knowledge, expertise and patience has made this possible.

Finally, I would like to thank my family, especially my wife Stephanie for support-

ing me through this processing and encouraging me at every step. I could not have done it without you.

Thank you.

# Bibliography

- [1] E. Fenimore, T. Cannon, "Coded Aperture Imaging with Uniformly Redundant Arrays," *Appl. Opt.*, vol. 17, no. 3, pp. 337-347, 1978
- [2] E.E. Fenimore, "Coded aperture imaging: the modulation transfer function for uniformly redundant arrays," *Journal of Applied Optics*, Vol. 19. No. 14, pp. 2465-2471, 1980.
- [3] Gottesman, S.R. and E.E. Fenimore, "New Family of Binary Arrays for Coded Aperture Imaging," *Journal of Applied Optics*, Vol. 28, No. 20, pp. 4344-4352, 1989.
- [4] B. Allen *et al.*, "ProtoEXIST: Advanced Prototype CZT Coded Aperture Telescopes for EXIST," *SPIE Space Telescopes and Instrumentation Proceedings*, Vol. 7732, 2010.
- [5] Gotz, D. and S. Mereghetti, "Observations of Gamma-Ray Bursts with INTEGRAL," *Proceedings of The Gamma Ray Universe*, Les Arcs, 9-16 March, 2002.
- [6] Grindlay *et al.*, "EXIST: mission design concept and technology program," *Proceeding of SPIE* Vol. 4851, 2002.
- [7] Parsons, A.M. "The Swift Gamma-Ray Burst Explorer Burst Alert Telescope (BAT)," *2001 IEEE Nuclear Science Symposium Conference Record*, Vol. 4, pp. 2382-2386, 2001.
- [8] R. Dicke, "Scatter-Hole Cameras for X-Rays and Gamma Rays," *Astrophys. J.*, vol. 153, iss. 2P2, pp. L101, 1968
- [9] Wunderer, C.B., *et al.*, "Imaging with the Coded Aperture Gamma-Ray Spectrometer SPI aboard INTEGRAL," *X-Ray and Gamma-Ray Telescopes and Instruments for Astronomy, Proc. SPIE*, Vol. 4851, 2003.

- [10] Ubertini, P., *et al.*, "IBIS: The Imager on-board INTEGRAL," *Astronomy and Astrophysics*, Vol. 411, pp. 131-139, 2003.
- [11] Limousin, O., *et al.*, "Qualification model of the space ISGRI CdTe gamma-ray camera," *NIM A*, Vol. 471, pp. 174-178, 2001.
- [12] Smith, L.E., *et al.*, "Hybrid collimation for industrial gamma ray imaging: combining spatially coded and Compton aperture data," *Nuclear Science Symposium 1998 Conference Record*, Vol. 2, pp. 1040-1045, 1998.
- [13] Mitchell, L.J *et al.* "Mobile Imaging and Spectroscopic Threat Identification (MISTI): System Overview," *2009 IEEE Nuclear Science Symposium Conference Record*, IEEE/NSS Oct. 24-Nov.1. 2009.
- [14] Wulf, E.A *et al.* "MISTI Imaging and Source Localization," *2008 IEEE Nuclear Science Symposium Conference Record*, 2008.
- [15] Mitchell, L.J *et al.* "Mobile Imaging and Spectroscopic Threat Identification (MISTI)," *2008 IEEE Nuclear Science Symposium Conference Record*, 2008.
- [16] Ziock, K.P. *et al.*, "A Fieldable-Prototype, Large-Area, Gamma-Ray Imager for Orphan Source Search," *IEEE Trans. Nuclear Science*, Vol. 55, No. 6, pp. 3643-3653, 2008.
- [17] J.D. Kurfess *et al.*, "An Advanced Compton Telescope Based on Thick, Position-Sensitive Solid-State Detectors," *New Astronomy Reviews.*, vol. 48, 2004 pp. 293-298.
- [18] L. Mihailescu *et al.*, "SPEIR: a Ge Compton Camera," *Nuclear Instruments and Methods in Physics Research, Section A (Accelerators, Spectrometers, Detectors and Associated Equipment)*, vol. 570, no. 1, 2007 pp. 89-100.
- [19] K. Vetter *et al.*, "High-sensitivity Compton imaging with position sensitive Si and Ge detectors," *Nuclear Instruments and Methods in Physics Research, Section A (Accelerators, Spectrometers, Detectors and Associated Equipment)*, vol. 579, no. 1, 2007 pp. 363-366.
- [20] T. Niedermayr *et al.*, "Gamma-ray imaging with a coaxial HPGe detector," *Nuclear Instruments and Methods in Physics Research, Section A (Accelerators, Spectrometers, Detectors and Associated Equipment)*, vol. 553, no. 3, pp. 501-511, 2005.



- [21] E. Wulf *et al.*, “Germanium Strip Detector Compton Telescope Using Three Dimensional Readout,” *IEEE Transactions on Nuclear Science*, vol. 50, no. 4, pp. 1182-1189, August 2003.
- [22] K. Vetter *et al.*, “Gamma-ray imaging with position-sensitive HPGe detectors,” *Nuclear Instruments and Methods, Section A (Accelerators, Spectrometers, Detectors and Associated Equipment)*, vol. 525, pp. 322-327, 2004.
- [23] K. Vetter *et al.*, “Large-Volume Si(Li) Orthogonal-Strip Detectors for Compton-Effect-Based Instruments,” *IEEE Trans. Nucl. Sci.*, vol. 52, no. 6, pp. 3181-3185, December 2005.
- [24] J.P. Sullivan, *et al.*, “Detector tests for a prototype Compton imager,” *IEEE Nuclear Science Symposium*, vol. 2, pp. 1384-1388, 2003.
- [25] J.P. Sullivan, S.R. Tornga and M.W. Rawool-Sullivan, “Extended radiation source imaging with a prototype Compton imager,” *Applied Radiation and Isotopes*, vol. 67, pp 617-624, 2009.
- [26] M.W. Rawool-Sullivan *et al.*, “A simple algorithm for estimation of source-to-detector distance in Compton imaging,” *Applied Radiation and Isotopes*, vol. 66, pp 1986-1991, 2008.
- [27] S.R. Tornga *et al.*, “Three-Dimensional Compton Imaging Using List-Mode Maximum Likelihood Expectation Maximization,” *IEEE Transactions on Nuclear Science*, vol. 56, no. 3, pp. 1372-1376, June 2009
- [28] T. Tanaka *et al.*, “Development of a Si/CdTe semiconductor Compton telescope,” *High-Energy Detectors in Astronomy, Proceedings of SPIE*, vol. 5501, pp. 229-268, 2004.
- [29] D. Xu *et al.*, “ $4\pi$  Compton imaging with single 3D position sensitive CdZnTe detector,” *Hard X-Ray and Gamma Detector Physics VI, Proc. SPIE*, vol. 5540, pp. 144-155, 2004.
- [30] C. Lehner *et al.*, “ $4\pi$  Compton Imaging Using a 3-D Position Sensitive CdZnTe Detector Via Weighted List-Mode Maximum Likelihood,” *IEEE Transactions on Nuclear Science*, vol. 51, no. 4, pp. 1618-1624, 2004.
- [31] E. Aprile *et al.*, “The LXeGRIT Compton Telescope Prototype: Current Status and Future Prospects,” *Proc. SPIE*, vol. 4851, pp. 1196-1209, 2003.

- [32] Rassmussen, J.O., "Alpha-Decay Barrier Penetrabilities with an Exponential Nuclear Potential: Even-Even Nuclei," *Physical Review*, Vol. 113, No. 6, pp. 1593-1598, 1959.
- [33] Knoll, G.F., "Radiation Detection and Measurement 3<sup>rd</sup> Edition," *John Wiley and Sons Inc.*, Print, 2000.
- [34] Moses, W.W. *et al.*, "Scintillator Non-Proportionality: Present Understanding and Future Challenges," *IEEE Transactions on Nuclear Science*, Vol. 55, No. 3, June 2008.
- [35] Friedlander, Kennedy, and Miller. "Nuclear and Radiochemistry 2<sup>nd</sup> Edition," *John Wiley and Sons, Inc.*, 1964. Print.
- [36] M.J. Berger *et al.*, "XCOM: Photon Cross Sections Database," *NIST Standard Reference Database 8 (XGAM)*, 2009.
- [37] A. Einstein, "On a heuristic viewpoint concerning the production and transformation of light," *Annalen der Physik*, vol. 17, pp. 132-148, 1905.
- [38] A. Compton, "A Quantum Theory of the Scattering of X-rays by Light Elements," *The Physical Review*, vol. 21, no. 5, pp. 484-501, 1923.
- [39] C. Ordonez, A. Bolozdynya and W. Chang, "Doppler Broadening of Energy Spectra in Compton Cameras," *IEEE Nuclear Science Symposium*, vol. 2, pp. 1361-1365, 1997.
- [40] O. Klein and Y. Nishina, "Scattering of radiation by free electrons on the new relativistic quantum dynamics of Dirac," *Zeitschrift fur Physik*, vol. 52, no. 11-12, pp. 853-868, 1929.
- [41] KVH Industries Inc., "KVH's GPS/IMU Continuous Navigation System," <http://www.kvh.com>.
- [42] Directorate of Analysis, "Circular Error Probable [CEP]," *HQ AFOTEC Technical Paper 6.0*, Kirtland AFB NM, July 1987.
- [43] Hamamatsu, "UBA SBA Photomultiplier Tubes," [http://jp.hamamatsu.com/resources/products/etd/eng/html/pmt\\_003.html](http://jp.hamamatsu.com/resources/products/etd/eng/html/pmt_003.html), Accessed: 17 Feb 2013.
- [44] D. Wakeford *et al.*, "The SORDS trimodal imager detector arrays," *Proc. Soc. Photo-Opt. Instrum. Eng. (SPIE)*, vol. 7310, 2009

- [45] A. Hoover *et al.*, “Simulation and Modeling for the Stand-Off Radiation Detection System (SORDS) using GEANT4,” *Nuclear Science Symposium Conference Record (NSS/MIC)*, 2009 *IEEE.*, pp. 914-917, 2009.
- [46] A. Hoover, R.M. Kippen, M. Wallace, “General Response Simulation System (GRESS) Software User’s Guide,” *Los Alamos National Laboratory*, Los Alamos, NM, July 2010.
- [47] A.S. Hoover, *et al.*, “The GLAST Burst Monitor Instrument Response Simulation System,” *Il nuovo cimento C*, Vol. 28 No. 4-5, pp. 797, 2005.
- [48] S. Agostinelli *et al.*, “Geant 4 - A simulation toolkit,” *Nuclear Instruments and Methods in Physics Research, Section A (Accelerators, Spectrometers, Detectors and Associated Equipment)*, vol. 506, no 3., pp. 250-303, 2003.
- [49] “Radioactivity in Nature,” *Idaho State University, Radiation Information Network*, Retrieved January, 28, 2013, from <http://www.physics.isu.edu/radinf/natural.htm>.
- [50] Hynes, M.V., personal communication, 2008.
- [51] M. Hynes *et al.*, “The Raytheon-SORDS trimodal imager,” *Proc. Soc. Photo-Opt. Instrum. Eng. (SPIE)*, vol. 7310, 2009
- [52] Covault, C. E., *et al.* “Techniques for Removing Non-uniform Background in Coded-Aperture Imaging on the Energetic X-ray Imaging Telescope Experiment,” *IEEE Trans. Nuc. Sci.*, Vol. 38, No. 2, pp. 591-596, 1991.
- [53] G.F. Benedict *et al.*, “Interferometric Astronomy of Proxima Centauri and Barnard’s Star Using Hubble Space Telescope Fine Guidance Sensor 3: Detection Limits for sub-Stellar Companions”, *Journal of Astrophysics*, Vol. 118, pp. 1086-1100, 1999.
- [54] LKB Resources, Inc., “NURE aerial gamma-ray and magnetic reconnaissance survey,” *United States Department of Energy*, Open-File Report GJBX-88-79, 5 Volumes, 1979.
- [55] Eisenbud, Merrill, and Tom Gesell. “Environmental Radioactivity from Natural, Industrial and Military Sources 4<sup>th</sup> Edition,” *Academic Press Inc.*, 1997. Print.
- [56] Kathren, Ron. “Radioactivity in the Environment,” *Taylor and Francis Pub.*, 1991. Print.

- [57] F. James, "MINUIT: Function Minimization and Error Analysis," *Computing and Networks Division*, CERN Geneva Switzerland, May 2000.
- [58] Kanungo, T. *et.al.*, "An efficient k-means clustering algorithm: analysis and implementation," *IEEE Transactions on Pattern Analysis and Machine Intelligence*, Vol. 24, No. 7, pp. 881-892, 2002.
- [59] S.P. Lloyd, "Least Squares Quantization in PCM," *IEEE Transactions on Information Theory*, Vol. 28, pp. 129-137, 1982.
- [60] J. MacQueen, "Some Methods for Classification and Analysis of Multivariate Observations," *Proc. Fifth Berkeley Symp. Math. Statistics and Probability*, Vol. 1, pp. 281-296, 1967.
- [61] E. Forgey, "Cluster Analysis of Multivariate Data: Efficiency vs. Interpretability of Classification," *Biometrics*, Vol. 21, pp. 768, 1965.
- [62] D. Waymire, D. Mitchell, "GADRASw User Manual;" Draft Report, Sandia National Laboratory, March 2004.
- [63] "Aerial Measuring System - Technical Integration - Annual Report," Remote Sensing Laboratory, June 2003.
- [64] M. Matsumoto, T. Nishimura, "Mersenne Twistor: a 623-dimensionally equidistributed uniform pseudorandom number generator," *ACM Transactions on Modeling and Computer Simulation*, vol. 8, no. 1, pp. 3-30, 1998.
- [65] "Unix time," Wikipedia, The Free Encyclopedia. Wikimedia Foundation, Inc. 22 July 2004. Web. 6 Dec. 2012.
- [66] Zweig M.H. and Campbell G., "Receiver-Operating Characteristic (ROC) Plots: A Fundamental Evaluation Tool in Clinical Medicine," *Clin. Chem.*, Vol. 39, No. 4, pp. 561-577, 1993.
- [67] Green, D.M. and Swets, J.A, "Signal detection theory and psychophysics," *John Wiley and Sons Inc.*, 1966. Print.
- [68] Zhang, J. and Mueller, S.T. "A Note on ROC analysis and non-parametric estimate of sensitivity" *Psychometrika*, Vol. 70, No. 1, pp. 203-212, 2005.
- [69] W.W.Peterson, and T.G. Birdsall, "The Theory of Signal Detectability," *Electronic Defense Group, University of Michigan*, Technical Report No. 13 (Unclassified), 1953.

# Chapter 16

## ACRONYMS

<b>ADC</b>	Analog-to-Digital Converter
<b>AGN</b>	Active Galactic Nuclei
<b>ASP</b>	Advanced Spectroscopic Portal
<b>ATD</b>	Advanced Technology Demonstration
<b>AUC</b>	Area Under the Curve
<b>BAT</b>	Burst Alert Telescope
<b>BTI</b>	Bubble Technology Industries
<b>CA</b>	mask array
<b>CAI</b>	Coded Aperture Imaging
<b>CCA</b>	Circuit Card Assembly
<b>CEP</b>	Circular Error Probable
<b>CDF</b>	Cumulative Distribution Function
<b>CdTe</b>	Cadmium-Telluride
<b>CSI</b>	Compton Scatter Imaging
<b>CsI</b>	Cesium-Iodide
<b>CsI(Na)</b>	Sodium Doped Cesium-Iodide

**CONOPS** Concept of Operations  
**COTS** Commercial-Off-The-Shelf  
**CZT** Cadmium-Zinc-Telluride  
**DA** detection array  
**DAS** Data Analysis System  
**DCA** Distance of Closest Approach  
**DNDO** Department of Homeland Security's Domestic Nuclear Detection Office  
**EMI** Electromagnetic Interference  
**ECU** Event Characterization Unit  
**EXIST** Energetic X-ray Imaging Survey Telescope  
**FAR** False Alarm Rate  
**FOV** Field-of-View  
**FPGA** Field-Programmable Gate Array  
**FWHM** Full-Width at Half-Maximum  
**GEANT4** Geometry and Tracking Toolkit v4  
**GPS** Global Positioning System  
**GRB** Gamma Ray Burst  
**GRESS** General Response Simulation System  
**HPGe** High-Purity Germanium  
**HPGC** Hybrid Portable Gamma Camera  
**HV** High-Voltage  
**HVCCA** High-Voltage Circuit Card Assembly  
**IBIS** Imager on-board the Integral Satellite  
**IMU** Inertial Measurement Unit

<b>INS</b>	Inertial Navigation System
<b>INTEGRAL</b>	International Gamma-Ray Astrophysics Laboratory
<b>LANL</b>	Los Alamos National Laboratory
<b>LBNL</b>	Lawrence Berkeley National Laboratory
<b>LED</b>	Light Emitting Diode
<b>MDA</b>	Minimum Detectable Activity
<b>MIDEX</b>	Medium Explorer Program
<b>MISTI</b>	Mobile Imaging and Spectroscopic Threat Identification
<b>Nal</b>	sodium iodide
<b>Nal(Tl)</b>	Thallium Doped Sodium-Iodide
<b>NASA</b>	National Aeronautics and Space Administration
<b>NORM</b>	Naturally Occurring Radioactive Material
<b>NRL</b>	Naval Research Laboratory
<b>PCFOV</b>	Partially Coded Field-of-View
<b>PCI</b>	Prototype Compton Imager
<b>PD</b>	Probability of Detection
<b>PFA</b>	Probability of False Alarm
<b>PMT</b>	Photomultiplier Tube
<b>PHA</b>	Pulse Height Amplitude
<b>PSF</b>	Point Spread Function
<b>ROC</b>	Receiver-Operator Characteristic
<b>ROI</b>	Region-of-Interest
<b>SBA</b>	Super Bialkali
<b>SMA</b>	SubMiniature version A

<b>SNR</b>	Signal-to-Noise Ratio
<b>SOH</b>	State-of-Health
<b>SORDS</b>	Stand-off Radiation Detection System
<b>SRS</b>	Savannah River Site
<b>TDC</b>	Time-to-Digital Converter
<b>TMI</b>	Raytheon-SORDS Tri-Modal Imager
<b>TOA</b>	Time-of-Arrival
<b>TTD</b>	Time-to-Detect
<b>TRL</b>	Technology Readiness Level